APPLICATION OF LINEAR INVERSION THEORY TOWARD THE ESTIMATION OF SEISMIC SOURCE PARAMETERS

Thesis by

Ralph Wilson Alewine, III

In Partial Fulfillment of the Requirements

for the Degree of

Doctor of Philosophy

California Institute of Technology

Pasadena, California

1974

(Submitted March 19, 1974)

ACKNOWLEDGMENTS

The author expresses gratitude to Dr. D. G. Harkrider for his support and guidance throughout this investigation. The advice and interest of the author's colleagues at the Seismological Laboratory, particularly that of Drs. J. B. Minster, T. H. Jordan, T. C. Hanks, and P. H. Jungels, is greatly appreciated. The critical reading and constructive suggestions of portions of this manuscript by Drs. H. Kanamori and J. C. Savage are also appreciated.

For their assistance in the preparation of the final draft of this thesis, the author extends his gratitude to Betty C. Alewine who so ably and patiently typed the manuscript and to Laszlo Lenches who prepared many of the figures.

Portions of this research were supported by the Earth Sciences Section National Science Foundation, Grant No. GA 29920, and by the Advanced Research Projects Agency of the Department of Defense and were monitored by the Air Force Office of Scientific Research under Contract Nos. F44620-72-C-0078 and F44620-70-C-0120. Computing funds for the calculations in the final chapter were supplied by Dr. M. D. Trifunac through the Advanced Research Projects Agency of the Department of Defense and were

monitored by the Air Force Office of Scientific Research under Contract No. F44620-72-C-0097.

ABSTRACT

A discussion is given concerning the development of methods for obtaining an accurate representation of the forward elastostatic problem of describing the processes which accompany faulting. A method is suggested by which a more complicated and arbitrary static dislocation function could be approximated with the formulations derived for simple dislocation sources. A stochastic inverse is used to provide optimum estimates of the source description when observed elastostatic phenomena are systematically related to the media response of the various source parameters. This method is applied to the observed static displacement data from the 1964 Alaska earthquake and the 1971 San Fernando, California, earthquake.

For the Alaskan event, the surface static displacements are calculated with the finite-element numerical modeling technique in which the effects of known geologic heterogeneities of the region are taken into account. The fault model used is that of a shallow angle fault underthrusting the Alaskan continental block. The calculated optimum static offset, stress drop, and strain energy density along the fault were found to be variable with a maximum offset of about 30 m. The region of maximum stress drop (218 bars) and maximum strain energy density change is found to

correspond to the region of maximum compressional wave radiation. The resolution and resolvability of the calculated static fault model is discussed.

For the San Fernando earthquake, the static dislocation along the assumed fault plane was also found to vary considerably. The observed surface displacements are fit to a high degree of accuracy by the given model. Included in the inversion data set are changes in the local gravity field caused by the earthquake. These changes can be predicted from known changes in elevation when a Bouguer correction is applied to the gravity data.

The spatial and frequency distribution of path-corrected Rayleigh waves from the San Fernando earthquake are systematically related to the faulting process. The surface wave source is taken to be a depth-distributed set of double couples. A least-squares inversion is used to find the set of source parameters which optimally fit the variance-weighted data. The inversion results indicate a depth-distributed moment of 1.7×10^{26} dyne-cm. The slip angles of the sources varied in such a way along the fault that the displacements became more predominantly dip slip as the dislocation propagated upward from the point of initial rupture at about 3.0 km/sec. A sophisticated error analysis is performed to estimate the uncertainties of the calculated model variables.

An appendix is included in which the analytical expressions are derived for the complete strain field due to a dislocation on an arbitrarily inclined fault in a homogeneous half-space. Although the expressions are lengthy, the strain values can be calculated quickly on a computer since no numerical integration is necessary.

TABLE OF CONTENTS

Page

Page

Page

Chapter 1
Introduction

In the following chapters of this thesis, we will concern ourselves with the problem of trying to estimate in some systematic fashion various parameters which describe an earthquake source when a set of surface observations due to this source is given. Since observations cannot be made directly about the deformation, strain release, etc., that occur in the hypocentral volume during the occurrence of an earthquake, an accurate investigation becomes a difficult problem. This problem is compounded even further by the fact that the information that is received from the source processes is filtered by the earth in the transmission to the point of observation. The success of the estimation of the characteristics of earthquake phenomena will depend basically on our expertise in two separate areas. The first is our ability to describe adequately the processes which accompany seismic activity. This is referred to as the forward problem. Solving the forward problem usually involves a theoretical description and parameterization of the source mechanism and the responsive nature of the medium to this mechanism. The second area is the ability to infer something indicative about the variables

which characterize these seismic processes when an observational ensemble of their effects is given. Both of these areas will be discussed and applied in some detail in this thesis.

Inherent in the success in the latter area mentioned above is our ability to collect pertinent data which can be related to the effects from seismic activity. The observed data which we associate with seismic activity can be classified into two categories: static observations and dynamic observations. The static observations normally involve the measurement of the permanent changes in the displacement, strain, and gravity fields on the surface of the earth. These data are usually limited to the region in the very near vicinity of the earthquake source region. With the exception of direct strain measurements, static data require some reference level to be established before the occurrence of an event. Dynamical data, on the other hand, require no prior data reference plane in the source region for the data to be meaningful. This latter type of data has the further advantage of being more readily detectable than statical data at observation points outside the source region.

In the following chapters, we will use both types of data to infer various source parameters. The effects that errors in these data have on the estimation of source

parameters is often neglected in source mechanism studies. In this thesis, we will try to minimize the errors in the data that are used to infer a source characterization, but we will also investigate how residual data errors are translated into uncertainties in the source description.

Chapter 2 is concerned with obtaining an optimum description of the zero-frequency component of the seismic source when a set of static data due to that source is given. Both areas of expertise which are necessary to the successful estimation of the source function are examined in some detail in this chapter. Several methods for parameterizing the source process are discussed: dislocation theory, stress pulse theory, stress relaxation theory, and numerical analogues. In the case for the dislocation theory, the parameterization is constructed such that the various source components can vary spatially on a set of arbitrarily oriented fault surfaces. The latter half of this chapter describes a stochastic inversion technique for obtaining an optimum estimate of the source parameters characterizing a fault model when a set of static observations which can be linearly related to the faulting sequence is given. This inversion method has the property of allowing the inclusion of the data variances. Inclusion of these variances gives rise to the formulation of

various operators which can be used to estimate the reliability of the derived optimum solution.

Chapter 3 deals with the applications of the inversion technique described in the previous chapter to the static displacement data caused by deformation resulting from the 1964 Alaska earthquake. For this earthquake, a two-dimensional finite element numerical model is used to calculate surface displacements from a dislocation imposed on a fault surface located in a heterogeneous medium. The inversion technique is used to calculate a dislocation model which fits the observed data to a high degree of accuracy. An error analysis is carried out for the plane-strain approximation, and the resolvability of the features of the calculated dislocation model is examined. The results of this chapter, which appear in a paper by Alewine and Jungels (1973), indicate that the observed deformation occurred as the result of massive underthrusting of the Alaskan continental block by the downgoing Pacific plate.

In Chapter 4, the static displacement data obtained from the 1971 San Fernando, California, earthquake are used to try to determine the faulting mechanism for that event. In this case, the forward problem is solved using a three-dimensional dislocation theory applicable to a homogeneous half-space. The dislocation models calculated

to optimally fit the observed data for both this earthquake and the Alaska earthquake indicate a large degree of spatial variability of dislocation along the assumed fault surfaces. Part of the data set used in the inversion for this earthquake is that obtained by converting changes in the gravity field into changes in elevation. The gravity survey and the method of conversion are described in Appendix 2. The gravity study done in connection with this thesis is incorporated into papers by Oliver et al. (1973) and Robbins et al. (1973). A brief paper describing the contents of this chapter is given by Alewine and Jordan (1973).

An analysis of the surface wave spectra obtained teleseismically from the 1971 San Fernando earthquake is presented in Chapter 5. A numerical method is presented to approximate a finite surface wave source. A spatially distributed source of this type is shown to have spectral values quite different from a point source when the source is distributed vertically. A weighted least-squares inversion technique (derived in Appendix 3) is used to obtain the combination of dynamic source parameters which optimally fit the observed spectra measured at different azimuths from this event. The results of this inversion of dynamic data are then compared to the source solution obtained with the static data.

Chapter 2

Development of the Stochastic Inverse as Applied to Static Dislocation Problems

2.1 Introduction.

The first requisite in the application of any theory toward the estimation of seismic source parameters is the ability to solve the forward problem for the observed data type for an appropriate seismic source. This means simply that given a certain method of physically describing a source (analytically, numerically, or by analogue) we are able to estimate changes in data for a given value, or change in value, of particular parameters which describe the source. Mathematically this is mapping changes in the source model space into changes in the data space. What will be discussed first in this chapter is just this process, and later we will look at the inverse of this process. By the inverse of this process, we mean that given some observations, what estimates can be made about the different source parameters which describe our source?

The inversion scheme for static data that we propose in this chapter has the provision for the inclusion of the estimated variance of the data that is to be inverted. The inclusion of this data variance gives rise to the

fact that we cannot now estimate the seismic source parameters exactly, since small perturbations in the model source parameters might cause changes in the calculated data values which lie inside the estimated data error limits. This concept gives rise to our wondering what ability that we have to actually resolve any detail of the various parameters of our fault model. This resolution question will be examined in some detail in this chapter.

We will first consider the problem of estimating source parameters for static data. The procedure developed for this case can then be extended to that of estimating dynamical source parameters. This extension is done in a later chapter. A brief review of the development of static field solutions due to various earthquake sources is in order.

2.2 Development of the Forward Static Problem.

Numerous attempts have been made in the past several years to interpret the observed permanent changes in the displacement and strain fields due to the occurrence of an earthquake. Various approaches to the solution of this problem have been proposed, each based on a slightly different interpretation of the earthquake source process as a whole. In each of these approaches, there exists in the interior of the elastic medium some discontinuity

surface which we can associate with a "fault". The different initial or boundary conditions that can be applied to this discontinuity surface give rise to the various approaches. These approaches can be broken into four main groups: stress pulse theory, stress relaxation theory, dislocation theory, and numerical analogues. With the exception of the dislocation theory, which will be treated in more detail, a short description of the approach of each of these theories will be presented. The dislocation theory is reviewed in more detail because it involves a parameter that is readily observable when the discontinuity surface breaks the free surface -- a physical offset. In addition, it is somewhat more straightforwardly pleasing to model static dislocations on the surface caused by static dislocations imposed within the medium rather than the more obscure parameters -- stress and strain. However, it will be seen that the other theoretical approaches can be equivalenced to some dislocation representation in the static limit.

Dislocation Theory. As a mathematical model of a "fault", the concept and formulation of a physical dislocation has been extensively used. The dislocation surface in an elastic medium is viewed as a surface over which there is a discontinuity in displacement. One of the first efforts

to explain the elastic displacements resulting from a dislocation was that done by Vvendenskaya (1956, 1958). Probably the most lucid explanation of the dislocation theory for calculating static changes that accompany faulting was given in a set of papers by Steketee (1958a, 1958b). In these papers, Steketee recognized that the relations for the displacement field in an infinite elastic medium strained by a dislocation over some surface as given earlier by Volterra (1907) would be appropriate in describing the deformation that accompanies faulting. Steketee derived, through the use of Galerkin vectors, the expressions for static displacements in an infinite elastic solid. These relations were given in compact form as integrals over the dislocation surface.

In his papers, Steketee poses the following problem. A dislocation surface, Σ , is created within an elastic solid which is bounded by some surface S . The medium is then strained by the introduction of a certain distribution of "nuclei of strain" (Love, 1944) along the dislocation surface. The nuclei were shown to exist in six basic forms corresponding broadly to a combination of a center of dilatation and a double force without moment, and secondly, two coplanar, mutually perpendicular double forces with moments. For pure shear dislocations, only

the latter type nuclei are applicable, whereas, for pure tensile dislocations, the former are applicable. The displacements at a point Q, $u_k(Q)$, within the elastic solid can be written as

$$u_k(Q) = \frac{1}{8\pi\mu}\iint_{\Sigma} \Delta u_i(P)\omega_{ij}^{k}(P,Q)\nu_j d\Sigma - \frac{1}{8\pi\mu}\iint_{S} u_i\omega_{ij}^{k}(P,Q)\nu_j ds \quad . \tag{2.1}$$

In this equation ν_j are the direction cosines of the normal to the dislocation surface elements, μ is the rigidity, and $\Delta u_i(P)$ is the dislocation function on the surface Σ. It is seen that for an arbitrary dislocation, a set of six of these functions is necessary. (i=1,2,3 j=1,2,3 with ij=ji.) The kernels of the integrals, $\omega_{ij}^{k}(P,Q)$, are the displacements at the observation point due to a single nucleus of strain. A summation over all nuclei is implied. As the surface S is enlarged to infinity, the displacements, u_i, on S approach zero and the second integral vanishes.

The formalism for this problem was extended to include a dislocation in a semi-infinite elastic medium by a

superposition of solutions, which together satisfy the required boundary conditions at the free surface. These boundary conditions require the solution to be a fairly complex boundary value problem, however, it is cleverly solved by a superposition of solutions in the following manner. The tangential stress at the free surface is made to vanish by the addition of an image dislocation "above" the free surface. This last superposition is commonly referred to as the Boussinesq problem. The strength of the Boussinesq load is such as to cancel the normal stress on the free surface which is doubled by the addition of the image source. Using the Volterra relations, the displacement field at a point Q in a semi-infinite medium is then given by

$$u_k(Q) = \frac{1}{8\pi\mu} \iint_{\Sigma} \Delta u_i(P) W_{ij}^k(P,Q) \nu_j d\Sigma \ . \qquad (2.2)$$

Comparison of (2.1) and (2.2) shows that only the values of the kernels are changed by the imposed boundary conditions. The kernels of (2.2), W_{ij}^k, are the set of Green's functions found from the superposition of solutions which satisfy these half-space boundary conditions.

Steketee (1958a) gives the exact form of one of these functions, W_{12}^{k}, which is all that is necessary to approximate a vertical strike slip fault. Chinnery (1961, 1963, 1965) took the general expression (2.2) and derived an exact analytical form of the displacement and stress fields on the surface of a semi-infinite medium for an internal rectangularly-shaped dislocation surface modeling a vertical strike slip (transcurrent) fault. In performing these calculations, Chinnery assumed that the dislocation discontinuity was constant over the entire fault, and he also assumed that the Lamé parameters for the solid were equal so that the integration could be carried out exactly. Thus, the elastic medium for which this theory is applicable is one in which the Poisson ratio is constant at 0.25. Steketee (1958a) showed, however, that (2.2) is valid where $\Delta u_i(P)$ takes any form (Somigliana dislocation) provided that the tensile forces across the dislocation surface sum to zero.

Maruyama (1964) has derived the remaining five sets of Green's functions needed in the solution of an arbitrary dislocation problem. He further gives explicit, analytic solutions for the displacement field at the free surface due to constant finite dislocations on rectangular surfaces. The dislocations considered are those only along

single primary axes. The examples that he presents include cases for which the dislocation surface, Σ, is both perpendicular and parallel to the free surface.

Maruyama (1963) and Burridge and Knopoff (1964) showed that the displacement fields produced by a dislocation on a mathematical description of a dislocation fault surface is equivalent to that produced by a suitable distribution of forces on the fault surface acting as if there was no fault present. Utilization of this fact makes possible the use of work in mathematical elasticity theory done much earlier than Steketee's (1958a) work. Notable in this early literature is that by Mindlin (1936) who treated the static problem of a single force acting in a homogenous half-space. Mindlin and Cheng (1950) give explicit expressions for the displacement and stress fields due to point forces and double forces acting in an elastic half-space. Maruyama (1964) gives a short summary of the early literature in Japan and elsewhere on this subject. This includes work done by Sezawa (1929), Honda and Miura (1935), Whipple (1936), Soeda (1944) and Yamakawa (1955). Press (1965) showed that the kernels of (2.2) could be derived in a straightforward manner from the results of Mindlin and Cheng (1950). Press obtained the same results for a vertical strike slip fault as Chinnery had done

previously, and obtained the same results for a vertical dip slip fault as Maruyama (1964) derived. In this paper, Press (1965) added the analytic expressions for tilts and strains for these particular fault orientations. Savage and Hastie (1966) used the theory given by Maruyama (1964) to calculate the vertical displacements induced by dislocations on fault surfaces that could have components of dip other than in a direction perpendicular to the free surface. This led to the ability to model more geologically realistic faults.

Mansinha and Smylie (1971) completed the derivation of the displacement fields due to buried dislocations on finite rectangular surfaces. These authors give the complete closed form, indefinite integral expressions for the entire displacement fields, both at the free surface and at any depth in the elastic half-space, due to a rectangular dislocation surface that can be arbitrarily inclined. The fields are presented in such a form that they are readily evaluated numerically on the computer and involve only simple algebraic and trigonometric functions. However, these authors do not give the formulas for the strain and tilt fields arising from a dislocation across an arbitrarily inclined surface. These strain and tilt fields can be easily obtained from differentiation of the

displacement fields. Appendix 1 of this thesis gives the results of this differentiation.

Chinnery and Petrak (1968) extended the work of Chinnery (1961) by considering a model of a vertical strike slip fault on which the dislocation uniformly and smoothly goes to zero near the edges of the dislocation surface. This variation was chosen so as to remove the stress singularity that was occurring at the edge of the fault surface in the original work. Except in extreme cases, the tapering of the dislocation near the edges of the surface had little effect on the overall displacement fields calculated on the surface.

Ben-Menahem and Singh (1968a) and Ben-Menahem and Gillon (1970) computed the integral expressions for the displacement field, both dynamic and static, at the free surface for a model of a vertical strike slip fault and a vertical dip slip fault for a medium which contains a layer of arbitrary thickness over a uniform half-space. These authors point out that due to the complexity of the problem, the use of the Galerkin vectors for elastic problems involving more than one layer over a half-space would be extremely difficult. These authors suggested the use of a method employing Hansen's eigenvectors in obtaining the static response of a multilayered homogeneous

half-space. McGinley (1969) and Sato (1971) achieved much the same results as these authors by the superposition of several half-space Green's functions solutions off-set in such a way as to represent a layered half-space. Braslau and Lieber (1968) solved the static linearly elastic problem of a concentrated vertical Volterra dislocation in a layer over a half-space. They made use of a special displacement function which they called a modified Galerkin vector to give the solution in a form which must be evaluated numerically. Singh (1970, 1971) has applied the Thomson-Haskell matrix propagation method (Thomson, 1950; Haskell, 1953) to solve the problem of static deformation in a multilayered elastic half-space. He obtains source functions for the six elementary dislocations that were given by Steketee (1958a). Explicit integral expressions are given for the surface displacements for a vertical strike slip and vertical dip slip fault when these faults can be represented by concentrated or point sources. Extension to finite size sources is given as another integration involving the dislocation surface. Recently Chinnery and Jovanovich (1972) have calculated the displacement field due to a vertical strike-slip fault of infinite length for an earth model consisting of two layers of arbitrary thickness and

rigidity over a half-space. Their expressions are given in series form so that no further integration is necessary. On the basis of this model, they conclude (and thus agree with McGinley (1969)) that the presence of a low rigidity layer would have a very strong (amplifying) effect on the observed displacements and strains in the far field.

Ben-Menahem and Singh (1968b) treated in detail the problem of deformation of a uniform non-gravitating sphere due to internal Volterra type dislocations of arbitrary orientation and depth. This work was subsequently expanded (Ben-Menahem et al., 1969, 1970; Singh and Ben-Menahem, 1969; Ben-Menahem and Singh, 1970; Wason and Singh, 1972) to include the computations for the displacement and strain fields everywhere on the surface of a homogeneous sphere induced by an internal dipolar source of finite size. The results for a sphere were shown to be quite different than that expected in the far-field half-space problem.

Stress Pulse Theory. This approach has seen limited use in explaining elastostatic phenomenon. Kasahara (1957) devised this method to model the mechanism of an earthquake as a distribution of stresses or strains imposed on an underground plane. When the conditions of elastic equilibrium are satisfied, the deformations at the surface can be calculated. He models an infinite strike-slip

fault with a zone of constant stress extending to a given depth. The faulting occurs by the liberation of this initially applied shear stress. Horizontal displacements were calculated for various depth extensions and comparisons were made to actual faults. By examining the diminution of horizontal displacement with distance, the depth of extension of this constant stress zone is determined. This mechanism is extended in a second paper (Kasahara, 1959) to include non-vertical strike-slip faults. The static mechanism presented by Kasahara is analogous to the stress pulse problems encountered in dynamical formulations of seismic sources. Minster (1974) describes the mathematical nuances of this approach.

Stress Relaxation Theory. A third method of determining the static deformation from a model of an earthquake is obtained through an entirely different approach to the theoretical problem. The methods considered thus far are all based on relations in which conditions on various boundaries are imposed (boundary-value problems). Archambeau (1964, 1968) has proposed an alternative mechanism of describing the processes which accompany the occurrence of earthquakes -- that of material failure. This theory is devised in the context of an initial-value problem in that a medium is assumed to be initially in some prestressed state. Deformation in the medium is

caused by introducing some surface, or volume, within the medium where the material fails. This failure is accomplished by making a significant reduction in the shear tractions across the failure surface. The medium then responds by "relaxing" to a new equilibrium state by radiating the energy released from the local reduction in strain energy in the source region. This theory has been very successful in the dynamical regime, most notably in the prediction of far-field radiation patterns from earthquakes and explosions accompanied by tectonic release (Archambeau and Sammis, 1970; Lambert et al., 1972; Archambeau, 1972). Because of the theoretical complexities, this source formulation has not yet been directly applied to near-field static deformation problems.

Minster (1974) has discussed from a mathematical point of view in some detail the similarities and differences between the various formulations of the earthquake processes. Although his approach is mainly based on dynamical considerations, he shows that in the static limit the general representation of the stress relaxation and stress pulse problems reduce to the displacement field as given by a generalized Somigliana dislocation along a surface of shear displacement discontinuity. This same proof was attempted by McGinley (1969), but the arguments presented by Minster (1974) are much more complete.

Therefore, we may express the source in terms of a Somigliana dislocation without loss of equivalency from the other source descriptions. An approximation to this Somigliana source will be adopted throughout this thesis.

Numerical Analogue. An altogether different approach to solving the forward problem for dislocations in an elastic half-space is afforded through the use of the finite element numerical technique. Use of this technique, which usually requires a large computing capability, enables solutions to be found to problems involving heterogeneities both lateral and vertical, and anisotropy just as easily as those involving a uniform homogenous, isotropic half-space. The mechanics of this method have been described extensively in the engineering literature (Martin, 1966; Przemieniecki, 1968; Jenkins, 1969; Zienkiewicz, 1971). In this technique, the elastic half-space continuum is divided into geometric elements which are inter-connected only at a finite number of nodal points. It is at these nodal points that displacements, stresses, or forces can be imposed on the system. Concurrently, stresses and displacements at a distance removed from these disturbances can only be measured at these nodal points. The solution to the system of simultaneous equations generated by a disturbance imposed on a given node is constrained by the boundary conditions relevant to the problem and is

solved numerically. Jungels (1973) gives a description of the adaptation of this method to the modeling of dislocation fault surfaces. The reader is referred to this work for a summary of the intricacies of this numerical method.

Jungels (1973) and Jungels and Frazier (1973) make a positive comparison between the calculated static displacement field due to a dislocation in a uniform homogeneous elastic half-space calculated by the finite element method and by the conventional exact Green's functions techniques. Although this author had at his disposal a numerical code which would allow only the modeling of plane strain problems, i.e., faults of infinite length, more recent finite element numerical codes can accommodate problems involving finite dimensions in all directions. The great advantage of this method in calculating displacement and strain fields from models of earthquakes is the ability to vary the elastic properties of the medium both over the fault surface and the source to observer path. This technique can be limited, however, by the sheer size of computer storage necessary to solve a problem in which the continuum must be very finely sampled in order to accurately approximate the continuum for the order of the disturbance being modeled.

2.3 Application of the Forward Problem toward the Explanation of Observed Static Data.

As is obvious from the preceding discussion, much progress has been made toward the static modeling of the earthquake source. The state-of-the-art is such that now an accurate description of the static processes accompanying faulting can be investigated. However, the inverse problem now remains. As the facility for calculating the displacement and strain fields from fault models became more sophisticated, a wider range of data came under scrutiny in trying to infer some information about the various parameters which affect the faulting process. The earliest attempt to extract source information from static data was applied to differential horizontal displacements measured near long vertical strike-slip faults. Kasahara (1957, 1959), Chinnery (1961), and Chinnery and Petrak (1968) tried to infer the depth and distribution with depth of dislocation faulting by fitting the rate of fall-off of horizontal displacements measured parallel to the fault strike as a function of distance away from the surface expression of the fault. A trial and error method was used to fit the data and to try to exclude possible faulting models. Press (1965) and Press and Jackson (1965) used Press' calculations to model the close-in vertical movements associated with the 1964 Alaskan earthquake.

These movements were modeled with a vertical dip-slip fault and an indication was sought as to the depth of faulting. A comparison of the calculated and observed far-field residual strain steps was also undertaken. Singh and Ben-Menahem (1969) attempted to fit the same strain observations using their method for taking into account the earth's curvature. In both these studies, no attempt was made to systematically vary the source parameters to achieve the best fit to the data.

As displacement data for large earthquakes became more abundant and reliable, it became apparent that the simple fault models having a constant dislocation over the entire fault surface could not adequately represent the observations. Stauder and Bollinger (1966) first proposed that differential slip on the fault surface might provide a more realistic model to better fit the data from the 1964 Alaskan earthquake. They approximated the differential movement by allowing the displacement on the fault, Δu, to vary piecewise along the direction of the slip. To do this, the total fault plane was taken to be a sum of the individual fault surface rectangles, each being weighted separately. Unfortunately, these authors used a rather simple source model representation in that it had differential movement only on a horizontal fault parallel to the surface. Furthermore, they gave no indication as to how

they arrived at their final model. One would guess that they used the trial and error method.

Savage and Hastie (1969) and Hastie and Savage (1970) have described a quasi-inversion process to be applied to the fitting of earthquake static displacement data using the dislocation models for an arbitrarily oriented finite fault surface imbedded in a homogenous half-space. In these studies, these authors swept through predetermined sets of sensitive fault parameters -- fault width, dip angle, depth, and slip -- calculating the degree of fit to all the data for each model tested. The model which best fit the data in a least-squares sense was termed the optimum model. These calculations seem to closely coincide with the Monte Carlo techniques used to find acceptable models of the radial distributions of the elastic parameters within the earth as described by Press (1968, 1970, 1972). In these cases a reasonable fit to the data was obtained, especially in the case for the Fairview, Nevada earthquake. Fitch and Scholtz (1971) later extended this work to some degree. However, the dislocation model used in these cases was highly idealized in that it was restricted to the Volterra type dislocation in which the slip was constant over the entire dislocation surface.

2.4 Construction of the Pseudo-Somigliana Dislocation Static Model.

Since it has been shown that the fault geometries can be more complicated than just plane rectangular surfaces, some means must be derived to allow in our mathematical representation of the faulting process for these complications. Complications to the simple models can occur in at least two ways. The first complication is that we wish to be able to allow the dislocation to take on arbitrary values as a function of position over the fault surface. Secondly, the fault surface may not be a single rectangular plane. Both of these complications can easily be represented approximately by discretizing the dislocation surface. That is, we want to approximate a curved fault surface by a series of planar surfaces juxtaposed in such a manner as to approximate the curvature of the surface to be matched. Curvature, or splaying, could be thus modeled in any direction. An example of matching curvature in the horizontal direction could be envisioned by a model of the San Andreas fault which includes the region of the bend in southern California. Here a series of plane vertical rectangular surfaces could be concatenated horizontally to match the observed curvature. Similarly, a dipping thrust fault in which the dip varies with depth could be approximated by a series of rectangular sheets positioned vertically to make a continuous surface in which the dip could

change discontinuously between fault elements. Examples of modeling dipping thrust faults in this manner is given in later chapters.

With this same scheme, the dislocation could be allowed to differ on each of the surface elements which comprise the total dislocation surface. Restriction on the variance of the source parameters from one surface element to the next would have to be imposed to keep the problem physical.

2.5 Linearization of the Forward Static Problem.

The net displacement or strain field at the surface, or at any point off the dislocation surface could be calculated separately for each of the individual segments using one of the forward problem formulations discussed earlier in this chapter. The total elastostatic field at a particular observation point would be a simple sum of the individual contributions from each of the comprising elements.

We wish to pose the problem in such a way as to be able to write down a succinct relationship between the values of the source parameters and the data functionals which we compute from the forward problem calculations. Suppose that we calculate the values of the elastostatic field at a single point exterior to the dislocation surface of our chosen fault model system which is made up of

M different variously-oriented dislocation surface elements. Consider that the elastostatic field can be described by N field variables, preferably those for which we can observe in the field following an earthquake. Suppose that there are L source parameters which can be linearly related to the elastostatic field through the forward problem formulations. Then this relationship is given through the system of linear equations

$$\sum_{j=1}^{L\cdot M} A_{ij} m_j = d_i \qquad \text{for } i = 1,N. \qquad (2.3)$$

In these sets of equations d_i are the calculated elastostatic field functional values, m_j are the values of the linear model source parameters, and the coefficients A_{ij} are the elastic media response of a particular data functional due to a particular fault surface element having a unitary source strength for the linear parameters. These coefficients are in general a function of position. If we treat the components of m_j and d_i as elements of a column and row vector respectively and if we put the coefficients, A_{ij}, in standard matrix form where the matrix has L·M columns and N rows, we can express (2.3) in the following

matrix notation,

$$\mathbf{A}\mathbf{m} = \mathbf{d} \ . \tag{2.4}$$

The model components of $\mathbf{m}$ are contained in the vector space $E^{L\cdot M}$ and the data functional components are contained within the vector space E^{N}. The matrix, $\mathbf{A}$, can be considered a vector operator which maps $E^{L\cdot M}$ into E^{N}.

We have been careful in this construction to limit ourselves to problems where the source parameters in the space $E^{L\cdot M}$ can be linearly related to the calculated elastostatic field functionals in space E^{N}. This strictly linear relation is valid for only a few source parameters in special instances. If the forward problem is to be solved by the analytic closed form Green's function solutions, for example equation (2.2), then we have to impose the Volterra restriction

$$\Delta u_i(P) \quad = \quad \text{constant.}$$

With this restriction we can write

$$u_k(Q) \quad = \quad \frac{\Delta u_i}{8\pi\mu} \iint_{\Sigma} W_{ij}^{k}(P,Q)\nu_j \, d\Sigma \ ,$$

and the problem is now linear with respect to slip in the

ith direction on the individual dislocation surfaces. In general, the solution cannot be so easily linearized with respect to other parameters which characterize the dislocation source-fault length, dip angle, depth, position, etc.. An examination of the forward equations given by Mansinha and Smylie (1971) is convincing in this respect. Fortunately, by numerically evaluating these expressions, we can show that they are <u>locally</u> linear. The extent of the locally linear domain varies from source parameter to source parameter and also with the absolute value of the source parameter. If sufficient care can be paid to these details, the problem can be approximately linearized for all the source parameters listed above. The linearization can be accomplished in the following simple way.

The degree of linearity or non-linearity of the forward problem functionals for the various source parameters will be model dependent, that is, it will vary from source model to source model. If we wish to describe the linear domain in a field about some chosen model, $\mathbf{m}_1$, we choose some other source model, $\mathbf{m}_2$, "near" $\mathbf{m}_1$ such that the following equation can be written

$$\mathbf{A}\,\delta\mathbf{m} = \delta\mathbf{d} + O[|\mathbf{m}_2 - \mathbf{m}_1|^2]. \qquad (2.5)$$

The following definitions have been applied:

$$\delta \mathbf{m} = \mathbf{m}_2 - \mathbf{m}_1 \tag{2.6}$$

$$\delta \mathbf{d} = \mathbf{d}(\mathbf{m}_2) - \mathbf{d}(\mathbf{m}_1) \ . \tag{2.7}$$

$\mathbf{d}(\mathbf{m}_i)$ is the elastostatic field for a particular source model $\mathbf{m}_i$. The problem is linearized only if $\delta \mathbf{m}$ is sufficiently small for equation (2.5) to hold. The conditions for linearity discussed here are equivalent to requiring the forward problem functionals to be Fréchet differentiable with respect to the source parameters.

If we calculate the forward problem for a source model description which we think will reasonably approximate the observed static field functionals, call this model $\mathbf{m}_s$, then for small perturbations about this model, $\delta \mathbf{m}_s$, an approximate linear relationship between the two vector spaces is established. This is to say that the coefficients of A_{ij} are linear. We note here that in general, the coefficients of A_{ij} are not independent of the model $\mathbf{m}_s$. Indeed, their dependence is a measure of the non-linearity of the operator coefficients in the region of the model space being sampled by the test model $\mathbf{m}_s$. The perturbations, $\delta \mathbf{m}_s$, must remain small in the sense that they are approximately linear throughout this region.

In our matrix notation the forward problem is now written

$$\mathbf{A}\,\delta\mathbf{m}_s = \delta\mathbf{d}_s \,. \qquad (2.8)$$

2.6 Derivation of the Stochastic Inversion Operators. Introduction. This section addresses the problem of obtaining the best estimate of the source parameters characterizing a fault model given a suite of observations which can be linearly related to the faulting process. The problem here follows closely that encountered in the studies regarding the estimation of the radial distribution of velocity and density within the earth. In this area of research, much theoretical progress has been made in the last six years in the treatment of inversion schemes to estimate these distributions. Perhaps the most successful and certainly the most elegant of these schemes falls in the general category of stochastic inversion theory. This theory, which will be applied to the treatment of elastostatic problems in this thesis, attempts to give the best estimate of a discretized approximation to the continuous faulting process when a limited amount of data is obtainable. As pointed out by Jordan (1972), the inverse problem when posed in this manner usually has no unique solution. However, the solution that is obtained is unique in certain respects, as will be discussed later.

Furthermore, the stochastic approach allows for the inclusion of inaccuracies in the estimation of the elastostatic field observations. How these inaccuracies affect our model estimations will be fully explored in the chapters devoted to the application of this theory.

The fundamentals of the theory for the solution of the underconstrained linear inverse problem for data that contain certain amounts of "noise" have been presented by Backus and Gilbert (1967, 1968, 1969, 1970). Jordan and Minster (1971) and Jordan (1972) incorporated portions of the Backus-Gilbert theory with the purely stochastic theory of Franklin (1970) to present a quite complete approach to the solution of this type of problem. The theory as applied here to static problems is essentially that due to Jordan (1972), and an attempt has been made to follow his notation throughout this thesis. Sophisticated discussions as to the validity of this type of inverse and the mapping functions of the operators are given in this reference. The derivation of the stochastic inversion operators below are given only in the context as to how they apply to the elastostatic problem. In the derivations, for reasons of simplicity the notation used is for a linear problem. If applied to non-linear problems that have been linearized in the procedure discussed above, the difference vectors defined in (2.6) and (2.7) are

merely substituted for the true model and elastostatic field vectors.

Derivation. Consider the problem of determining some M-dimensional vector model, $\mathbf{m}$, contained in the space E^M, given a N-dimensional elastostatic field vector, $\mathbf{d}$, in the space E^N. The elastostatic field values are related to by the system of linear equations

$$\sum_{j=1}^{M} A_{ij} m_j = d_i \qquad i = 1, N \; . \tag{2.9}$$

In matrix notation

$$\mathbf{A}\,\mathbf{m} = \mathbf{d} \quad , \tag{2.10}$$

where the operator $\mathbf{A}$ solves the forward problem for each of the N elastostatic field values contained in $\mathbf{d}$ by mapping E^M into E^N. Thus for every model $\mathbf{m}$ there exists some unique determination of $\mathbf{d}$ where

$$\mathbf{d} = \mathbf{d}\,(\mathbf{m}) \; . \tag{2.11}$$

If we take the actual field observations which are measured following the occurrence of an earthquake to be in vector form, $\mathbf{d}_0$, and these measurements are made perfectly with no

inaccuracies, then

$$\mathbf{d}_0 = \mathbf{d}(\mathbf{m}) \ . \tag{2.12}$$

Assuming, of course, that the formulation of the forward problem will exactly determine the elastostatic field values. However, if there are any inaccuracies in the observed field values, then these observed values, $\mathbf{d}_0$, can be written as a combination of the projected field values plus some measure of the uncertainty in these observations,

$$\mathbf{d}_0 = \mathbf{d}(\mathbf{m}) + \mathbf{n} \ , \tag{2.13}$$

or by substitution from (2.10)

$$\mathbf{A}\,\mathbf{m} = \mathbf{d}_0 - \mathbf{n} \ . \tag{2.14}$$

Here $\mathbf{n}$ is a vector containing the components of the "noise" in the observed field data. We assume that this noise is randomly distributed in a Gaussian fashion and that any bias to the data is removed before the noise is estimated. Each component, d_{0_i}, is assumed to be the mean of a Gaussian random variable with variance, σ_i^2. We can define a diagonal variance operator, $\mathbf{C}_{nn}$, to be

$$\mathbf{C}_{nn} = \begin{bmatrix} \sigma_1^2 & \cdot & \cdot & \cdot & 0 \\ \cdot & \sigma_2^2 & & & \cdot \\ \cdot & & \cdot & & \cdot \\ \cdot & & & \cdot & \cdot \\ \cdot & & & & \cdot \\ 0 & \cdot & \cdot & \cdot & \sigma_N^2 \end{bmatrix} , \qquad (2.15)$$

where σ_i^2 is the estimated variance of the ith data value. In assuming this diagonal form, we are implicitly assuming that there is no co-variance between data.

Since the only information that we have about **m** is contained in (2.14), we know nothing about the components of **m** which lie outside the space $\mathbf{R} \subseteq E^N$ which is spanned by the base vectors of R. It is reasonable to require that our estimate of **m**, call it $\tilde{\mathbf{m}}$, lie totally within the subspace **R**; then we can assign a non-zero value to only those components for which we have information. Under this restriction, we can write

$$\tilde{\mathbf{m}} = \mathbf{A}^* \mathbf{b} \qquad (2.16)$$

for some vector **b** contained in the vector data space E^N. In this last equation, we are using the notation $\mathbf{A}^*$ to represent the transpose of the matrix **A**. This convention will be used throughout this thesis. To select an optimal **b**, call this $\tilde{\mathbf{b}}$, we wish to minimize a suitable quadratic

measure of the errors involved in this estimation. We choose to minimize some weighted sum of two measures of the errors involved in this problem. This weighted sum can be parameterized by a trade-off curve between these two errors, with the position along this curve used as the parametric factor. Specifically, we want to minimize

$$\varepsilon^2(\theta,\mathbf{b}) = \varepsilon_1^2(\mathbf{b})\,\cos(\theta) + \varepsilon_2^2(\mathbf{b})\,\sin(\theta) \quad , \tag{2.17}$$

where

$$\varepsilon_1^2(\mathbf{b}) = ||\mathbf{m} - \mathbf{A}^*\mathbf{b}||^2 \quad , \tag{2.18}$$

and

$$\varepsilon_2^2(\mathbf{b}) = \mathbf{b}^*\,\mathbf{C}_{nn}\,\mathbf{b} \quad . \tag{2.19}$$

The first measure of error, $\varepsilon_1^2(\mathbf{b})$, is the square of the Euclidian norm, defined by

$$||\,\mathbf{X}\,||^2 = \sum_{i=1}^{M} x_i^2 \quad ,$$

of the difference between our estimate of the model, $\tilde{\mathbf{m}}$, and the actual vector we are estimating. This quantity decreases as we more closely approximate $\mathbf{m}$. The second

measure of error associated with $\tilde{\mathbf{b}}$ arises from uncertainty in the components of $\mathbf{d}_0$. This quantity decreases as our estimate becomes more reliable. The parameterization angle, θ, is allowed to vary on the interval $[0,\pi/2]$, so that at $\theta = \pi/2$, $\varepsilon_2^2(\mathbf{b})$ is minimized, indicating maximum reliability of the model. At $\theta = 0$, $\varepsilon_1^2(\mathbf{b})$ is minimized, indicating maximum accuracy in the estimation of the model.

We note here that these two errors are measured with two different norms, each in the model space. We must establish some common norm on each of these errors so that the parameterization of the sum of these errors can be accomplished. This normalization is performed through the introduction of a correlation operator, $\mathbf{W}$. This correlation operator can be thought of simply in terms of a weighting function for the various model components. The norm of this operator is fixed so that at the critical point on the trade-off curve between the two types of errors, at $\theta = \pi/4$, the absolute value of the two errors are equal.

For the present, we assume that the correlation operator, $\mathbf{W}$, is the idemfactor, $\mathbf{I}$, so that this effect can be ignored in our minimization calculations. The results of this minimization then will be generalized to include an arbitrary correlation operator.

In order to minimize $\varepsilon^2(\theta,\mathbf{b})$ given in equation (2.17), we take $\delta\mathbf{b}$ to be a small arbitrary perturbation of $\mathbf{b}$. To first order in $\delta\mathbf{b}$ we can write

$$\delta\varepsilon^2(\theta,\mathbf{b}) = \varepsilon^2(\theta, \mathbf{b}+ \delta\mathbf{b}) - \varepsilon^2(\theta,\mathbf{b}) \quad .$$

Performing this first order perturbation on equation (2.17) we find that

$$\delta\varepsilon^2(\theta,\mathbf{b}) = 2[\mathbf{b}\mathbf{A}\mathbf{A}^* - \mathbf{m}\mathbf{A}^*]\delta\mathbf{b}\cos(\theta) + 2\,\mathbf{b}\mathbf{C}_{nn}\delta\mathbf{b}\sin(\theta) \quad .$$

In order to minimize $\varepsilon^2(\theta,\mathbf{b})$, we set $\delta\varepsilon(\theta,\mathbf{b}) = 0$. When this is done, we see that $\delta\mathbf{b}$ truly is an arbitrary perturbation, and $\varepsilon^2(\theta,\mathbf{b})$ will be stationary if and only if

$$(\mathbf{A}\mathbf{A}^* + \tan(\theta)\,\mathbf{C}_{nn})\mathbf{b} = \mathbf{A}\mathbf{m} \quad . \tag{2.20}$$

It can be shown (Jordan, 1972) that this stationary point is a unique minimum, and the vector, $\mathbf{b}$, which satisfies this condition is our optimum vector, $\tilde{\mathbf{b}}$.

If $\mathbf{C}_{nn}$ is non-singular, that is, each $\sigma_1^2 \neq 0$, and $\theta > 0$, then the matrix $(\mathbf{A}\mathbf{A}^* + \tan(\theta)\,\mathbf{C}_{nn})$ is non-singular and

$$\tilde{\mathbf{b}} = (\mathbf{A}\mathbf{A}^* + \tan(\theta)\,\mathbf{C}_{nn})^{-1}\mathbf{A}\mathbf{m} \quad . \tag{2.21}$$

In this last equation, $\mathbf{m}$ is unknown but by substituting from equation (2.10) we get

$$\tilde{\mathbf{b}} = (\mathbf{A}\mathbf{A}^{*} + \tan(\theta)\, \mathbf{C}_{nn})^{-1}\, \mathbf{d}_0 \ . \qquad (2.22)$$

Substituting this optimal value of $\mathbf{b}$ into equation (2.16) we see that the optimal estimate of the model for a fixed value of θ will be given by

$$\tilde{\mathbf{m}} = \mathbf{A}^{*}\, (\mathbf{A}\mathbf{A}^{*} + \tan(\theta)\, \mathbf{C}_{nn})^{-1}\, \mathbf{d}_0 \ . \qquad (2.23)$$

In the above results all components of $\mathbf{m}$ are equally weighted with the identity operator. A more general weighting can be introduced by considering a set $\{W_j ; j=1,M\}$ of non-zero positive weights for the model components. Let us define this weighting, or correlation matrix, in the following manner,

$$\mathbf{W} = \begin{bmatrix} W_1^2 & . & . & . & . & 0 \\ . & W_2^2 & & & & . \\ . & & . & & & . \\ . & & & . & & . \\ . & & & & . & . \\ 0 & . & . & . & . & W_M^2 \end{bmatrix} \ .$$

This leads us to define a normalized elastic media response operator

$$\mathbf{A}' = \mathbf{A}\mathbf{W} \quad . \tag{2.24}$$

With this normalized definition, equation (2.10) is now written

$$\mathbf{A}'\mathbf{W}^{-1}\mathbf{m} = \mathbf{d}_0 \quad . \tag{2.25}$$

Following the same procedure as before, we require

$$\tilde{\mathbf{m}} = \mathbf{A}'^{*}\mathbf{b} \quad , \tag{2.26}$$

and minimize

$$\varepsilon_W^2(\theta,\mathbf{b}) = ||\mathbf{m} - \mathbf{A}'^{*}\mathbf{b}||_W^2 \cos(\theta) + \mathbf{b}^{*}\mathbf{C}_{nn}\mathbf{b} \sin(\theta) \quad ,$$

where $||\cdot||_W$ is the weighted norm defined by

$$||\mathbf{Z}||_W^2 = \mathbf{Z}^{*}\mathbf{W}^{-1}\mathbf{Z} = \sum_i \left(\frac{z_i}{W_i}\right)^2 \quad .$$

This weighted norm, of course, reduces to the Euclidian norm if $W_i = 1$ for all $i = 1,M$. The minimization of $\varepsilon_W^2(\theta,\mathbf{b})$ with respect to a variation of $\mathbf{b}$ proceeds as before. The results are

$$\tilde{\mathbf{m}} = \mathbf{W}\mathbf{A}^{*}(\mathbf{A}\mathbf{W}\mathbf{A}^{*} + \tan(\theta)\,\mathbf{C}_{nn})^{-1}\,\mathbf{d}_0 \quad . \tag{2.27}$$

Now since there are uncertainties in the observed elastostatic field, the best estimate of the model, $\tilde{\mathbf{m}}$, is some filtered average of the true model, $\mathbf{m}$, given by

$$\tilde{\mathbf{m}} = \mathbf{R}\,\mathbf{m} \quad . \tag{2.28}$$

This averaging operator, which contains the response kernels for the elements of $\mathbf{m}$ can easily be found by substituting for $\mathbf{d}_0$ in equation (2.25). Performing this substitution in equation (2.27) we obtain

$$\tilde{\mathbf{m}} = \mathbf{W}\mathbf{A}^{*}(\mathbf{A}\mathbf{W}\mathbf{A}^{*} + \tan(\theta)\,\mathbf{C}_{nn})^{-1}\mathbf{A}\,\mathbf{m} \ ,$$

or by inspection from equation (2.28)

$$\mathbf{R} = \mathbf{W}\mathbf{A}^{*}(\mathbf{A}\mathbf{W}\mathbf{A}^{*} + \tan(\theta)\,\mathbf{C}_{nn})^{-1}\mathbf{A} \quad . \tag{2.29}$$

Individual rows of this operator contain the averaging of the estimated values of the individual model components with respect to the other model components. This averaging is taking place in a sense that the estimation of the ith model component is actually the true value of this component "convolved" in the model space with the function defined on the model space by the components of the ith row of the averaging operator. If a particular model component is perfectly determined, say the ith value, that is, its value is perfectly resolvable, then $R_{ii} = 1$ and all other $R_{ij} = 0$.

In the limit of infinite resolution on all model components, that is, either $\theta = 0$ or $\mathbf{C}_{nn} = 0$, the averaging operator approaches the idemfactor, $\mathbf{I}$.

By similar substitutions, we can express equation (2.19) as

$$\varepsilon_2^2(\theta,\mathbf{b}) = \mathbf{m}^* \mathbf{V}(\theta)\,\mathbf{m} \quad , \tag{2.30}$$

where we have defined a new operator

$$\mathbf{V}(\theta) = \mathbf{W}\,\mathbf{A}^*(\mathbf{A}\mathbf{W}\,\mathbf{A}^* + \mathbf{C}_{nn}\tan(\theta))^{-1}\,\mathbf{C}_{nn}(\mathbf{A}\mathbf{W}\,\mathbf{A}^* + \mathbf{C}_{nn}\tan(\theta))^{-1}\mathbf{A}\mathbf{W} \quad . \tag{2.31}$$

This operator is termed the variance operator. Examining equation (2.30) we see that the bilinear product of this operator and the model components is a measure of the error induced from the data space, through the variance matrix $\mathbf{C}_{nn}$, into the model space. Since we are assuming that the errors exhibited in $\mathbf{C}_{nn}$ are normally distributed, we can determine the following about the errors induced from the data space due to inaccuracies in the description of the elastostatic field into inaccuracies in the estimated source model parameters. Use of this operator does not tell us the absolute inaccuracies of our estimated model

per se; instead, it can only tell us whether or not a certain perturbation in the model is resolvable to a certain degree by the data. So in practice, we have to prescribe a perturbation vector on our source model and test to see if the data can "see" this perturbation. This ability to distinguish model perturbations by the observed data will depend directly on the accuracy of the data. The more accurate the data, the smaller a model perturbation these data will be able to detect. Since we are now mapping errors in the opposite direction to that defined in equation (2.30), clearly the inverse of this operator is the projection that we desire. Since the errors are induced in directions along the eigenvectors of $\mathbf{V}(\theta)$, then we choose to take the inverse of this operator as the generalized inverse given by

$$\mathbf{V}^{\dagger}(\theta) = \sum_{i=1}^{J} \frac{1}{\lambda_i^2} \mathbf{u}_i \bullet \mathbf{u}_i^{*} \quad . \tag{2.32}$$

Here we are assuming that $\mathbf{V}(\theta)$ has a total of J non-zero eigenvalues (λ_i^2, i=1,J) with the associated eigenvectors $\mathbf{u}_i$. The notation $\mathbf{u}_i \bullet \mathbf{u}_i^{*}$ indicates an outer-product expansion between the two vectors $\mathbf{u}_i$ and $\mathbf{u}_i^{*}$. Since $\mathbf{V}^{\dagger}(\theta)$ is a generalized inverse of $\mathbf{V}(\theta)$, then the inner product of $\mathbf{V}(\theta)$ and $\mathbf{V}^{\dagger}(\theta)$ is not necessarily the identity operator

but rather some projection operator, $\mathbf{P}_V$ that is both idempotent ($\mathbf{P}_V \mathbf{P}_V = \mathbf{P}_V$) and symmetric ($\mathbf{P}_V = \mathbf{P}_V^*$).

In particular, some vector perturbation in the model space, $\mathbf{q}$, is resolvable to within a certain confidence limit, to which we can assign some confidence coefficient k(c), if the following inequality holds.

$$\underline{\mathbf{q}}^* \mathbf{V}^\dagger \mathbf{q} > k^2(c) \ . \tag{2.33}$$

For example, for the 95% confidence limit, k(c) can be found in any good statistics reference to be 1.96.

A two-dimensional geometrical argument will illustrate the use of equation (2.33). Assume that the errors induced from the data space onto the model space by the variance operator (eigenvalues of this operator) are $\sigma^2_{m_1}$ and $\sigma^2_{m_2}$. (This variance should not be confused with the data variance defined in equation (2.15)). These errors lie along the eigenvector directions, $\hat{x}_1$ and $\hat{x}_2$ respectively. Now if a vector $\mathbf{x}$ has components along these directions then the equation

$$\mathbf{x}^* \mathbf{V}^\dagger \mathbf{x} = k^2$$

can be written out

$$\frac{x_1^2}{\sigma^2_{m_1}} + \frac{x_2^2}{\sigma^2_{m_2}} = k^2 \ .$$

This is just the equation of an ellipse whose semi-major axes are $k\sigma_{m_1}$ and $k\sigma_{m_2}$. This ellipse, or hyper-ellipsoid when this argument is extended to higher dimensions, is called the confidence ellipse. The enclosure of this ellipse represents the area of unresolvable model perturbations, and the area exterior to the ellipse represents a model perturbation which is large enough to be resolvable by the data at a certain confidence limit associated with the axis parameter k. By making k larger, we are increasing the confidence limit and increasing the size of the confidence ellipse thus requiring larger model perturbations before they can be detected by the data at that confidence limit. In order to check the resolvability of a given model perturbation, we choose our value of k (say 1.96) and merely test to see if this vector protrudes the confidence ellipse. We note here that this resolvability criterion depends only on relative perturbations to the source model parameters and not on the absolute configuration of the final or optimum model that we obtain from the inversion process. Thus we have to propose a hypothetical perturbation, or a series of perturbations, judiciously chosen to explain or disclaim certain features of our model, and expose them to this testing procedure. Only on this basis can we determine the limits the model source

parameters can take and still fit the observed elastostatic field. The power of this operator becomes apparent when applied to actual problems as we shall see in later chapters.

2.7 Discussion.

In this chapter we have discussed the development of methods of obtaining an accurate representation of the forward elastostatic problem for a given description of the faulting process. We have reviewed the early uses of these forward formulations in attempting to deduce source parameters which can characterize a given event. A method was suggested by which a more complicated and arbitrary static dislocation function could be approximated with the formulations derived from simple dislocation sources. It was found that by making possible a more complex static source description some means must be used to systematically relate the observed elastostatic phenomena to the media response from the various source parameters. The stochastic inversion scheme provided an ideal means to give the best estimates to the solution for the usually underdetermined static problem. By use of this inversion scheme, we can benefit from the use and knowledge of the various operators which fall out of the derivations. These operators deal with the errors in both the observations and those in our solutions. Quantitative appraisals of the

decency of a given solution to a particular static problem become available through the use of these operators.

For the special case of $\theta = 0$, equation (2.23) is commonly known as the generalized inverse. For this case, Noble (1969, p. 143) has shown through the method of Lagrange multipliers that the generalized inverse also minimizes the norm of $\tilde{\mathbf{m}}$. We can think of this as physically giving the longest wavelength, or smoothest model solution, for a given set of data. In elastostatic problems, this property is especially valuable, since we would expect the displacement on a fault surface to locally vary in some fairly smooth fashion.

By combining all of the formalisms discussed in this chapter, we should be able to take a formidable advance in our understanding of the static processes which accompany earthquakes. The theory discussed here will be applied to data from actual earthquakes in the following chapters.

Chapter 3

A Static Dislocation Model of the 1964 Alaska Earthquake

3.1 Introduction.

The Alaska earthquake of 28 March 1964 which was centered near Prince William Sound was probably the largest seismic event in North America this century. The magnitude of this event has been estimated to be between M_s = 8.3 to M_s = 8.6. With the possible exception of the 1971 San Fernando, California earthquake, this earthquake has been the most intensely studied occurrence in the history of geophysics. The regional deformation accompanying this event involved changes in land level of unprecedented areal extent, encompassing some 200,000 km^2. The residual vertical displacements produced were measurable geodetically along a 400 km profile approximately perpendicular to the Gulf of Alaska and approximately 800 km adjacent and parallel to the coastline. Yet despite the importance that this earthquake had on the tectonic character of the affected region and the importance of the contributions that the data from this event provided toward an increased scientific understanding of the origin of earthquakes, considerable controversy still surrounds the exact source mechanism. It is hoped that the results from

this chapter will help allay some of this controversy.

3.2 Fault Representation.

Since the first studies of the 1964 Alaska earthquake, the main focal mechanism and the accompanying sense of motion have remained somewhat of a controversy primarily because of the ambiguity of the fault plane solutions based on P-wave first arrival data. The two contesting mechanisms are one having the geometry of a nearly vertical reverse fault, and the other a low angle thrust fault. Figure 3.1 shows a profile extending from the southeast to the northwest approximately bisecting the elongated area of deformation. This cross section corresponds to profile BB' shown in Figure 3.2. In Figure 3.1 we have diagrammatically represented the two possible fault plane mechanisms and their relation to the hypocenter, shown at the intersection of these two planes. The representative geometry that we choose to explain in detail the static fields which accompanied this earthquake must be in reasonable compatibility with the geometry necessary to explain the following observed or calculated entities:

1) epicenter location and hypocentral depth
2) P-wave first motion polarities and S-wave polarizations
3) aftershock distribution
4) radiation patterns of long period Love and

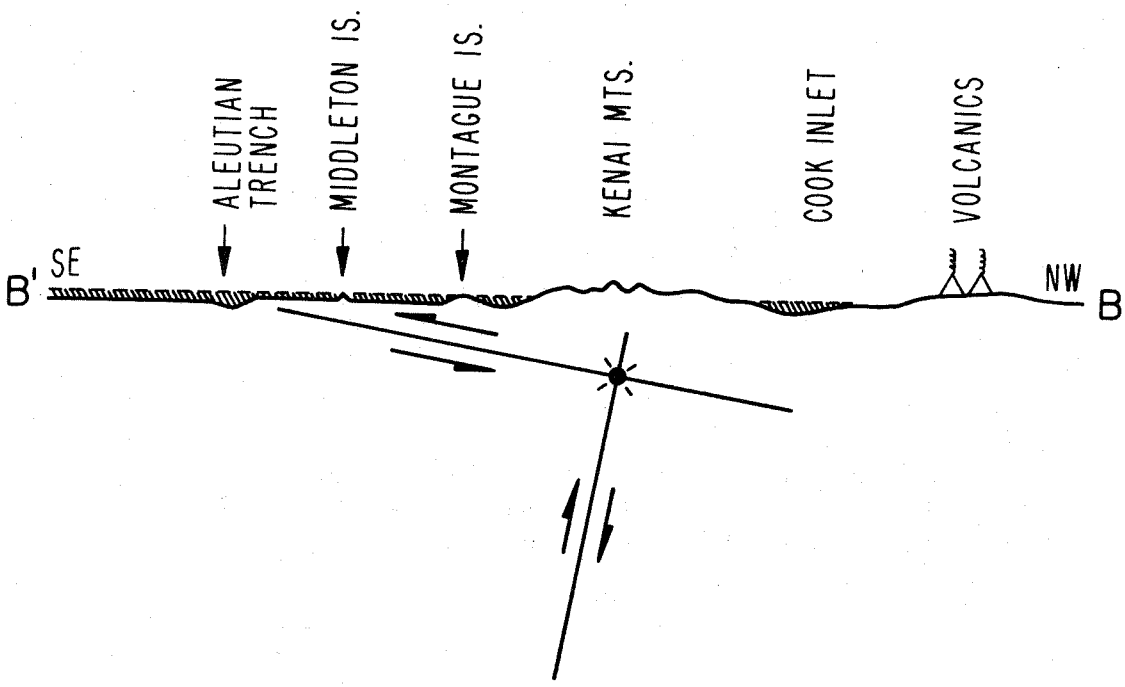

Figure 3.1. Schematic diagram of the two possible nodal planes and the relative dislocation on each. The hypocenter of the main shock is located at the intersection of the two planes.

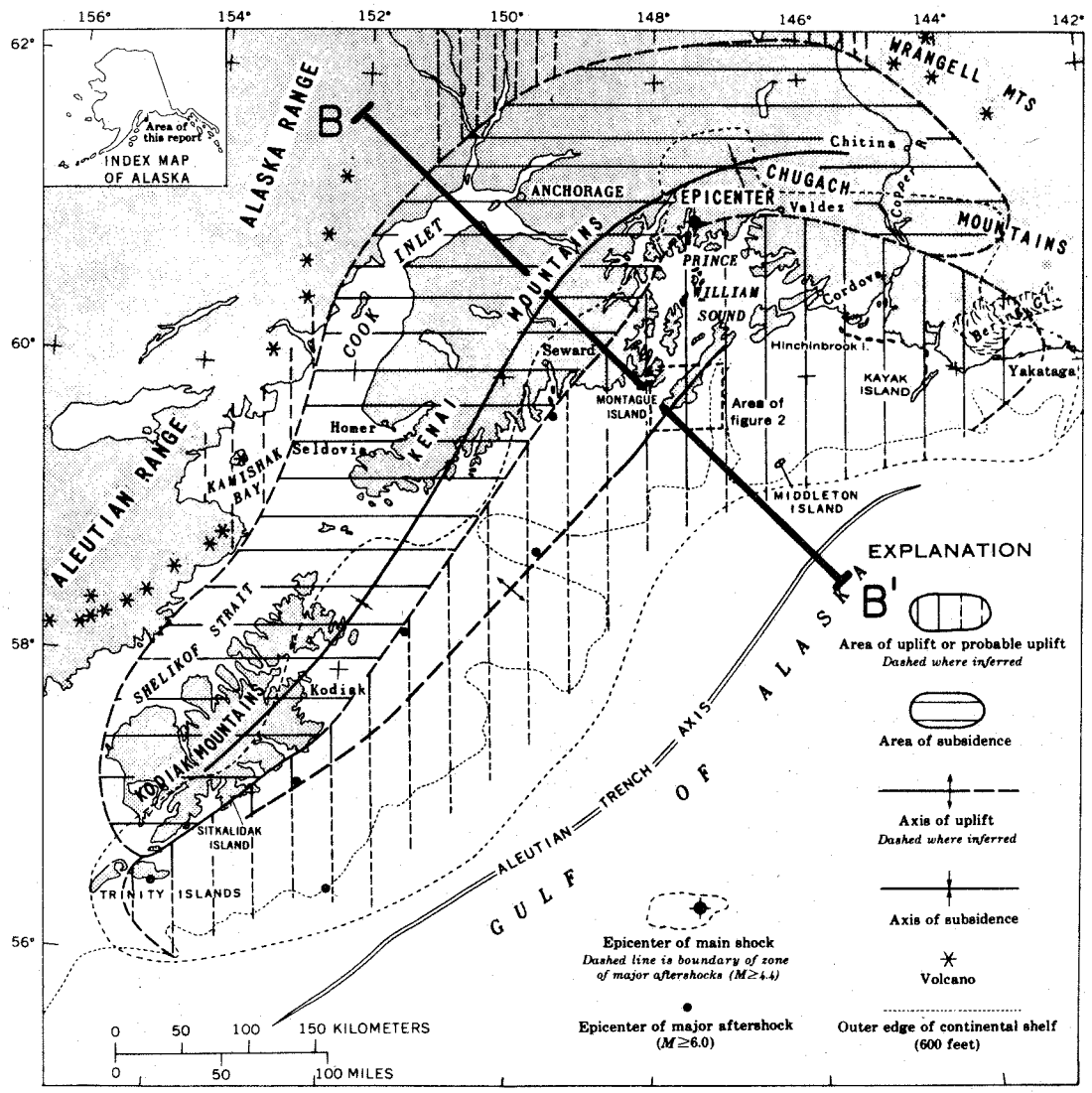

Figure 3.2. Regional deformation that accompanied the March 28, 1964, Alaska earthquake. Cross section used in this study is labeled BB'. The Patton Bay fault is indicated as the axis of uplift. Figure is from Plafker (1967).

Rayleigh waves

5) geological reasoning for faulting -- island arc implications

6) near field displacements.

We will briefly review the geophysical literature for supportive arguments to favor one or the other of the proposed mechanisms. We will then adopt a model which we think will best fit all of these criteria.

The hypocentral depth for the main event was first given to be about 20 km, and in later calculations with the inclusion of more data the depth was restricted to 33 km. (This restricted depth is the standard depth assigned a shallow event when the depth determination algorithm does not converge, or else converges to a negative depth.) No depth sensitive phases, such as pP or sP could be positively identified on records of the main shock. A reasonable assumption would be to place the depth as lying between 20 km and 50 km. The hypocenter certainly was not deep as evidenced by the large amplitude surface waves generated by this earthquake. The epicenter of the main shock was located by Sherburne et al. (1969) and von Hake and Cloud (1966) to be near the north shore of the Prince William Sound on the small peninsula separating College Fiord and Unakwik Inlet. The coordinates of the epicenter are given as 61.04° $\pm$ 0.05° north latitude and 147.73°

± 0.07° west longitude.

The focal mechanism for the first motion of this earthquake has been studied by a number of authors (Algermissen, 1964, 1965, 1966; Harding and Algermissen, 1969; Berg, 1965; Stauder and Bollinger, 1966). These studies show only one fairly well-defined nodal plane. There is some slight ambiguity in the exact orientation of this plane due to non-impulsive, or emergent P-wave first arrivals at a number of key stations, but this is a second order effect. The preferred orientation of this nodal plane is given to be strike N 62° E, dip 82° S. The definition of the second nodal plane is limited because of the almost total lack of geographical control in the station locations. Berg (1965) attempted with limited success to determine the orientation of this second nodal plane by observing a dilatation at one station, Yellowknife, Canada. The location of this station is critical in defining this second nodal plane. The orientation of this plane has been estimated to give a dip of 26° to the northeast. This unfortunate distribution of stations to the north of the epicenter precludes the identification of the nodal plane that would be present due to a low angle thrust, although the plane has been restricted by the data presented by Stauder and Bollinger (1966). These authors conclude that the second nodal plane can have a dip varying from less

than 25° to the northeast through 5° to the northwest to less than 60° to the southeast. S-wave polarization studies suffer from the same restriction in the station distribution respect. The results from the S-wave polarization angle study by Harding and Algermissen (1969) indicate that for a double couple type source on a nearly vertical fault the required motion to fit the observed S-wave polarities would be predominantly strike-slip.

One suggestion that must be kept in mind when trying to interpret the orientation of the nodal planes from first motion data is that presented by Wyss and Brune (1967). These authors suggested that the faulting which occurred over the entire segment involved a complex multiple rupture mechanism. If this mechanism is in fact the way the faulting took place, then the initial motion at the hypocenter can have little, if any, bearing on how the faulting proceeded as a whole.

One clue as to the possibility of deciding which type faulting took place is given by examining the spatial distribution of aftershocks. Algermissen et al. (1972) present just such data for over 2,000 locatable aftershocks. Special attention was given to a sub-set of this aftershock location data which were well located and contained positively identifiable depth phases. These events showed that, especially in the vicinity of Prince William Sound, the

aftershocks were shallow. In fact, approximately 62% were located at depths less than 20 km with only 1% of the events located at depths greater than 40 km. This depth distribution of aftershocks suggests that most or all of the faulting was confined within the crust and perhaps the top of the upper mantle along the continental margin. These authors depict the foci of the aftershocks located in this area under consideration as defining a plane which dips at a shallow angle (4°-6°) under the continental block. Focal mechanism studies of the aftershock by Stauder and Bollinger (1966) delineate a fault plane some 600 km in length and at least 200 km in width having an average dip of about 10°, while the main shock had a depth of focus of between 20 and 50 km and had a body wave nodal plane solution dipping between 10° and 15°.

The outer limits of the aftershock region appear to be very well defined and the region is not confined along the surface trace of the postulated steep-fault model. The aftershocks lie mainly in a broad belt roughly paralleling the continental margin mostly falling in the area of mapped or inferred major uplifting. The aftershock zone is not even approximately centered on the epicenter of the main shock.

Surface wave studies of this earthquake have been limited to long period multiple Love and Rayleigh waves due

to the tangled complexity of the large amplitude records at the WWSSN stations. With only few exceptions, the first multiples to be fully recovered have been the R4 and G4 wave trains. These signals have been analyzed in two different, but hopefully equivalent, ways. Toksöz et al. (1965) and Ben Menahem et al. (1972) used the spectral phase and amplitude equilization method while Kanamori (1970) used a time-domain analysis. For a simple point double couple source, the radiation patterns for surface waves for the two contesting fault orientations are approximately equivalent. However, if the source has some finiteness as exhibited by propagating in a given direction then asymmetries in the Love and Rayleigh wave radiation patterns are introduced. As pointed out by Savage and Hastie (1966, p. 4899-4900), the asymmetries between Love and Rayleigh wave radiation patterns will be different only if the rupture propagation is not along the null axis. If rupture does take place in a direction away from this axis then there is a possibility of distinguishing uniquely the two fault orientations. Because of differences in azimuthal coverage, Ben Menahem et al. did not detect any asymmetries in his radiation patterns while Kanamori did. Kanamori interprets this asymmetry in terms of a measured component of rupture propagation normal to the strike of the fault. His solutions favor

the low-angle thrust mechanism and his model is compatible with the long period surface waves radiation patterns for a fault dipping at about 20°.

Plafker (1965) uses his interpretation of a vast quantity of field observations in the area of deformation to argue rather forcefully for the low angle thrust mechanism. These arguments will not be repeated here but are based mainly on the large displacements in relation to the focal mechanism studies and the spatial distribution of aftershock seismicity. Plafker (1972) extends much the same arguments for a low angle thrust fault in the context of being consistent with the mechanism expected for island arc tectonics (Isacks et al., 1968; Stauder, 1968). He concludes that the earthquake occurred as shear failure on a fairly complex major low angle thrust fault, or megathrust, that dips from the vicinity of the offshore trench to beneath the continental margin. The overthrusting is interpreted in terms of elastic rebound resulting from the progressive underthrusting of the oceanic crust and mantle beneath the continental margin prior to 1964. This mechanism is consistent with Benioff's (1954) theory for oceanic trenches and associated mountain ranges.

On the basis of modeling the observed vertical displacements, Press and Jackson (1965) and Press (1965) attempted to demonstrate that the observed uplift and

subsidence could be accounted for by about 10 m of constant dip-slip motion on a vertical plane extending from a depth of about 15 km down to a depth of 150 km or more. These authors did not include in their data set all vertical displacement points available. Savage and Hastie (1966) and Hastie and Savage (1970) got better results trying to fit the same data with a low angle thrust fault with about 10 m of constant displacement over the entire surface. Savage and Hastie showed that the vertical reverse fault model geometry placed the zone of maximum subsidence too close to the zone of maximum uplift, whereas for the low angle thrust geometry, this observed lack of symmetry in the vertical displacements is approximately satisfied. Stauder and Bollinger (1966) accomplished a more realistic modeling of the displacements on a horizontal thrust fault on which differential movement on the fault surface was allowed. These authors tried to include the effects of local or subsidiary faulting on Montague Island (see Figure 3.2). The local faulting shows a dominance of vertical slip and has been described by Plafker (1965) and Grantz et al. (1964a,b). Stauder and Bollinger (1966) model this secondary fault as a constant dip-slip dislocation on a vertical surface directly beneath Montague Island.

Additionally, the low angle geometry is preferable in

describing the behavior of the observed extensive horizontal surface deformation as reported by Parkin (1966). The sense of this deformation is mainly consistent with the seaward overthrusting of the continental block. This direction of motion is especially predominant in the area between the Kenai Mountains and the offshore islands. However, we see from Figure 3.1 that we would intuitively expect the horizontal displacements to be in the opposite direction if the steeply dipping reverse faulting mechanism were adopted. Thus we have decided to adopt the low angle thrust geometry for our fault model in explaining the surface displacement data because it seems most consistent with the seismic, geodetic and geologic observations pertaining to this earthquake.

In each of these attempts in modeling the vertical displacements the formulation of a dislocation in a uniform elastic half-space was used (Green's functions solutions). Since this is a region where there is a large contrast in the juxtaposed crustal types -- oceanic crust underthrusting continental crust -- this uniform elastic half-space approximation may not be appropriate. This approximation will be investigated later in this chapter. All of the above models are able to fit only the gross features of the zero-frequency data of this earthquake, not just because the earth's crust is not a uniform elastic

half-space and the slip varies continuously along the fault plane, but also because the estimates of the fault offsets were not related to the observations in a systematic fashion.

For this earthquake we will model the tectonic environment with a laterally heterogeneous geologic model. The finite-element formulation will be used to compute the static response of a structural model of the crust to a unit offset imposed on a series of nodal segments representing the fault, and the inversion technique will be used to invert any free-surface statical observations to obtain the proper linear combination of these offsets which will result in a computed movement of the surface which fits the observed data to some chosen degree of accuracy. Since the finite-element formulation used in this chapter is limited to solving problems involving plane strain elasticity, any displacement profile that is to be modeled correctly must be approximately free of fault end effects and movement due to strike slip motion. The effect of assuming an infinite length fault will be discussed in a later portion of this chapter.

The structural model chosen for this study is given in Figure 3.3. The geometry is based upon that suggested by Plafker (1972) and Stonley (1966) as being the most consistent with the regional tectonic setting of the

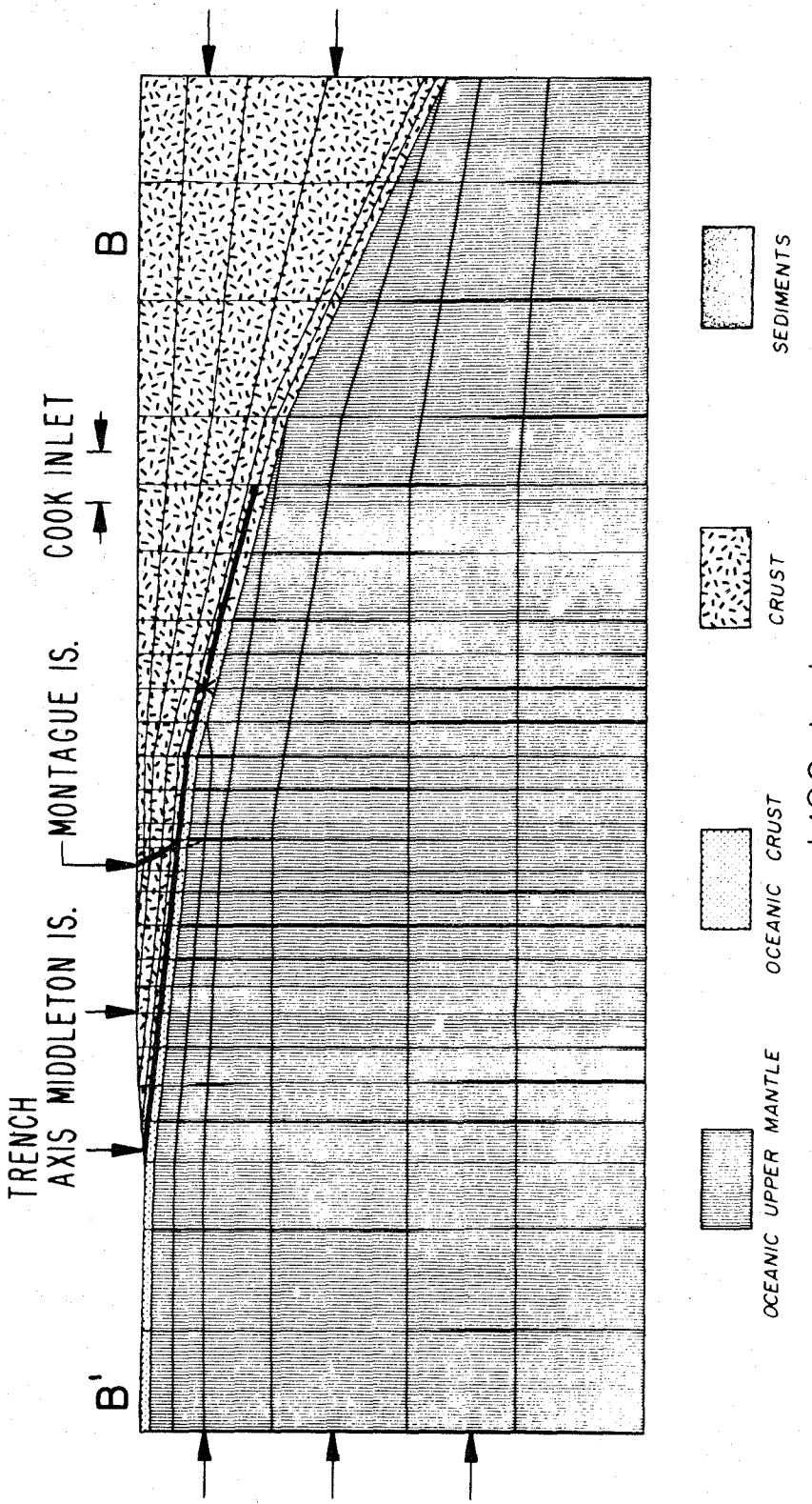

Figure 3.3. Finite element grid and structural model used. The elastic constants used are given in Table 3.1. The main fault segment and the Patton Bay fault are indicated by heavy lines. The epicenter as projected onto this profile is given by the "star". The arrows on the lateral boundaries indicate the imposed displacement boundary condition used to model the average regional prestress field expected from tectonic plate motion.

earthquake, seismic refraction studies, and the earthquake distribution of the area (Tobin and Sykes, 1966). The region is modeled by four geologic provinces, and the elastic parameters for these units have been adopted from the seismic refraction work of Shor (1962) and Hales and Asada (1966) and the microaftershock array work of Matumoto and Page (1969). The seismic velocities given in these studies are essentially those of typical crustal and upper mantle material. The velocities and elastic parameters for these units are listed in Table 3.1. Superposed upon Figure 3.3 is the finite-element grid used in modeling the fault and accompanying dislocations. The grid represents an area that is 800 km long and 300 km thick. The figure shows the Pacific oceanic plate underthrusting the continental margin beneath the eastern Aleutian arc. The majority of the material modeled in this finite element grid is that corresponding to the oceanic upper mantle. Overlying the oceanic upper mantle is a 5 km thick zone of oceanic crust which also underthrusts the continent down to a depth of about 44 km. Just under the Alaska trench we have inserted a thin layer of typical oceanic sediments. The fault model which we have assumed is at the contact between the oceanic crust and the continental crust. The fault starts under the trench with a dip of about 6° and slowly increases its dip until at a depth of 28 km the

TABLE 3.1

Unit	v_p (km/sec)	v_s (km/sec)	ρ (gram/cm^3)	μ (10^{11}dyne/cm^2)
Oceanic Upper Mantle	7.84	4.36	3.3	6.3
Oceanic Crust	6.05	3.4	3.0	3.4
Continental Crust	5.8	3.4	2.71	3.1
Trench Sediments	3.8	2.5	2.5	1.6

Table 3.1. Velocities and elastic parameters for units in the structural model of the earthquake region.

fault is dipping at 12°. The dip continues to increase so that the dip is 15° at the hypocenter and reaches a maximum of 20° below the hypocenter.

There are only two surface faults associated with this earthquake, both of which are exposed on Montague Island -- the Patton Bay fault and the Hanning Bay fault. Geologic relations (Plafker, 1967) indicate that these faults are not major geologic boundaries but rather they are subsidiary to the zone on which the primary faulting motion took place. These faults can be considered as minor imbrications of the megathrust. Both of these faults have been mapped to strike approximately parallel to the continental margin and the fault motion is reverse thrust dipping fairly steeply to the northwest. The Patton Bay fault has a large component of dip-slip motion associated with its entire length, which extends for possibly as much as 450 km to the southwest (Plafker, 1972; Malloy, 1964, 1965). Reimnitz (1966) has inferred that this fault zone extends to the northeast of Montague Island to at least Hichinbrook Island some 50 km away. The strike-slip component is measured as being less than one meter on this fault so that the motion is almost totally dip-slip. Von Huene et al. (1967) carried out seismic and echo sounder profiles in this area between Montague Island and Kodiak Island. Their results indicate a long narrow zone of faulting with the vertical attitude

of the fault plane estimated to be 60°. By the observed deformation of the sea floor, they conclude that the motion was reverse slip along this steeply dipping plane that is inclined landward. This fault is included into the structural finite-element model as a reverse fault dipping at 58° toward the continent. This fault terminates where it intersects the main thrust fault at a depth of about 25 km. The second subsidiary reverse fault observed on Montague Island, the Hanning Bay fault, was not modeled in this study because of the short length (6 km) of the fault. Another high-angle imbricate reverse fault has been proposed to break the surface between the Patton Bay fault and the Aleutian trench. This fault has been inferred to explain the large vertical displacements on Middleton Island. However, no direct physical evidence confirms the existence of such a fault, and it is not included into our model. In all, a total of 26 nodes in the finite-element grid were used to represent the megathrust and the Patton Bay fault, 21 nodal elements for the megathrust and 5 nodal elements for the subsidiary fault.

3.3 Static Data.

As mentioned in the introduction to this chapter, the crustal deformation accompanying this earthquake was very extensive. Plafker (1969) has described in detail the regional vertical and horizontal displacements. (See

Plates 1 and 2 in that paper for detailed contour maps of the ground deformation and the location of the observation sites.) The vertical displacements were based on a variety of methods of measurements, some of which would be reliable only if the net vertical deformation was large, as is the case for this event. The great majority of the measurements involved measurements of the movements of the shoreline which meanders throughout the area of maximum deformation. These measurements include changes in tide gauge levels, measuring the change in the upper limit of barnacle growth, direct shoreline changes, etc.. Taken individually, these measurements cannot be given much reliability, however, when the entire mass of these observations is considered, including correlation between geodetically determined changes in bench mark levels, the data become quite informative. Plafker (1969) discusses the acquisition of this data and the associated estimate of the errors involved.

Although the vertical displacements measured after this earthquake were large, the horizontal displacements appear to be even larger (Whitten, 1964, 1965). Unfortunately, horizontal displacements do not lend themselves to the ease of facility of measurement as do the vertical displacements for this case. Parkin (1966) has described the retriangulation network that was occupied after the

earthquake. Horizontal displacements, generally in the direction of the seaward motion of the continent, of up to 20 m were observed. Pope (1972) used these data to compute the components of strain on the surface. The surveys to determine horizontal movements are too poorly controlled and too easily subject to bias to enable a detailed qualitative inversion of the strains.

In this chapter we will limit our inversion data set to vertical displacements only. The reason for this is that we consider the vertical displacement data to be much more accurate than other features of the tectonic deformation such as horizontal shortening, horizontal displacements, and changes in the local gravity field. The vertical displacement data are taken from Plafker (1965, 1969). Since with this finite-element method we are limited to plane-strain problems we will have to limit our data set to points that define a profile perpendicular to the strike of the megathrust. We chose our displacement profile to coincide with profile BB' in Plafker's papers (1965, 1969, 1972). Only one major surface fault intersects this profile, the Patton Bay fault on Montague Island. By choosing our cross section near the center of the large area of deformation, the vertical displacements are due almost totally to dip-slip motion on the fault, thus contamination of the data set due to contributions from any strike-slip motion is

minimized. By choosing the profile in this position, any effects due to the finite length of the fault are also minimized. As noted above, only slight amounts of strike-slip motion were observed along this cross section with most of it being on the subsidiary reverse faults found on Montague Island. This absence of large strike-slip motion over long lengths of the fault allows accurate plane-strain modeling of the motions involved. We also restricted the data set to those vertical displacements that could be confidently projected onto this profile. Figure 3.4 shows this cross section and the positions of the data available for projection onto this profile. The maximum distance away from the profile of a data point was about 75 km, but about 90% of the available data points were within 40 km of the profile. A total of 47 vertical displacement data points were chosen along the profile which is defined for 400 km from Middleton Island to 75 km northwest of Cook Inlet. Many more observations were available within the 40 km swath on either side of the profile, however, only those points that were not near a curve in the contours or crossed a contour were acceptable to be projected onto the profile. The projection was done parallel to the contours as defined by Plafker (1969). This projection was very close (within 10° in most instances) to a perpendicular projection onto the profile, so that the relative location

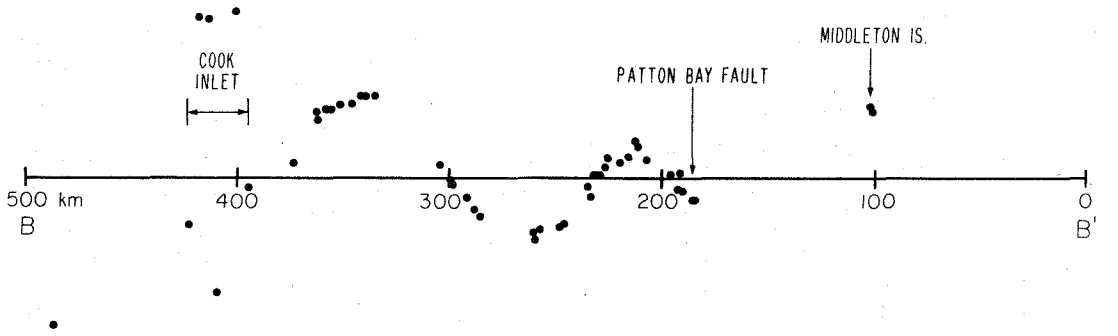

Figure 3.4. Location of the vertical displacement data points relative to the profile.

TABLE 3.2

Distance (km)	Vertical Displacement (m)	Distance (km)	Vertical Displacement (m)
101.0	3.36	259.0	-0.28
102.0	3.40	285.0	-1.20
182.0	4.56	289.0	-1.28
184.0	4.72	291.0	-1.40
184.5	7.32	298.0	-1.54
185.0	10.88	300.0	-1.62
190.0	9.16	304.0	-1.62
191.0	7.92	335.0	-1.72
192.0	7.30	339.0	-1.80
196.0	5.48	342.0	-1.75
207.0	3.22	346.0	-1.70
211.0	2.68	350.0	-1.64
212.0	2.56	351.0	-1.59
214.0	2.36	355.0	-1.52
219.0	2.32	359.0	-1.40
226.0	1.88	362.0	-0.92
229.0	1.84	373.0	-0.92
231.0	1.72	401.0	-0.30
232.0	1.68	409.0	-0.24
233.0	1.56	413.0	-0.24
235.0	1.48	418.0	-0.22
245.0	0.44	423.0	-0.24
247.0	0.50	454.0	0.00
258.0	-0.30	486.0	0.44

Table 3.2. Observed vertical displacement data along profile BB'.

of the data points on this profile can be considered accurate to within about 5 km in the most unfavorable cases. The corresponding values of the individual projected data points on the profile are given in Table 3.2. These values and their respective locations along the profile will appear in several later figures in this chapter. The origin of the profile is some 100 km southeast of Middleton Island. For reference, the most southeasterly data point on Middleton Island is 101.0 km from the origin, and the profile crosses the Patton Bay fault at a distance of 185.0 km from the origin (B'). The sources of the individual data points and their associated errors are discussed elsewhere (Plafker, 1969). In general, the data are accurate to within $\pm$ 0.3 m, and this value was taken in the inversion calculations.

3.4 Calculated Dislocation Model.

The media response matrix, **A**, discussed in the previous chapter was calculated by the finite-element technique for the structural model shown in Figure 3.3. In this technique, the static displacement on the nodal segments at the free surface are linearly related to offsets imposed on the designated fault nodes. The displacement at every one of the nodal segments on the free surface due to a unit offset (1 m) on a specified fault node was calculated. This was then repeated for each of the nodes describing the

fault system. However, since the observed vertical displacement data were only near 16 of the nodal segments on the surface, the response matrix was limited to those nodes. Thus we have defined the problem of estimating the static dislocation on 26 fault nodes given the permanent static offset of 16 nodal segments located on the free surface. This is precisely the type of problem that was discussed in Chapter 2 for which we formulated the stochastic inversion scheme to solve.

In this problem, the operator **A** is a M x N matrix, where A_{ij} is the displacement, calculated at the point on the surface where the ith data point is taken due to a unit dislocation of the jth nodal segment of the fault. Here M=26 and N=16. Based on experience in calculating best model estimates by equation (2.27), it was found that much smoother, hence longer wavelength, solutions were calculated if the starting model was some "distance" in the model space away from the null model. Therefore we chose to use Stauder and Bollinger's (1966) estimate of the fault dislocation as the starting point for our inversion. This starting model turned out to be a good choice because the inversion scheme smoothly and quickly iterated convergingly to a final "best fit" model. Just to make sure that the final model that we obtained was not wholly dependent on the starting model that we chose, we then repeated the

inversion using Hastie and Savage's (1970) fault dislocation estimate as the starting model. The results were very similar to that obtained before. We therefore feel that this final model is not very dependent on the starting model.

The upper part of Figure 3.5 shows these vertical surface displacement data plotted in profile and the calculated displacement at the surface nodes of the finite element grid. The fit to the observed data is extremely good with the calculated surface displacement field fitting the observed data used in the inversion to within a RMS residual of about 3-1/2 cm, and the fit to all the points in the data set is not far from this value. For accuracy, only those data points which were very near a surface node in the finite element grid were used. Thus, out of the set of 46 data points along the profile, only 16 points could be actually used in the inversion. An increase in the number of surface nodes in the finite element grid would probably not add to the resolvability or accuracy of the slip model, since the limitations in these quantities were the lack of spatial coverage of the data, not the lack of data used. The slip model from the inversion process is shown in the lower half of Figure 3.5. The maximum slip along the fault is 33 m at a point below Montague Island. A displacement of about 30 m is maintained over a fault

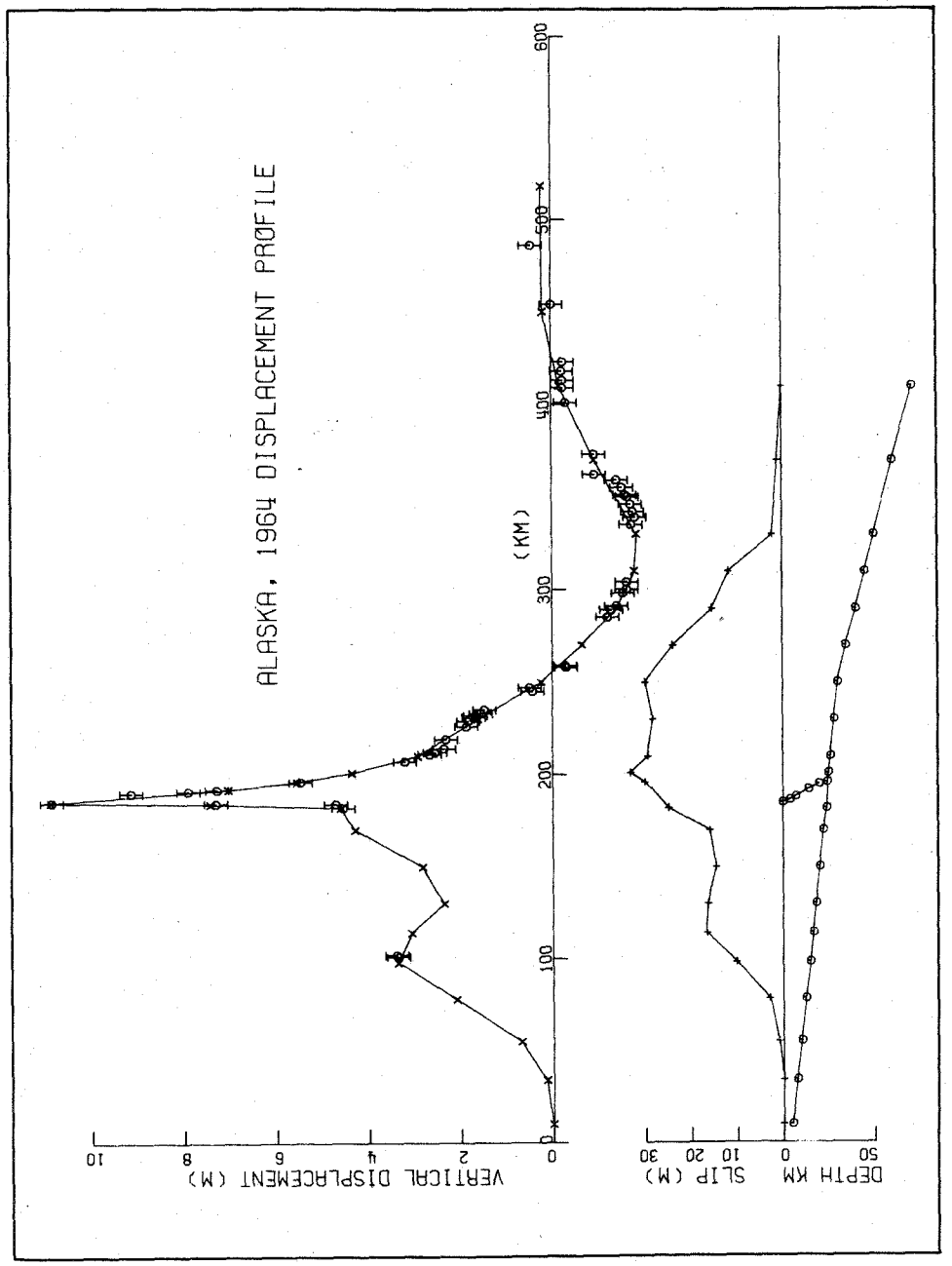

Figure 3.5. Observed and calculated vertical surface displacements and dislocations along the fault width. The dislocations plotted are offsets in a direction parallel to the fault.

width of about 60 km, then decreases almost linearly at a rate of 0.3 m/km over the next 100 km as the fault depth increases. At more shallow depths, there is a plateau in slip of about 17 m, which would correspond to the fault surface between Middleton Island and Montague Island. However, the two data points on Middleton Island are very important in this model in that their values almost completely determine the amount of slip along the top 150 km of the fault. The resolvability of this plateau will be discussed below. The slip on the secondary fault is not shown in this figure, but it averages 4 m over its entire width with the static offset on the node at the surface constrained to be equal to that measured for the scarp on the Patton Bay Fault as reported by Plafker (1967). The fault offset profile on the main fault is similar in shape to that proposed by Stauder and Bollinger (1966) who used a much simpler fault model and ignored the effects of geology.

Integrating the area under the slip versus fault width curve, we find that we have an average slip of 18.5 m over a 260 km fault width. This slip is at least 50% greater than that predicted by Stauder and Bollinger (1966), Savage and Hastie (1966), and Hastie and Savage (1970). One check to see if the average dislocation is reasonable is to calculate the average moment and compare with that

obtained from long period seismic waves. This average moment is given by

$$M_0 = \bar{u} L w \mu$$

where $\bar{u}$ is the average fault offset (18.5 m), L the length (600 km), W the width (260 km), and μ is the average rigidity of the region around the fault (3.1×10^{11} dyne/cm^2). By using the rigidity of the continental crust, the material in which most of the deformation takes place, we obtain an average moment of 0.9×10^{30} dyne-cm. Kanamori (1970) arrives at a moment of 0.75×10^{30} dyne-cm on the basis of long period (300 sec) multiple path Love and Rayleigh waves. At these long periods, the surface waves are sampling the entire fault width and thus should give a good indication of the average moment. These two values compare very favorably indicating that indeed there were very large displacements occurring along the fault surface. B. Minster (personal communication, 1973), on the basis of a systematic inversion of world-wide plate motion data, states that the Pacific plate and the Alaskan continental block are moving relative to one another at a rate of about 6 cm/year at the location of our profile.

The computed average slip on the fault leads to a recurrence time of an earthquake of this magnitude in this area of once every 300 years. However, if the central portion

of the megathrust with its average 30 m slip is used as representing the event, this gives a recurrence time of 500 years. Plafker and Rubin (1967) obtain a repeat time of about 850 years for major events on Middleton Island based on the radiometrically determined dates of a set of uplifted marine terraces found on that island. However, Sykes (1971) has expressed great uncertainty about estimations of recurrence times for major events in this region.

Although not included in the data set for the inversion, the measured horizontal displacement field was extensive. Parkin (1966) gives these horizontal movement vectors which are made with a free adjustment relative to a fixed station (Fishook station) located about 14 km north of Palmer, Alaska, an area that was then considered to be the most stable. This fixed station is 120 km northwest of the epicenter of the main shock. As in the case of the vertical displacements, only those horizontal displacement vectors near the profile line were chosen. There were 23 of these vectors in the vicinity of our section. These vectors were projected onto the profile and their component of motion in the direction of the profile taken. The resulting displacements are shown in Figure 3.6. The data points nearest the fixed station are the most accurate, being first order surveys, while the data on Montague Island are much less accurate, being based on third order

observations. The direction of motion for each of these points shown is to the southeast. The horizontal displacement in this same direction is calculated from the best fit slip model discussed above and shown in the figure. These calculated points are translated relative to the displacement at the node on which the observed apparent zero isobase is projected. The resulting displacements form a smooth curve except for the irregularity at the Patton Bay Fault. This irregularity is not resolvable in the data shown here. Even though these lateral displacements were not used in the inversion scheme, because of their lack of accuracy, the fit is surprisingly good. The model predicts a movement of 4 m to the southeast at the fixed station. A stable area for displacement reference is given to be at least 120 km farther to the northwest than the chosen fixed station. The consistency of the fit to both the horizontal and vertical displacement data seems to indicate that the model geometry that was initially assumed is reasonably accurate.

Figure 3.7 shows a contour plot of the calculated displacement field in two dimensions along this chosen section. The contour values are indicated on the figure and the units are in km. In the upper half of this figure is displayed the calculated two dimensional vertical displacement (Y direction in figure). From this figure, we see that the

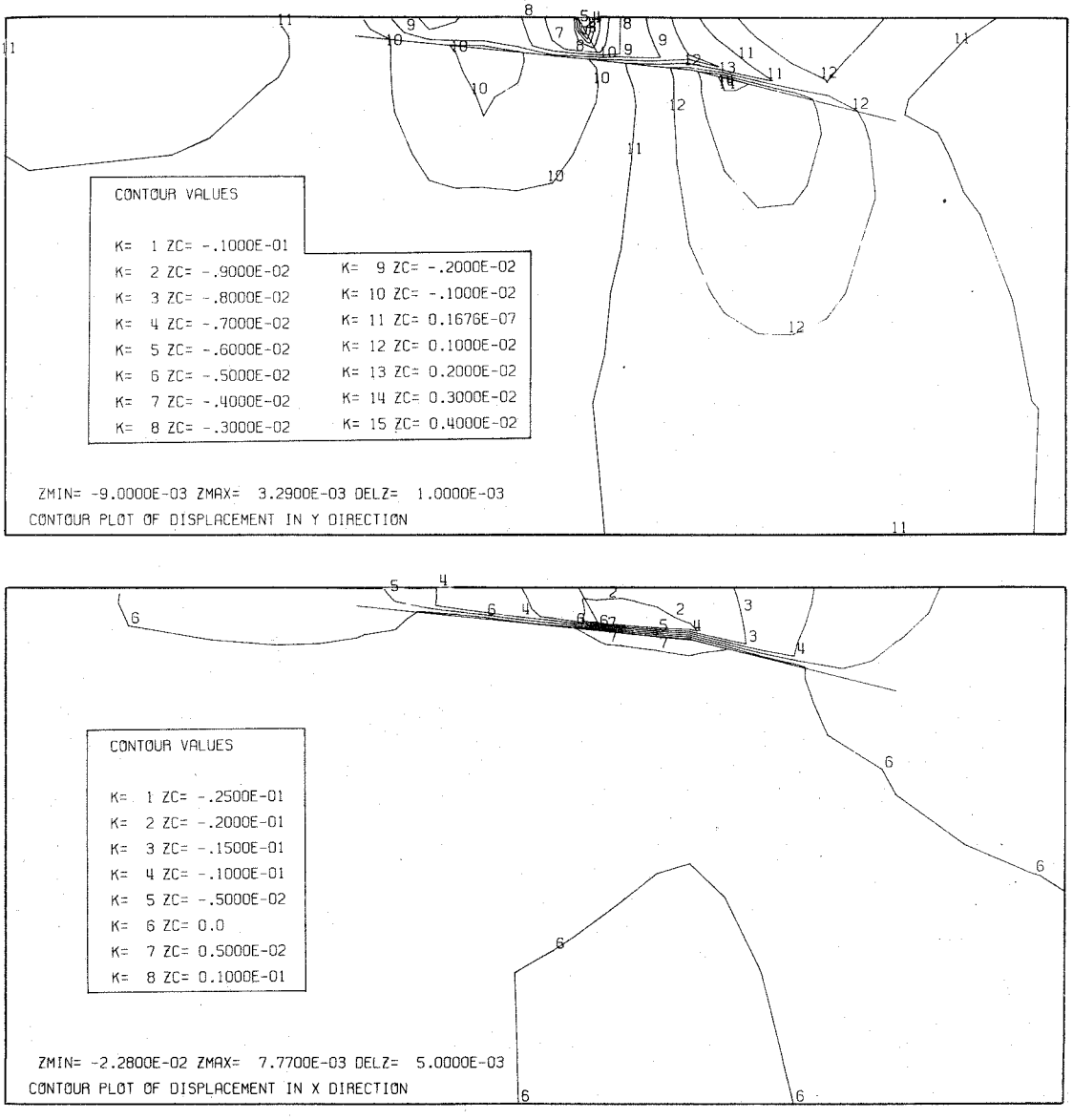

Figure 3.7. Contour plots through the cross section of relative displacement caused by the best fit dislocation solution. The contour values have units of km. The upper figure is a plot of the vertical displacements and the lower figure is a plot of the horizontal displacements.

displacement is concentrated under Montague Island and above the fault surface. The presence of the Patton Bay Fault is clearly visible on this plot. This partitioning of the displacement field is due to the effect of the nearby free surface. In the lower part of this figure, we see that the horizontal displacement (labeled the X direction in figure) is likewise concentrated immediately above the fault surface.

3.5 Resolvability of Features in the Slip Model.

Since the data used in the inversion are not perfectly accurate, there exist model perturbations which when added to our best fit slip model would still fit the observed surface displacement data to some chosen degree of confidence. If we can estimate the errors in our data, then we want to somehow relate these errors to errors in our model. Such a relation between the data space and the model space exists in the form of a variance operator (equation (2.33)). This operator is useful in this application in the following manner. If we take some perturbation, $\delta\mathbf{m}$, to the calculated slip, then this perturbation is resolvable by the data to within a certain confidence interval if the following inequality holds,

$$\delta\mathbf{m}^* \mathbf{V}^\dagger \delta\mathbf{m} > k^2(c) .$$

$\mathbf{V}^{\dagger}$ is the generalized inverse obtained by spectral decomposition of the variance operator, and k(c) is the coefficient associated with a particular confidence interval. In this study we have chosen to examine model perturbations at the 95% confidence level, so that in this case the coefficient associated with this interval is 1.96. Using this method, we can test chosen perturbations to our calculated slip model and compute the maximum perturbation that can be resolved at the 95% confidence level by the data. We note that these tests are independent of the values of the slip model itself, and only perturbations to this model can be checked for resolvability.

The variance operator, $\mathbf{V}$, for this case is a 26 x 26 matrix. The generalized inverse of this matrix is found by using the eigenvector expansion described in equation (2.32). We found that there were 16 non-zero eigenvalues associated with this operator. For problems where the estimated errors are very small, numerical problems may be encountered in calculating the generalized inverse of this operator. These numerical problems arise from the fact that round-off errors occur in the computer calculations of the eigenvalues. For small eigenvalues, the problem of distinguishing non-zero eigenvalues from the zero eigenvalues can become serious. Fortunately, this is not the case in this problem. The non-zero eigenvalues are well

defined. We have empirically noted that the number of non-zero eigenvalues of the variance operator **V** is equal to the number of independent data points used in the inversion. The inner product of the variance operator and its generalized inverse form a projection operator. This projection operator is then checked for its idempotent properties to make sure that all scaling is correct. This test is done in the following manner:

$$(\mathbf{V}\mathbf{V}^{\dagger})(\mathbf{V}\mathbf{V}^{\dagger}) - (\mathbf{V}\mathbf{V}^{\dagger}) < \mathbf{E} \qquad (3.1)$$

where the components of **E**, ε_{ij}, are taken to be some small number relative to the size of the components of **V**.

The question that we would ultimately like to answer with a study of this type is, "What is the maximum pertubation that we can add to our 'best fit' slip model and still satisfy the observed data?" Since we know that the size of the maximum perturbation that is at the threshold of detection by the data depends on the distribution of the perturbation, we choose three perturbations which will elucidate the total resolvability of our slip model. We first consider how much of a slip perturbation we can add to the dislocations in the hypocentral region, so that the rapid fall-off from the 30 m plateau is not so rapid. Figure 3.8a shows this maximum slip perturbation. The

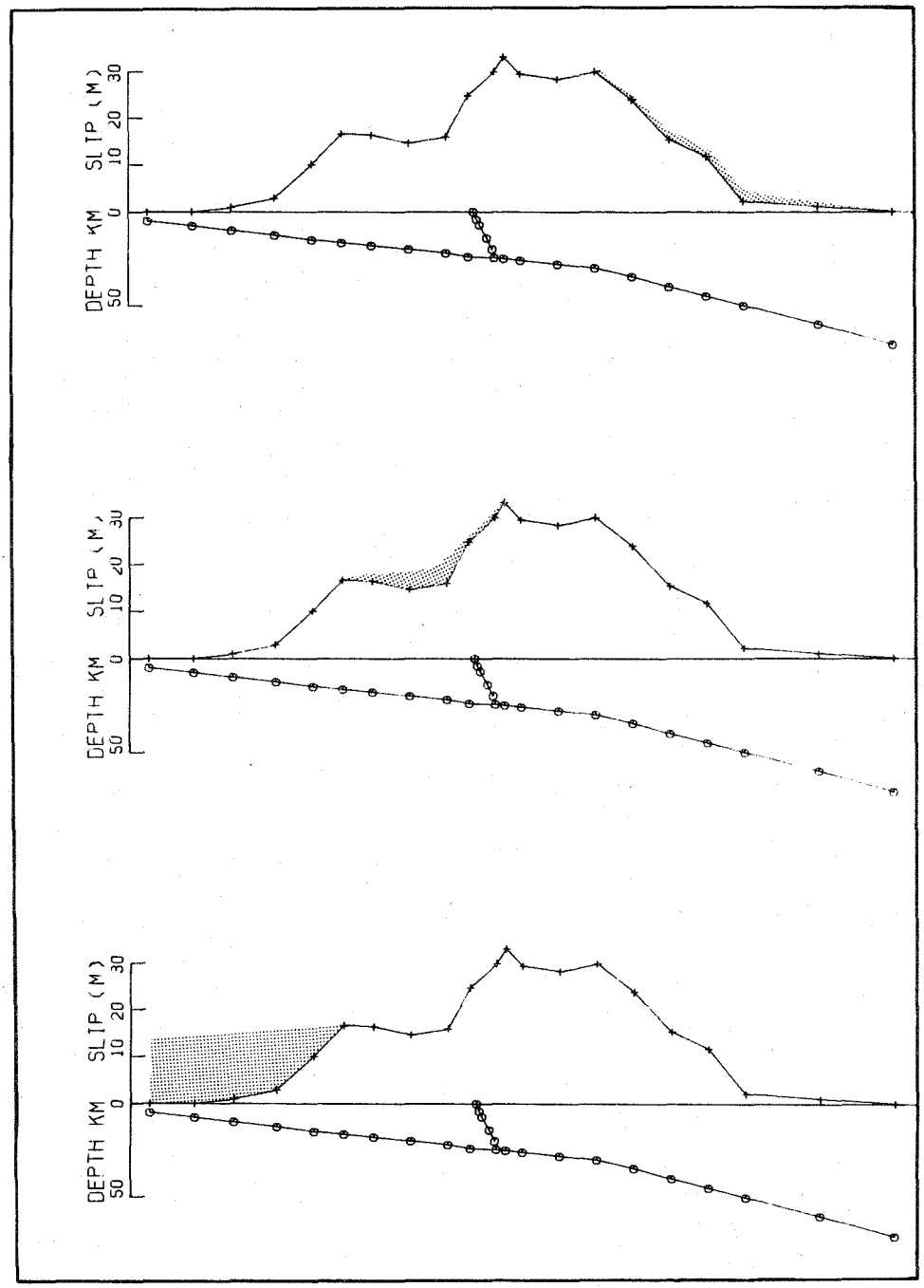

Figure 3.8. Examples of the resolvability of the best fit solution.

stippled area on this curve is the maximum slip that could be added in this region and still be undetected by the data. It is seen from the small size perturbation in this figure that the data control very closely the rate of fall-off of slip in this area of the fault. This is due mainly to the fact that there is a dense network of data points just above these particular nodes. Next, we try to determine if the data demand the existence of the 17 m plateau in the shallow part of the fault. Figure 3.8b shows the amount of slip that could be added in this region. We see that the slip gradient in this region could be smaller than that presented in our best-fit slip model, although there still appears to be a requirement for a sharp decay in slip up the fault from the 30 m plateau. The slight minimum in slip that appears in this region of the model is not resolvable by the data. In Figure 3.8c we see that there is almost no resolution along the upper part of the fault. This is due to the paucity of data on the surface above this region. In order to explain the behavior of the fault slip in this region we have to appeal to arguments based on other geophysical data than the statical displacements. For instance, it can be shown that large fault offsets in the area of the trench would result in a significant amount of strain energy stored by the fault in that region.

3.6 Averaging Operators.

In Chapter 2 we say that our "best fit" estimate of the slip model is in reality some filtered average of the true slip model. This filtering operator is commonly known as the averaging operator. Before discussing features of our final model it is to our advantage to know the extent of the averaging that is taking place in our model. The kernels of the averaging operator are taken to be individual rows of the operator matrix, **R**, as defined in equation (2.29), with a single kernel being defined for each fault element comprising the total fault system. We note here that if the problem is linear, as it is in this case, these kernels do not depend on the final estimate of the "best fit" model.

If a particular slip model value were perfectly well-known by the inversion then the averaging component centered on that fault element would be unity and all the other components of this kernel would be zero. However, in the general case where we have less than infinite data and the data that we do have are somewhat corrupted by noise, the center averaging values are not unity and the other components (off-diagonal components of the matrix **R**) are non-zero. The ability to resolve the details of the actual dislocation function depends on two features of this operator. One is the size of the kernels. This depends

in a general way on the availability of data to be included into the inversion that are sensitive to a dislocation over the part of the fault model that we are testing. As the value of a particular diagonal component of **R** becomes substantially less than unity, our ability to even estimate the slip value for the corresponding model component decreases. The other factor is the averaging width of the kernels. This averaging width is expressed by the off-diagonal elements of **R**. If these off-diagonal components, corresponding to the fault elements "near" the particular fault element we are examining are substantially non-zero, then the estimated "best fit" value of slip that we obtain from the inversion is really some linearly averaged value of the actual slip values in the vicinity of this fault element. These ideas are probably best expressed by examining an example of their use.

Figures 3.9 and 3.10 show examples of the averaging kernels for the Alaska earthquake model. The coefficients of the rows of the averaging operator are shown diagrammatically at the position of the respective fault node corresponding to the components of this row. The height of the bar plotted on each node signifies the absolute value of the averaging coefficient for that node. For absolute reference, in Figure 3.10c, the height of the outstanding bar is 0.997. In Figure 3.9, we have plotted

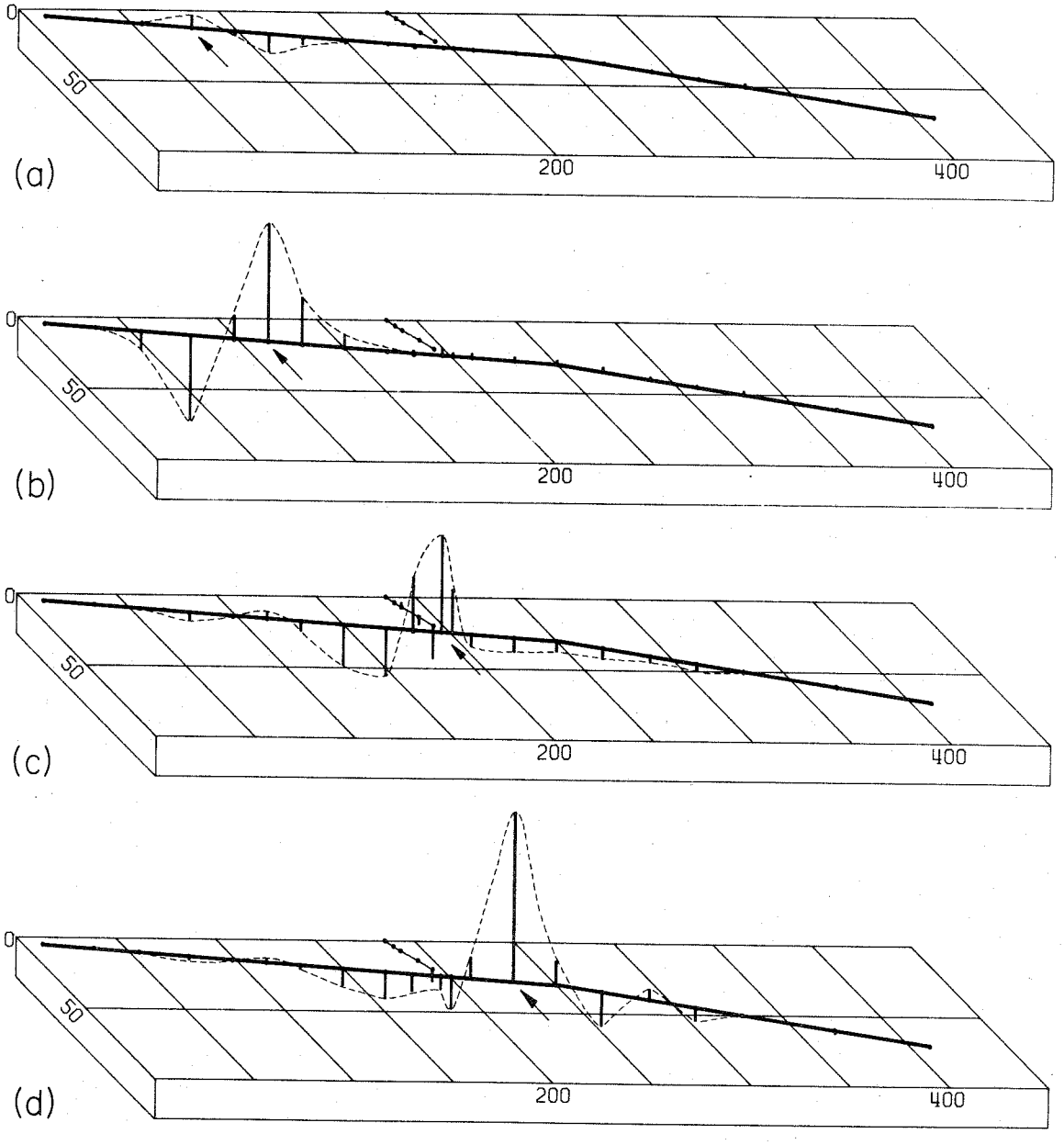

Figure 3.9. Resolving kernels for selected nodal segments along the megathrust. View is a perspective of the megathrust from the southeast (left) to the northwest (right). Depths and profile distances are in km.

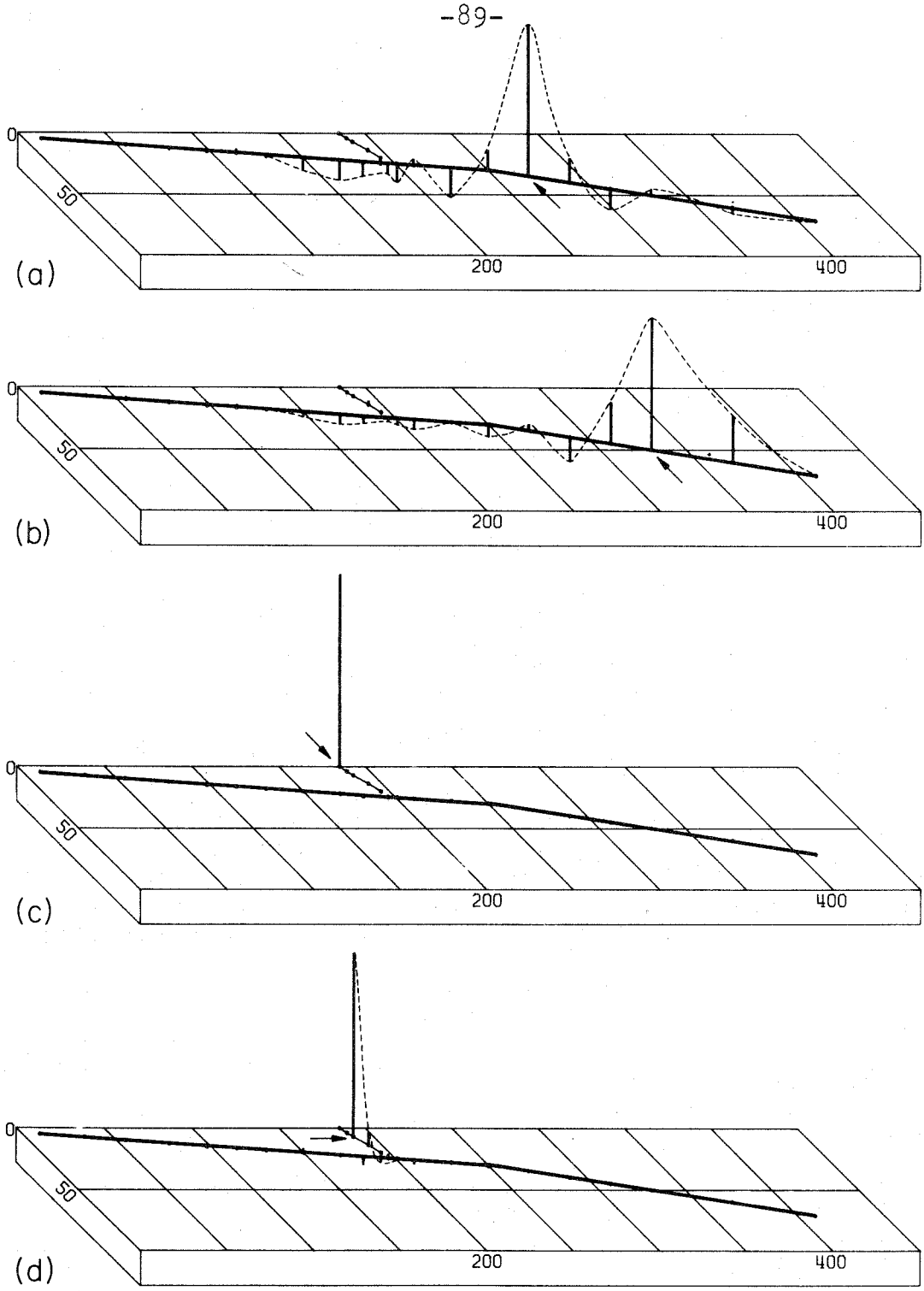

Figure 3.10. Resolving kernels for selected nodal segments along the megathrust (a,b) and subsidiary fault (c,d). View is a perspective of the megathrust from the southeast (left) to the northwest (right). Depths and profile distances are in km.

the averaging for representative nodes along the megathrust presented here in a perspective view. The arrow in the figure indicates on which node the averaging is centered. In Figure 3.9a we see that for the upper part of the megathrust, the averaging values are very small, again showing our lack of resolvability in this area of the fault. In Figure 3.9b the kernel values are larger in amplitude indicating our ability to estimate the slip in this portion; however, we see that there are large side lobes. The negative averaging coefficient, indicated by the bar extending downward, means that a positive dislocation on the centered fault node could be traded off with a negative dislocation on this node, and the data would not be able to tell the difference. In Figure 3.9c we see that the averaging over the adjacent nodes to either side of the central node is fairly severe, and that there is a slight amount of coupling to the subsidiary fault. In the bottom figure, we see that the amplitudes start to become more peaked, indicating better resolvability. We also note that the slip in this area is completely uncoupled from the slip on the subsidiary faulting. This shows how the effect of the subsidiary fault is very localized with respect to the megathrust.

The examples are continued in Figure 3.10. Sections a and b of this figure continue to show that on the lower part of the megathrust we are able to determine fairly well

the "best fit" estimate of the slip, but this slip is generally averaged over the one or two adjacent nodal segments. Figure 3.10c shows the averaging kernel for the topmost nodal segment of the representation of the Patton Bay fault. Here, the displacement is almost exactly determined. The height of the bar is almost unity, 0.997, and there is practically no spatial averaging. We would expect this result, considering that this fault segment breaks the surface and the amount of dislocation on this nodal segment is constrained by the scarp size on Montague Island. Likewise in Figure 3.10d, the dislocation at some depth on the subsidiary fault is well determined, and there is practically no trade-off in dislocation here to a dislocation on the megathrust.

The information contained in the averaging operator can be summarized by defining a resolvability ratio for each kernel. This ratio is defined as the ratio of the value of the diagonal coefficient of **R** to the averaging half-width. This averaging half-width, though somewhat ambiguous in some instances because of asymmetries, can usually be estimated,however. The averaging half-width is measured from the central fault node to the point where the averaging first crosses zero. This ratio is convenient and meaningful in the sense that it takes into account both the variables involved in estimating resolvability: the height

of the kernel and the averaging distance. For well resolvable features of our model we would expect large ratios; for less well resolvable features, smaller ratios. The results for this particular fault model are shown in Figure 3.11.

In this figure, we see that for the upper 75 km of the megathrust, there is a total lack of resolvability, controlled by the lack of data which are sensitive to a dislocation in that area. The resolvability is slightly peaked for the area of the megathrust immediately under Middleton Island, but again there is no resolvability in the area between the islands. The resolvability decreases rather evenly for the lower end of the megathrust. This is thought to be due to the fact that the dislocations are occurring at distances farther and farther away from the data, thus dislocation averaging starts to become a problem and the resolvability is reduced.

3.7 Stress and Strain Energy Density Change.

In terms of understanding the focal processes of earthquakes, an important parameter is the stress drop. In previous studies of earthquakes, the stress drops were obtained through empirical formulas or exact derivations for special purpose geometry of the crack (for example, Starr, 1928; Knopoff, 1958; Aki, 1966). The stress drop over some fault dislocation area is usually given by the following

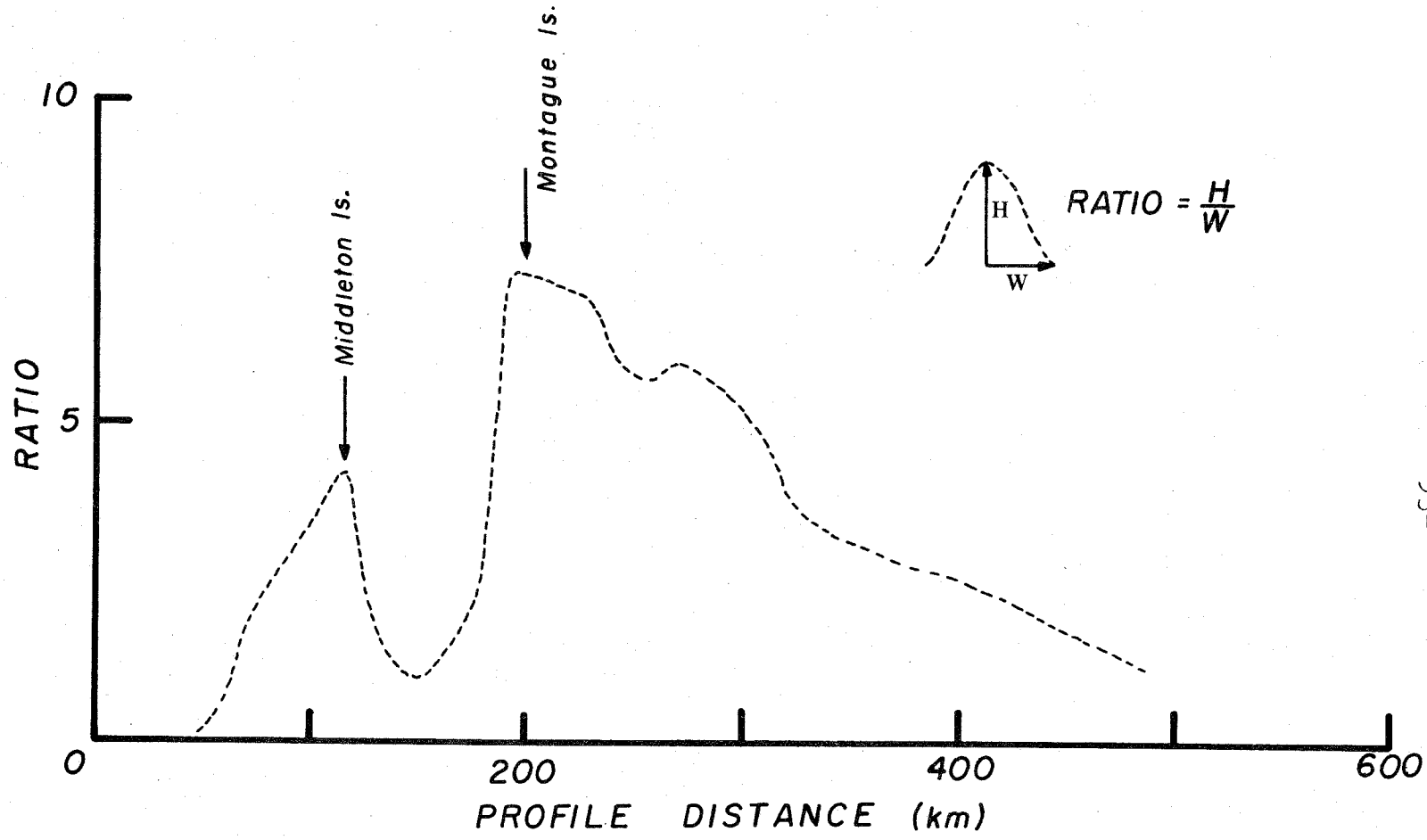

Figure 3.11. Resolvability ratios for the nodal segments along the megathrust plotted as a function of their projected distance along the profile BB'. Large values of this ratio indicate good resolvability and vice versa.

type relation,

$$\Delta\sigma = \frac{\eta U_m \mu}{W} \qquad (3.2)$$

where μ is the rigidity, U_m is the maximum displacement, W is some measure of the size of the fault, and η is some constant dependent upon the geometry and nature of the faulting. Use of this formula results in stress drop values that are averaged over the entire fault plane. For instance, Brune and Allen (1967) estimate the stress drop from the average offset given by Savage and Hastie's (1966) dislocation of the 1964 Alaska earthquake to be 27 bars. In this calculation, η is taken to be 1.33, W=200 km, U_m= 13.3 m, and $\mu=3.0 \times 10^{11}$ dyne/cm^2. If we were to use their formulation with our average dislocation, we would obtain a stress drop of 30 bars. Chinnery (1969) and Sato (1972) point out that in order to evaluate η the assumption of an infinite length fault is usually made. These two authors have derived the expression for the stress drop for a finite rectangular fault, and they show that the stress drops obtained for these faults are smaller than what one would obtain for infinite length faults. For the Alaska earthquake, Sato (1972) estimates η to be 0.97 when a constant displacement over the fault surface in an idealized medium is considered. His resulting estimate of the

stress drop using this parameter and our average dislocation would be about 22 bars. This last value is still an estimate of the stress drop averaged over the entire fault surface. However, it is obvious that if the dislocation is varying over the fault plane, and the geometry of the plane changes with distance, the stress change will not be a constant over the entire fault surface. Jungels (1973) has shown that for several earthquakes the stress drop can vary along the fault by as much as an order of magnitude.

To estimate the stress drop along the width of the fault we can apply equation (3.2) to each of the nodal segments which define the fault plane, but there is always uncertainty in the estimate of the parameter η. Jungels (1973) has shown a more direct method of calculating the fault stress drop distribution with the finite element method. This is accomplished by first imposing a composite prestress field on the structural model. This is done by applying a dislocation to the edges of the structural model. From this initial state, we can compute the equilibrium final state that would be caused by the introduction of our best fit dislocation model. Then, at every point of the structure, the difference between the initial and final stress fields defines the stress change. If $\Delta\sigma$ is positive, then the particular model caused a stress drop. If $\Delta\sigma$ is negative, then we have a stress increase.

It is clear that for a "dislocation" model the magnitude of the stress change is controlled only by the magnitude of the fault offset and the elastic constants of the structural model. Thus the prestress only has importance in terms of the strain energy change where the sign of the stress drop matters. The shear stress change approximately parallel to the megathrust is calculated by this method and is contoured throughout the cross section studied. (Figure 3.12). The values contoured are exact away from the fault plane, but for the nodes defining the plane itself, the actual stress drop is approximately twice the value shown. This error arises from the fact that a linear behavior of displacement is assumed inside each element in the finite-element grid. This error results in an underestimate of the stress change on the fault surface (Jungels, 1973). Assuming that the error is exactly a factor of 2 in this problem, we see that for our best fit model the stress change along the fault itself varies from a stress increase of 86 bars to a stress drop of 215 bars. The stress change over the entire width of the fault averages a stress drop of approximately 40 bars. This indicates how misleading a value of the average stress drop could be.

The details of the stress change are very interesting. We see that both ends of the fault underwent a net increase in shear stress. For the shallow portion of the megathrust,

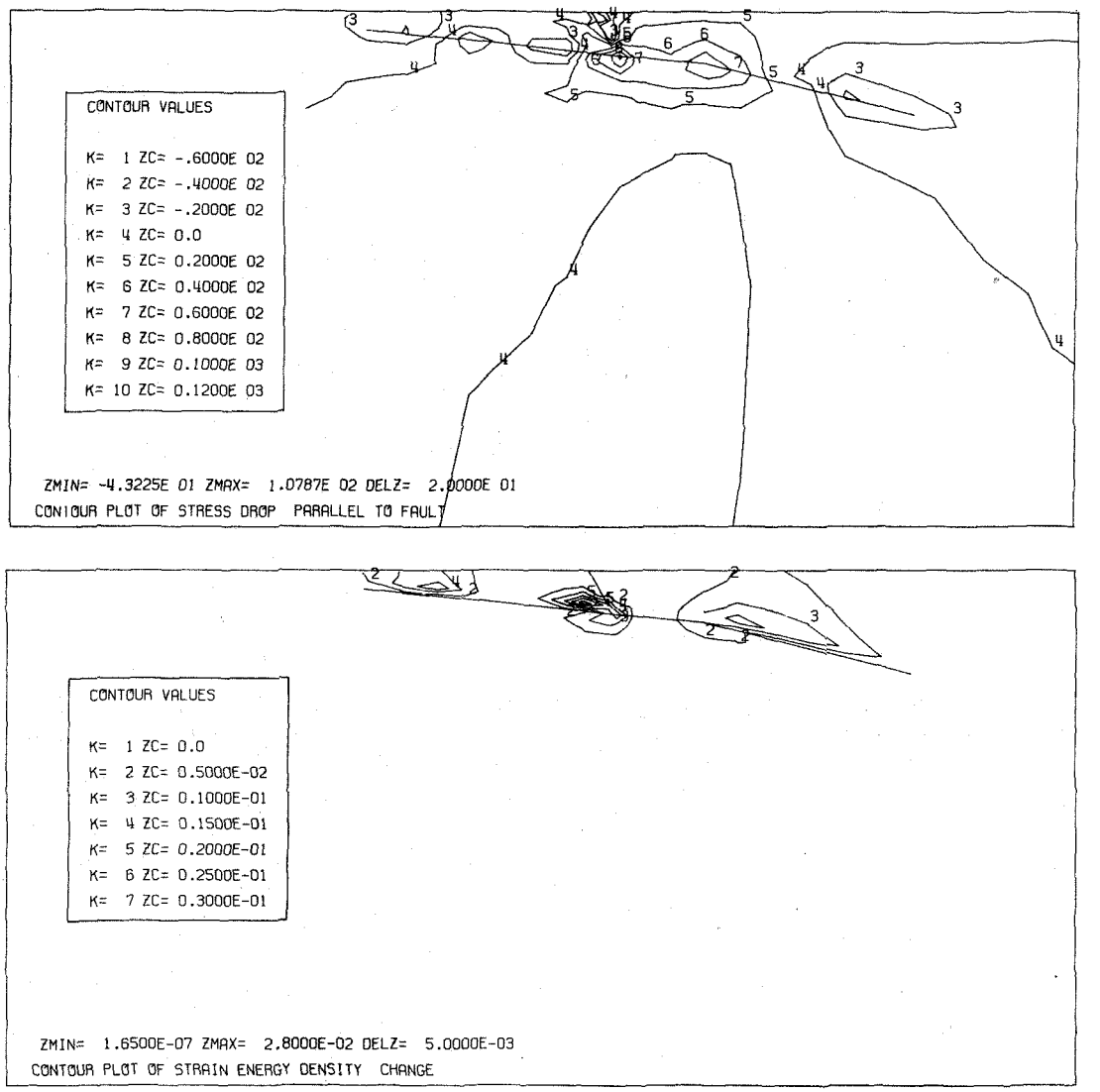

Figure 3.12. Stress change and strain energy released around the fault surface for an average prestress level equal to the average stress drop. Positive contour values of stress change represent stress drops. Units are bars and 10^{21} ergs per km^3.

this is an argument in favor of our best fit solution with its small offset in this region. It follows that if we increased the offset on the shallow end of the fault, even though we could not resolve this increase with the surface data, the stress change would increase in proportion and this in turn would make that region a prime candidate for aftershock activity. The fact that significant aftershocks were not observed here (Algermissen et al., 1972) argues for our best fit solution. On the other hand, if the offset at the shallow end of the megathrust were the maximum amount indicated on Figure 3.8, in all likelihood the displacements would rupture the free surface. If this was the case, the stored stress would be relieved and thus there would be very little or no aftershock activity. A search of the literature concerning this earthquake revealed that there seems to have been no post-earthquake reconnaissance of the ocean floor in the vicinity of Middleton Island and further toward the Aleutian trench, so that the possibility of this occurring cannot be ruled out. A hydrographic and ocean-bottom-scanning sonar survey of the area to the southwest of Montague Island revealed fresh scarps on older en echelon faults sub-parallel to the extension of the Patton Bay fault (Malloy and Merrill, 1969.) These authors attribute these scarps to the Patton Bay fault system. It is conceivable that much of the strain

from the large dislocations on the very shallow end of the megathrust could be relieved in this fashion. That is, large displacements on the fault surface are absorbed through a system of high angle bifurcations of the main thrust sheet. We will see in the next chapter that this is precisely what occurred during the 1971 San Fernando, California earthquake. Unfortunately, for the Alaska earthquake, the data are not adequate to prove or disprove that this condition existed, and further speculation along these lines seems fruitless.

Another area of slight stress increase on this figure is found in that region where the offset function in the best fit model goes through a local minimum between the 30 m slip plateau and the 17 m slip plateau. We have seen from the above discussion, however, that this minimum is not resolvable, so therefore the existence of the stress increase in this region is not resolvable by the data. Most of the stress drop along the fault surface occurs where the fault dislocation is the greatest. The maximum stress drop, 215 bars, is found along the megathrust just below the intersection of the Patton Bay Fault.

A plot of the strain energy density change in the media as seen in the lower half of Figure 3.12 illustrates that most of the energy available for seismic radiation would come from the central area of the megathrust in the

same region where the maximum stress drop occurs. The contours in the figure are in units of 10^{21}ergs/km^3. A direct comparison can be made between this strain energy density plot and the multiple rupture characteristics that Wyss and Brune (1967) found for this event. These authors interpret the P-wave radiation as caused by a multiple event source mechanism whereby the rupture initiating at the hypocenter travels up the fault plane triggering discrete seismic events larger than the initial event. The largest of these discrete events has been located on the megathrust 20 km southeast of Montague Island. The pulse from this region was delayed from the initial pulse by a time corresponding to a rupture velocity of 3.5 km/sec and had an amplitude significantly larger (up to 30 times larger) than that radiated by the initial shock. This agrees qualitatively with our estimate of a large strain energy density change of up to 0.28 x 10^{20}ergs/km^3 concentrated below Montague Island, while in the hypocentral region, the energy density change is computed to be only 0.02 x 10^{20}ergs/km^3.

3.8 Accuracy of the Plane-Strain Approximation.

We would like to somehow approximate the errors that occur by making the plane-strain approximation that we have taken in this example. One way of getting an estimate of this error is to approximate the fault model by a series of

three-dimensional Volterra planes and to use the static dislocation theory (Mansinha and Smylie, 1971; or equation (2.2)) for a three-dimensional fault in a homogeneous half-space. Although this model will not have the influences of the lateral heterogeneities included, it will serve to estimate how good or bad the approximation is that we have made. A Volterra approximation to the finite-element structural model was made. This model consisted of 22 individual fault elements, 18 to describe the megathrust and 4 to describe the subsidiary faulting. The Volterra fault elements are planar surfaces centered on the position of the finite-element fault nodal segments and extending halfway to the adjacent fault nodal segments. Only those fault nodal segments were modeled on which there was a calculated non-zero displacement. Several of the nodal segments, at the shallow end of the megathrust and at the very deep end of the megathrust, had "best fit" dislocation estimates of zero. These segments were not modeled with the Volterra approximations. The dislocation which is constant over the planar surfaces was taken to be equal to that of the finite-element fault nodal segment at the center. The parameters for this model approximation are given in Table 3.3.

We first calculated the vertical displacement for a profile due to this fault model with the length of each

TABLE 3.3

Fault Segment	Dip (deg)	d (km)	W (km)	$\langle \Delta u \rangle$ (m)
1	6.0	8.5	22.8	0.99
2	6.0	11.0	21.4	2.93
3	6.0	13.0	18.0	10.17
4	6.0	15.0	16.2	16.72
5	6.0	17.0	18.2	16.39
6	6.0	19.0	20.1	14.66
7	6.0	21.0	16.0	16.05
8	6.0	22.5	13.0	24.91
9	6.0	24.0	9.7	29.98
10	6.0	25.0	7.1	33.22
11	6.0	26.0	14.2	29.42
12	6.0	27.5	20.0	28.28
13	8.0	29.5	20.0	29.99
14	11.5	32.5	20.4	23.91
15	14.0	36.5	20.4	15.35
16	15.0	41.5	20.8	11.70
17	15.0	47.0	31.2	2.17
18	15.0	55.5	41.6	1.03
19	58.0	0.0	2.4	4.05
20	58.0	2.0	4.0	3.31
21	58.0	5.5	5.8	7.18
22	58.0	10.5	8.0	2.83

Table 3.3. Source parameters for the 3-dimensional homogenous approximation to the finite-element model of the Alaska earthquake. d is the depth to the top of the planar fault surface; W is the width of the fault surface measured along the dip; and $\langle \Delta u \rangle$ is the fault dislocation.

planar surface taken to be 10,000 km, or effectively infinity, to thus approximate the plane-strain criterion. The profile was taken to be equidistance from the ends of the fault elements and perpendicular to the strike of the system. The vertical displacements in a profile were then calculated from this fault system but now the lengths of the individual fault elements were set to 600 km, the approximate lower limit for the fault length estimated to be appropriate for this event. The profile was taken, not across the center of the fault system, but at a position 80 km from the center and still perpendicular to the strike of the fault system. This profile is 220 km from one end of the fault and 380 km from the other end. This is approximately the maximum distance profile BB' in Figure 3.2 can be considered from the center of the fault system. The estimated errors arising from the plane-strain approximation was taken to be the difference between the computed displacements for these two profiles. This difference is a function of the distance away from the origin of the fault system. The origin of the fault system is taken to be the point at which the shallow end of the megathrust projects to the surface. The differences are presented in Figure 3.13a. It is seen from this figure that the maximum displacement error expected from the plane-strain approximation would be about 0.35 m for this particular model. The

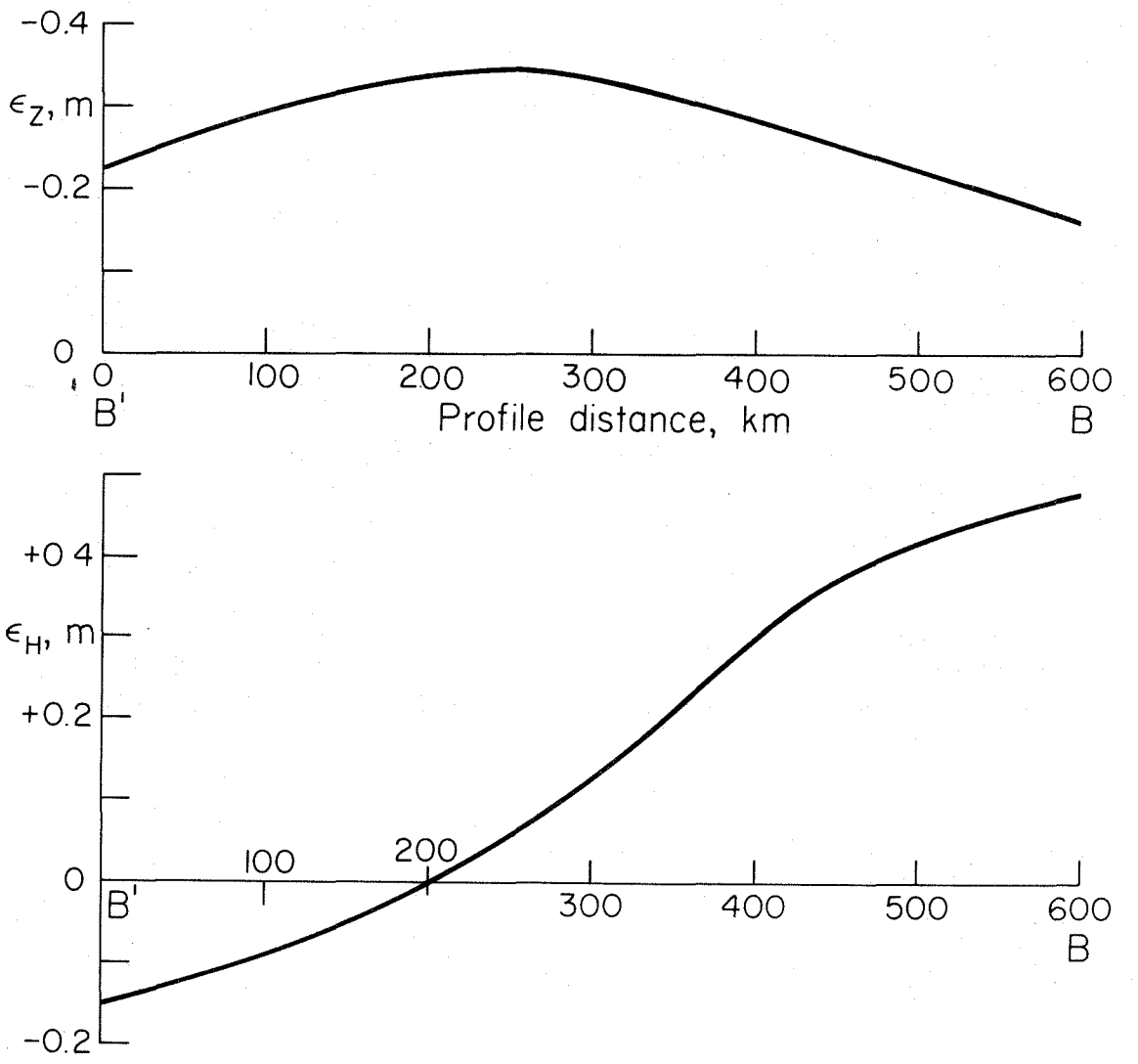

Figure 3.13. Estimates of the errors to the calculated vertical displacements (top) and horizontal displacements (bottom) due to the plane-strain assumption as a function of distance along profile BB'.

differences between these two profiles are relatively constant at about 0.25 m, and the sign of the error is such that the deformation at the surface is being underestimated. This implies that the free surface displacements for a fault dislocation model with a finite size length are slightly larger than those from a model in which each fault component has infinite length. Thus, we can say that the displacements calculated for the finite-element model are an upper bound to that necessary to fit the data. Considering the finiteness of the length of the actual fault, we would need only slightly less displacement on the megathrust.

Now the horizontal displacements are put to the same test. Horizontal displacements in the direction perpendicular to the strike of the fault system from the Volterra dislocation model were calculated for both a profile due to an infinite length fault and for a profile 80 km away from the center of a fault system that has fault element lengths of 600 km. Figure 3.13b shows the differences between the former and the latter profiles. It is seen here that as the profile distance becomes greater than half the fault length, the errors due to the plane-strain approximation start to become more significant. It is seen here that for the farthest distance along the profile, the expected error in the calculated horizontal displacements

is about 0.5 m. The sense of this error is that the estimated horizontal displacements made under the plane-strain criterion are too large. Thus in Figure 3.6 where we estimated that the reference station for the measured horizontal displacements (Fishook station) actually moved 4 m to the southeast, we have to revise this estimate to be about 3.5 m. The area of horizontal stability, that is, the area where no horizontal movement was expected, is still some 75-100 km to the northwest of the reference station.

We will now briefly examine the implications of the estimated error due to the plane-strain approximation. Since only the vertical displacements were actually used in the inversion procedure, only the errors associated with these measurements will affect the resolution of our model. Since the estimated errors due to the plane-strain assumption affecting the data points used in the inversion were about equal to the estimated observational error of the data themselves, we can estimate that at most, the total variance of the data should be multiplied by a factor of 4. As we can see from equation (2.33), if we want to recognize a given perturbation to our model at the same confidence limit as before (95%), then the size of the perturbation will have to be doubled. This means that in Figure 3.8 the amplitude of the stippled area will be doubled if we keep the shape of the perturbation as before. This implies

that the steepness of the rate of dislocation fall-off with distance from the maximum plateau going toward the hypocenter is not quite as resolvable as before. For the other two perturbations considered, the conclusions arrived at before are unchanged.

3.9 Conclusions.

A dislocation model has been presented for the 1964 Alaska earthquake. The surface displacements from this model are calculated with the finite-element numerical modeling technique in which the effects of both the known geologic heterogeneities of the region and the non-linearity of the assumed fault plane are taken into account. The dislocation model, which was obtained using a stochastic inversion scheme, fits with high precision both the observed vertical and horizontal displacements. The calculated static offset along the fault plane was found to be variable and to have a maximum amplitude much greater than previously imagined, although the average moment agrees with that observed from long period surface waves. The two-dimensional displacement field was found to be strongly partitioned above and below the fault surface, with most of the displacement occurring above the fault. The calculated displacement at the shallow end of the fault model was found to be almost non-resolvable due to the lack of surface displacement data, while the displacement near the

hypocenter was well constrained by the data. Along with the displacement calculated along the fault surface, both the stress drop and the strain energy density varied widely. The maximum stress drop found was 218 bars, while at both ends of the fault the stress field increased as a result of the static dislocations. The region of maximum stress drop and maximum strain energy density change calculated from this static study was found to correspond to the region of maximum compressional wave radiation. The errors caused by the plane strain approximation for this event were analyzed and found not to affect any of the above conclusions.

Chapter 4

A Static Dislocation Model of the 1971 San Fernando Earthquake

4.1 Introduction.

On February 9, 1971, a local magnitude 6.4 earthquake was initiated below the San Gabriel Mountains north of the San Fernando Valley, California. The surface ruptures from this event occurred some 13-15 km to the south of the epicenter along the Santa Susana-Sierra Madre fault zone which forms the frontal system of the southern boundary of the San Gabriel Mountains. The behavior and pattern of the faulting that occurred during this earthquake exactly repeated and further developed the older, already recognized geologic features--faulting and uplift--of the southern boundary of the San Gabriel Mountains which began in mid-Pleistocene time (Oakeshott, 1958). The stratigraphy and geologic structure of this area have been recently described by Wentworth and Yerkes (1971) and by Proctor et al. (1972).

In this chapter, we will not dwell on the geologic setting of the area since it is covered in some detail by the above references; rather, we will propose a fault model, the geometry of which we think to be most consistent with all the geological and geophysical observations that

have been made concerning this earthquake. These observations include the focal mechanism of the main shock, the mechanism and spatial distribution of the aftershock sequence, and the geologic character of the surface faulting. As in the previous chapter, once we have fixed the fault model geometry we will then use the static displacement data available to us along a profile bisecting the surface trace of the fault to determine the static dislocation function for our fault model which is most consistent with these data. Features of this calculated static dislocation model will then be examined for its resolvability, and implications of the model with its associated stresses and strains will then be discussed. Let us look first at the geological and geophysical observations that will constrain our fault model geometry.

4.2 Fault Model Constraints.

Main Shock Focal Mechanism. Unlike the 1964 Alaska earthquake, there seems to be no controversy of the choice of fault planes derived from the first motion studies of the 1971 San Fernando earthquake. The natural ambiguity in the choice of fault planes (assuming a double couple mechanism) is essentially removed by the geometric relation of the determined hypocenter and the observed thrust fault surface ruptures. Because the earthquake occurred in the midst of a dense seismographic network, the fault plane

solution is extremely well determined (Whitcomb, 1971; Dillinger and Espinosa, 1971; Canitez and Toksöz, 1972). This mechanism is primarily thrust faulting on a northerly-dipping fault. Whitcomb et al. (1973) give the following fault plane parameters: strike, N67°(±6°)W; dip, 52°(±3°) to NE; rake, 72°(67°-95°).

Surface Faulting. With the exception of the dip, these parameters derived from the faulting in the hypocentral region agree well with those determined by examining the surface ruptures. This surface faulting has been described in detail by a number of authors and agencies, most notably Kamb et al. (1971), Palmer and Henyey (1971), and Proctor et al. (1972). The observed surface faulting can be broken into three main groups:

1. A fault line extending approximately westward from the mouth of Big Tujunga Canyon to Foothill Boulevard, labeled the Tujunga fault segment. Proctor et al. (1972) argue that the name Lakeview thrust fault is the appropriate appelation for this segment. Nevertheless, we will refer to this fault segment as the Tujunga segment so as to be consistent, no matter if incorrect, with previous work.
2. A complex group of short length semi-continuous faults located 0.3-0.9 km to the north of and

sub-parallel to the Tujunga fault segment. This group will be referred to later as the splay fault group.

3. A fault zone extending approximately westward from Pacoima wash to Sylmar. This fault zone is slightly over 1 km to the north of the Tujunga segment and is called the Sylmar segment.

The surface scarps of the Tujunga segment extend more or less continuously for 11 km at an average strike of N70°W. The observed dips on the well defined scarps are in the range 20-25° to the north, and the motion is shallow thrust and left lateral. In the sub-parallel splay group, the scarps tend to parallel the sediment bedding which dips at about 65° to the north. These faults have been identified as bedding plane reverse faults with about equal amounts of vertical and left lateral motion (Kamb et al., 1971). No direct measurement of the dip was possible on the Sylmar segment which extends about 3 km in an east-west direction. Unlike the Tujunga segment, the surface scarps are less well defined here, and the scarp displacements become more diffusely distributed (up to 50 m) toward the western end of this branch (U. S. Geological Survey Staff, 1971).

Aftershocks. The aftershocks of this earthquake have been studied intensely by a number of researchers. Hanks et al.

(1971), Wesson et al. (1971), and Allen et al. (1971, 1973) have described the location and depths of these events, and Whitcomb (1971, 1973) has gone into considerable detail interpreting the mechanisms and classifying these events. The epicentral locations of the aftershocks outline an area that is roughly crescent-shaped. The locations are clustered on the exterior of this outline indicating that, except at the edges perhaps, the stress was completely relieved in the region where the fault plane approached the free surface. The distribution also suggests that if we take the edge of the faulting plane to be defined by the outer limits of the aftershock distribution, then this edge is well defined. The hypocenter of the main shock is located at the lower, northernmost edge of this zone of aftershocks. Hanks (1972), Whitcomb (1971), Allen et al. (1973), and Whitcomb (1973) suggest that the western edge of the aftershock zone represents a steep flexure in the fault plane. The aftershocks along this flexure are predominantly left lateral strike slip and tend to occur at deeper depths than on the main fault plane.

Allen et al. (1973) give evidence for the fault plane to have an intermediate dip which is less than that obtained from the focal mechanism of the initial event but greater than the shallow surficial dips. These authors report that the slip motion vectors for the aftershocks

located between the hypocenter of the main event and the surface ruptures had an average plunge of 36° toward N 20° E. Additional supportive evidence for this intermediate dip angle for the fault plane between the two extremities is given by the calculated hypocentral depths of the aftershocks. Whitcomb et al. (1973) report that these events line up in a zone which has a dip to the north of between 35° to 40°.

4.3 Assumed Fault Model.

We have assumed the following fault system to conform with all the geological and geophysical properties that have been determined about this system which was discussed previously. The fault system is shown schematically in Figure 4.1. The main thrust branch of this system is composed of 21 adjacent fault elements. From the surface down to a depth of 7 km, these elements define a plane which dips at a constant angle of 35°. From 7 km to 9 km depth, the main thrust branch has a dip of 40°, and below this depth, each of the elements has a dip of 52°. The lower edge of the fault system is at a depth of 14.5 km. The splay fault system is modeled by a series of imbricate reverse thrust fault planes intersecting the main fault plane in the upper 1 km block. These 20 fault elements have a constant dip of 65°. We will see later in this chapter what effect the addition of these splay faults has

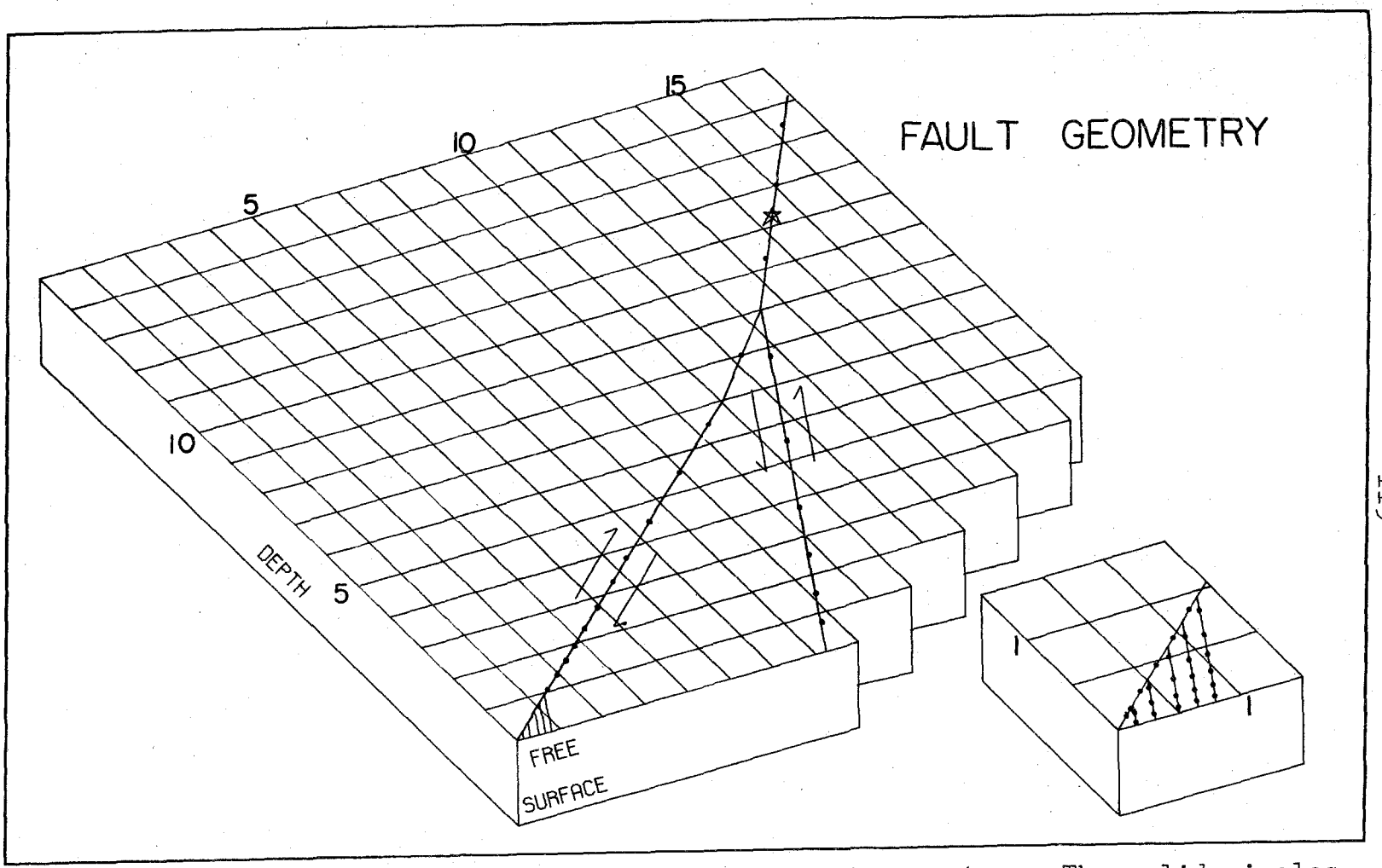

Figure 4.1. Perspective view of the assumed fault geometry. The solid circles indicate the mid-point depth (km) of the individual fault elements; the hypocenter of the event is indicated by the star. The block offset on the right is an expanded view of the upper 1.5 km to show the details of the splay fault group. The inversion profile extends from left to right along the surface.

on the calculated dislocation function. Also included in the fault system is a model of the San Gabriel fault. This fault is perhaps the major geologic feature of the entire epicentral area. Wesson and Wilson (1972) have postulated that this fault was involved in the seismic activity that accompanied this earthquake. Kamb et al. (1971) report, however, that there was no field evidence of displacement occurring on this fault in the aftershock region. We do note that there is a correlation of the area of positive gravity changes and the position of this fault. This suggests that if any displacement did occur on this fault during the earthquake, it occurred at depth, and the motion was of the normal faulting type. This fault is located some 7.2 km north of the main surface breaks on the Tujunga segment and is modeled by a plane of constant, 62°, dip composed of 6 fault elements. In this representation, the San Gabriel fault intersects the main thrust fault at a depth of 9 km. Thus, the total fault system is composed of 47 separate fault surface elements. Individual elements can be eliminated from the system by merely setting the weighting coefficient for that particular element to zero.

We have chosen to take the length of the fault elements near the surface to be 15 km. We have interpreted the clustering of the aftershocks in the epicentral area which form the top of the inverted "U" to be caused by the

fault length becoming somewhat less as the fault goes to greater depths. The fault lengths in our assumed model taper from 15 km at the surface to 9 km at the hypocenter. Table 4.1 gives the source parameters necessary for a description of this fault system. This table has been split into two parts. Part a gives the parameters for the fault elements which comprise the main fault. Part b gives the parameters for the splay fault group and the San Gabriel fault approximation.

In the fault representation given here, we have not accounted for the 1 km north-south offset between the Tujunga and Sylmar fault segments, but rather have considered the Tujunga segment as a continuous fault extending linearly over the surface for 15 km. Because this offset occurs close to a lateral extremity of the fault plane and we intend to choose our data for the inversion process from near the center of the fault plane, this approximation should be a good one. We will see later in this chapter how this offset can be modeled with the fault system geometry given here.

4.4 Static Data.

Although unfortunate from a humanitarian standpoint, the earthquake propitiously produced its maximum surface deformation in an area of exceptionally good geodetic control. This deformation was mainly mapped by measuring

TABLE 4.1a

Element #	Length	Dip	Mid Pt Depth	Width
M1	15	25°	0.050	.24
M2	15	25°	0.150	.24
M3	15	30°	0.275	.30
M4	15	30°	0.425	.30
M5	15	35°	0.600	.35
M6	15	35°	0.800	.35
M7	15	35°	1.050	.35
M8	15	35°	1.350	.52
M9	15	35°	1.650	.52
M10	15	35°	1.950	.52
M11	15	35°	2.300	.70
M12	15	35°	2.750	.87
M13	15	35°	3.250	.87
M14	15	35°	3.750	.87
M15	15	35°	4.500	1.74
M16	14	35°	5.500	1.74
M17	13	35°	6.500	1.74
M18	12	40°	8.000	3.11
M19	11	52°	10.100	2.79
M20	10	52°	11.950	1.90
M21	9	52°	13.450	1.90

Table 4.1a. Source Parameters for San Fernando Fault. Parameters are in km.

TABLE 4.1b

Element #	Length	Dip	Mid Pt. Depth	Width
S1	15	60°	0.25	0.12
S2	15	60°	0.075	0.12
S3	15	60°	0.04	0.12
S4	15	60°	0.11	0.12
S5	15	60°	0.18	0.18
S6	15	60°	0.04	0.12
S7	15	60°	0.13	0.12
S8	15	60°	0.22	0.23
S9	15	60°	0.31	0.22
S10	15	60°	0.04	0.12
S11	15	60°	0.13	0.12
S12	15	60°	0.23	0.17
S13	15	60°	0.31	0.17
S14	15	60°	0.44	0.31
S15	15	60°	0.04	0.12
S16	15	60°	0.13	0.12
S17	15	60°	0.24	0.17
S18	15	60°	0.34	0.17
S19	15	60°	0.46	0.23
S20	15	60°	0.60	0.28
SG1	15	62°	0.75	0.57
SG2	15	62°	1.50	1.13
SG3	15	62°	2.50	1.13
SG4	15	62°	3.75	1.70
SG5	14	62°	5.50	2.27
SG6	12	62°	7.75	2.83

Table 4.1b. Source Parameters for San Fernando Fault. Parameters are in km.

elevation and horizontal line length changes by comparing pre-earthquake and post-earthquake measurements. These data have been compiled principally by the U. S. Geological Survey (Burford et al., 1971; Savage et al., 1973), the City of Los Angeles, Bureau of Engineering (personal communication, 1971), and the Survey Division, Department of County Engineer, County of Los Angeles (1971). From these sources, over 100 vertical displacement data points were obtained. These points were then plotted and contoured for equal elevation changes. This contour plot is shown in Figure 4.2. With the exception of a few points located just to the south of the surface ruptures, all the data points obtained from the geodetic releveling show an uplift. In addition to the releveling data, we can estimate changes in elevation by examining the changes in the gravity field caused by this change in elevation. For this earthquake, we have measured gravity changes in unsurveyed areas where elevation changes would otherwise be unattainable. Appendix 2 of this thesis describes the gravity changes which accompanied this earthquake and the relationship between the measured elevation changes and the gravity changes.

Figure 4.2 also shows a profile which approximately bisects the area of deformation. In this study, we will limit our inversion data set to vertical displacement data

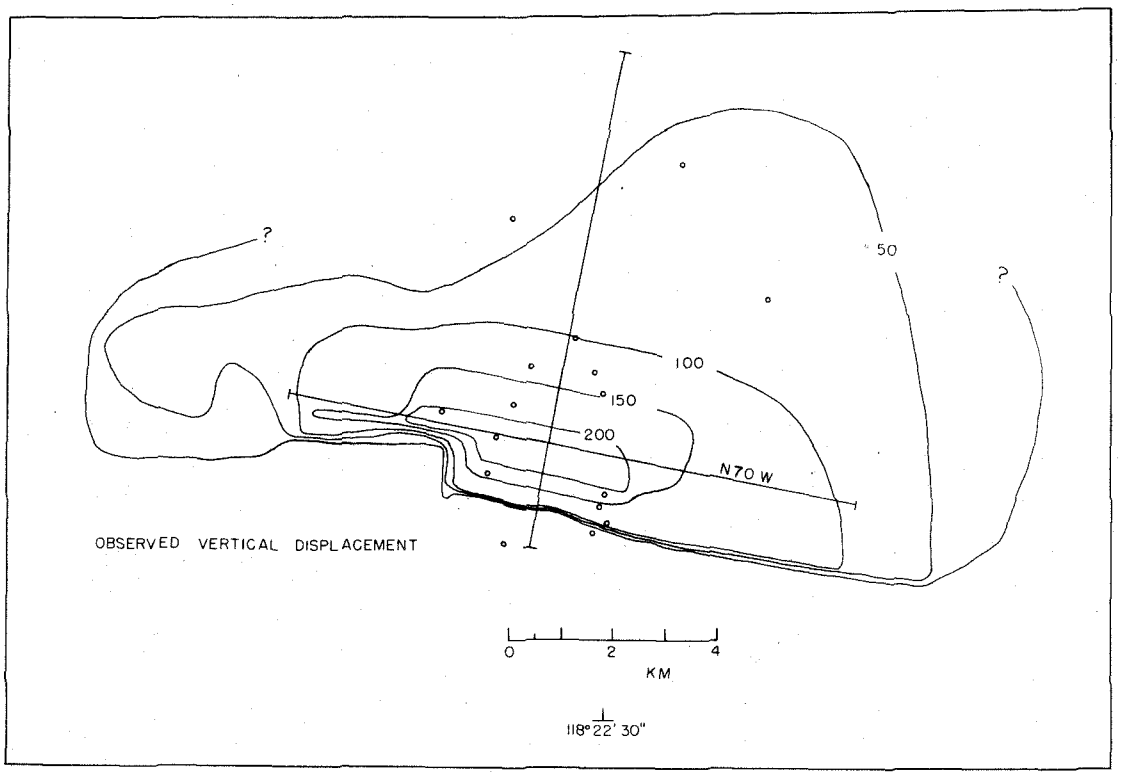

Figure 4.2. Contour plot of observed vertical static displacements. Open circles indicate the location of the data values used in the inversion profile. Profile is indicated as the line perpendicular to the strike of the surface deformation.

only. An attempt was made to use horizontal shortening in the direction perpendicular to the strike of the fault, but the only data which were least contaminated by end effects were relative line changes between stations both of which were located very near the surface ruptures. These data are shown in Figure 4.3 (eg. TUJ-6P10). This kind of data is particularly ill-suited for inclusion in the inversion because if the surface ruptures are mislocated by even 10-20m, the relative line change can change drastically. Since the Tujunga scarp has this much local variation in linearity, we considered these data too unstable to use in the inversion scheme. We therefore limited the inversion data set to vertical displacements only.

As in the case of the Alaska earthquake, we restricted our data set to only those points which could be projected onto a profile without crossing a contour line. There were 16 releveling points near the profile which met this criterion. These points are shown in Figure 4.2. It is seen on this figure that along the profile the contours for displacements greater than 100 cm are quite regular. By regular, we mean that they are orthogonal to the profile. On the 50 cm contour line north of the surface ruptures some asymmetry is apparent. Since we wanted to include information over as much of the profile as possible, we

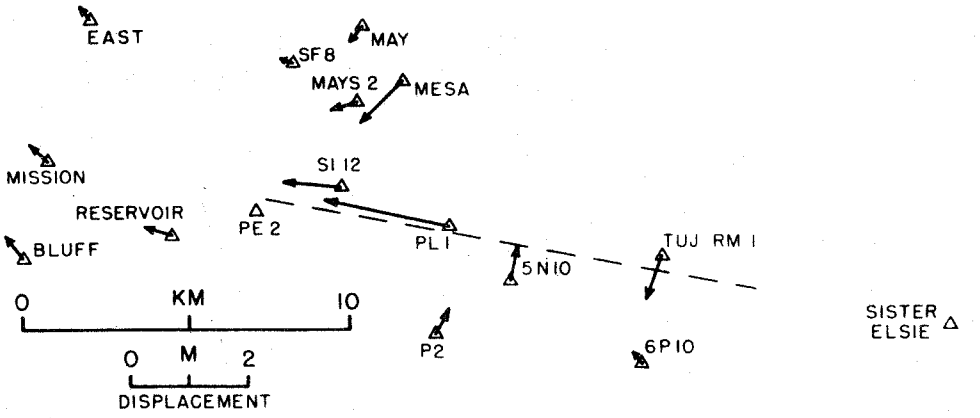

Figure 4.3. Horizontal displacements (relative length changes) in the area (Savage et al., 1972; reproduction permitted by Dr. J. C. Savage).

decided to include an estimation of the displacement here. The data point between the 50 cm contour line and the 0 cm contour line to the west of the profile shows 35 cm of uplift, and the data point within the 50 cm contour line to the east of the profile indicates 65 cm of uplift. The 50 cm contour line was drawn halfway between these two points, and a 50 cm data value was included into the inversion data set at the point where the 50 cm contour line intersected the profile. In making this approximation, we have included a larger variance to this point. We will see later that a lateral variation of $\pm$ 0.5 km of the location of this particular data point along the profile does not degrade the fit of our final model. There are other releveling points along this profile in the epicentral area along Sand Canyon Road. The vertical displacement values of these points range from 25 cm to 30 cm over a length of 2-3 km. We have chosen to include this cluster of points as a single value of 25 cm and to increase the variance associated with this datum. This was done because Ellingwood and Williamson (1971) report that these points might have as much as 8-11 cm of uplift due to secular change.

Four more vertical displacement data points were added to the inversion data set by converting gravity changes to elevation changes. Three of these points are located to

the north of the points shown in Figure 4.2, but still south of the epicenter. One point is located north of the Sand Canyon Road releveling points. The exact locations of these gravity points are shown in Figure A2.4 given in Appendix 2. Further discussion about the gravity points can be found in that section of this thesis.

In this investigation, we will assume that all the vertical displacement occurred at the time of the initial earthquake. Displacements occurring after this main event were found by a number of surveys to be very minor when compared with the total vertical displacement (Nason, 1971; Lahr et al., 1971; Burford et al., 1971; Savage et al., 1973; Sylvester and Pollard, 1973). Any vertical afterslip that was measured for a particular datum is included in the variance of the displacement for that datum.

Table 4.2 gives the entire data set that we will use in the inversion. The origin of the profile is taken at the surface breaks with positive distance taken to be in the direction of N 20° W. Also included in this table is the estimated error in the data. This error estimate is taken to be that estimated by the individual investigators who measured the data.

4.5 Calculated Dislocation Model.

Starting Model. Since several other investigators (Savage et al., 1973; Canitez and Toksöz, 1972) have proposed a

TABLE 4.2

Distance (km)	Δz (cm)	δ(Δz) (cm)	Reference Year	Source
-0.73	-1.0	3.0	1960	LABE
-0.23	-3.0	3.0	1960	LABE
0.22	114.0	4.0	1963	USGS
0.34	142.0	4.0	1963	USGS
0.50	185.0	4.0	1963	USGS
0.55	192.0	4.0	1963	USGS
1.26	228.0	4.0	1963	USGS
1.48	207.0	4.0	1960	LABE
1.87	173.0	4.0	1963	USGS
2.40	149.0	4.0	1963	USGS
2.66	122.0	6.0	1963	USGS
2.78	135.0	6.0	1963	USGS
3.42	98.0	4.0	1963	USGS
4.82	71.0	4.0	1929	USGS
6.52	50.0	8.0	*	USGS
8.22	29.0	13.0	**	USGS-GRAV
9.92	0.0	13.0	1970	GRAV
11.50	-15.0	20.0	1970	GRAV
17.00	22.0	17.0	1964	GRAV-USGS
20.00	10.0	17.0	1964	GRAV

* Average - 65 cm (1929) and 38 cm (1960)
** Average along Sand Canyon Road (1963-1968)

Table 4.2. Vertical uplift data along Inversion Profile. Distance is measured from origin of profile, Δz is the uplift, δ(Δz) is the estimated uncertainty of the measurement. LABE = Los Angeles Bureau of Engineering, USGS = U. S. Geological Survey, and GRAV = Gravity measurements (see Appendix 2).

constant dislocation on some constant-dipping fault plane to be consistent with the static data for this earthquake, one such starting model would be to assume a constant dislocation throughout the assumed main fault system. A simple numerical experiment was devised to test the applicability of this constant dislocation model to the inversion data set. This experiment is described as the following.

From Table 4.2 we see that the maximum vertical displacements occur at about 1 km to the north of the origin of our fault system. (The origin of the fault system is taken as the point where the Profile AA' intersects the line formed when the main fault surface intersects the free surface.) If we normalize the observed displacement data to this maximum value, we see that there is a rapid diminution with distance away from the surface ruptures. One way of affecting this rapid distance-decay of the vertical displacements is to have the fault plane dip at a steep angle. In the case of this earthquake, the dip of a single fault plane representation is limited by the spatial relationship of the surface ruptures and the epicentral location. If we assume that the hypocenter marked the lower bound of the fault plane, then the maximum angle that a single plane could take would be about 45°. This takes into consideration the uncertainty in the

locations of both the epicenter and hypocenter. Another factor that affects the vertical displacement at distance away from the surface ruptures is the depth to the bottom of the fault plane. In this problem, this is correlated with the fault dip. The minimum value of depth that this fault plane could take would be about 9 km. If we calculate the vertical displacement from a fault plane with these parameters, we see that the diminution is much smaller than that exhibited by the data. These results after a similar normalization are shown in Figure 4.4. For a more reasonable geometry of a constant dip of 35° and a depth of faulting of 10 km, the fit to the data is even worse. Intermediate to these two curves in this figure is that for a fault plane dipping at 45° and extending to a depth of 12 km.

One might argue that local geologic heterogeneities might cause such a departure from the idealized elastic case which we have assumed in these calculations. This same experiment can be carried out with the finite element modeling technique. When the geologic structures of this area are used in this technique, practically the same results are obtained (Jungels, personal communication, 1972).

If we take a planar dislocation surface of constant dip, but allow the displacement to vary along this surface, we can fit the observed vertical displacement much better

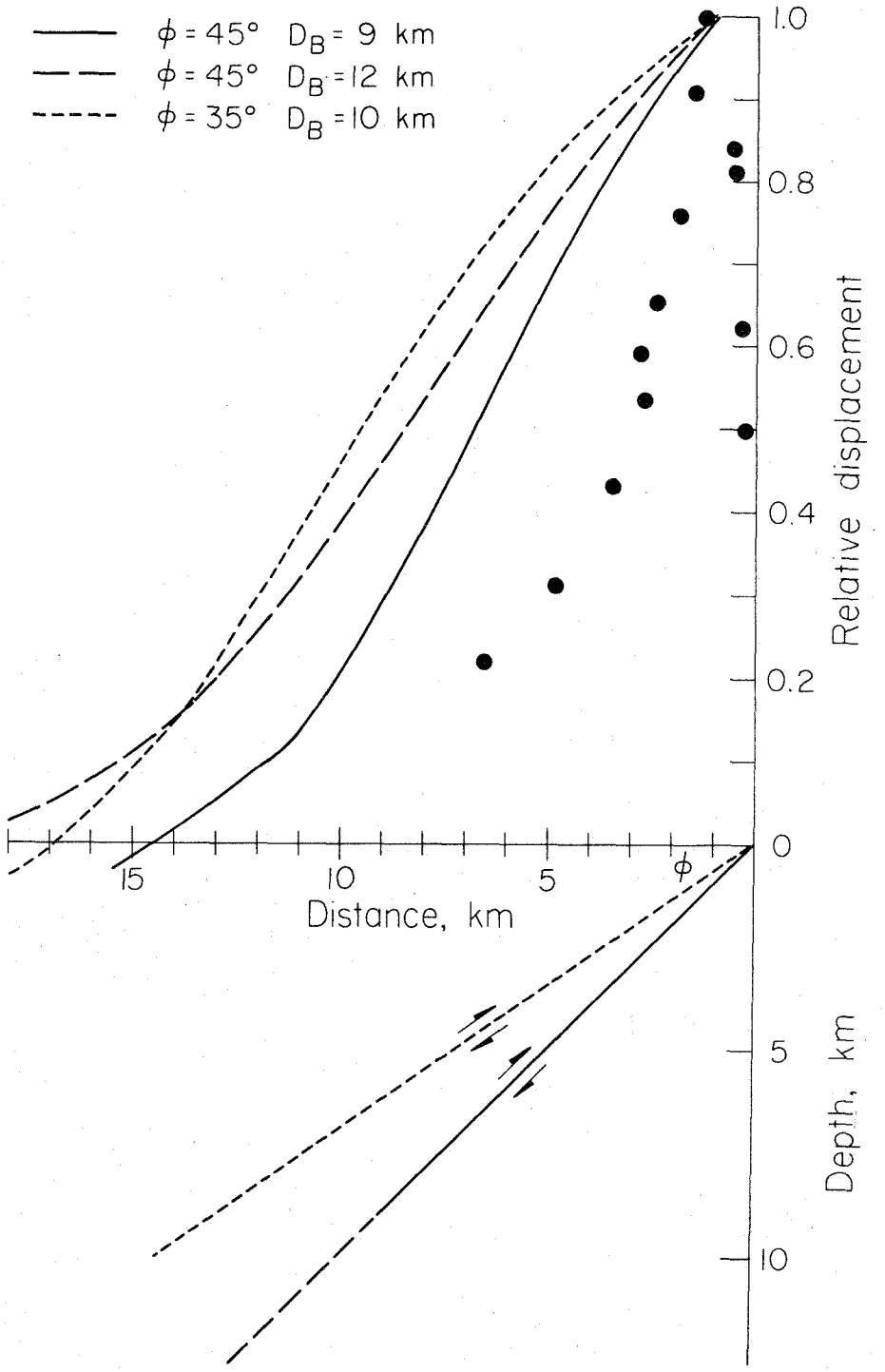

Figure 4.4. Test to see if a constant dislocation on a fault surface could fit the observed vertical displacements. The data (solid circles) are normalized to the maximum value.

if the displacement is allowed to vary piece-wise with depth in a manner $e^{-\gamma h^2}$. No inversion was used in these calculations, but rather different slip models, each having a different slip decay-rate away from the surface, were tried. The constant, γ, necessary to fit the data in this case can vary from 0.07 km^{-2} to 0.12 km^{-2} depending on the chosen dip of the fault plane. Mikumo (1973) has arrived at a similar result.

This simple calculation has been rather unsophisticated, but we think that this illustration clearly shows that the observed vertical displacement data require a fault dislocation function which varies along the fault. This variation in the fault slip should be in the direction of decreasing with increasing depth in order to properly fit the data. Since we have normalized the amplitudes to that obtained about 1 km distance from the point at which the fault surface intersects the free surface, this conclusion might not hold for the upper 1 km (approximately) of the fault surface.

We can now proceed with the actual inversion of the displacement data to get the "best fit" dislocation function. We will use as a starting model one in which the displacement varies in an exponential manner as that described above. We can note here that we would intuitively expect that the displacement data shown in Figure 4.4

would be affected by only the upper 5-7 km of the fault system that we have chosen. This fault system was made to consist of many small fault elements in order to more adequately estimate this large slip variation which we will expect.

Inversion Results. The media response matrix, **A**, was calculated from the analytic expressions given by Mansinha and Smylie (1971) for the structural model given in Table 4.1. Using this formalism, the static displacement response on the surface at the positions of the observed data due to a unit (1 cm) dislocation on each of the individual fault elements was calculated. Since there were 20 data points, or 20 positions on the surface at which the displacement response was calculated, the media response matrix was composed of 20 rows. The number of columns of the matrix indicates the number of fault elements which were used to represent the fault system. This number was varied, as we shall see below.

Initially, we assumed that the fault system was composed of only the 21 elements listed in Table 4.1a (M1-M21). We will refer to this fault system as the main thrust sheet. The media response matrix for this fault system was composed and the inversion scheme initiated with the exponental decay starting model described in the previous section. The inversion converged quickly to a

"best fit" solution. This solution is presented in Figure 4.5.

The lower part of Figure 4.5 shows this "best fit" dislocation on each of the 21 fault elements which comprise this present fault system. We see that the dislocation at the surface is calculated to be 266 cm. This value immediately decreases to 160 cm at a depth of about 0.3 km. The maximum dislocation (515 cm) on the fault surface is at a depth of 0.8-0.9 km. At depths greater than 1 km, the dislocation on the fault surface decays almost linearly. A minimum is reached at about 8.5 km depth, and the dislocation function increases slightly in the hypocentral region. The maximum displacement in the hypocentral region in this case is 140 cm. The resolvability of the features of this particular model will be discussed in a later section.

The displacement at the surface due to this particular dislocation function was calculated along a profile at 0.2 km increments. This displacement profile is shown in the upper part of Figure 4.5. The observed displacement data as projected onto this profile are indicated along with the estimate of their errors. In this figure, we see that for the observed data located to the north of the surface breaks (given by positive distances along the abcissa in the figure), the fit as given by this "best fit" model is

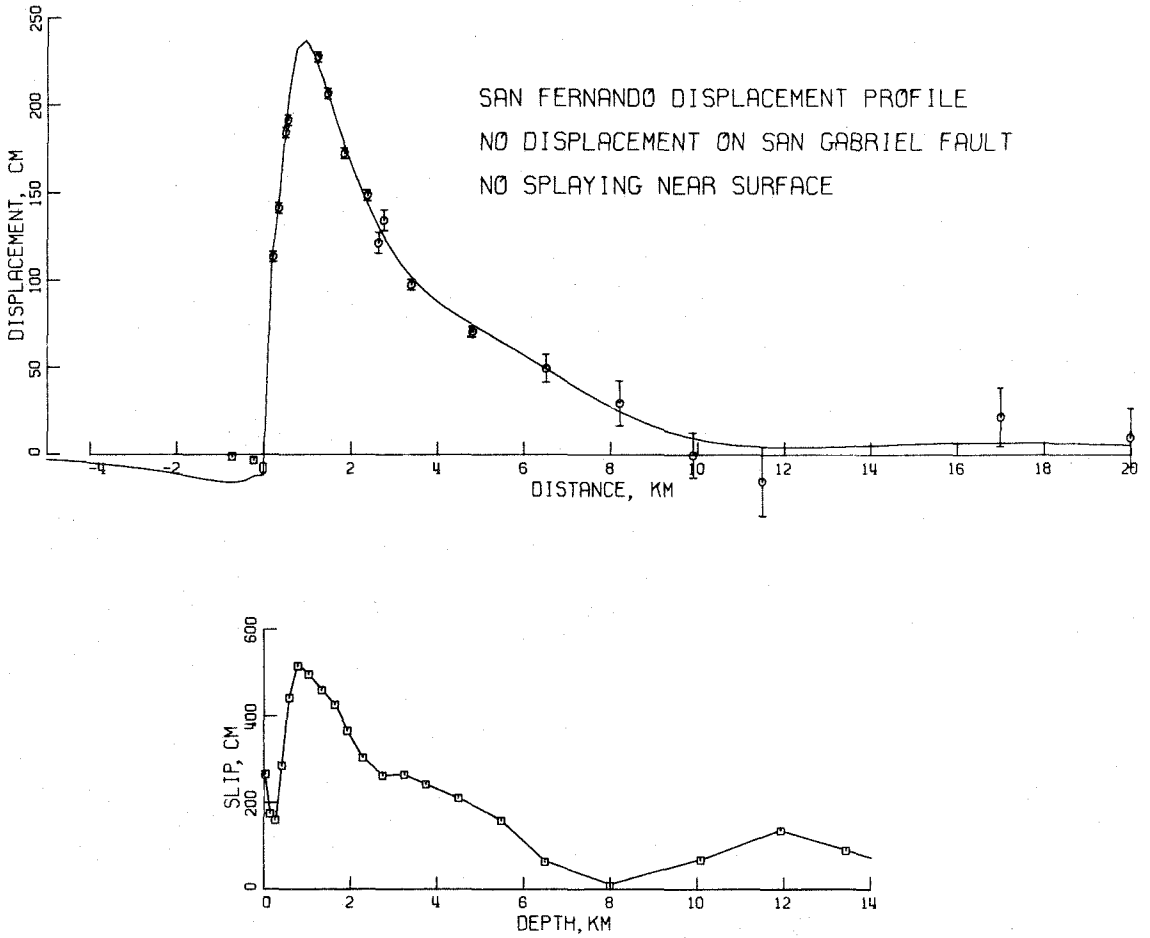

Figure 4.5. Lower--Best fit dislocation function for the main thrust sheet. Upper--Comparison of the calculated surface displacements from this model to the observed profile data.

quite good. To the south of the surface breaks, the calculated model predicts a larger negative surface displacement than is observed. A noteworthy feature of this particular fit is the importance, as far as spatial coverage along the profile is concerned, of having included the gravity-converted displacement points in the inversion data set. These converted data points force the calculated displacement field to go through a slight minimum in the profile distance 10-13 km away from the surface breaks. The displacements at distances greater than at the point where this minimum occurs are dependent almost totally on the dislocation function in the hypocentral region. The RMS error residual (observed-calculated) for all the data is about 8 cm.

In the next figure (Figure 4.6), we see what effect there is on this "best fit" solution when we exclude from the inversion data set the gravity-converted displacement data. In this figure, we see that the dislocation function along the upper 6 km of the fault system is essentially unchanged. Below this depth, the dislocation minimum along the fault sheet is reduced from what was previously calculated and shifted to a slightly smaller depth. Larger dislocations (maximum-275 cm) are now given in the hypocentral region. However, we note that only one data point, located at 17 km along the profile, is controlling the

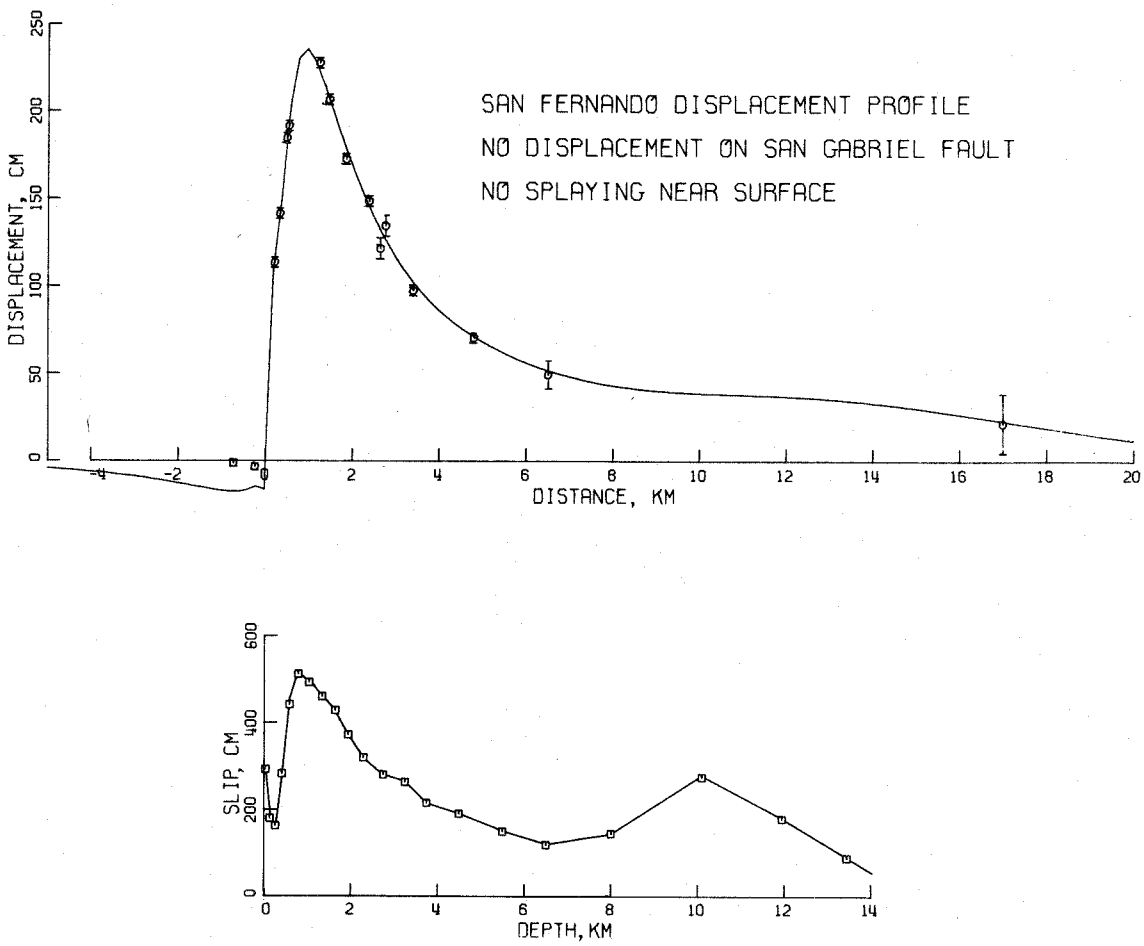

Figure 4.6. Lower--Best fit dislocation function for main thrust sheet when gravity-converted data points are excluded from inversion data set. Upper--Comparison of the calculated surface displacements from this model to the observed profile data.

amount of dislocation in this region. The resolvability of the dislocations in the hypocentral area will thus be highly dependent on the variance of this one data point. In the section on averaging in this chapter, we will see how the inclusion of the gravity-converted displacement data, inaccurate as they are, affects the resolution in the hypocentral area.

Next, we want to look at the effect of including a representation of the San Gabriel fault into our fault system for which we will use the inversion scheme to obtain a dislocation model. The structural parameters for this addition, which is composed of 6 elements, are given in Table 4.1b (SG1-SG6). The media response from these elements was computed and included in the response matrix. Figure 4.7 shows the results of the inversion of the data set (including the gravity-converted points) for this particular fault system. Comparing the dislocation function found in this figure and that obtained by the single thrust sheet (Figure 4.5), we see that practically the only difference between the two models is the amount of fault dislocation in the hypocentral area. In this present model, the slip in the hypocentral area is about 60% greater than that shown in Figure 4.5. This larger displacement in this region is necessary to accommodate the slip calculated for the San Gabriel fault. The slip

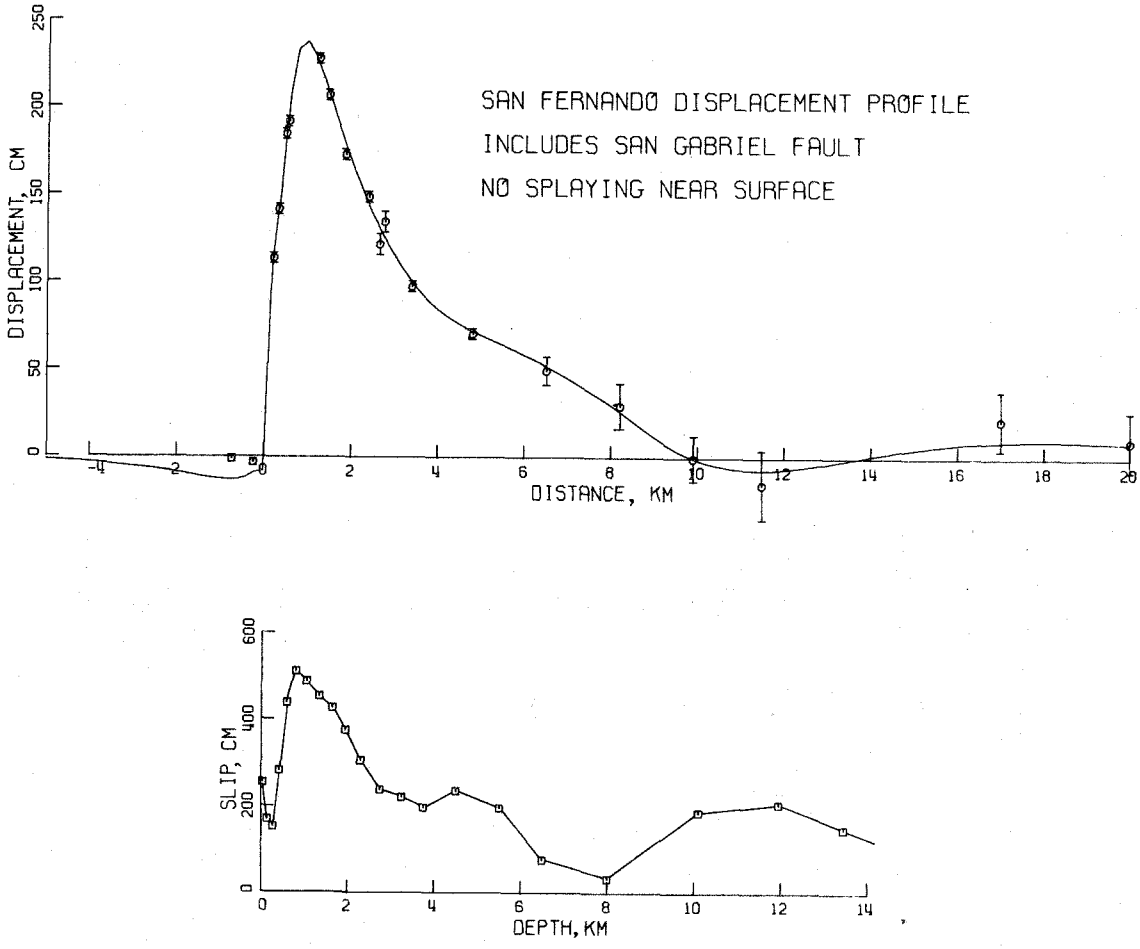

Figure 4.7. Lower--Best fit dislocation function for the main thrust sheet and San Gabriel fault representation. Upper--Comparison of the calculated surface displacements from this model to the observed profile data.

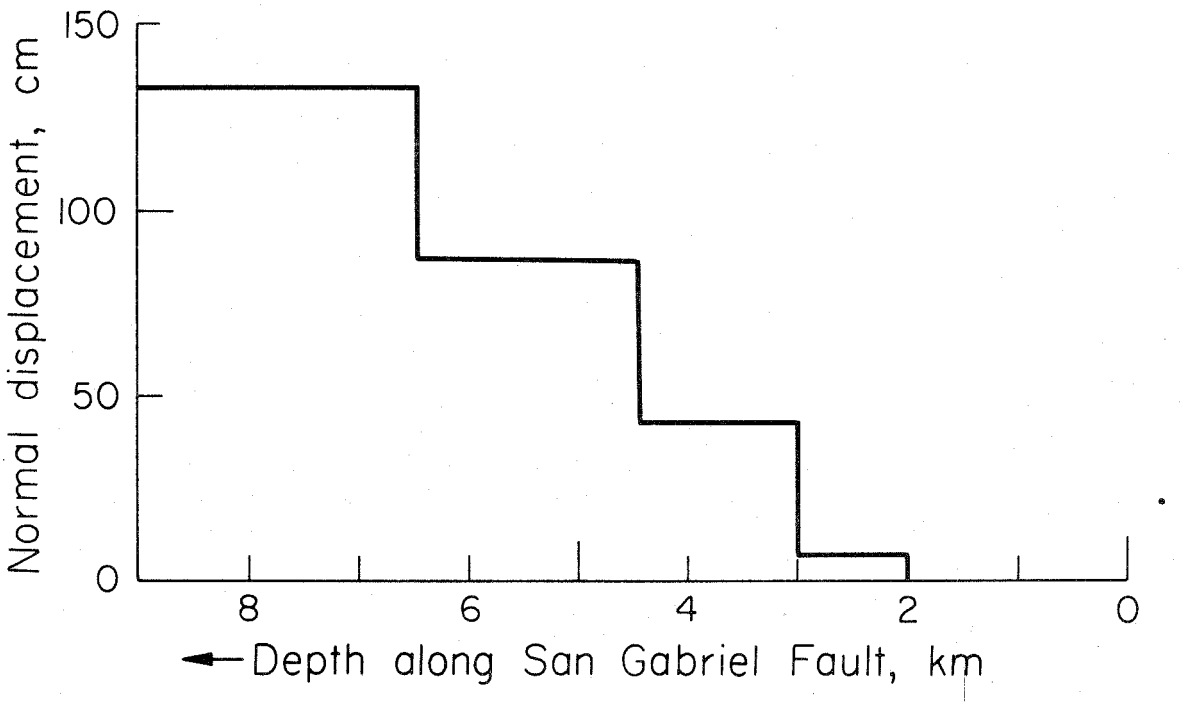

Figure 4.8. Best fit solution for normal slip on the San Gabriel fault representation.

calculated for the elements representing the San Gabriel fault is not shown in Figure 4.7 but is indicated in Figure 4.8. The sense of motion of the slip calculated on the San Gabriel section is opposite that on the main thrust sheet, i.e., normal faulting. We see here that the normal slip decays rapidly almost linearly toward the surface. This model predicts no motion on this fault for the upper 2 km, agreeing with the lack of observable expressions of surface motion on this fault after the earthquake (Kamb et al., 1971). A later section of this chapter goes into detail about whether this slip is required by the data.

Some mild supportive evidence for the existence of normal faulting on the San Gabriel fault representation is given in the following discussion. Whitcomb et al. (1973) give a strong correlation to the noted areas of compressional release (normal faulting) as determined by focal mechanism studies and the area of mapped gravity increases. If the areas of the San Gabriel fault representation that were computed to have undergone normal faulting were projected to the surface, then this projection would approximately coincide with the area of gravity increase and the correlated compressional release.

Calculation of the averaging operator (equation (2.29)) for this structural model reveals a strong coupling between thrust slip in the hypocentral area and normal slip along

the lower part of the San Gabriel fault representation. This coupling is in the sense that in order to keep the same displacement at the surface while increasing the thrust displacement in the hypocentral region, it would be necessary to increase the normal slip along the lower part of this auxiliary fault. This coupling is illustrated by the results shown in Figure 4.9. In this figure, we have significantly increased the dislocation in the hypocentral area. Hanks (1974), on the basis of an analysis of the Pacoima Dam strong motion records, postulated that this earthquake initiated with large (4-9 m) ruptures in the hypocentral region. In this example, we will see if the surface static displacement data support this hypothesis. In this calculation, we have initially set the fault dislocation for the three bottom fault elements of the main thrust sheet at the levels indicated in Figure 4.9. In the inversion calculations, the model weights for these elements were set such that these three dislocation values remained fixed. The result from the inversion is the smooth model given in the figure. The fit to the observed data for this particular model is extremely good, with the RMS error residual found to be less than 5 cm. We see that the minimum in the fault dislocation function is shifted to a much shallower depth than in previous examples. The dislocation function calculated for the upper part of the

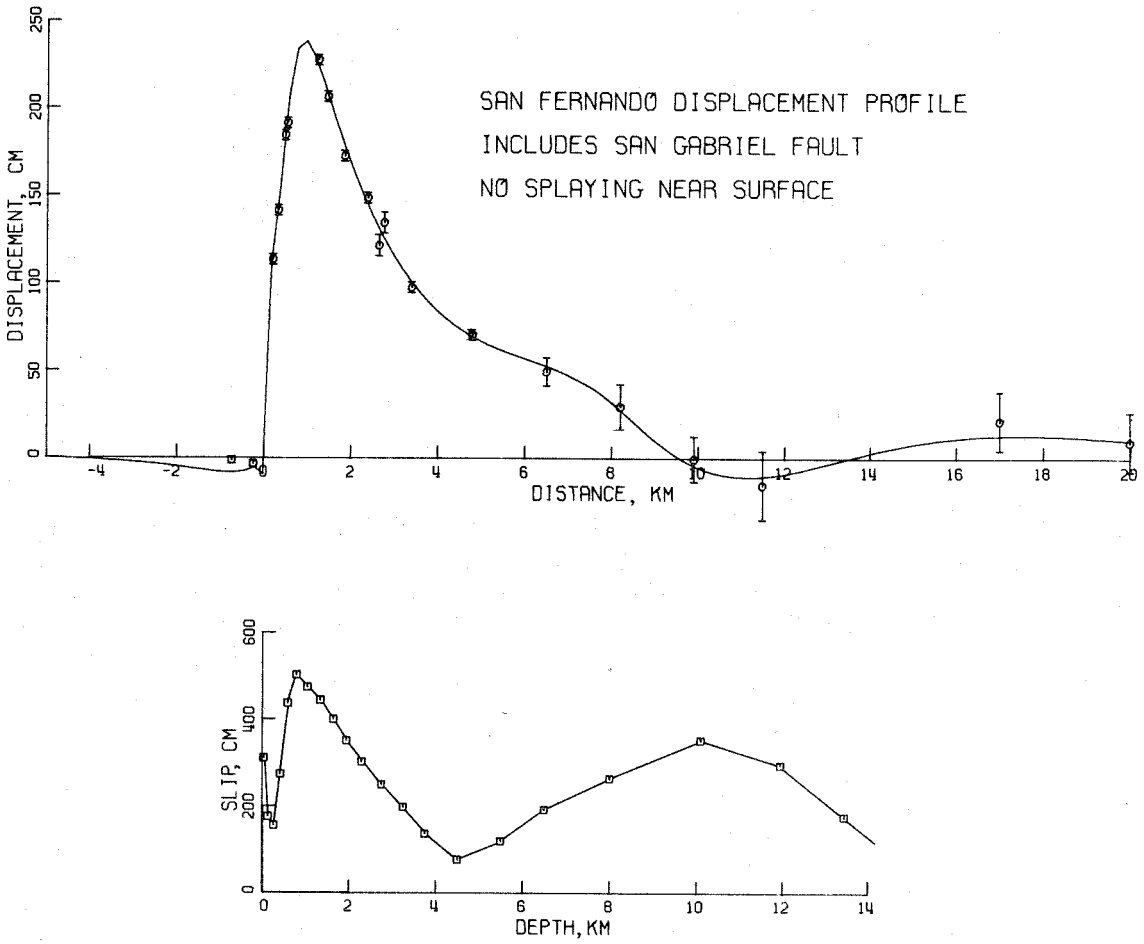

Figure 4.9. Lower--Best fit dislocation function for the main thrust sheet and San Gabriel fault representation when large displacements are forced in the hypocentral region. Upper--Comparison of the calculated surface displacements from this model to the observed profile data.

fault sheet is the same as before. However, the maximum normal slip on the San Gabriel fault has been increased to almost 300 cm -- approximately double that shown in Figure 4.8. The dislocation function on the auxiliary fault retained the relative shape which is shown in Figure 4.8.

We next include the splay group of fault elements into our fault system. The structural characteristics of these elements are listed in Table 1b (S1-S20). The media response to these elements was calculated, and the response matrix was expanded to include these values. For comparison, we chose as our starting model for the inversion the final model given in Figure 4.9. The results of this inversion are shown in Figure 4.10.

A comparison of the slip model in this figure and that shown in the previous figure reveals that the two models are practically identical except for the upper 1.5-2.0 km. This is to be expected since the fault geometry was only changed for the upper 1 km, and we would expect this small part of the fault system to be relatively uncoupled from the rest of the fault system. For this model, the fit to the data to the north of the surface ruptures is equally satisfactory as with the unsplayed fault geometry, but the fit to the two data points to the south of the surface ruptures is degraded somewhat. For the dislocation on the main thrust sheet near the surface, instead of varying

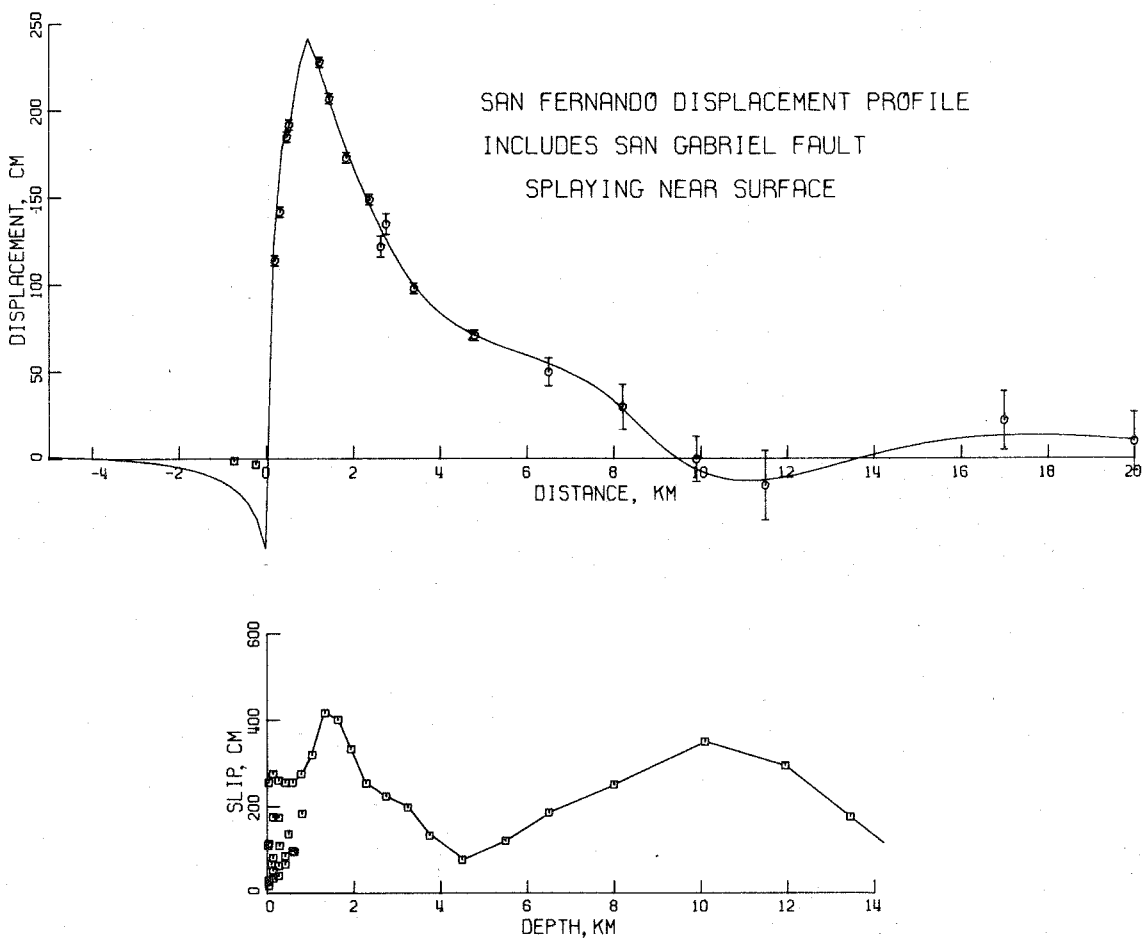

Figure 4.10. Lower--Best fit dislocation function for fault system when near-surface splay faults are introduced. Upper--Comparison of the calculated surface displacements from this model to the observed profile data.

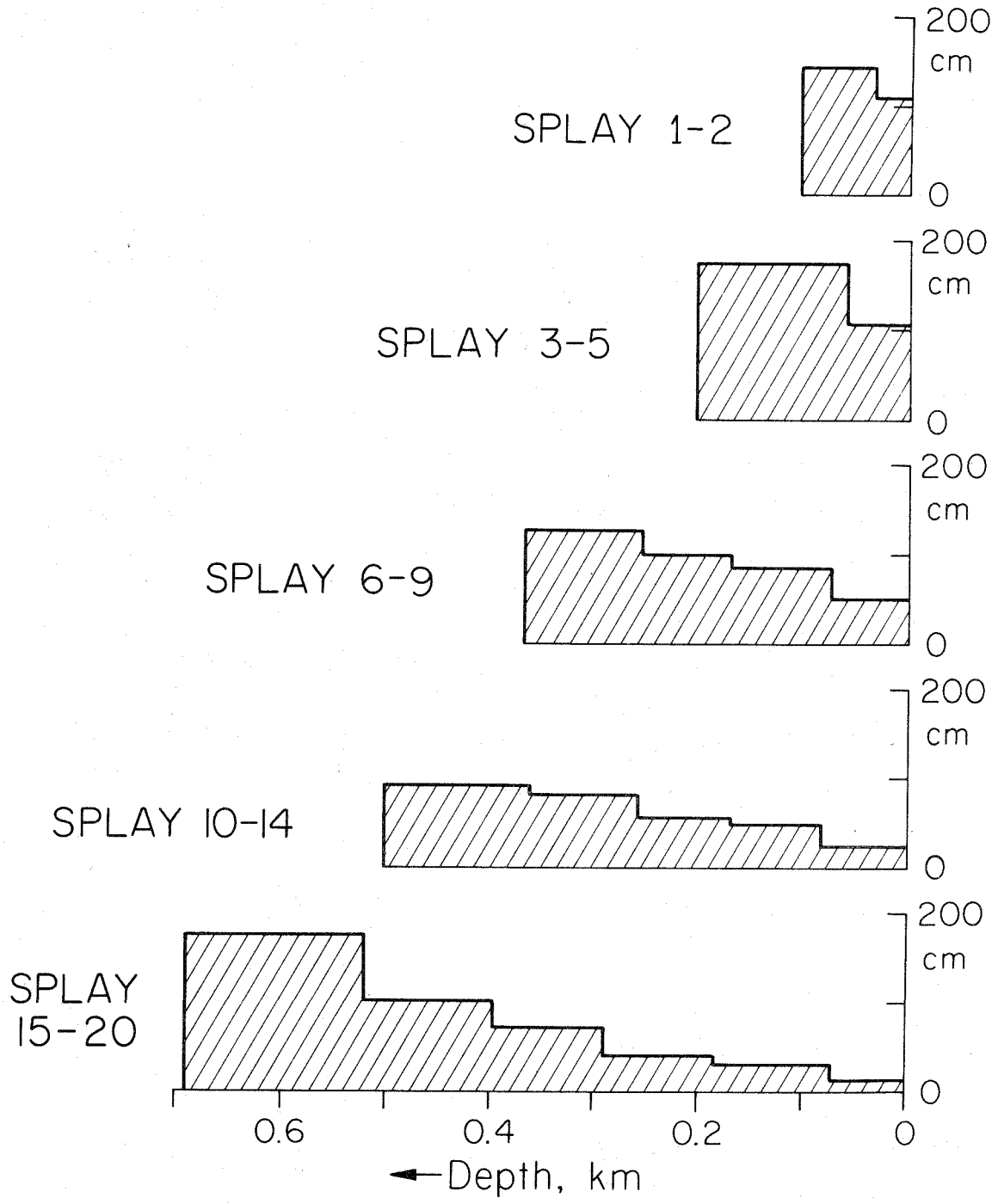

Figure 4.11. Best fit solution for slip on the near-surface splay faults.

rapidly as in Figure 4.9, the slip is almost constant at 250 cm, and the maximum slip on the thrust sheet is reduced by about 20% to 400 cm. The slips on the small splay faults vary smoothly away from the value on the main thrust sheet where they intersect that sheet. The slip on the splay faults is better illustrated in Figure 4.11. Here we see that not only does the calculated slip decay smoothly toward the surface, the displacements at the surface decrease away from the surface ruptures.

Since we have limited our inversion data set to points which were located near the profile which approximately bisects the observed surface deformation, we would now like to see how the calculated displacement from this model compares to what is observed in areas away from this profile. For observation points away from the center of deformation, one must consider the contribution to the vertical displacement caused by any strike slip component of fault dislocation. In this calculation, we will arbitrarily assume that the dislocation slip vector on each of the fault elements has a constant rake angle of 60°. This is about the maximum component of left lateral motion that would be allowable based on the focal mechanism data of Whitcomb et al. (1973). At this rake angle, the left lateral strike slip dislocation is 0.6 of the pure dip slip component. For the majority of the observations, the

calculated vertical displacement from the strike slip component of dislocation is a secondary effect.

One obvious feature of the observed surface vertical displacements is the offset between the Tujunga and Sylmar fault segments. This offset is easily modeled by slightly altering the geometry of the upper part of the fault system. An advantage of including the small splay faults near the surface, in addition to approximating the surface ruptures observed north of the main Tujunga scarp, is that it allows one to easily model the observed offset in the surface faulting. This is done by letting the upper six elements of the main thrust sheet and all the splay fault elements (S1-S14), except the ones farthest from the main surface breaks, terminate at the Tujunga-Sylmar offset. This means that these particular fault elements have lengths of only 10 km with the coordinate system origin of these elements shifted 2.5 km to the east. The total contribution to the surface deformation from all the fault elements was calculated taking into consideration this lateral offset where appropriate. The results are shown in Figure 4.12. The fault dislocation function used for these calculations is the same as that given in Figure 4.5 with the addition of the splay fault system.

A comparison of the contours presented in this figure and the areal displacement given in Figures 4.2 and A2.4

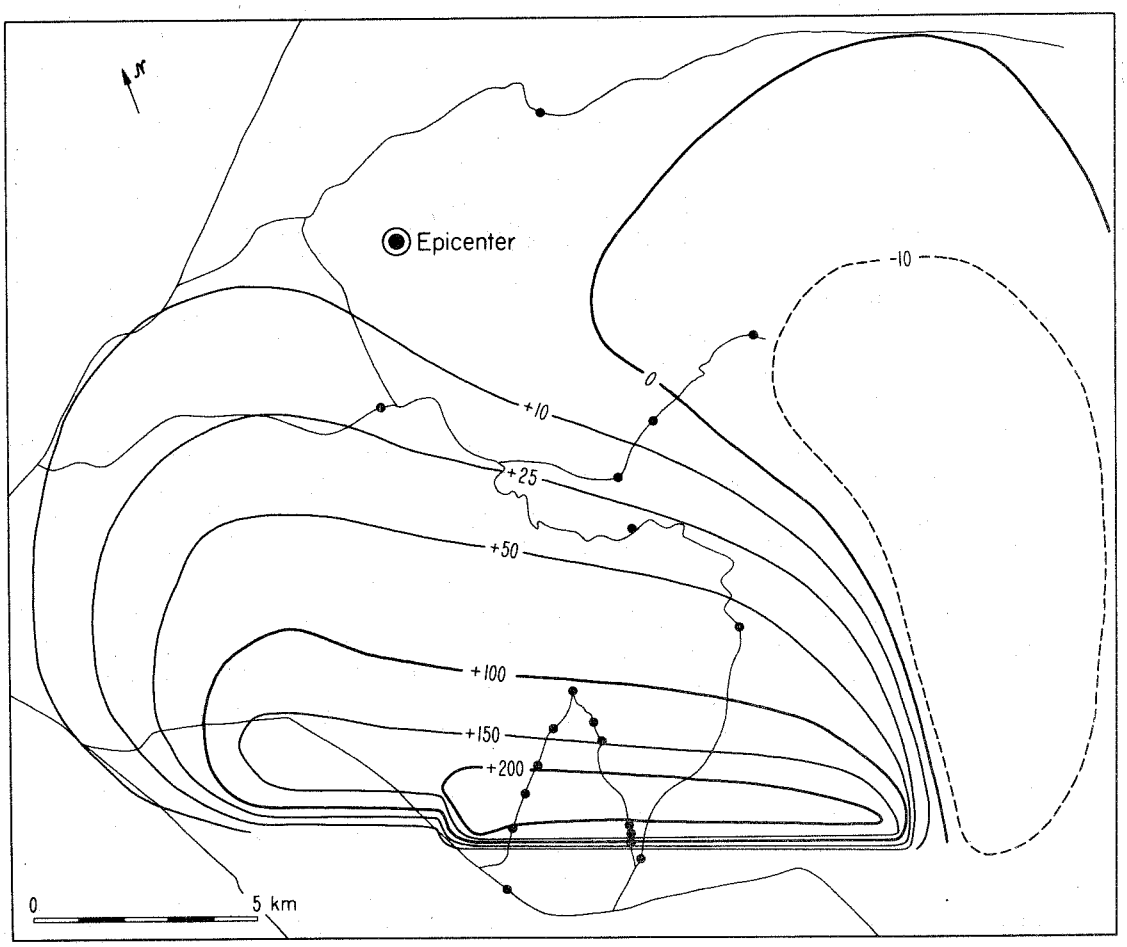

Figure 4.12. Computed vertical displacement field from best fit model given in Figure 4.5 with the addition of the near-surface splay faults. The fault dislocation includes a component of left-lateral strike slip taken to be 0.6 that of the dip slip motion. Contours are in cm of uplift. The solid circles show the location of the data used in the inversion. Superposed on the contours is a map of the roads in the area.

shows the degree of fit the calculated model has to the observations. If instead we had used the dislocation function like that indicated in Figure 4.7, the effect on the area deformation would be to increase the magnitude of the downward displacement in the northeast area and to increase the northward extent of the 10 cm contour line. For contour levels 25 cm and above, there is practically no discernible difference between the two plots.

One feature of Figure A2.4 which does not appear in the theoretical contour plots is the delineation of a zone of downwarping to the west of the profile line. One possible explanation for the occurrence of this area is that it is associated with the seismic activity along the seismically mapped down step of the main fault plane (Whitcomb et al., 1973). A significant amount of left lateral motion on a steeply dipping plane could produce the localized downward displacements that are observed in this area. The addition of this fault geometry was not considered in this study, however.

4.6 Resolvability of Features in the Slip Model.

The variance operator, $\mathbf{V}$, for this case is a 47 x 47 matrix. This matrix was calculated in the same manner in the previous chapter. For simplicity, the splay fault elements were suppressed in these resolvability calculations. This suppression should cause no change in the

conclusions reached in this section. Again, to test the resolvability of a particular feature of a model, a model perturbation affecting this feature will be considered. This perturbation will then be tested for detectability at the 95% confidence level.

The initial model that we consider is that shown in Figure 4.5. The first question that we ask about this slip model is the following: "Considering that the fault geometry of this model is appropriate, do the data demand that there exists a sharp minimum in the slip in the upper 1 km of the fault sheet?" To answer this question, we assume a perturbation, which when added to the calculated slip model, will just cancel this minimum. This perturbation is then tested and uniformly reduced until it is at the 95% confidence limit detectability threshold. The resulting perturbation is shown in Figure 4.13a. We see that the maximum perturbation allowable by the data is not large enough to erase this minimum.

Next, we try to determine if the data demand the existence of the broad minimum in slip between the upper and lower parts of the thrust sheet. Figure 4.13b shows the amount of slip that could be added in this region. We see here that the slip gradient could be smaller than that given in the original slip model, but nevertheless, the

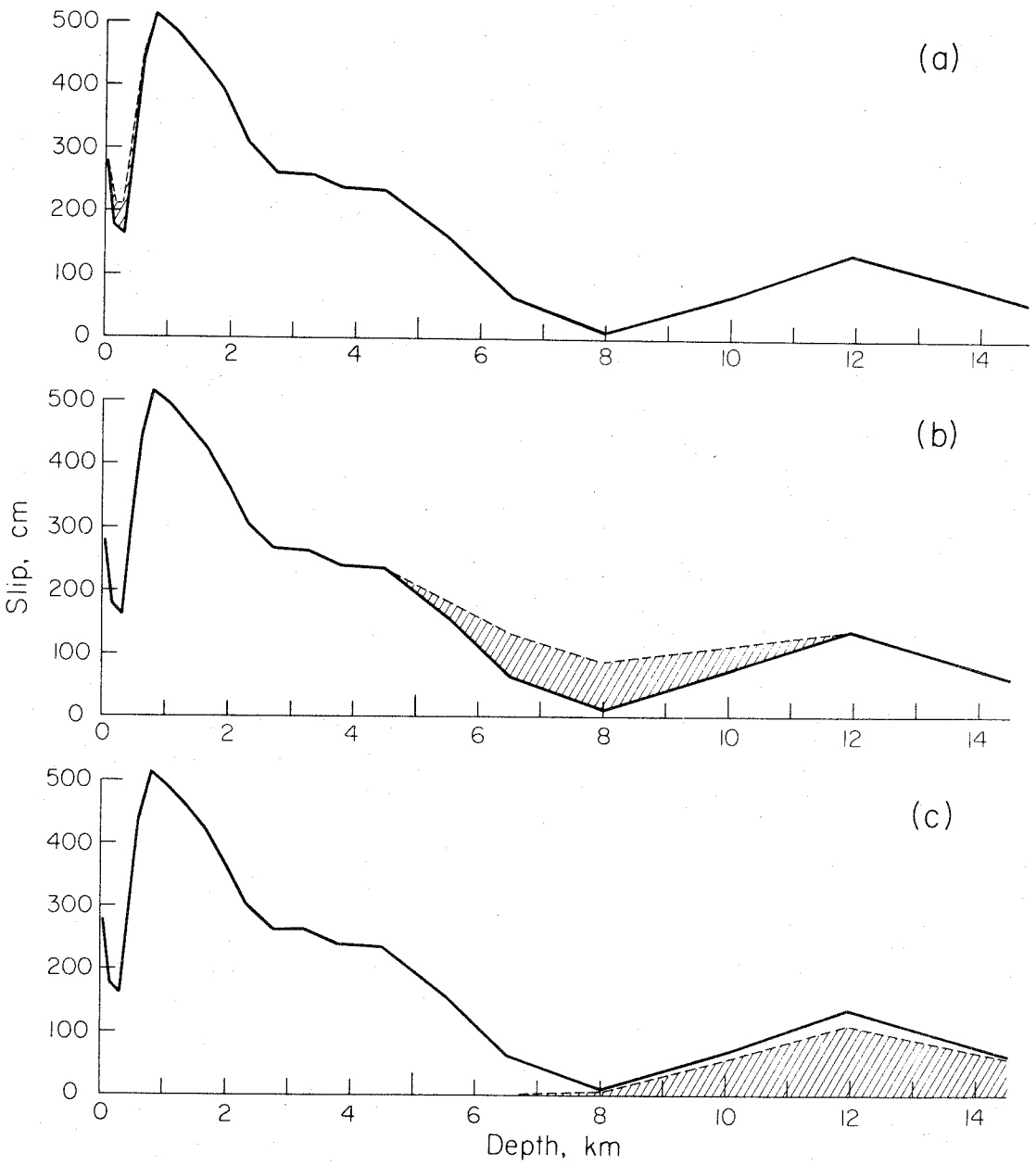

Figure 4.13. Examples of the resolvability of features of the best fit model solution given in Figure 4.5.

dislocation does become smaller with increasing depth in this region.

Intuitively, we would expect that the resolvability would be less in the hypocentral area than in other parts of the fault system because the fault elements in this region are located farther from the points on the surface where we have data. Also the density of data points on the surface near the epicenter is smaller than near the surface ruptures and the data in this area are generally not as accurate. In testing the resolvability of the calculated dislocation in the hypocentral area, we will consider what is the maximum perturbation that we can subtract from the calculated values and still be resolvable by the data. From equation (2.33) we see that the sign of the perturbation to be tested by our resolvability criterion is not important, only the magnitude of the perturbation. Thus, we can either add or subtract a perturbation tested at a particular confidence level to the calculated model dislocation and still not be detected by the data at that confidence level. In Figure 4.13c, we see that we can add or subtract about 100 cm of displacement in the hypocentral region for this perturbation shape. From this type of analysis, we indeed find that the slip in the hypocenter is poorly determined, since the uncertainty in slip is almost the equivalent of the calculated

values. If required to give bounds for the slip in this area as predicted by the static data used here, we would say that the maximum slip is approximately 130 cm ± 100 cm.

We now consider the variance operator in which the San Gabriel fault representation is included in the fault geometry, but the splay system is still excluded. The slip model for which perturbations are considered is that given in Figures 4.7 and 4.8. Figure 4.14 shows these perturbations. In the upper part of this figure, we see that considering displacement on the San Gabriel fault alone, that is, not taking into account any coupling between fault elements, there would be about a 100 cm uncertainty in the estimate of the slip. The lower part of this figure shows the maximum undetectable perturbation possible when slip on this auxiliary fault and slip in the hypocentral region are considered simultaneously. We see here that the uncertainty in slip in the hypocentral area is almost the same as that in Figure 4.13c, while the uncertainty on the San Gabriel fault has been reduced to about 50 cm.

4.7 Averaging Operators.

As discussed in the previous chapter, examination of the kernels of the matrix operator, $\mathbf{R}$, provides information about the filter through which we are able to view our "best fit" estimate of the fault slip. We say that the

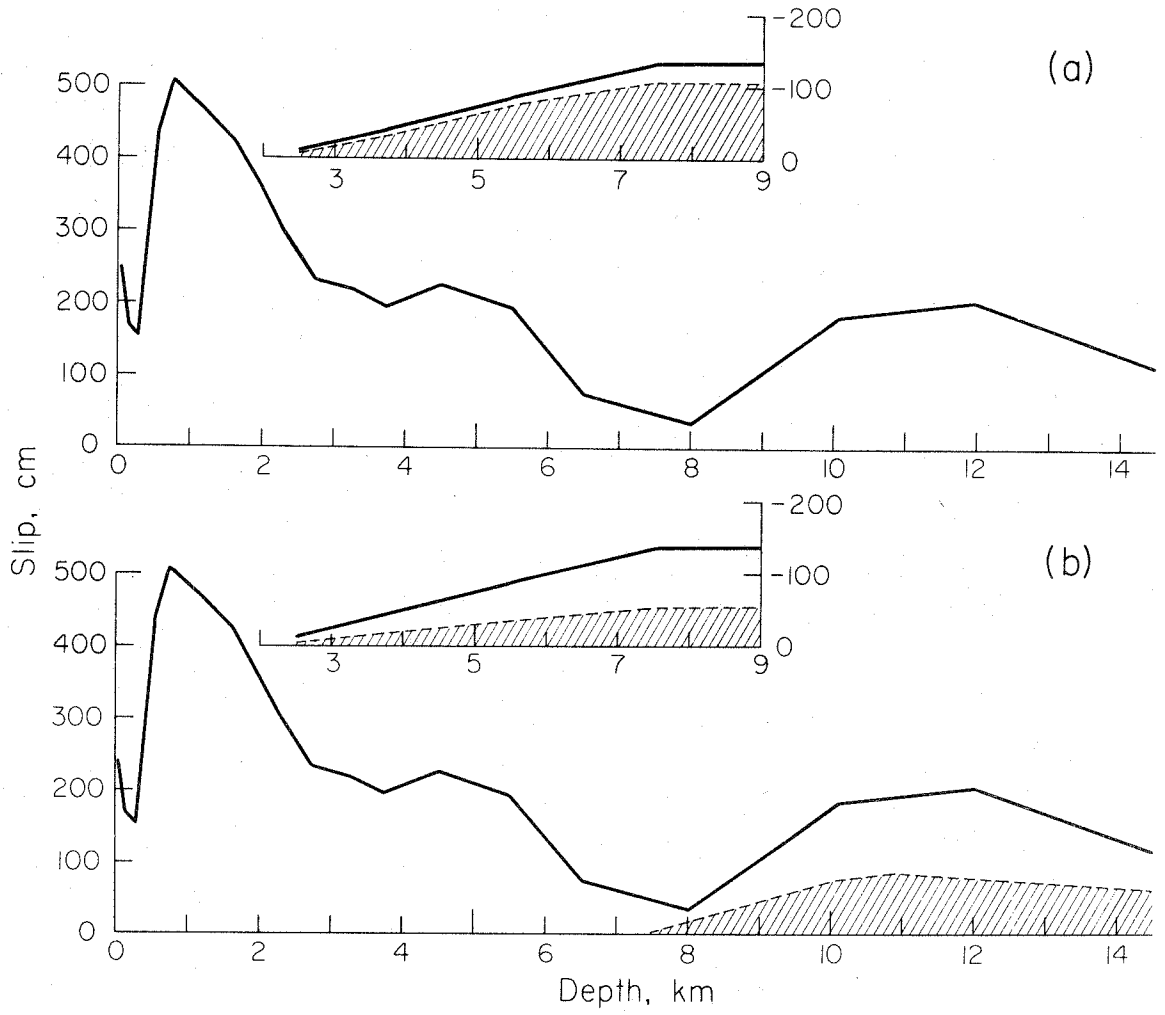

Figure 4.14. Examples of the resolvability of features of the best fit model solution given in Figures 4.7 and 4.8.

ability to resolve the details of the actual dislocation function depends on the size of the kernels and the averaging widths of the kernels. The ratio of the size of the kernels to the averaging widths provides a convenient medium for expressing the resolution at a given point in the fault system. First of all in this section, we would like to examine these ratios to determine the effect of the addition of the gravity-converted displacement points to the data set. The averaging operator was calculated both with and without these data points in the inversion data set and the averaging ratios calculated in both instances.

Figure 4.15 shows the difference in the averaging ratios the addition of these data cause. The fault geometry considered in this case is that of a single thrust sheet. In the figure, we see that the upper part of the fault is unaffected by the addition of these data. The area of the fault which has the maximum effect is in the range from 7-11 km depth. In this range, the resolvability ratio is doubled. The reason for the increase is not so much an increase in the value of the averaging kernels for these elements, but more , the fact that the averaging widths of these elements are reduced. Thus, the addition of these data does not help much in the determination of the actual

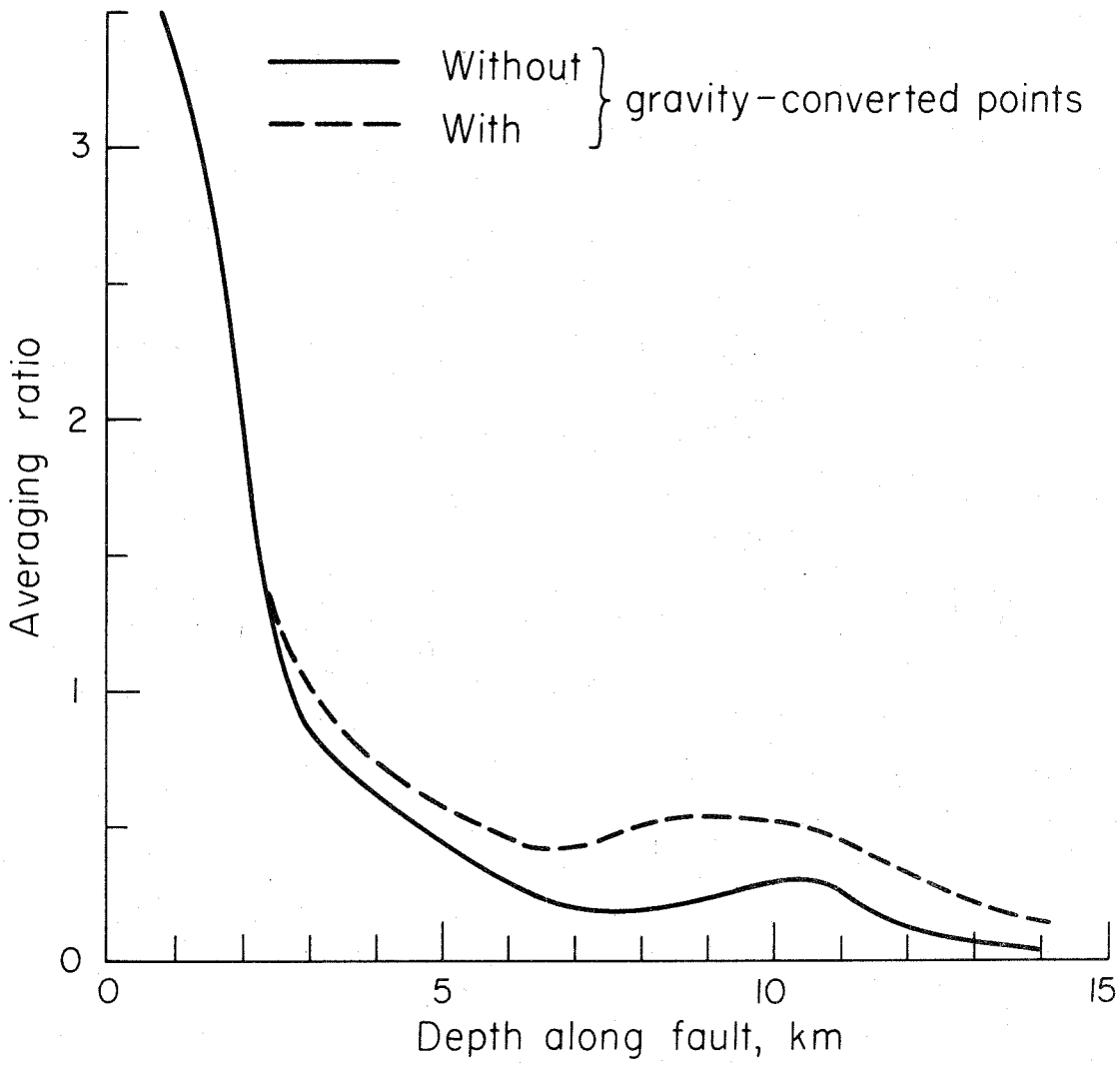

Figure 4.15. Averaging ratios for data sets with and without the gravity-converted displacement data. Curve has been made continuous by connecting values calculated at the fault element mid-point depths.

slip in this area, but the slip that is determined is much more localized than could be determined without these data.

Figure 4.16 shows examples of the averaging kernels for the San Fernando earthquake model consisting of a simple thrust sheet. The arrows in the figure indicate the elements around which the averaging is centered. The block offset to the right is an expanded view of the upper 1.5 km of the cross section to elucidate the fault geometry in that area. Examining this figure, we see that the averaging is very localized in the upper part of the fault, but the averaging length increases with increasing depth along the fault. In the bottom figure, the averaging length (half-width) is about 4.5 km. In comparing the averaging kernels presented here with those given for the Alaska earthquake, we notice that the strong negative side lobes are not as much in evidence in this present example. This is probably caused by the better spatial distribution of data in the San Fernando case.

Figure 4.17 indicates the averaging kernels for selected fault elements when the San Gabriel fault geometry is introduced. The top figure is centered on a fault element that is located on the main thrust sheet directly under the San Gabriel fault representation. We see from this picture that there is no coupling in this area between

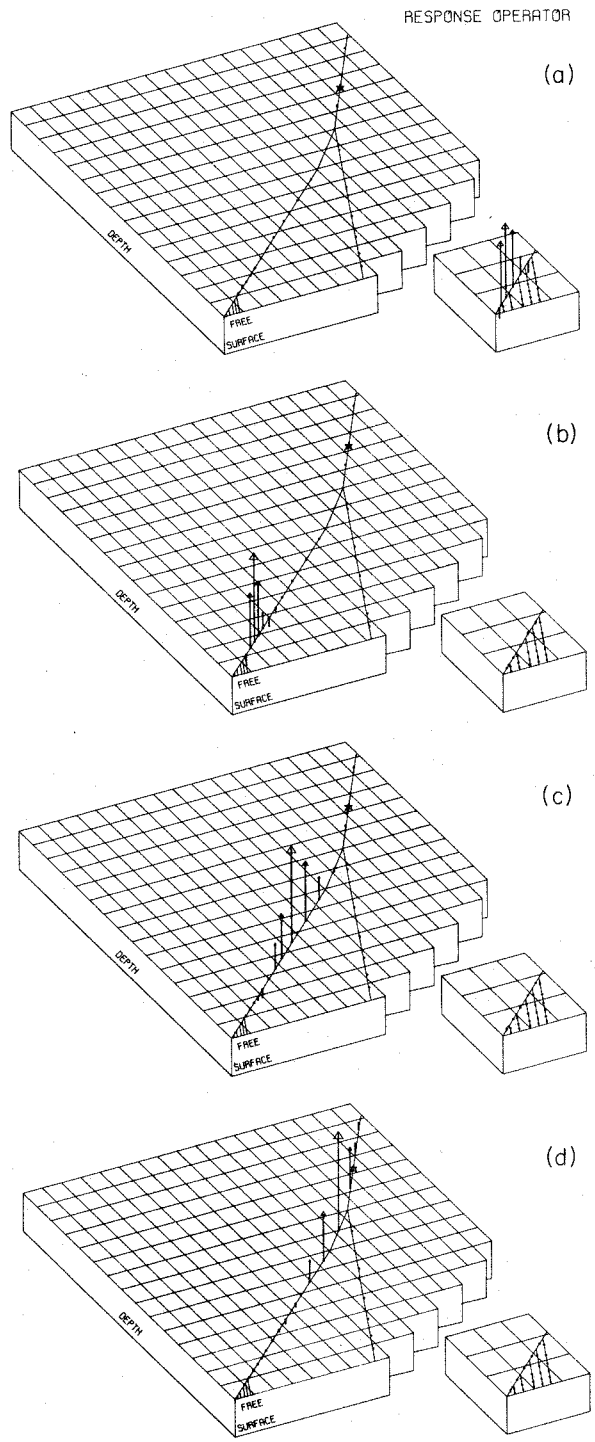

Figure 4.16. Spatial averaging of slip on the single thrust sheet model.

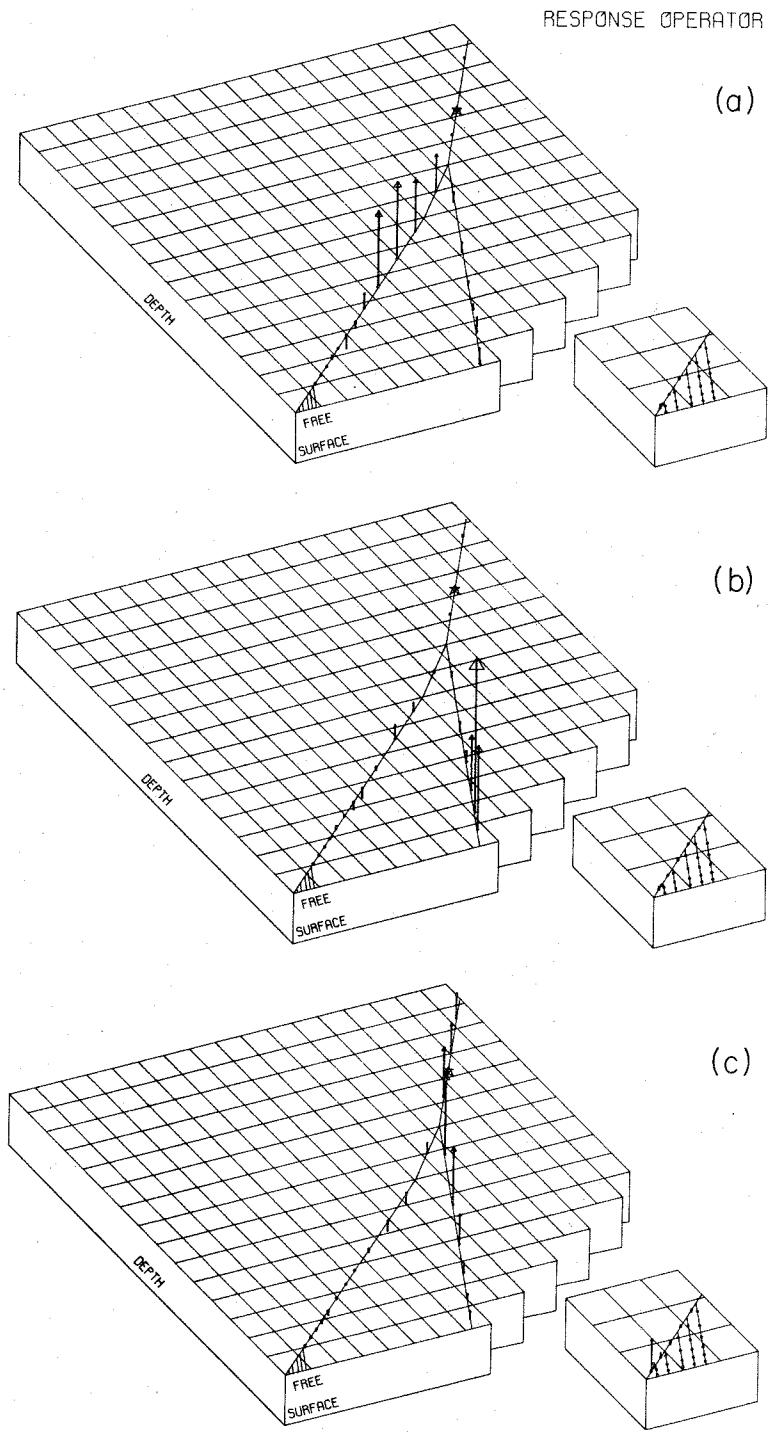

Figure 4.17. Spatial averaging of slip in model with San Gabriel fault representation.

the main fault and the auxiliary fault. This means that there can be no trade-off in displacement between the two faults to affect the resolvability test of the slip in this area as indicated in Figure 4.13b. Figure 4.17b shows the spatial averaging of slip for the upper part of the San Gabriel fault. We see here that this too is uncoupled from the rest of the fault system. We note here that the best fit solution for the fault geometry which included this fault indicated little or no slip on this portion of the fault. Figure 4.17c indicates the extent of the spatial averaging for the lower part of the San Gabriel fault. We see here that there is very strong coupling to the fault elements in the hypocentral area. We note that the averaging between the two fault segments is in the same direction indicating that any normal slip on this portion of the San Gabriel fault will be seen by the data as normal slip averaged over both the San Gabriel fault and the main fault in the hypocentral area. However, we can rule out the possibility of the occurrence of normal faulting on the main fault from consideration of the focal mechanism of the initial motion. These observations are taken to mean that this portion of the San Gabriel fault is effectively decoupled from the rest of the fault system. If this is true, then from the results indicated by the resolvability calculations in Figure 4.14a, the slip on this fault is not

detectable by the data. This conclusion is not surprising considering that we have presented two separate dislocation models -- one without slip on the San Gabriel fault (Figure 4.5) and one with slip on the San Gabriel fault (Figure 4.7) -- each of which is geophysically plausible and fits the data to a satisfactory degree.

4.8 Conclusions.

Several possible fault dislocation models have been presented to explain the observed vertical displacement which accompanied the 1971 San Fernando, California earthquake. The fault geometry assumed in calculating these models was made to conform to most of the geological and geophysical observations that were associated with the faulting. In each of the models computed from the inversion scheme, a significant variation in slip along the fault was calculated. The maximum displacement was computed to have occurred on the shallow end of the fault surface. The resolution of slip in this shallow part was very good, and the spatial averaging of slip was relatively small. A model was calculated in which there was extensive splaying away from the main fault as the fault neared the surface. The slip model calculated for this geometry is preferable to that of a single fault for the following two reasons: 1) The maximum displacement on the fault necessary to fit the data was reduced, and large variations in slip in

the upper 1 km of section was reduced; and 2) evidence for the existence of and movement on these splay faults was observed in the field, and their existence admits the possibility of modeling the observed lateral offset in the surface faulting. We caution here that the exact number, location and offset on the splay elements should not be taken as absolute. The addition of these elements into the fault system was taken to represent in some systematic fashion the observable imbricate ruptures which did not appear to be so systematic. However, we think that the inclusion of these elements has led to a better understanding of the faulting process near the surface.

Dislocation models were calculated for fault geometries which both included and excluded a representation of the San Gabriel fault. It was found that there was very little resolution of slip along the San Gabriel fault. If slip did occur, this slip would be normal fault movement and confined to the lower part of the fault. These two models indicated that between 140 and 200 cm of slip occurred in the area of initial motion. The uncertainty of this slip in the hypocentral area as determined by the static data is about 100 cm. All of these calculations have been based on the initial assumption that the fault sizes were fixed. If we have misjudged the length of the

fault elements, the calculated slip would be in slight error. For distances away from the fault elements, this error is about linear with length. That is, if the lengths of the fault elements in the hypocentral area are actually 10% smaller than the value that was fixed in the inversion, the calculated slip on the smaller fault element would be about 10% larger.

The moment for this event can now be calculated for each of the slip models. In the calculations, the value of the shear modulus was taken from the estimates given by Jungels (1973, p. 29). The values of moment range from 1.0×10^{26} dyne-cm for the slip model presented in Figure 4.5 to 2.2×10^{26} dyne-cm for the model given in Figure 4.10. These two extremes just about span the values obtained by both static and dynamic observations given in the literature by various authors (Aki, 1971; Wyss, 1971; Wyss and Hanks, 1972; Canitez and Toksöz, 1972; Jungels and Frazier, 1973; Savage et al., 1973).

On the basis of choosing the simplest possible model necessary to fit the data, we give as our preferred "best fit" model the slip function given in Figure 4.5 with the addition of the splay slip shown in Figures 4.10 and 4.11.

Chapter 5

Least-Squares Inversion of Surface Wave Spectra to Obtain Source Parameters: The 1971 San Fernando Earthquake

5.1 Introduction.

In this chapter, we will examine the spatial and frequency distribution of Rayleigh waves from the 1971 San Fernando, California, earthquake and how this distribution is related to the faulting processes of that event. The use of surface waves to determine gross source parameters has been a common tool in recent seismological investigations, e.g.,Wu (1968), Tsai and Aki (1970, 1971), Canitez and Toksöz (1971, 1972), and Mitchell (1973). Unfortunately, the problem of systematically finding values of the source variables which optimally fit the observed data has not yet received the attention due the problem. With the exception of a Monte Carlo technique by Tsai (1972) and an iterative technique by Turnbull et al. (1973), the "trial and error" method was usually employed in finding suitable variables which describe the data.

We hope to extend the usefulness of surface observations by showing how an inversion procedure can be applied to surface wave observations in order to see what information can and cannot be gained about the earthquake source.

Along with this inversion, we will use a method of expressing the finiteness of the fault plane by numerically summing point source solutions. This method will allow for the variation of parameters over the fault surface. Finally, we would like to compare the solution that we obtained for the San Fernando source mechanism from the static study in the previous chapter to that obtained by the dynamical surface waves.

5.2 Theoretical Model.

Spectra from a Point Source. Theoretical surface wave spectra will be computed for a source in a multilayered medium which approximates the San Fernando area. The elastic parameters for this medium are given in Appendix 5. Far-field amplitude spectra depend on the surface wave amplitude response of the layered medium and also the source type, depth and orientation. Expressions for the frequency dependent media response factor, which is dependent on the source, are given by Harkrider (1964). Computation of this factor involves use of the Thomson-Haskell matrices for the multilayered half-space (Haskell, 1953). The formulation for the component of the surface wave spectra which is due to different source types and the orientation of the source was developed by Ben-Menahem and Harkrider (1964). The far-field solution for Rayleigh wave

spectra for a point double-couple can be written as

$$A(\omega) = \frac{S(\omega)\ k\ A_R\ \chi(\theta,h)e^{-i(kr+\frac{3\pi}{4})}}{\sqrt{kr}} \quad , \qquad (5.1)$$

where

$S(\omega)$ = transformed spectral source function

k = Rayleigh wave wave number

A_R = medium response factor

r = radial distance to receiver

$\chi(\theta,h)$ = complex radiation pattern function, where θ is the azimuth of the station relative to the source and h is the source depth.

The radiation pattern function is given by Ben-Menahem and Harkrider (1964) and by Harkrider (1970). This function is dependent on the source parameters and the source depth. At a given depth, this azimuth dependent function is characterized by the slip, or rake, angle and the dip of the source-equivalent fault. The numerical techniques used in the computer programs which calculate these functions are discussed by Harkrider (1970).

The source function is assumed to be a step function in moment. This is given by

$$S(t) = \begin{cases} 0 & \text{for } t < 0 \\ M_0 & \text{for } t > 0 \end{cases} \quad , \qquad (5.2)$$

where t is the origin time of the event.

Source Finiteness Effects. In the above discussion, the source was represented by a point source. However, if the dislocation on the actual fault surface initiates at one point and propagates to another point, the fault finiteness and rupture velocity can become important. Ben-Menahem (1961) has shown how the dimensions of the source and the speed of rupture play an important role in the resulting spectral radiation patterns. This author shows that spectra from a source which radiates energy evenly as propagation occurs was modulated by the shift factor,

$$\frac{\sin(X)}{X} \; e^{iX} \quad , \tag{5.3}$$

where

$$X = \frac{\omega\, b}{2C} \left[\frac{C}{v} - \cos(\beta_0)\right] .$$

The following parameters are defined:

ω = angular frequency

C = Rayleigh wave phase velocity

b = horizontal rupture length

v = horizontal rupture velocity

β_0 = angle measured from the direction of rupture.

However, if the source radiates energy unevenly during propagation, then this simple modulation no longer applies. One such method of uneven radiation can occur by having the dislocation (i.e., moment) vary along the fault. The fact that surface wave excitation is depth dependent means that a fault which has a vertical component of propagation can also give rise to uneven radiation during propagation. The analytic modeling of such rupture would be very difficult for a layered medium, however, we give here a numerical approximation to this phenomena.

Numerical Approximation of a Propagating Fault. In this section, we will present a method of numerically approximating the surface wave spectra due to a propagating rupture. To do this, we will consider the fault to be modeled by a discrete number of double couple sources arranged spatially to reflect the length of a fault. Propagation along the fault occurs by "turning on" each of the sources sequentially at a time given by

$$T_{d_i} = \frac{\Delta_{s_i}}{V_R} \quad ,$$

where Δ_{s_i} is the distance to the ith individual source from some origin and V_R is some rupture, or propagation, velocity that we wish to approximate. The spectra from

each of the sources will have a different phase at some fixed observation point. The total spectra measured at this point will be the complex sum of the individual contributions. The phase delay of the individual propagation sources relative to the initial source taken to occur at the origin is given by

$$\tau_{p_i} = \frac{\hat{R}_i - R_0}{C(\omega)} + T_{d_i} \quad ,$$

where R_0 is the distance from the initial, or reference source, to the exterior observation point and $\hat{R}_i$ are the distances from the other sources to the observation point. $C(\omega)$ is the phase velocity. The geometry of this problem is illustrated in Figure 5.1. From this figure, we can write

$$\hat{R}_i = [d_{s_i}^2 + R_0^2 - 2\, d_{s_i} R_0 \cos(\lambda_R - \theta_F)]^{1/2},$$

where d_{s_i} is the horizontal separation of the individual sources relative to the initial source taken in the direction of rupture, λ_R. θ_F is the "azimuth" to the station relative to the initial source. Appendix 4 goes into the details of how the spectra are summed given this phase information. Both strike slip and dip slip faulting can be approximated with this geometry.

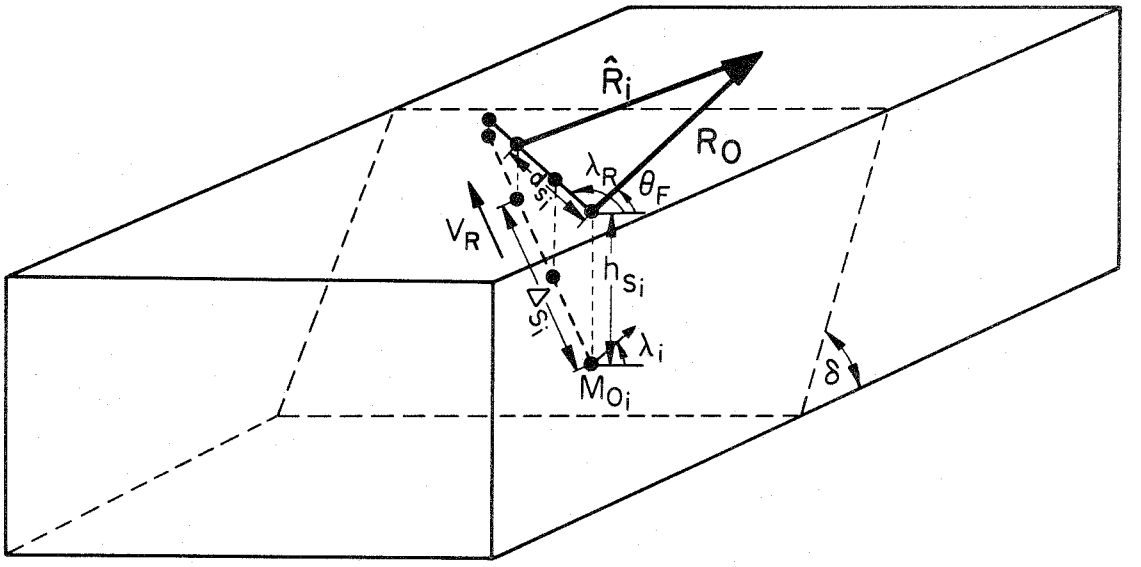

Figure 5.1. Geometry of the assumed multiple double couple source.

We caution here that the angle θ_F as defined in Figure 5.1 is not the same angle as the angle θ in the complex radiation pattern term of equation (5.1). A preliminary examination of Figure 1 in the Ben-Menahem and Harkrider (1964) paper would indicate that these two angles are equivalent, but their definition of θ is in error. The angle θ should be measured positively clockwise from the positive strike direction when viewed above the half-space.

As a check to this numerical approximation, we will model a vertical strike slip earthquake and check the resulting spectra with that calculated by the method of Ben-Menahem (1961). This model consisted of 16 sources, each at a depth of 20 km, with dip 90°, slip angle 0° (pure left lateral faulting), and identical moments. The sources were spaced at 2 km increments along the strike of the origin source (λ_s=180°) so that the fault length and propagation length were 30 km. Spectra were computed for apparent propagation velocities of 1.5, 3.0 and 4.5 km/sec at a point in a direction 45° to the direction of propagation in order to avoid a node in the radiation pattern of strike slip events. These spectra were then compared to that calculated for a single point source with the shift term for this fault length and propagation velocities. The moment of the single source was taken as the simple sum of

the moments in the discretized model. The results are shown in Figure 5.2.

In this figure, we have normalized the amplitudes to the values calculated for a non-propagating point source at the depth of the source at the point of initial rupture. By utilizing this normalization, we cancel the media source depth effects on the spectra. The ratio shows only the effects of the fault finiteness. In Figure 5.2a, we see that the directivity calculated by this numerical technique matches very closely that given by Ben-Menahem (1961). For propagation velocities 3.0 km/sec and greater, there is less than 1% difference in the two calculations. We see that the directivity is a very pronounced function in the period range of interest for slow propagation velocities.

Now that we have shown that the directivity function can be accurately calculated numerically, we now examine the effect of dip slip propagation on surface wave amplitude spectra. A model of a 45° pure dip slip fault was constructed. The initial motion occurs at a depth of 20 km and propagates at a constant velocity up the fault to a depth of 2 km. A total of 10 double couple sources were spaced at a 2 km depth and lateral increments to approximate this fault. The propagation distance along the fault is 28.3 km, and the pure horizontal propagation distance is

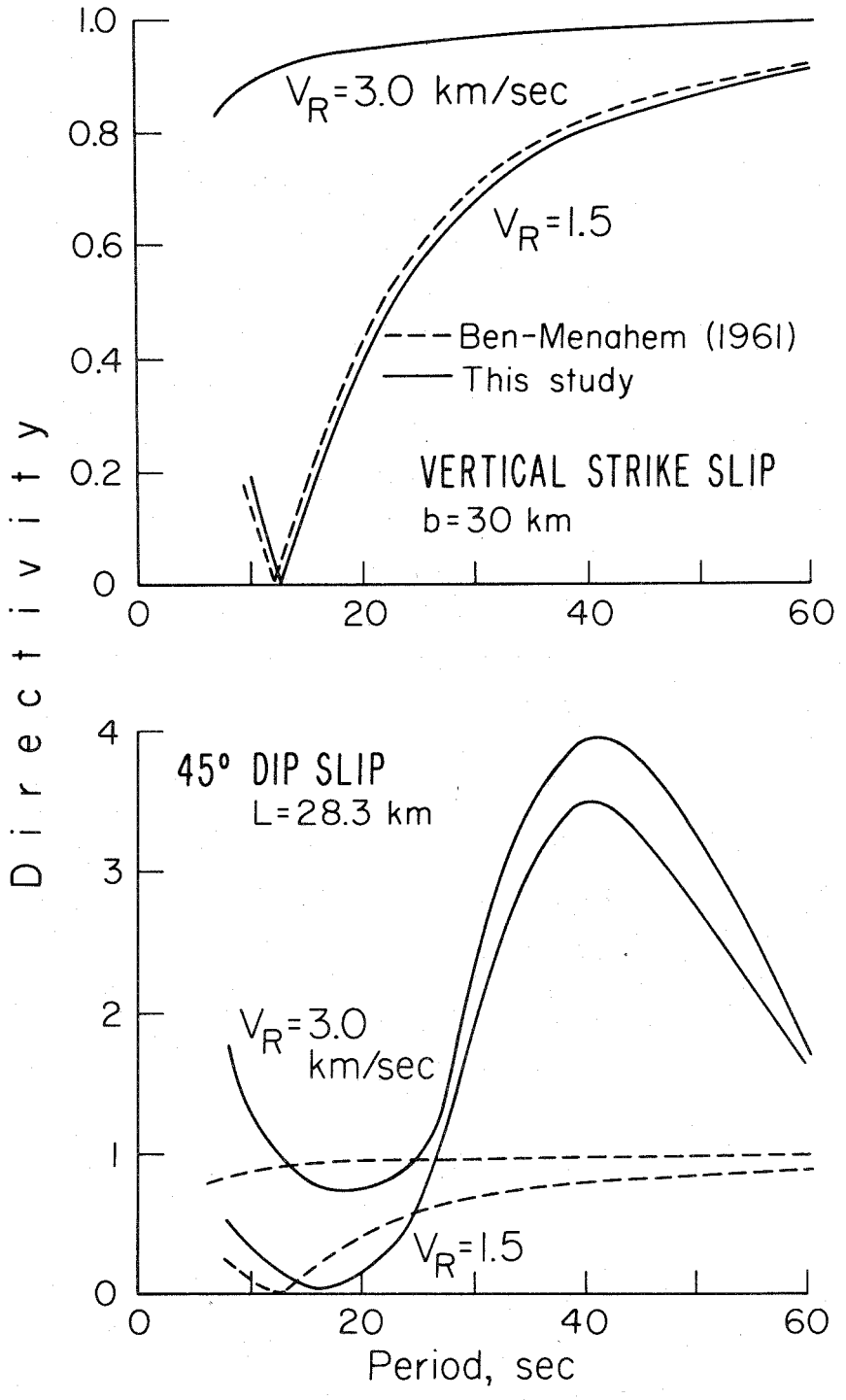

Figure 5.2. Comparison of the frequency-dependent directivity function given by the Ben-Menahem formulation and the numerical approximation. Upper--results for a 30 km long left lateral strike slip fault. Lower--results for a 28.3 km wide 45° dip slip fault.

18 km. The spectra were calculated at an exterior point which is in the direction of propagation. Spectra were also calculated using the Ben-Menahem formulism for the same parameters. All the amplitudes were normalized to a non-propagating point source at a depth of 20 km. Figure 5.2b shows a comparison of the resulting directivities for this dip slip case.

We see in this figure that there is a vast difference in the spectra computed by the two methods. The most significant difference is the accentuation of the amplitudes in the 25-60 sec period range. As a check as to whether the large amplitudes calculated in the numerical case were due to a Doppler effect or due to the non-uniform depth excitation along the propagation length, we normalized these amplitudes to the spectrum which was calculated using the numerical approach when an infinite propagation velocity was used. This normalization cancels any non-uniform depth excitation since the depth distribution was identical in both cases. The resulting directivity was almost identical to that calculated by the Ben-Menahem method and shown in the lower part of the figure.

We thus conclude that the effect of a source radiating energy as it propagates from one depth to another during faulting can be much larger than the Doppler effect and

cannot be ignored when spectra due to this type of faulting are being modeled. The depth effect on the spectra will vary from medium to medium and from source type to source type. No attempt was made here to catalogue this effect for various media and propagation parameters.

Approximation of San Fernando Faulting. In the previous chapter, we discussed the geophysical observations which constrained the fault model geometry for the 1971 San Fernando, California, earthquake. In this chapter, we would like to adopt an approximation to this same geometry to try to explain the radiation of surface wave energy from this fault. This approximation is accomplished by using four double-couple sources. The primary constraint for limiting the approximation to only four sources was economic, since the forward problem had to be recalculated after each iteration for the partial derivative matrix. However, we consider that the approximation chosen is adequate in light of the periods of the surface waves used. The parameters which describe this fault geometry and remain fixed in the inversion are listed below.

Source No.	depth(km)	dip	d_s(km)
1	14.5	52°	0.0
2	10.5	52°	2.49
3	6.25	35°	7.51
4	2.00	35°	14.36

These loci of the four point sources do not lie on a straight depth-distance line, but rather define the center line of a fault plane whose dip increases with depth. In calculating the propagation delay time for each of the elements, the distance, Δ_i, is used. Δ_i is given by

$$\Delta_i^2 = (h_{s_i} - h_{s_1})^2 + d_{s_i}^2 .$$

These distances are the straight line distances from the initial source to the three other double-couples. The delay time error caused by using this distance rather than the distance measured along the curved "fault plane" is less than 1 sec in the extreme case.

5.3 Forward Problem Formulation.

In this section, we wish to pose a relationship between the source model parameters and the observed spectra in a linear form as in equation (2.3). As we did for the static problem, we will propose some fault geometry and use an inversion scheme to solve the fault model parameters for this geometry. In order to describe the data, we will use a set of double-couple sources that are arranged spatially to approximate the fault model system which was presented in the previous chapter. Some of the parameters of the individual sources, specifically those which

describe the geometry of the fault system, will be set initially and not changed in the inversion. These parameters are the depth and dip associated with individual source elements and the spatial relationship between elements. The variable parameters for each element are taken to be the moment and slip angle. In addition, we will include the propagation velocity and propagation direction as variables for the entire system.

The model response matrix, **A**, for this problem is given to be composed of partial derivatives of the form

$$\frac{\partial S_i}{\partial X_k} \quad , \tag{5.4}$$

where S_i is the spectral amplitude value at some frequency f_ℓ (ℓ=1,L) measured at some "azimuth" θ_{F_j} (j=1,J) with respect to the fault system. X_k (k=1,K) is the source parameter which is allowed to be varied. The matrix **A** has K columns and L x J rows, where K is the number of model variables (specified below), L is the number of discrete spectral points at a single station and J is the number of stations used. For this case, L=10, J=18, K=10.

We see from Appendix 4 that the addition of multiple sources is a non-linear operation. This problem can be overcome by mapping only small increments of the model into

changes in the data. The criterion for this linearization is the same as was discussed in Chapter 2. The partial derivatives which compose the matrix **A** were computed numerically for a given model. This was done by the simple differencing,

$$\left.\frac{\partial S_i}{\partial X_k}\right]_m \approx \frac{S_i(m+\Delta m_k) - S_i(m)}{\Delta m_k} . \qquad (5.5)$$

The incremental values of the source parameters used were:

ΔM_0 - moment = 0.1 x 10^{26} dyne-cm

$\Delta\lambda$ - slip angle = 10°

$\Delta\lambda_R$ - propagation direction = 10°

ΔV_R - propagation velocity = 0.25 km/sec .

5.4 Inversion Procedure.

An inversion procedure will be adopted to find the model parameters which best fit the observed spectral data. Since the number of data points far exceed the number of variables, we will fit the data in a least-squares sense. Appendix 3 gives the derivation of the inversion operators for the general least-squares case.

Since we have mixed units in the source model parameters and thus mixed units in **A** and $\delta\mathbf{m}$, a problem of

scaling arises. One way of correcting for the dimensionality of the parameters is through the use of the weighting, or model correlation, coefficients. The weights of the source parameters can be adjusted so that the weighted coefficients of the rows of **A** are about equal. For a non-linear problem, this scaling would be model dependent and thus would probably vary in the inversion. This method, although it can give satisfactory results in obtaining a fit to the data, is not esthetically pleasing. A satisfactory method was found to solve this scaling problem. This was accomplished by non-dimensionalizing the problem,

$$\mathbf{A}\,\delta\mathbf{m} = \delta\mathbf{d} \quad ,$$

by dividing through by the data and model parameters. The dimensional matrices and vectors are replaced by their non-dimensional counterparts in the inversion. The components of the quantities are defined as:

$$\hat{A}_{ij} = \frac{m_j}{d_{o_i}} A_{ij} \qquad \delta\hat{d}_i = \frac{1}{d_{o_i}} \delta d_i$$

$$\hat{C}_{nn_{ii}} = \frac{1}{d^2_{o_i}} C_{nn_{ii}} \qquad \delta\hat{m}_j = \frac{1}{m_j} \delta m_j \quad .$$

We note that this scaling is also non-linear.

Throughout the inversion calculations carried out in this chapter, we will limit the absolute value of a model perturbation in one iteration to that used in the differencing method of calculating the partial derivatives in the forward problem. This was done to avoid projecting any model perturbation outside the range of assumed linearity.

As a test to the inversion scheme, we will calculate the theoretical spectra at 18 far-field points (corresponding to the location of the 18 stations which are described in the next section) for a given set of source parameters. The non-variable source parameters are the same as those used to describe the San Fernando faulting. These theoretical spectra were then input into the inversion scheme as "data" to see how accurately the corresponding variable source parameters could be recovered. The results of this test are shown in Figure 5.3. The initial values for the source parameters are that shown on the left at Iteration = 0. The source values used in calculating the "data" are shown by the arrows on the right hand side of the figure. We see that at least 6 iterations are required before the solution starts to converge to the true values, and after 11 iterations, the estimated values are very close to the true values. The restriction that the maximum size of the perturbations can be no larger than the differencing

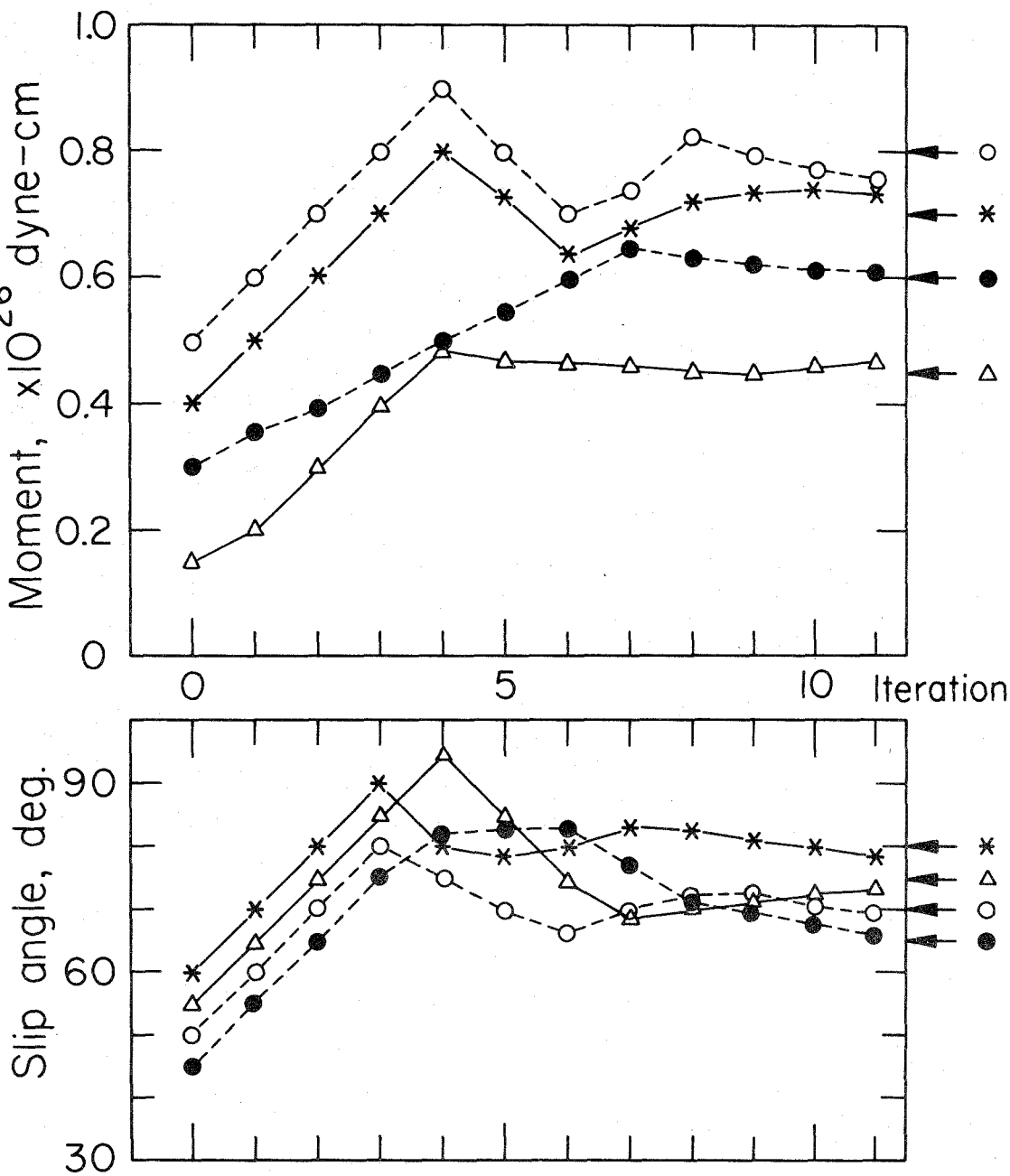

Figure 5.3. Test to check the amplitude spectra inversion technique. Initial values of the fault parameters are shown on the left; the theoretical values are indicated by arrows on the right.

values slows the convergence somewhat. Not shown in this figure is the estimate of the propagation velocity and propagation direction for each iteration. These two quantities varied more smoothly and converged more quickly to the theoretical values than did the moments and slip angles. The propagation velocity and propagation direction converged to 4.2 km/sec and 120° from an initial value of 3.2 km/sec and 100°, respectively.

In this test, the variance of each "datum" was taken to be 5% of the calculated value. The test was repeated with the data variances set at 25% of the calculated values. Although the convergence to the true model values was not as good as in the previous example, the solution remained stable through the iterations, and a fair estimate of the model parameters was obtained. The results from these experiments were encouraging enough to attempt to apply the technique to actual observed surface wave spectra.

5.5 Data.

The source of the surface wave data used in this study was from the long period vertical component instruments of the World-Wide Standard Seismograph Network (WWSSN). Only the vertical Rayleigh wave component at each station was considered in this study. Data from the Canadian Standard Stations and the WWSSN stations located in the continental

United States could not be used since either the long period vertical component was inoperative or off-scale during the passage of the Rayleigh wave train. The original intent in collecting these data was to limit the stations used to those whose epicentral distances were less than 60°-70°. However, to provide a more uniform and extensive azimuthal coverage of stations, this condition was relaxed somewhat. The closest station in a given azimuthal increment from the epicenter which gave a readable record was chosen. A total of 18 records was chosen to be examined, and these stations provided a fairly good azimuthal coverage for this event. Table 5.1 gives a list of all these stations used, the epicentral distances, and the geodetic azimuth of the station with respect to the epicenter.

The Rayleigh wave signal was identified on each of the records and digitized at an irregular interval taking adequate care to sufficiently define the trace. These data were then linearly interpolated to an equal increment rate of one sample every two seconds. The digitization was restricted to a velocity window of between about 4.3 km/sec to about 1.5 km/sec. There was a slight variance to this window depending on the distance and source-receiver path. The choice of the velocity window was based on a visual judgment as to when the signal arrived and essentially

TABLE 5.1

Station	Geodetic Azimuth	Distance (Deg)	% Land	% Ocean	Geom. Fact.	Geographic Location
NOR	10	58	90	10	1.66	Nord, Greenland
KTG	23	60	77	23	1.68	Kap Tobin, Greenland
AKU	27	63	75	25	1.70	Akureyri, Iceland
VAL	38	74	55	45	1.76	Valentia, Ireland
MAL	47	86	61	39	1.80	Malaga, Spain
BEC	77	45	78	22	1.51	Bermuda
SJG	96	49	69	31	1.56	San Juan, Puerto Rico
CAR	104	53	43	57	1.61	Caracas, Venezuela
BHP	116	44	70	30	1.50	Balboa Heights, Canal Zone
GIE	137	44	11	89	1.50	Galapagos Islands
PEL	141	81	16	84	1.79	Peldehue, Chile
SBA	194	120	0	100	1.67	Scott Base, Antarctica
WEL	224	97	0	100	1.79	Wellington, New Zealand
AFI	236	70	0	100	1.74	Afiamalu, Samoa
KIP	260	38	0	100	1.41	Kipapa, Hawaii
GUA	285	88	0	100	1.80	Guam Island
MAT	307	80	1	99	1.79	Matsushiro, Japan
COL	339	35	69	31	1.36	College, Alaska

Table 5.1. Stations used in this surface wave study.

ended at a particular station and on the dispersion curves expected for the traveled path. Typical of the dispersion curves used were those of Brune and Dorman (1963), McEvilly (1964), Santo (1963), Tryggvason (1962), and Brune (1969).

The Fourier spectra of these records were then taken with a numerical transform routine. The spectra were calculated for the frequency range from 60 sec period to 8 sec period, with 512 discrete frequency points in this range. The spectra were smoothed slightly with a two-point Hanning filter such that for the ith frequency component of a particular record

$$f_i(\omega) = \frac{2}{5}\left\{\frac{1}{4}[f_{i-2}(\omega)+f_{i+2}(\omega)]+\frac{1}{2}[f_{i-1}(\omega)+f_{i+1}(\omega)]+f_i(\omega)\right\} .$$

Instrument Correction. The instrument frequency and amplitude response for the World-Wide long period seismograph system were calculated from the published instrument and coupling constants for that instrument. These calculations are based on the relations given by Hagiwara (1958) and Mitchell and Landisman (1969). Both an amplitude and frequency correction were supplied. Since some of the stations that were used in this study operate at different instrument gains during different parts of the year, a check was made on each seismogram to verify the listed

instrument gain. This was done by comparing the height of the calibration pulse to the applied current impulse. The magnification computed in this fashion was within about 10% of the listed magnification except for station SBA which appeared to be off by a factor of 2.

Geometrical Spreading Correction. All of the amplitude spectra $A(\omega)$ are corrected back to a common distance, Δ_c, by multiplying by the well-known relation for spreading on the surface of a sphere

$$C_{GS} = \sqrt{\frac{\sin \Delta}{\sin \Delta_c}} \quad , \tag{5.6}$$

where Δ and Δ_c are given in radians. For the data in this case, we chose our reference distance, Δ_c, to be 2000 km.

Attenuation Correction. Following the instrumental and geometrical spreading corrections, the spectral amplitudes were corrected for attenuation. This correction takes the form

$$A_c(\omega) = A(\omega)\, e^{\gamma(\omega)\, x} \quad , \tag{5.7}$$

where $\gamma(\omega)$ is the amplitude attenuation coefficient appropriate for the particular source to receiver path, and x is the epicentral distance. Since the paths from the San Fernando epicenter to most of the WWSSN stations used in

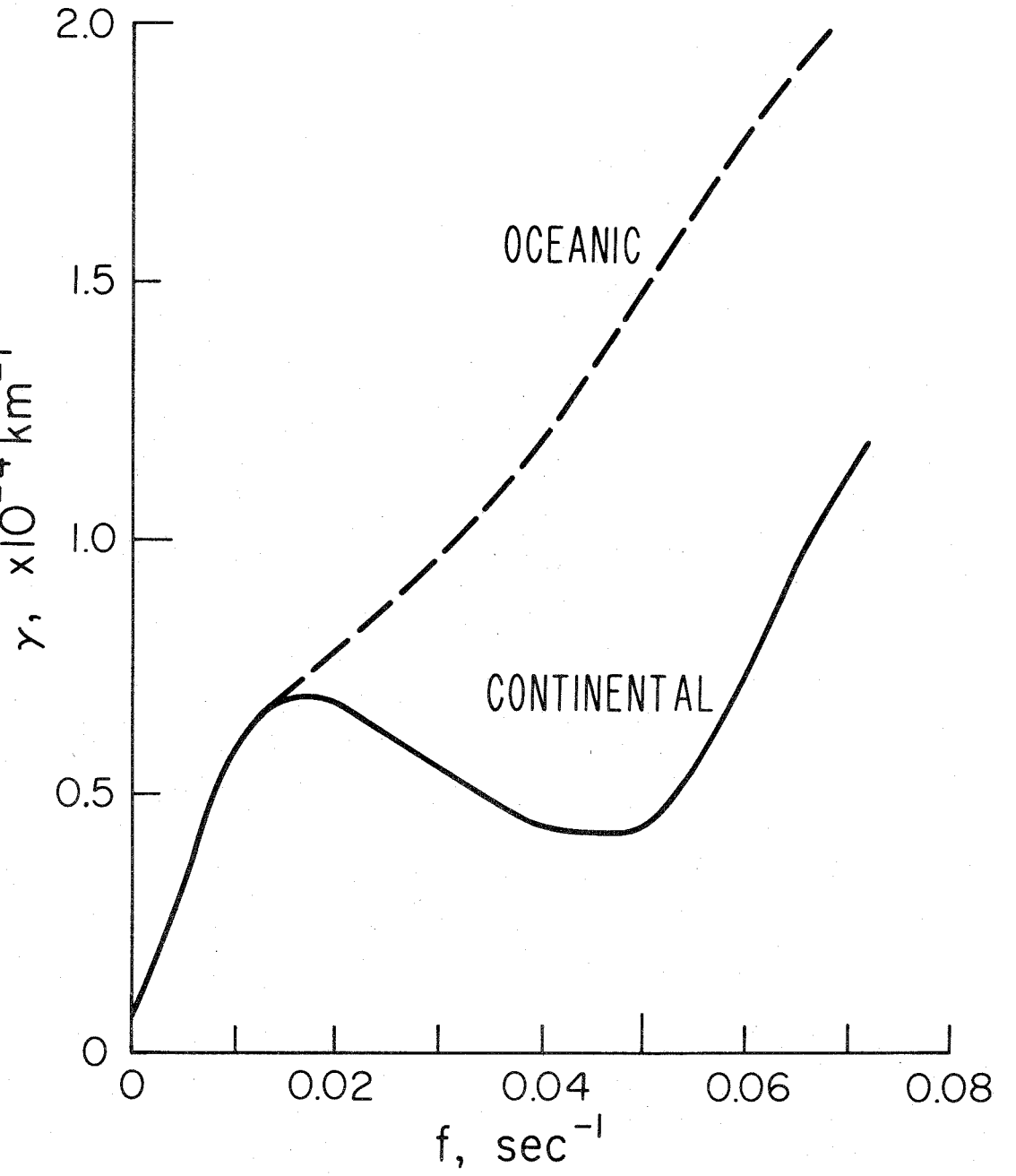

Figure 5.4. Amplitude attenuation coefficients assumed for the two structures used in this study.

this study involve mixed crustal type paths, the appropriate attenuation coefficient would necessarily be a path-averaged value. We attempted to take this into consideration in the following manner.

We assume that each of the transmission paths can be divided into two types: continental and oceanic. From the literature, we compiled estimates of the fundamental model Rayleigh wave attenuation coefficients for these two media. These estimates are summarized in Figure 5.4. The continental attenuation coefficients are reduced from data given by Gutenberg (1945), Gutenberg and Richter (1936), Tryggvason (1965), Nuttli (1973) and Mitchell (1973). The oceanic attenuation coefficient curve was reduced from data in papers by Gutenberg (1945), Ben-Menahem (1965), and Tsai and Aki (1969). The partitioning of continental and oceanic travel paths was estimated for each station, and the spectral amplitudes measured at that station were corrected by multiplying by the following relation,

$$C_A = e^{[x_L \gamma_L(\omega) + x_O \gamma_O(\omega)]}, \qquad (5.8)$$

where

$\gamma_L(\omega)$ = the continental, or land, amplitude dissipation coefficient

$\gamma_O(\omega)$ = the oceanic amplitude dissipation coefficient

x_L = the distance traveled over a continental type path

x_O = the distance traveled over an oceanic type path.

Table 5.1 lists the percentage of the total path length that is spent in each of the assumed attenuation provinces. Also listed in this table is the geometrical spreading factor given by the equation in the above paragraph.

Local Crustal Correction. This correction attempts to compensate for the effects of surface waves traveling laterally from one structure to another. In the case under consideration, there are marked variations in the structure of the crust and upper mantle between the area in which the surface waves were generated and the area around the stations at which they are measured. Fortunately, the corrections applied along the path between these two points cancel out so that only a local crustal correction at the receiver needs to be applied to correct the spectral amplitudes back to the medium in which they were generated. An approximation which has given satisfactory results in predicting the amplitude changes of Rayleigh waves traveling across a lateral boundary has been given by McGarr (1969) and McGarr and Alsop (1967). The validity of this

approximation has been verified by wave propagation studies in laterally heterogeneous media using the finite-difference numerical technique (D. Boore, personal communication, 1974).

If we assume that the total energy in the fundamental mode Rayleigh wave remains constant in the process of transmissions across the boundary margin, then we can write

$$\frac{A_R}{A_S} = \sqrt{\frac{W_S(\omega)}{W_R(\omega)}} \quad ,$$

where

$A_S(\omega)$ = the amplitude in the source medium

$A_R(\omega)$ = the amplitude in the receiver medium

$W_S(\omega)$ = the normalized energy flux in the source medium

$W_R(\omega)$ = the normalized energy flux in the receiver medium.

The normalized energy flux is given by

$$W(\omega) = 2\ E(\omega)\ U(\omega) \quad ,$$

where $E(\omega)$ is the total potential or kinetic energy at a particular frequency normalized to the surface displacement. The calculation of this energy excited in a given layered earth model is given by Harkrider and Anderson

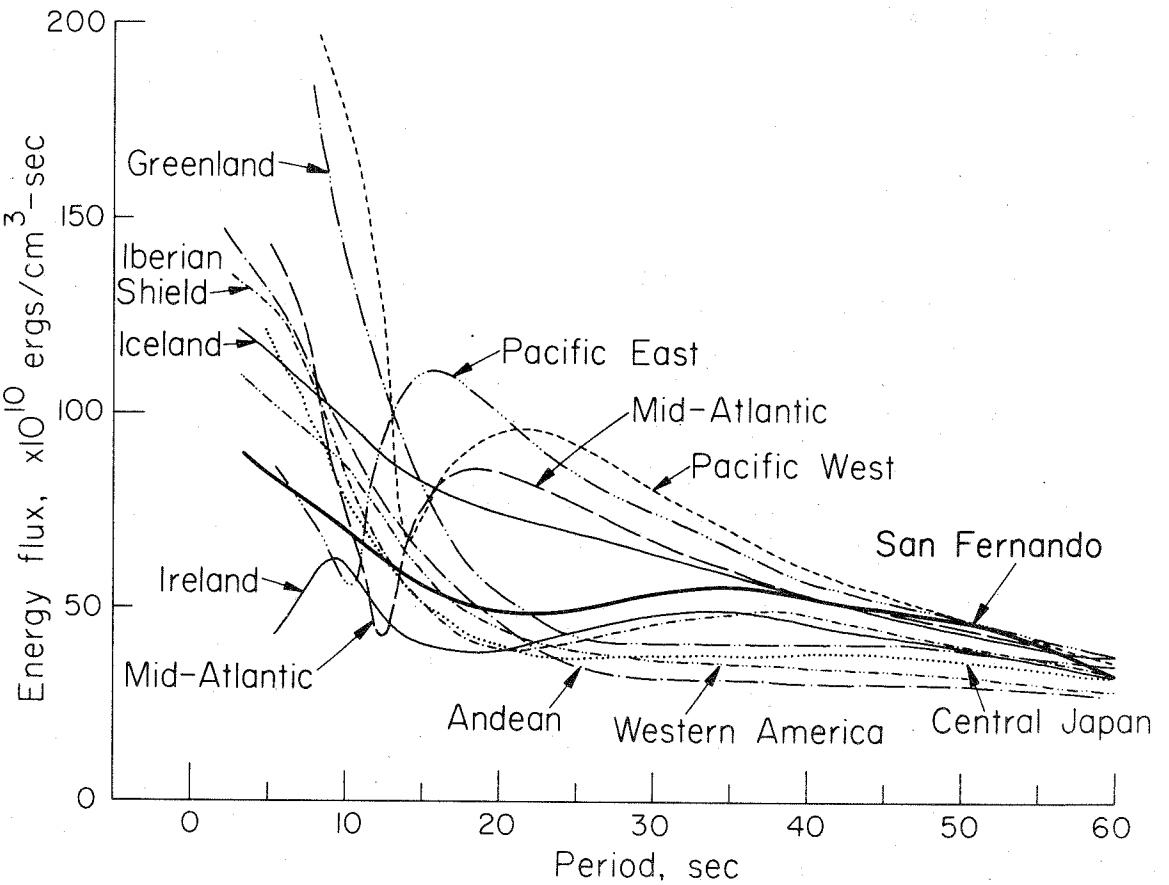

Figure 5.5. Energy flux as a function of frequency calculated for various crustal and upper-mantle models. The velocity-density structures for the various models are given in Appendix 5.

TABLE 5.2

Crust & Upper Mantle Type		Station
San Fernando Crust over Gutenberg Continent	-	Source Medium
Greenlandic Shield with Ice Cap	-	NOR, KTG, SBA
Iceland	-	AKU
Irish Continental Shelf	-	VAL
Iberian Shield	-	MAL
Mid-Atlantic Ocean	-	BEC, SJG
Western America Tectonic	-	CAR, BHP, COL
Pacific Ocean East	-	GIE
Pacific Ocean West	-	AFI, KIP, GUA, WEL
Andean	-	PEL
Central Japan	-	MAT

Table 5.2. Crust and upper mantle structure used for the local crustal structure spectral amplitude correction. Velocity-density models for the different structures are given in Appendix 5.

(1966, equation 1). $U(\omega)$ is the group velocity for the particular medium.

At each of the 18 WWSSN stations used in this study, the crustal structure at that station was approximated and the velocity dispersion and the spectral energy density calculated. The crustal models used in this calculation and the references for these models are given in Appendix 5. The energy flux, $W(\omega)$, given by these calculations is summarized in Figure 5.5. The stations for which each crustal model correction was used are listed in Table 5.2.

In order to correct the spectral amplitudes back to a common medium, we multiply by a correction which normalizes the amplitudes to the source medium. This correction takes the form

$$C_{LC} = \sqrt{\frac{W_R(\omega)}{W_S(\omega)}} \quad . \tag{5.9}$$

Multipath Propagation Removal. The complex cepstrum technique which was established by Schafer (1969) has proven to be an effective means of removing spectral modulations caused by the interference of simultaneously arriving signals. Two or more signals can arrive simultaneously at a given station due to either multipathing of a single signal or can result from the addition of several seismic

signals, multisourcing, or some combination of these two effects. In this study, we want to eliminate as best we can from our observed spectra that modulation which is due to any multipathing effects and retain any modulations which may arise from the addition of multiple sources. The spectra which have been de-modulated from multipathing effects can then be examined by this method to try to determine the existence of whether the source is a single or multiple event.

Cohen (1970) and Flinn et al. (1973) have used the technique to detect the separation of the body phases P and pP for very shallow events, while Linville (1971) and Tsai (1972) have applied the method to surface waves. In the cepstrum technique, a homomorphic deconvolution is applied to separate the components of a convolution of a seismic signal and a multipath operator. Basically, the method acts like a filter applied to the amplitude spectra where the interference effect appears as a scalloping of the spectra over a wide frequency range. When a long pass filter is applied, the spectrum modulating effects are removed. This filtering is done by applying the appropriate bandpass to the cepstrum. Tsai (1972) and Linville (1971) give a summary of the technique involved and the appropriate filter bands to use in correcting spectra in the

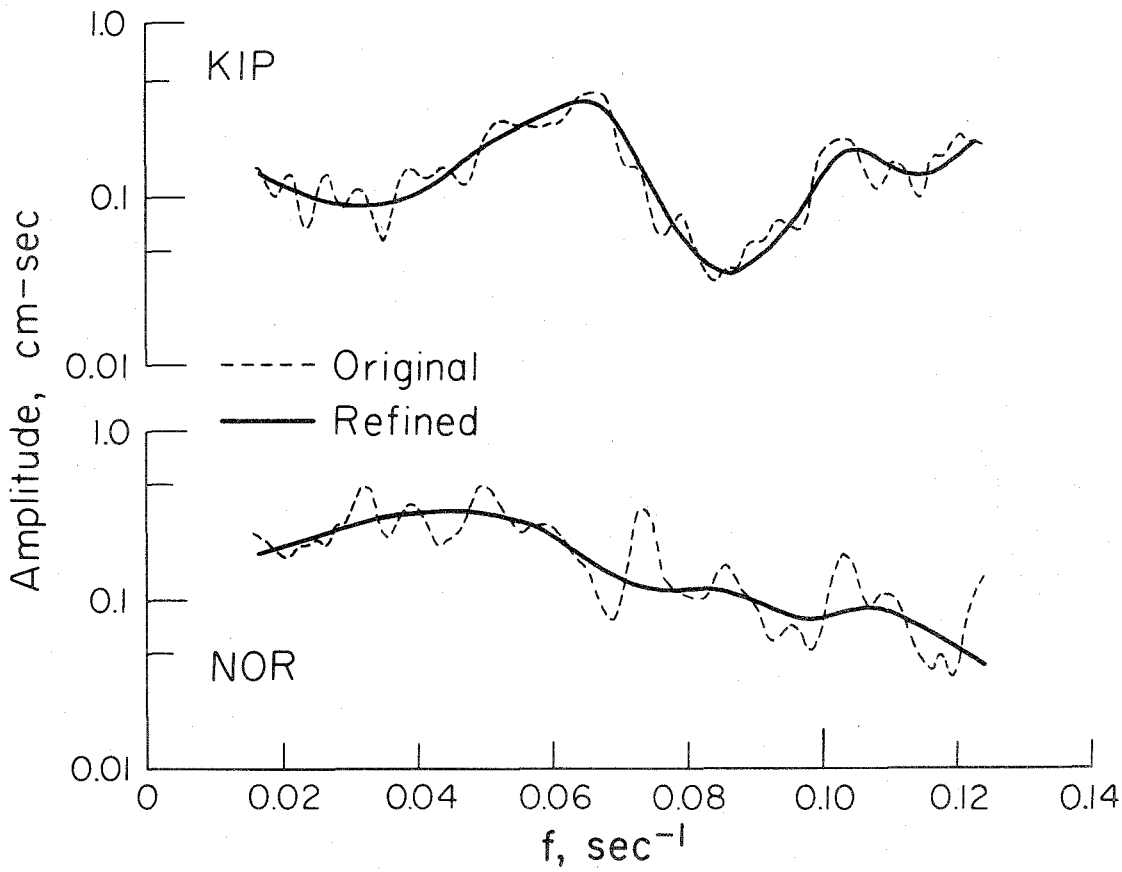

Figure 5.6. Example of cepstral filtering at two stations. Original spectra are shown by dashed line; the refined, or filtered, spectra are shown by the solid line.

bandwidth which is involved in this study. Such a long pass filter was applied to the observed spectra. This spectral filtering had little effect except to smooth the spectra. A typical example of the removal of the spectral modulations is shown in Figure 5.6. The spectra are presented as a function of frequency to show how the modulations are frequency distributed. In this figure, the original spectra are shown by the dashed line, and the spectra after the application of the cepstrum technique are shown as a solid line.

We saw in the last chapter from the static dislocation models of the San Fernando earthquake that there appeared to be two areas of large dislocation -- one in the hypocentral region and one near the surface. If the dislocations from these two areas acted like two separate sources, separated spatially and temporally, then the interference of these two sources should appear in the complex cepstrum. The cepstra were calculated at several of the stations chosen in the opposite direction of the apparent rupture. This was done to maximize the effect of the final separateness of the sources. At station COL, there appeared to be some signal interference at a delay time of about 8 sec and at 11.5 sec. This might be interpreted as the interference of the signal excited at the hypocenter by another

signal which was excited when the fault became near or broke the surface. This effect was not as apparent at station NOR, so we feel that no firm conclusions should be drawn from this particular analysis.

Corrected Data. All of the above corrections were applied to the measured amplitude spectra at the WWSSN stations. These spectra are shown in Figure 5.7. The upper part of this figure shows the location and azimuthal distribution of the stations used. The lower part of the figure gives the corrected amplitude spectra at each of the stations. The spectra are arranged by columns with geodetic azimuth increasing from top to bottom. The spectral values indicated by a dashed line in the figure are the values for which the total correction exceeded a factor of 10. These data will have to be considered less reliable than the longer period data because of the uncertainties in the corrections. Samples of the spectral values were chosen at ten discrete periods: 60, 50, 40, 34, 30, 26, 22, 20, 18, and 16 sec. It was felt that this sampling interval was adequate to reflect the spectra shape at the individual stations. Periods shorter than 16 sec were not included into the inversion data set because of the larger uncertainty in the corrections at these periods, particularly in the attenuation factor.

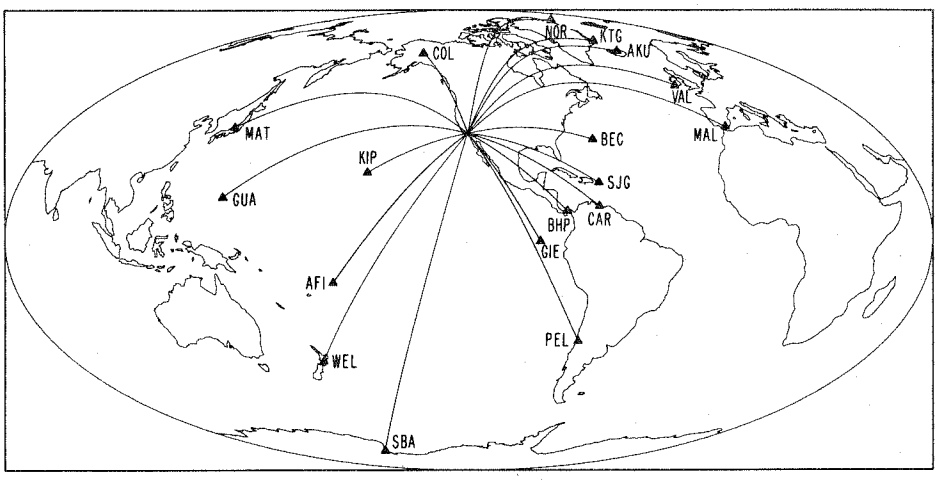

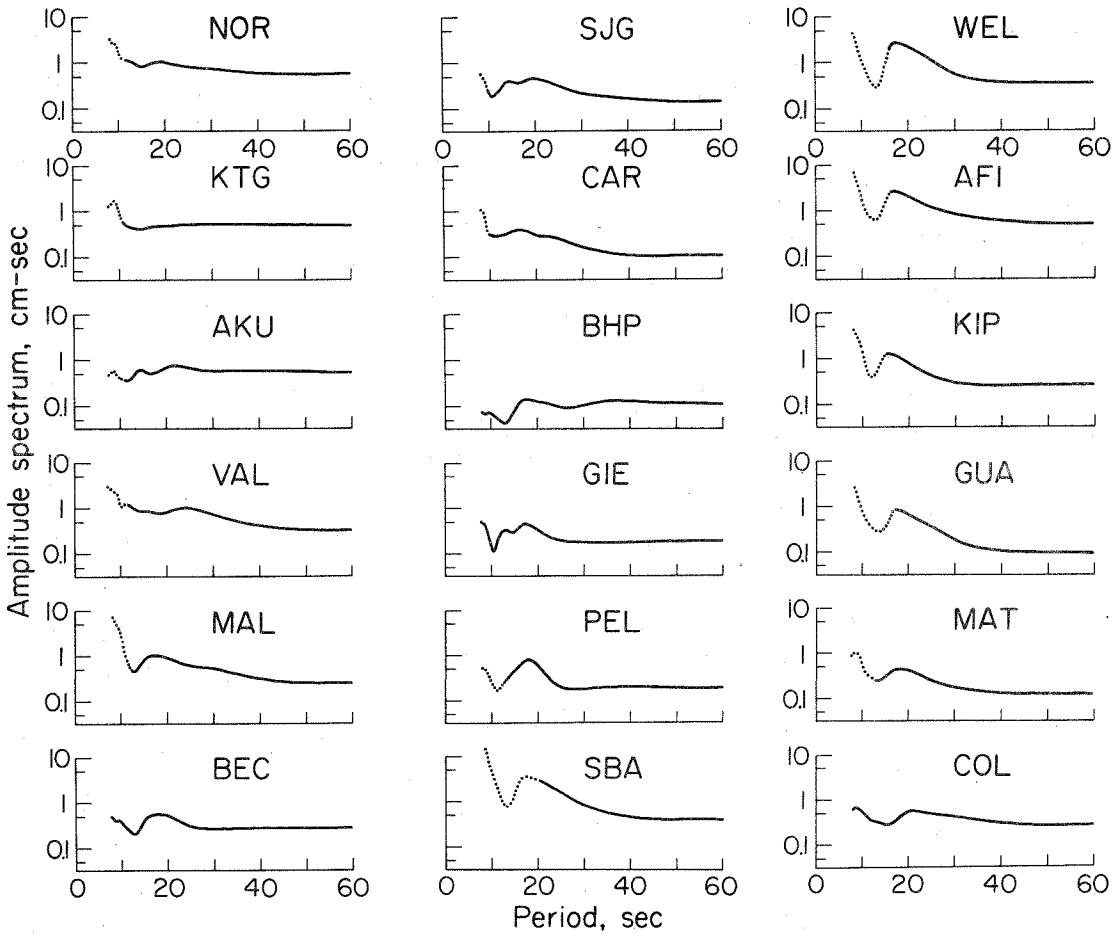

Figure 5.7. Observed spectral amplitudes after all corrections have been applied. Dotted line indicates when the corrections exceed a fator of 10.

Estimated Errors in the Data. Errors to the spectra which we have measured for this event arise from two sources: 1) errors in measuring the spectra at the different stations and 2) errors in applying the corrections to the spectra.

Errors from actually measuring the spectra could arise from digitizing errors and from taking too short a signal to get all the spectral information at certain frequencies. One station, KIP, was redigitized to include a much larger signal and the spectral amplitudes recomputed. The recalculated amplitudes were found to be at most 3-4% different on the average than that originally computed. A value of 3% error was taken as the estimate for this error.

By far, the largest error involved in the application of the spectral corrections arises from the attenuation correction. If we assume that we know the attenuation values to only 25% of the values given in the figure, then the estimated error for this correction would be

$$E_c(\omega) = e^{\frac{\gamma}{4}\Delta}.$$

We next can assume that we know the crustal corrections to only 25%. This turns out to be a small error, except at very short periods, because the original correction is small.

Distribution of Data Information. In Appendix 3, we have derived an operator, **J**, which tells how the information in the data set are distributed. The use of this operator has been demonstrated by Minster et al. (1974), and these authors give a lucid description of its properties. The importance of a particular datum, which is a spectral amplitude at a particular frequency measured at a particular spatial location, depends on both the location and the accuracy of the datum. If we consider each WWSSN station to be a subset of the entire data set, then the relative importance of that station is simply the sum of the importances of the data in that subset. Figure 5.8 shows how the information in the chosen data set is distributed. In this figure, we have summed the relative importances of the frequencies at the individual stations and plotted this importance as a function of the geodetic azimuth of those stations. The results of this plot are somewhat surprising. We see that two stations, COL and KTG, contain a total of 30% of the total information in the data set. In fact, the data set could be reduced by half and only 25% of the total information which constrains the model variables would be lost.

From Appendix 3, we see that the importance of a datum does not depend on the actual value of the datum

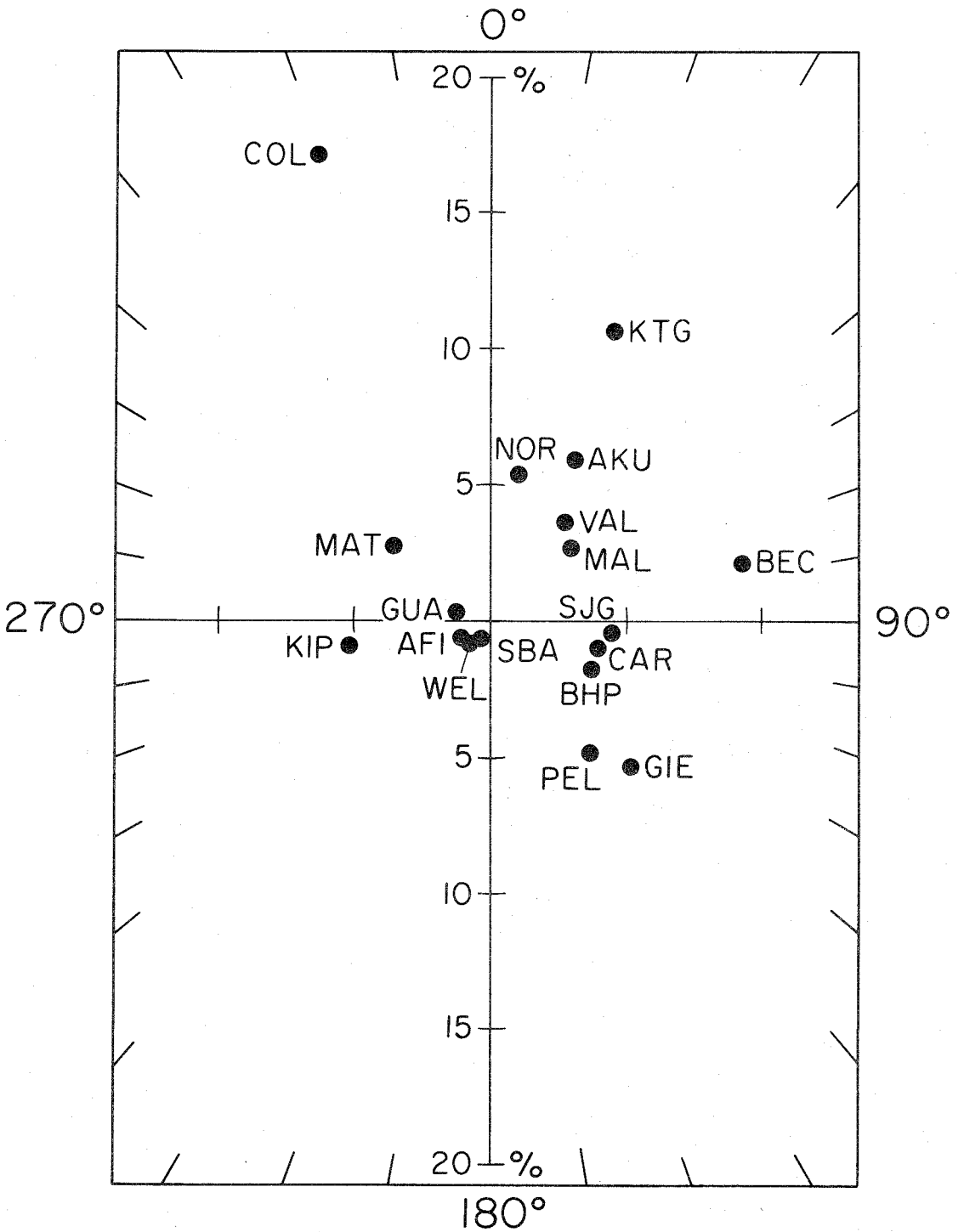

Figure 5.8. Distribution of data information with respect to summed information density at a single station. Information density is normalized such that the total from all stations is 100%.

itself but rather the estimated error in the datum and the model response operator, **A**. The importance values are dependent on the source model only in the sense that **A** is model dependent. Although not done in this case, this type of calculation could be carried out before the data set is gathered to determine an optimum distribution of stations to use.

5.6 Inversion Results.

Fault Model. The ten model parameters which describe the source system were found by the least-squares fit to the observed spectral data measured at the 18 WWSSN stations. The best fit model parameters as determined from the inversion procedure are as follows:

Source #	Depth (km)	Moment (10^{26} dyne-cm)	Slip Angle (λ_i)
1	14.5	0.62	66°
2	10.5	0.20	78°
3	6.25	0.51	82°
4	2.0	0.39	70°

propagation direction (λ_R) = 99°

propagation velocity = 2.95 km/sec.

Figure 5.9 illustrates the degree of fit to the data that this model exhibits. The dashed straight line in the center of each radiation pattern indicates the orientation

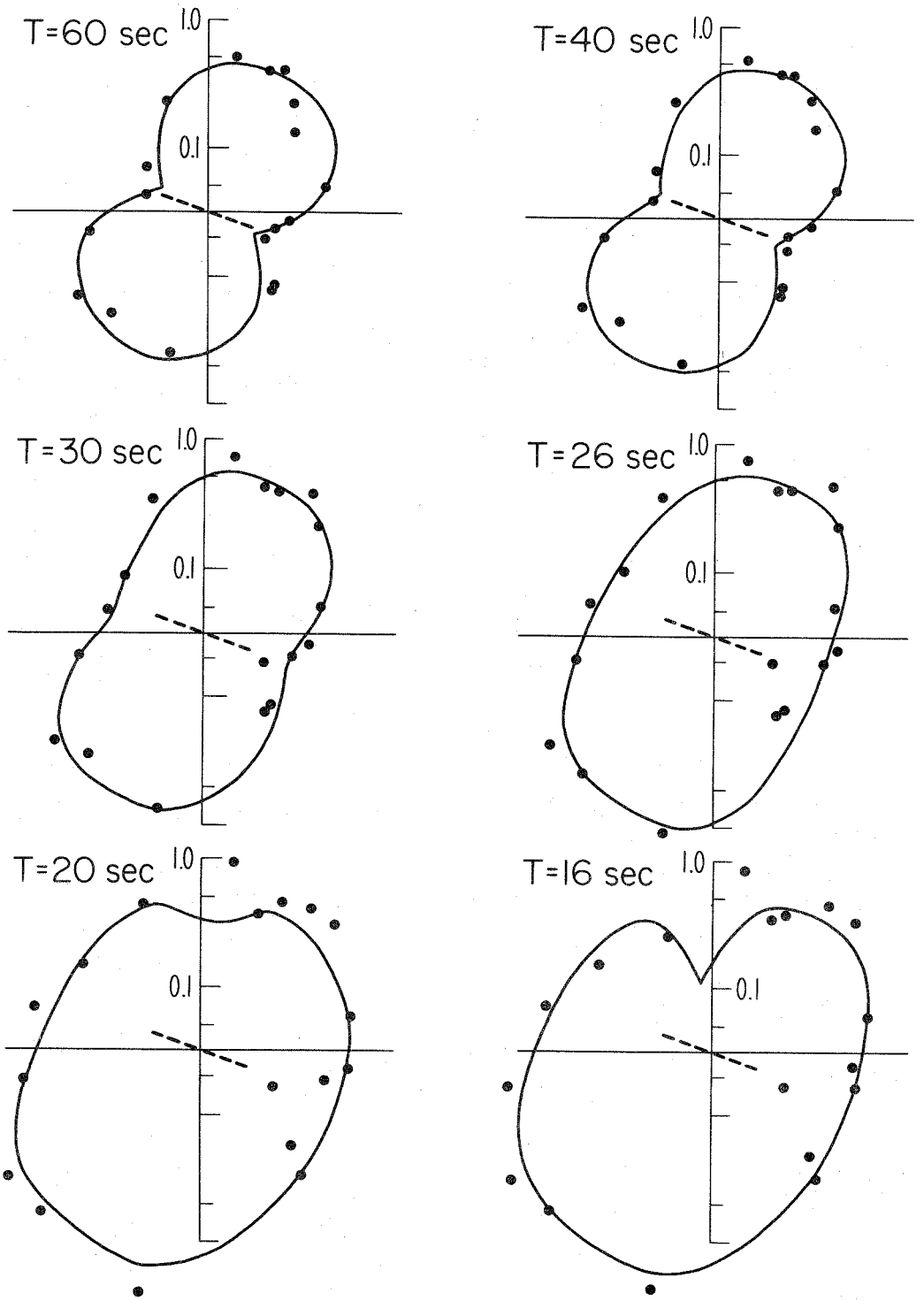

Figure 5.9. Calculated and observed radiation patterns. Orientation of the fault plane (N70°W) is shown by the dashed line in the center of each pattern. The amplitudes of the patterns are in units of cm-sec.

of the strike of the fault system, taken to be in the direction of N70°W. Rupture initiates at a depth of 14.5 km and propagates in the direction of S11°W. The fit to the long period data (40-60 sec) shows that the radiation pattern is a symmetric dipole pattern. These two patterns show very little, if any, signs of fault finiteness. The finiteness of the fault starts to become apparent in the middle two figures. For these periods (26-30 sec), the patterns are symmetric in a direction perpendicular to the direction of propagation but not in the direction of propagation. For the shorter periods (16-20 sec), the effects of the rupture length and non-uniform excitation become very important in shaping the radiation patterns.

Uncertainty in Model. We would now like to estimate the uncertainties in these best fit model parameters. As done in Chapter 2 for the stochastic inverse case, we will calculate these uncertainties at a particular confidence level by mapping the estimated errors in the data into errors in the model. The least-squares solution matrix for unweighted model parameters which performs this mapping is the matrix given by Mathews and Walker (1964, p. 366-367)

$$\mathbf{Q} = \mathbf{A}^{*}\mathbf{C}_{nn}^{-1}\mathbf{A} \quad . \tag{5.10}$$

We note here that this solution does not take into account

the possible weighting of the different model parameters. This is no problem in this case, or in any other case, since the problem can be non-dimensionalized as we have done here. The non-dimensional form of this operator has the same form as that given above.

The bilinear product of the matrix, $\mathbf{Q}$, and some model perturbation, $\mathbf{q}$, yields a confidence region of resolvability. That is,

$$\mathbf{q}^{*}\mathbf{Q}\,\mathbf{q} = k^{2}(c) \; . \tag{5.11}$$

This equation defines the hyperellipsoid of uncertainty for a particular model perturbation at a confidence interval, k(c).

By fixing k(c) to a particular value, taken to be 1.96 in this problem, we calculate possible model perturbations for which the equation of the ellipsoid is solved. Any model perturbation vector which lies inside this ellipsoid is unresolvable at the confidence interval, k(c), while any model perturbation vector which protrudes this ellipsoid is resolvable at that confidence level. In the example considered here, we will limit the analysis to two dimensions. With this limitation, we can define an ellipse of uncertainty for combinations of model parameter pairs. As we will see in the examples below, this analysis also allows

the consideration of the coupling between the various model parameters.

The ellipse of uncertainty is shown for various fault model parameter pairs in Figure 5.10. In Figure 5.10, the moments are given in units of 10^{26} dyne-cm, and the angles are expressed in degrees. In Figure 5.10a, we have considered the area of uncertainty when the moments of the two deepest source double couples are allowed to vary. We see that M_{o_1} has an uncertainty of only .05 x 10^{26} dyne-cm when it is allowed to vary alone. Perturbations larger than this value would be resolvable by the data unless the magnitude of the moment on the adjacent double couple (M_{o_2}) was also allowed to vary. The maximum uncertainty that M_{o_1} can take in this coupled system is shown by the projection of the maximum excursion of the ellipse onto the M_{o_1} axis. The maximum uncertainty of M_{o_2} is similarly calculated.

The ratio of the uncertainty measured at the point where the ellipse crosses the axis of a model variable and the maximum uncertainty of that variable defines a coefficient which reflects the coupling of the two variables. We will call this ratio the model co-variance coefficient (MCVC). For a co-variance coefficient equal to 1.0, there is no coupling between parameters. That is, the maximum

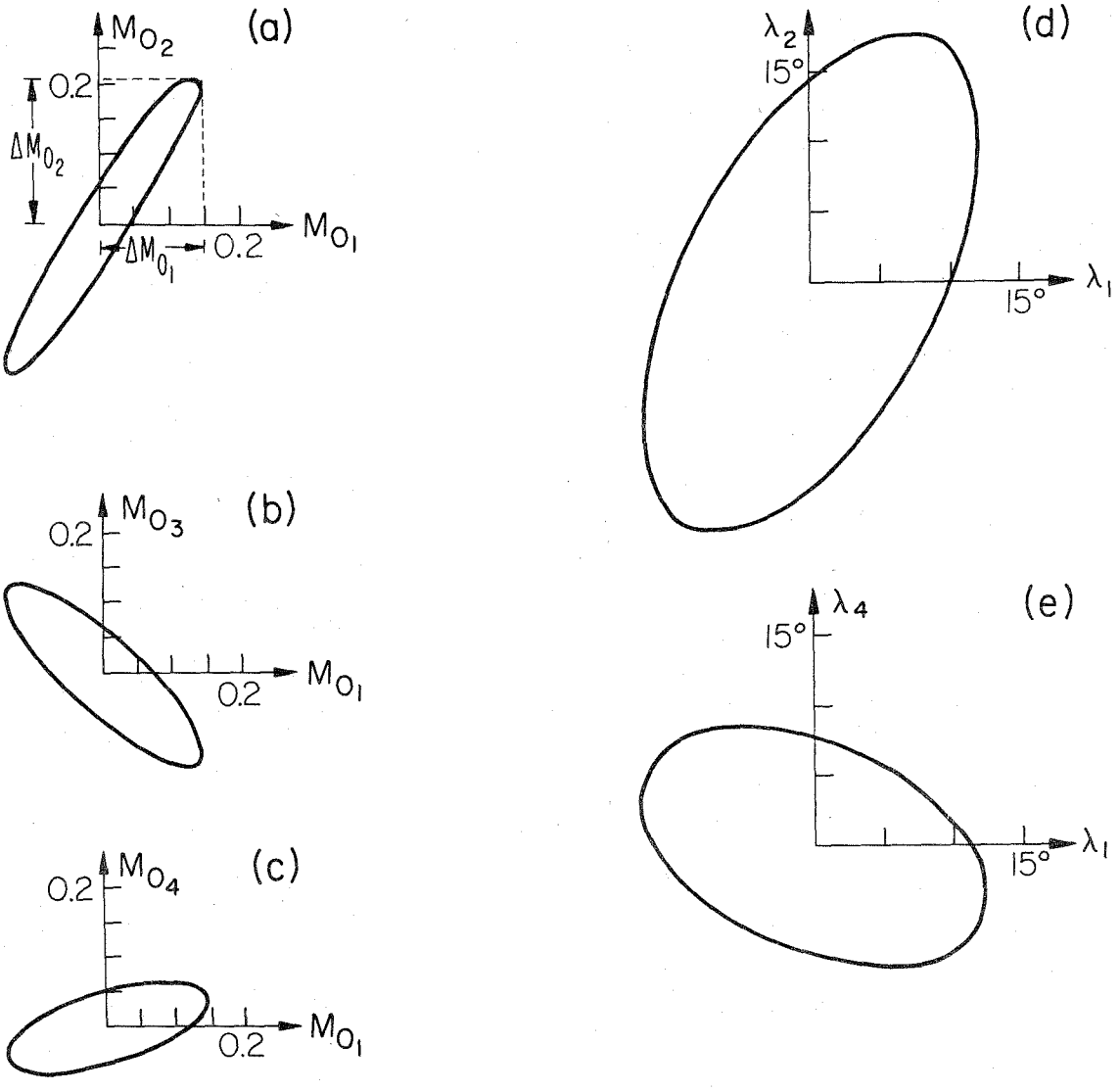

Figure 5.10 (a-e). Uncertainty ellipses for various fault model parameter pairs. Combinations of perturbations which fall inside the ellipses are not detectable by the data at the 95% confidence level. Moments are given in units of 10^{26} dyne-cm; angles are expressed in degrees.

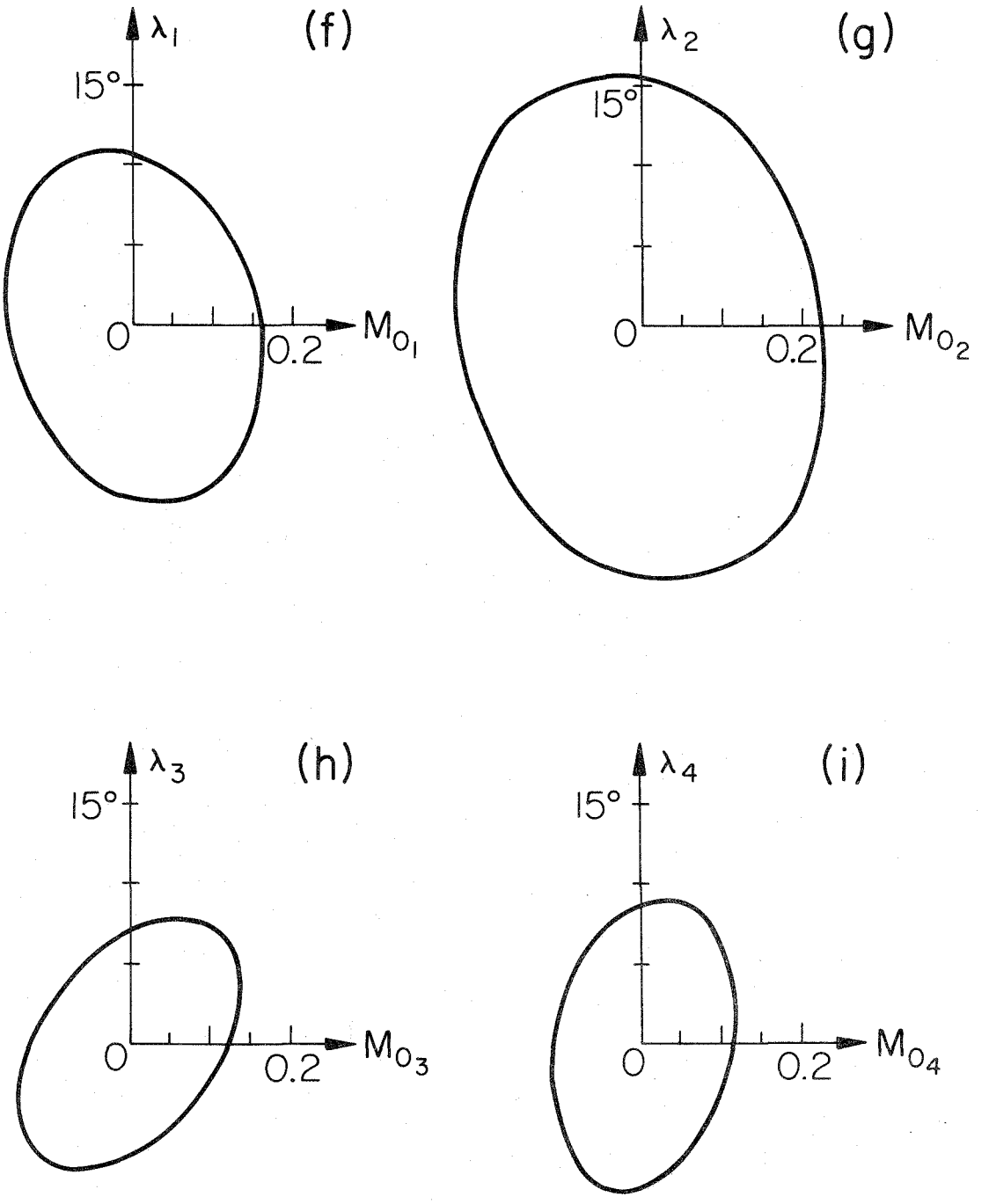

Figure 5.10 (f-i). Uncertainty ellipses for various fault model parameter pairs. Combinations of perturbations which fall inside the ellipses are not detectable by the data at the 95% confidence level. Moments are given in units of 10^{26} dyne-cm; angles are expressed in degrees.

uncertainty of one variable is not dependent on the uncertainty of the other variable. For coefficient values less than 1.0, the coupling increases with decreasing values. Figures 5.10a-c show how the coupling between the individual sources decreases with increasing distance between the sources. We see that there is strong coupling between M_{o_1} and M_{o_2} (MCVC=.30) but very little coupling between M_{o_1} and M_{o_4} (MCVC=.85). In part a of the figure, we see that the coupling is in a positive sense between M_{o_1} and M_{o_2}, i.e., an increase in one moment is traded-off with an increase in the other. Between M_{o_1} and M_{o_3}, the coupling is in the opposite sense, and between M_{o_1} and M_{o_4} the coupling that exists is in a positive direction. Figures 5.10d-e show that adjacent slip angles are slightly coupled, but much less so than their respective moment values. The MCVC for the λ_1-λ_2 pair is .75. As the distance increases between sources, the relative coupling between the slip angles of the sources decreases rapidly. Figures 5.10f-i show how the moment and slip angle for the individual sources are related. These results are somewhat surprising in that the slip angle and moment for individual sources are almost completely decoupled. The MCVCs for these parameter pairs range from .90 to .95.

In these figures, we observe that the maximum coupled

uncertainty a particular variable can acquire is constant from comparison to comparison. This uncertainty is the standard error for that variable. Mathews and Walker (1964) show that this standard error is given by

$$\varepsilon_i = \sqrt{Q_{ii}^{-1}} .$$

Generalizing this expression, we can say that the values of the model parameters are known at a confidence level c when the errors are expressed as

$$\varepsilon_i = \sqrt{Q_{ii}^{-1}}\ k(c) . \qquad (5.12)$$

This is the uncertainty which we will assume for the model variables. These uncertainties at the 95% confidence level are given below:

$$\Delta M_{o_1} = 0.15 \times 10^{26} \text{ dyne-cm}$$
$$\Delta M_{o_2} = 0.21 \times 10^{26} \text{ dyne-cm}$$
$$\Delta M_{o_3} = 0.13 \times 10^{26} \text{ dyne-cm}$$
$$\Delta M_{o_4} = 0.11 \times 10^{26} \text{ dyne-cm}$$
$$\Delta\lambda_1 = 13^\circ$$
$$\Delta\lambda_2 = 18^\circ$$

$\Delta\lambda_3 = 10°$

$\Delta\lambda_4 = 9°$

$\Delta\lambda_R = 5°$

$\Delta V_R = 0.2$ km/sec.

Comparison with Static Solution. We would now like to compare the solution for the fault model of the San Fernando earthquake derived with surface data to that obtained with the static displacements. To do this, we will sum the moments of the individual static fault elements for the elements that fall within a depth range around the location of the double couple sources. We will assume that the actual static moment distribution will be bracketed by the acceptable dislocation models which gave the maximum and minimum moments. The moments for the two models are shown in Figure 5.11. We see here that for the upper 10 km of the fault system there is very good agreement in the static and dynamical solutions. The only significant difference between the two solutions is the moment in the hypocentral region. The surface wave study indicates a moment which is a factor of 2-3 times greater than that predicted by the static data. We recall from the previous chapter that the uncertainties in this area were larger than for the more shallow areas. In the surface wave study, this was not the case. The uncertainty in the hypocentral region was not

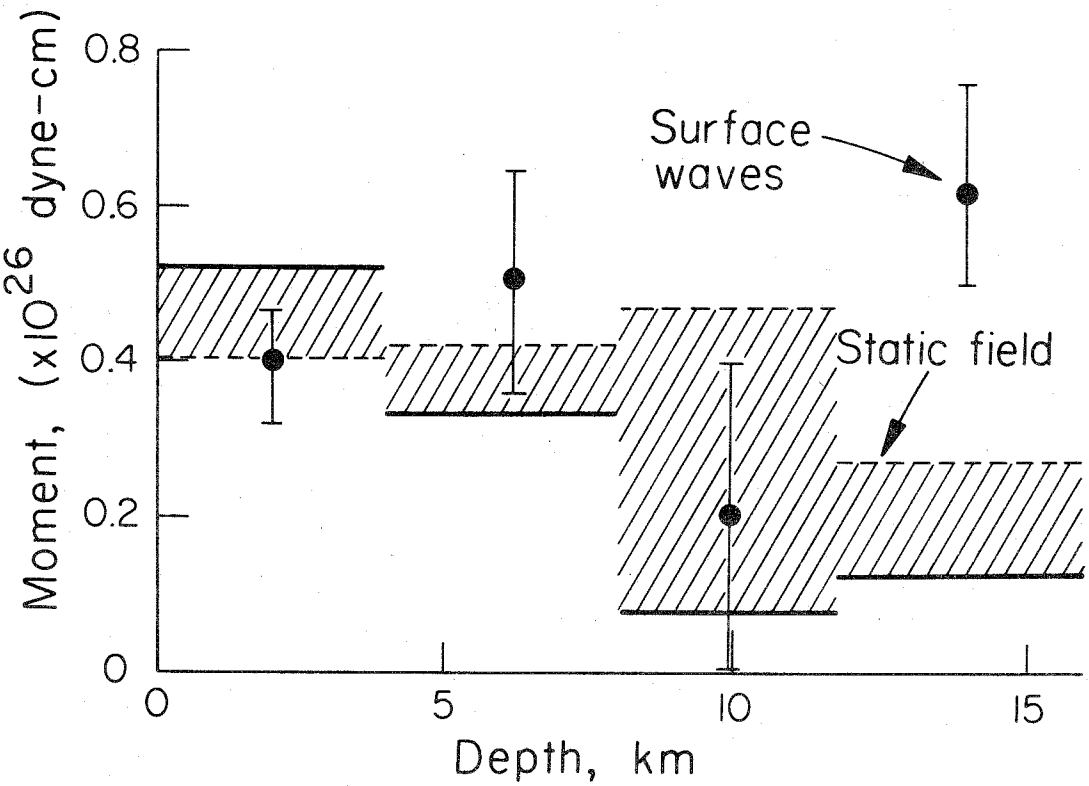

Figure 5.11. Comparison of the moment-depth distribution function found from the static study and the surface wave study. Static moments are averaged over the indicated depth ranges. The static moment distribution from the dislocation model shown in Figure 4.5 and 4.10 is shown as a solid and dashed line respectively.

substantially different from the other areas. If we assume that the fault geometry used in the last chapter is correct, then the surface wave study indicates 5.5 m of displacement over an area of 36 km^2 in the hypocentral region. This compares favorably with that derived by Hanks (1974) of 7.5 m over about the same area. This last calculation was based on still another data set of this event, namely near-field strong motion records.

5.7 Conclusions.

In this chapter, we have seen how theoretical spectral values of surface waves can be calculated numerically for an approximation to a finite source. We have shown that when non-uniform excitation of energy occurs during faulting over some depth-distributed fault surface, the resulting spectral amplitudes can be far different from that of a non-depth-distributed source at the same depth of initiation.

Rayleigh wave data were calculated from a set of 18 WWSSN stations and normalized by correcting for the various source to receiver paths. An inversion scheme was used to find the set of fault model parameters which fit the observed spectral data in a least-squares sense. The best fit solution gave a distributed moment of 1.7×10^{26} dyne-cm, and it was found that both the moment and slip angle for this event varied along the down-dip width of the fault.

The slip angle varied in such a way that the displacements became more predominantly dip slip as the dislocation propagated upward from the point of initial rupture at about 3.0 km/sec. Also indicated by the surface wave data is that the propagation proceeded in a direction 5°-10° away from the normal of the strike of the fault. The fault model solution obtained by the surface wave inversion compares very favorably with that given by the inversion of the static displacement data with the exception of the initial dislocation in the hypocentral region where the static data field gives poor resolution.

Wyss (1971) obtains an average moment from the long period surface waves at two European stations (which were not included in this data set) of 1.9×10^{26} dyne-cm. Canitez and Toksöz (1972) fit the surface wave spectra at 6 stations in the northeast and southeast geodetic azimuths with a single point source at a depth of 14 km. These authors obtain a moment of 0.75×10^{26} dyne-cm and a rake angle of 45°. Obvious reasons for obtaining different values of moment and slip angle by these authors and the present study are 1) the non-depth-distributed source gives rise to a different radiation pattern than a depth-distributed source, and 2) the azimuthal coverage of stations was more limited in the Canitez-Toksöz data set than

in the data set used here. Comparing their data set to that used here, we find that, if the spectra at the stations used in those authors' study were discretized in the same manner as in this chapter, then their data set would have only approximately 40% of the total information which constrains the model variables as was used in this study.

Finally, we feel that the technique of the hybridization of the numerical approximation of a finite fault and the least-squares inversion formalism allows the maximum derivation of information about the source from a set of corrected surface wave observations. Use of the operators associated with the inversion methods provides a powerful tool to determine a priori which data would be most beneficial in determining the source parameters and to estimate the uncertainties in the calculated model parameters and to determine the relative coupling between various parameters. It is hoped that these techniques can be extended to the inversion of other seismic data. The simplest extension would be the inversion of Rayleigh/Love spectral ratios. This type of data would yield far better results than when each is analyzed separately because of the cancellation of error inducing path effects.

BIBLIOGRAPHY

Aki, K., Generation and propagation of G waves from the Niigata earthquake of June 16, 1964, Part 2. Estimation of earthquake moment, released energy, and stress-strain drop from the G wave spectrum, *Bull. Earthquake Res. Inst., Tokyo Univ., 44*, 73-88, 1966.

Aki, K., Seismic moment and stress-drop, Paper presented at the Annual Meeting of the Seismological Society of America, Symposium on the San Fernando earthquake of February 9, 1971, Riverside, CA, March 25, 1971.

Alewine, R. W., III, and T. H. Jordan, Generalized inversion of earthquake static displacement fields, *Geophys. J. Roy. Astr. Soc., 35*, 357-361, 1973.

Alewine, R. W., III, and P. H. Jungels, Application of stochastic inversion theory and the finite-element method to zero-frequency seismology: The 1964 Alaska earthquake, submitted to *Geophys. J. Roy. Astr. Soc.*, 1973.

Alexander, S. S., Crustal structure in the western United States from multi-mode surface wave dispersion, Ph.D. thesis, California Institute of Technology, Pasadena, 229 pp., 1963.

Algermissen, S. T., Seismological investigation of the Prince William Sound earthquake and aftershocks, *Trans. Am. Geophys. Union, 45*, 633, 1964.

Algermissen, S. T., Prince William Sound, Alaska earthquake of March 28, 1964, and aftershock sequence, *Geol. Soc. Amer. Spec. Pap., 82*, 2, 1965.

Algermissen, S. T., Mechanism of the Prince William Sound earthquake, *ESSA Symposium on Earthquake Prediction*, U. S. Dept. of Commerce, Environmental Science Services Admin., 20-25, 1966.

Algermissen, S. T., W. A. Rinehart, R. W. Sherburne, and W. H. Dillinger, Preshocks and aftershocks, *in*, (K. B. Krauskopf, Ed.), *The Great Alaska Earthquake of 1964, Seismology and Geodesy*, U. S. National Academy of Sciences, Washington, D.C., 313-364, 1972.

Allen, C. R., G. R. Engen, T. C. Hanks, J. M. Nordquist, and W. R. Thatcher, Main shock and larger aftershocks of the San Fernando earthquake, February 9 through March 1, 1971, *U.S. Geol. Surv. Prof. Pap. 733*, 17-20, 1971.

Allen, C. R., T. C. Hanks, and J. Whitcomb, San Fernando earthquake: Seismological studies and their implications, *Calif. Div. Mines and Geol. Bull. 196*, in press, 1973.

Archambeau, C. B., Elastodynamic source theory, Ph.D. thesis, California Institute of Technology, Pasadena, 1964.

Archambeau, C. B., General theory of elastodynamic source fields, *Rev. Geophys., 6*, 241-288, 1968.

Archambeau, C. B., The theory of stress wave propagation from explosions in prestressed media, *Geophys. J. Roy. Astr. Soc., 29*, 329-366, 1972.

Archambeau, C. B., and C. Sammis, Seismic radiation from explosions in prestressed media and the measurement of tectonic stress in the earth, *Rev. Geophys., 8*, 473-499, 1970.

Asada, T., and S. Asano, Crustal structures of Honshu, Japan, *in, The Crust and Upper Mantle of the Japanese Area, Part 1- Geophysics*, Earthquake Res. Inst., Tokyo Univ., 45 pp., 1972.

Backus, G. E., and J. F. Gilbert, Numerical applications of a formalism for geophysical inverse problems, *Geophys. J. Roy. Astr. Soc., 13*, 247-276, 1967.

Backus, G. E., and J. F. Gilbert, The resolving power of gross earth data, *Geophys. J. Roy. Astr. Soc., 16*, 169-205, 1968.

Backus, G. E., and J. F. Gilbert, Constructing P-velocity models to fit restricted sets of travel-time data, *Bull. Seismol. Soc. Am., 59*, 1407-1414, 1969.

Backus, G. E., and J. F. Gilbert, Uniqueness in the inversion of inaccurate gross earth data, *Phil. Trans. Roy. Soc. London, Ser. A., 226*, 123-132, 1970.

Bamford, S. A. D., Applications of simulated data studies to crustal refraction seismology, *Bull. Seismol. Soc. Am.*, *61*, 1013-1031, 1971.

Barnes, D. F., Gravity changes during the Alaska earthquake, *J. Geophys. Res.*, *71*, 451-456, 1966.

Båth, M., Crustal structure of Iceland, *J. Geophys. Res.*, *65*, 1793-1805, 1960.

Benioff, H., Orogenesis and deep crustal structure: additional evidence from seismology, *Geol. Soc. Amer. Bull.*, *65*, 385-400, 1954.

Ben-Menahem, A., Radiation of seismic surface waves from finite moving sources, *Bull. Seismol. Soc. Am.*, *51*, 401-435, 1961.

Ben-Menahem, A., Observed attenuation and Q values of seismic surface waves in the upper mantle, *J. Geophys. Res.*, *70*, 4641-4651, 1965.

Ben-Menahem, A., and A. Gillon, Crustal deforamtion by earthquakes and explosions, *Bull. Seismol. Soc. Am.*, *60*, 193-215, 1970.

Ben-Menahem, A., and D. G. Harkrider, Radiation patterns of seismic surface waves from buried dipolar point sources in a flat stratified earth, *J. Geophys. Res.*, *69*, 2605-2620, 1964.

Ben-Menahem, A., M. Roseman, and M. Israel, Source mechanism of the Alaskan earthquake of 1964 from amplitudes of free oscillations and surface waves, *Phy. Earth and Planet. Interiors*, *5*, 1-29, 1972.

Ben-Menahem, A., and S. J. Singh, Multipolar elastic fields in a layered half-space, *Bull. Seismol. Soc. Am.*, *58*, 1519-1572, 1968a.

Ben-Menahem, A., and S. J. Singh, Eigenvector expansions of Green's dyads with application to geophysical theory, *Geophys. J. Roy. Astr. Soc.*, *16*, 417-452, 1968b.

Ben-Menahem, A., and S. J. Singh, Deformation of a spherical earth by finite dislocations, *in*, (L. Mansinha et al., Ed.), *Earthquake Displacement Fields and the Rotation of the Earth*, 39-42, 1970.

Ben-Menahem, A., S. J. Singh, and F. Solomon, Deformation of a spherical earth model by internal dislocations, *Bull. Seismol. Soc. Am.*, *59*, 813-853, 1969.

Ben-Menahem, A., S. J. Singh, and F. Solomon, Deformation of a homogenous earth model by finite dislocations, *Rev. Geophys.*, *8*, 591-632, 1970.

Berg, E., The Alaska earthquake, its location and seismic setting, *in*, *Science in Alaska, 1964: Proc. 15th Alaskan Sci. Conf., College, Alaska*, Amer. Assoc. Advanc. Sci., 218-232, 1965.

Biehler, S., Geophysical study of the Salton Trough of Southern California, Ph.D. thesis, California Institute of Technology, Pasadena, 1964.

Blundell, D. J., and R. Parks, A study of the crustal structure beneath the Irish Sea, *Geophys. J. Roy. Astr. Soc.*, *17*, 45-62, 1969.

Braslau, D., and P. Lieber, Three dimensional fields due to a Volterra dislocation imbedded in a layered half-space: Analytical representation of a seismic mechanism, *Bull. Seismol. Soc. Am.*, *58*, 613-628, 1968.

Brune, J. N., Surface waves and crustal structure, *in*, (P. J. Hart, Ed.), *The Earth's Crust and Upper Mantle, Geophysical Monograph 13*, American Geophysical Union, 230-242, 1969.

Brune, J. N., and C. R. Allen, A low stress-drop, low magnitude earthquake with surface faulting: the Imperial, California, earthquake of March 4, 1966, *Bull. Seismol. Soc. Am.*, *57*, 501-514, 1967.

Brune, J. N., and J. Dorman, Seismic waves and earth structure in the Canadian shield, *Bull. Seismol. Soc. Am.*, *53*, 167-210, 1963.

Bucher, R. L., and R. B. Smith, Crustal structure of the eastern Basin and Range Province and the northern Colorado Plateau from phase velocities of Rayleigh waves, *in*, (J. G. Heacock, Ed.), *The Structure and Physical Properties of the Earth's Crust, Geophys. Monograph 14*, American Geophysical Union, 59-70, 1971.

Burford, R. O., R. O. Castle, J. P. Kinoshita, S. H. Kirby, R. T. Ruthven, and J. C. Savage, Preliminary measurements of tectonic movement, *U. S. Geol. Surv. Prof. Pap. 733*, 80-85, 1971.

Burridge, R., and L. Knopoff, Body force equivalents for seismic dislocations, *Bull. Seismol. Soc. Am., 54*, 1875-1888, 1964.

Canitez, N., and M. N. Toksöz, Focal mechanism and source depth of earthquakes from body and surface wave data, *Bull. Seismol. Soc. Am., 61*, 1369-1379, 1971.

Canitez, N., and M. N. Toksöz, Static and dynamic study of earthquake source mechanism: San Fernando earthquake, *J. Geophys. Res., 77*, 2583-2594, 1972.

Chapman, R. H., Gravity base station network, *Calif. Div. Mines and Geol. Special Report 90*, 49pp., 1966.

Chinnery, M. A., The deformation of the ground around surface faults, *Bull. Seismol. Soc. Am., 51*, 355-372, 1961.

Chinnery, M. A., The stress changes that accompany strike-slip faulting, *Bull. Seismol. Soc. Am., 53*, 921-932, 1963.

Chinnery, M. A., The vertical displacements associated with transcurrent faulting, *J. Geophys. Res., 70*, 4627-4632, 1965.

Chinnery, M. A., Theoretical fault models, *Pub. Dominion Obs., Ottawa, 17*, 211-223, 1969.

Chinnery, M. A., and D. B. Jovanovich, Effect of earth layering on earthquake displacement fields, *Bull. Seismol. Soc. Am., 62*, 1629-1639, 1972.

Chinnery, M. A., and J. A. Petrak, The dislocation fault model with a variable discontinuity, *Tectonophysics*, *5*, 513-529, 1968.

Cisternas, A., Crustal structure of the Andes from Rayleigh wave dispersion, *Bull. Seismol. Soc. Am.*, *51*, 381-388, 1961.

Cohen, T. J., Source-depth determinations using spectral, pseudo-autocorrelation, and cepstral analysis, *Geophys. J. Roy. Astr. Soc.*, *20*, 223-231, 1970.

Corbató, C. E., Bouguer gravity anomalies of the San Fernando Valley, California, *California Univ. Pubs. Geol. Sci.*, *46*, 1-32, 1963.

Dillinger, W., and A. F. Espinosa, Preliminary fault-plane solution for the San Fernando earthquake, *U.S. Geol. Surv. Prof. Pap. 733*, 142-149, 1971.

Dorman, J., M. Ewing, and J. Oliver, Study of shear velocity distribution in the upper mantle by mantle Rayleigh waves, *Bull. Seismol. Soc. Am.*, *50*, 87-115, 1960.

Ellingwood, C. F., and R. O. Williamson, Control resurveys and the San Fernando earthquake (a preliminary analysis), *in*, *Papers from the 1971 ASP-ACSM Fall Conv.*, Amer. Cong. on Surveying and Mapping, Washington, D. C., 148-178, 1971.

Ewing, J., Seismic model of the Atlantic Ocean, *in*, (P. J. Hart, Ed.), *The Earth's Crust and Upper Mantle, Geophysical Monograph 13*, American Geophysical Union, 220-225, 1969.

Ewing, J., M. Ewing, and R. Leyden, Seismic profiler study of the Blake Plateau, *Bull. Am. Assoc. Petrol. Geol.*, *50*, 1948-1971, 1966.

Ewing, M., R. Houtz, and J. Ewing, South Pacific sediment distribution, *J. Geophys. Res.*, *74*, 2477-2493, 1969.

Ewing, M., and F. Press, Determination of crustal structure from phase velocity of Rayleigh waves, 3, The United States, *Bull. Geol. Soc. Amer.*, *70*, 229-244, 1959.

Fisher, R. L., and R. W. Raitt, Topography and structure of the Peru-Chile trench, *Deep-Sea Res.*, *9*, 423-443, 1962.

Fitch, T. J., and C. H. Scholtz, Mechanism of underthrusting in southwest Japan: a model of covergent plate interaction, *J. Geophys. Res.*, *76*, 7260-7292, 1971.

Flinn, E. A., T. J. Cohen, and D. W. McCowan, Detection and analysis of multiple seismic events, *Bull. Sesimol. Soc. Am.*, *63*, 1921-1936, 1973.

Franklin, J. N., Well-posed stochastic extensions of ill-posed linear problems, *J. Math. Anal. Appl.*, *31*, 682-716, 1970.

Grantz, A., G. Plafker, and J. E. Case, Tectonics of Alaska's Good Friday earthquake, *Program, 1964 Ann. Meeting, Geol. Soc. Amer.*, *77*, 1964a.

Grantz, A., G. Plafker, and R. Kachadoorian, Alaska's Good Friday earthquake, March 27, 1964, *U.S. Geol. Surv. Circ. 491*, 1964b.

Gregersen, S., Surface wave dispersion and crustal structure in Greenland, *Geophys. J. Roy. Astr. Soc.*, *22*, 29-39, 1970.

Gutenberg, B., Travel times of principal P and S phases over small distances in southern California, *Bull. Seismol. Soc. Am.*, *34*, 13-32, 1944.

Gutenberg, B., Amplitudes of surface waves and magnitudes of shallow earthquakes, *Bull. Seismol. Soc. Am.*, *35*, 3-12, 1945.

Gutenberg, B., and C. F. Richter, On seismic waves (third paper), *Ger. Beitr. zur Geophys.*, *47*, 73-131, 1936.

Hagiwara, T., A note on the theory of the electromagnetic seismograph, *Bull. Earthquake Res. Inst., Tokyo Univ.*, *36*, 139-164, 1958.

Hagiwara, Y., and H. Tajima, Secular changes in gravity, *in, Publications for the 50th anniversary of the great Kanto earthquake, 1923*, Earthquake Res. Inst., Tokyo, Univ., 311-327, 1973.

Hales, A. L., and T. Asada, Crustal structures in coastal Alaska, *in*, (J. S. Steinhart and T. J. Smith, Ed.), *The Earth beneath the Continents, Geophysical Monograph 10*, 420-432, 1966.

Hanks, T. C., A contribution to the determination and interpretation of seismic source parameters, Ph.D. thesis, California Institute of Technology, Pasadena, 184 pp., 1972.

Hanks, T. C., The faulting mechanism of the San Fernando earthquake, submitted to *J. Geophys. Res.*, 1974.

Hanks, T. C., T. H. Jordan, and J. B. Minster, Precise locations of aftershocks of the San Fernando earthquake, 2300 (GMT) February 10 - 1700 February 11, 1971, *U.S. Geol. Surv. Prof. Pap. 733*, 21-23, 1971.

Harada, Y., Geodetic work in Japan with special reference to the Matsushiro earthquakes, *Trans. Amer. Geophys. Union, 50*, 390-391, 1968.

Harding, S. T., and S. T. Algermissen, Focal mechanism of the Prince William Sound, Alaska, earthquake of March 28, 1964, *Bull. Seismol. Soc. Am., 59*, 799-811, 1969.

Harkrider, D. G., Surface waves in multilayered media I. Rayleigh and Love waves from buried sources in a multilayered elastic half-space, *Bull. Seismol. Soc. Am., 54*, 627-679, 1964.

Harkrider, D. G., Surface waves in multilayered elastic media. Part II. Higher mode spectra and spectral ratios from point sources in plane-layered earth models, *Bull. Seismol. Soc. Am., 60*, 1937-1987, 1970.

Harkrider, D. G., and D. L. Anderson, Surface wave energy from point sources in plane-layered earth models, *J. Geophys. Res., 71*, 2967-2980, 1966.

Harkrider, D. G., A. Hales, and F. Press, On detecting soft layers in the mantle with Rayleigh waves, *Bull. Seismol. Soc. Am., 53*, 539-548, 1963.

Harrison, J. C., and C. E. Corbato, The Mt. Wilson calibration range--new geodetic measurements in the western United States and some submarine gravity measurements in the northeastern Pacific Ocean, *Trans. Amer. Geophys. Union, 46,* 212-214, 1965.

Haskell, N. A., The dispersion of surface waves in multilayered media, *Bull. Seismol. Soc. Am., 43,* 17-34, 1953.

Hastie, L. M., and J. C. Savage, A dislocation model for the 1964 Alaska earthquake, *Bull. Seismol. Soc. Am., 60,* 1389-1392, 1970.

Heezen, B. C., Inland and marginal seas, *in,* (A. R. Ritsema, Ed.), *The Upper Mantle, Tectonophysics, 13,* 293-308, 1972.

Honda, H., and T. Miura, On the strain produced in a semi-infinite elastic solid by statical surface forces, with some applications to seismology, *Geophys. Mag., 9,* 61-81, 1935.

Hunt, T. M., Gravity changes associated with the 1968 Inanguhua earthquake, *New Zealand J. Geol. and Geophys., 13,* 1050-1051, 1970.

Isacks, B., J. Oliver, and L. R. Sykes, Seismology and the new global tectonics, *J. Geophys. Res., 73,* 5855-5899, 1968.

James, D. E., Andean crustal and upper mantle structure, *J. Geophys. Res., 76,* 3246-3271, 1971.

Jenkins, W. M., *Matrix and Digital Computer Methods in Structural Analysis,* McGraw-Hill, 1969.

Jordan, T. H., Estimation of the radial variation of seismic velocities and density in the earth, Ph.D. thesis, California Institute of Technology, Pasadena, 199 pp., 1972.

Jordan, T. H., and J. B. Minster, Applications of a stochastic inverse to the geophysical inverse problem, *in,* (L. Colin, Ed.), *The Mathematics of Profile Inversion,* Marcel Dekker, Inc., 1972.

Jungels, P. H., Models of tectonic processes associated with earthquakes, Ph.D. thesis, California Institute of Technology, Pasadena, 198 pp., 1973.

Jungels, P. H., and G. A. Frazier, Finite element analysis of the residual displacements for an earthquake rupture: Source parameters for the San Fernando earthquake, *J. Geophys. Res.*, *78*, 5062-5083, 1973.

Kamb, B., L. T. Silver, M. Abrams, B. Carter, T. Jordan, and B. Minster, Pattern of faulting and nature of fault movement in the San Fernando earthquake, *U.S. Geol. Surv. Prof. Pap. 733*, 41-54, 1971.

Kaminuma, K., The crust and upper mantle structure in Japan, Part 2, Crustal structure in Japan from phase velocity of Rayleigh waves, *Bull. Earthquake Res. Inst., Tokyo Univ.*, *44*, 495-510, 1966.

Kanamori, H., The Alaska earthquake of 1964: Radiation of long-period surface waves and source mechanism, *J. Geophys. Res.*, *75*, 5029-5040, 1970.

Kanamori, H., Velocity and Q of Mantle waves, *Phys. Earth Planet. Interiors*, *2*, 259-275, 1970.

Kasahara, K., The nature of seismic origins as inferred from seismological and geodetic observations, I, *Bull. Earthquake Res. Inst., Tokyo Univ.*, *35*, 473-532, 1957.

Kasahara, K., Physical conditions of earthquake faults, II, (A model of strike-slip faults with various dip angles), *Bull. Earthquake Res. Inst., Tokyo Univ.*, *37*, 39-51, 1959.

Kasahara, K., The source region of the Matsushiro swarm earthquakes, *Bull. Earthquake Res. Inst., Tokyo Univ.*, *48*, 581-602, 1970.

Katz, S., and M. Ewing, Seismic refraction measurements in the Atlantic Ocean, Part VII, Atlantic Ocean Basin west of Bermuda, *Bull. Geol. Soc. Amer.*, *67*, 475-487, 1956.

Knopoff, L., Energy release in earthquakes, *Geophys. J. Roy. Astr. Soc.*, *1*, 44-52, 1958.

Kovach, R. L., and F. Press, Rayleigh wave dispersion and crustal structure in the eastern Pacific and Indian Oceans, *Geophys. J. Roy. Astr. Soc., 4,* 202-216, 1961.

Kurita, T., Inferences of a layered structure from S wave spectra, Part 2. Study of the structure in selected regions of Japan, *J. Phys. Earth, 19,* 111-130, 1971.

Lahr, J. C., M. Wyss, and J. A. Hileman, Repeated surveys of small scale figures established across surface fault ruptures following the earthquake, *U.S. Geol. Surv. Prof. Pap. 733,* 86-88, 1971.

Lambert, D. G., E. A. Flinn, and C. B. Archambeau, A comparitave study of the elastic wave radiation from earthquakes and underground explosions, *Geophys. J. Roy. Astr. Soc., 29,* 403-432, 1972.

Latham, G., and A. Nowroozi, Waves, weather and ocean bottom microseisms, *J. Geophys. Res., 73,* 3945-3956, 1968.

Linville, A. F., Rayleigh wave multipath analysis using a complex cepstrum technique, Special Report No. 2, Long-period array processing development, Texas Instruments Inc., Dallas, Texas, 1971.

Love, A. E. H., *A Treatise on the Mathematical Theory of Elasticity,* 4th Edition, Dover Publications, New York, 1944.

Malloy, R. J., Crustal uplift southwest of Montague Island, Alaska, *Science, 146,* 1048-1049, 1964.

Malloy, R. J., Seafloor upheaval, *Geo-Marine Technology, 1,* 22-26, 1965.

Malloy, R. J., and G. F. Merrill, Vertical crustal movement of the sea floor associated with the Prince William Sound, Alaska, earthquake, *in,* (L. E. Leipold, Ed.), *The Prince William Sound, Alaska, Earthquake of 1964 and aftershocks,* U.S. Dept. of Commerce, Envir. Sci. Serv. Admin., Pub. 10-3, II, 327-338, 1969.

Mansinha, L., and D. E. Smylie, The displacement fields of inclined faults, *Bull. Seismol. Soc. Am.*, *61*, 1433-1440, 1971.

Martin, H. C., *Introduction to Matrix Methods of Structural Analysis*, McGraw-Hill, 1966.

Maruyama, T., On the force equivalents of dynamical elastic dislocations with reference to the earthquake source mechanism, *Bull. Earthquake Res. Inst., Tokyo Univ.*, *41*, 467-486, 1963.

Maruyama, T., Statical elastic dislocations in an infinite and semi-infinite medium, *Bull. Earthquake Res. Inst., Tokyo Univ.*, *42*, 289-368, 1964.

Mathews, J., and R. L. Walker, *Mathematical Methods of Physics*, W. A. Benjamin, Inc., 1964.

Matumoto, T., and R. A. Page, Microaftershocks following the Alaska earthquake of March 28, 1964: Determination of hypocenters and crustal velocities in the Kenai Peninsula-Prince William Sound area, *in*, (L. E. Leipold, Ed.), *The Prince William Sound, Alaska, Earthquake of 1964 and Aftershocks*, U.S. Dept. of Commerce, Envir. Sci. Serv. Admin., Pub. 10-3, II, 157-183, 1969.

McEvilly, T. V., Central U. S. crust-upper mantle structure from Love and Rayleigh wave phase velocity inversion, *Bull. Seismol. Soc. Am.*, *54*, 1997-2015, 1964.

McGarr, A., Amplitude variations of Rayleigh waves--propagation across a continental margin, *Bull. Seismol. Soc. Am.*, *59*, 1281-1305, 1969.

McGarr, A., and L. E. Alsop, Transmission and reflection of Rayleigh waves at vertical boundaries, *J. Geophys. Res.*, *72*, 2169-2180, 1967.

McGinley, J. R., A comparison of observed permanent tilts and strains with those calculated from displacement dislocations in elastic earth models, Ph.D. thesis, California Institute of Technology, Pasadena, 290 pp., 1969.

Mikumo, T., A study on crustal structure in Japan by the use of seismic and gravity data, *Bull. Earthquake Res. Inst., Tokyo Univ., 44*, 965-1007, 1966.

Mikumo, T., Faulting process of the San Fernando earthquake of February 9, 1971, inferred from static and dynamic near-field displacements, *Bull. Seismol. Soc. Am., 63*, 249-269, 1973.

Mindlin, R. D., Force at a point in the interior of a semi-infinite solid, *Physics, 7*, 195-202, 1936.

Mindlin, R. D., and D. H. Cheng, Nuclei of strain in the semi-infinite solid, *J. Appl. Physics, 21*, 926-930, 1950.

Minster, J. B., Elastodynamics of Failure in a Continuum, Ph.D. thesis, California Institute of Technology, Pasadena, 530 pp., 1974.

Minster, J. B., T. H. Jordan, P. Molnar, and E. Haines, Numerical modeling of instantaneous plate tectonics, submitted to *Geophys. J. Roy. Astr. Soc.*, 1974.

Mitchell, B. J., Radiation and attenuation of Rayleigh waves from the Southeastern Missouri earthquake of October 21, 1965, *J. Geophys. Res., 78*, 886-899, 1973.

Mitchell, B. J., and M. Landisman, Electromagnetic seismograph constants by least-squares inversion, *Bull. Seismol. Soc. Am., 59*, 1335-1348, 1969.

Nason, R. D., Instrumental monitoring of postearthquake fault movements, *U.S. Geol. Surv. Prof. Pap. 733*, 89-90, 1971.

Noble, B., *Applied Linear Algebra*, Prentice-Hall, Inc., Englewood Cliffs, N.J., 1969.

Nuttli, O. W., Seismic wave attenuation and magnitude relations for eastern North America, *J. Geophys. Res., 78*, 876-885, 1973.

Oakeshott, G. B., Geology and mineral deposits of the San Fernando Quadrangle, Los Angeles County, California, *Calif. Div. Mines and Geol. Bull. 172*, 147 pp., 1958.

Officer, C. B., M. Ewing, and P. Wuenshel, Seismic refraction measurements in the Atlantic Ocean, Part IV, Bermuda, Bermuda rise and Nares Basin, *Bull. Geol. Soc. Amer., 63*, 777-808, 1952.

Oliver, H. W., S. L. Robbins, R. B. Grannell, R. W. Alewine, and S. Biehler, Surface and subsurface movements determined by remeasuring gravity, *Calif. Div. Mines and Geol. Bull. 196*, Chapt. 10, in press, 1973.

Palmer, D. F., and T. L. Henyey, San Fernando earthquake of 9 February 1971: Pattern of faulting, *Science, 172*, 712-715, 1971.

Parkin, E. J., Horizontal displacements, pt. 2 of *Alaskan surveys to determine crustal movement*, U.S. Coast and Geodetic Surv., 11 pp., 1966.

Payo, G., Crustal phases across the Iberian Peninsula region, *Ann. Geofis., 17*, 523-532, 1964.

Payo, G., Structure of the crust and upper mantle in the Iberian shield by means of a long period triangular array, *Geophys. J. Roy. Astr. Soc., 20*, 493-508, 1970.

Piermattei, R., and A. Nowroozi, Dispersion of Rayleigh waves for purely oceanic paths in the Pacific, *Bull. Seismol. Soc. Am., 59*, 1905-1926, 1969.

Plafker, G., Tectonic deformation associated with the 1964 Alaska earthquake, *Science, 148*, 1675-1687, 1965.

Plafker, G., Surface faults on Montague Island associated with the 1964 Alaska earthquake, *U.S. Geol. Surv. Prof. Pap. 543-G*, 42 pp., 1967.

Plafker, G., Tectonics of the March 27, Alaska earthquake, *U.S. Geol. Surv. Prof. Pap. 543-I*, 74 pp., 1969.

Plafker, G., Alaskan earthquake of 1964 and Chilean earthquake of 1960: Implications for arc tectonics, *J. Geophys. Res., 77*, 901-925, 1972.

Plafker, G., and M. Rubin, Vertical tectonic displacements in South-Central Alaska during and prior to the great 1964 earthquake, *J. Geosci., Osaka City Univ., 10*, 1-14, 1967.

Pope, A. J., Strain analysis of horizontal crustal movements in Alaska based on triangulation surveys before and after the earthquake, *in*, (K. B. Krauskopf, Ed.), *The Great Alaska Earthquake of 1964, Seismology and Geodesy*, U.S. National Academy of Sciences, Washington, D.C., 435-447, 1972.

Press, F., Displacements, strains, and tilts at teleseismic distances, *J. Geophys. Res., 70*, 2395-2412, 1965.

Press, F., Earth models obtained by Monte Carlo inversion, *J. Geophys. Res., 73*, 5223-5234, 1968.

Press, F., Zero frequency seismology, *in*, (P. J. Hart, Ed.), *The Earth's Crust and Upper Mantle, Geophysical Monograph 13*, American Geophysical Union, 171-173, 1969.

Press, F., Earth models consistent with geophysical data, *Phys. Earth and Planet. Interiors, 3*, 3-22, 1970.

Press, F., The earth's interior as inferred from a family of models, *in*, (E. C. Robertson, Ed.), *The Nature of the Solid Earth*, McGraw-Hill, 1972.

Press, F., and D. Jackson, Alaskan earthquake, 27 March 1964: Vertical extent of faulting and elastic strain energy release, *Science, 147*, 867-868, 1965.

Proctor, R. J., R. Crook, M. H. McKeown, and R. L. Moresco, Relation of known faults to surface ruptures, 1971 San Fernando earthquake, southern California, *Geol. Soc. Amer. Bull., 83*, 1601-1618, 1972.

Przemieniecki, J. S., *Theory of Matrix Structural Analysis*, McGraw-Hill, 1968.

Raitt, R. W., Seismic refraction studies of the Pacific Ocean basin, Part I: Crustal thickness of the central equatorial Pacific, *Bull. Geol. Soc. Amer., 67*, 1623-1640, 1956.

Reimnitz, E., Quaternary history and sedimentation of the Copper River delta and vicinity, Ph.D. thesis, University of California, San Diego, 1966.

Rice, D. A., Gravity observations in Alaska, 1964-1965, including some repeat observations, *in*, (L. E. Leipold, Ed.), *The Prince William Sound, Alaska, Earthquake of 1964 and aftershocks*, U.S. Dept. of Commerce, Envir. Sci. Serv. Admin., Pub. 10-3, III, 5-20, 1969.

Robbins, S. L., R. B. Grannell, R. W. Alewine, S. Biehler, and H. W. Oliver, Descriptions, sketch maps, and selected pictures of 87 gravity stations reoccupied after the San Fernando earthquake of February 9, 1971, *U.S. Geol. Surv. Open File Report*, 72 pp., 1973.

Saito, M., and H. Takeuchi, Surface waves across the Pacific, *Bull. Seismol. Soc. Am.*, *56*, 1067-1091, 1966.

Santo, T. A., Division of the Pacific area into seven regions in each of which Rayleigh waves have the same group velocities, *Bull. Earthquake Res. Inst., Tokyo Univ.*, *41*, 719-741, 1963.

Sato, R., Crustal deformation due to a dislocation in a multilayered medium, *J. Phys. Earth*, *19*, 31-46, 1971.

Sato, R., Stress drop for a finite fault, *J. Phys. Earth*, *20*, 397-407, 1972.

Savage, J. C., R. O. Burford, and W. T. Kinoshita, Earth movements from geodetic measurements, *Calif. Div. Mines and Geol. Bull. 196*, in press, 1973.

Savage, J. C., and L. M. Hastie, Surface deformation associated with dip-slip faulting, *J. Geophys. Res.*, *71*, 4897-4904, 1966.

Savage, J. C., and L. M. Hastie, A dislocation model for the Fairview Peak, Nevada, earthquake, *Bull. Seismol. Soc. Am.*, *59*, 1937-1948, 1969.

Schafer, R. W., Echo removal by discrete generalized linear filtering, Ph.D. thesis, Massachusetts Institute of Technology, Cambridge, 1969.

Sezawa, K., The tilting of the surface of a semi-infinite solid due to internal nuclei of strain, *Bull. Earthquake Res. Inst., Tokyo Univ., 7*, 1-14, 1929.

Sherburne, R. W., S. T. Algermissen, and S. T. Harding, The hypocenter, origin time, and magnitude of the Prince William Sound earthquake of March 28, 1964, *in*, (L. E. Leipold, Ed.), *The Prince William Sound, Alaska, Earthquake of 1964 and Aftershocks*, U.S. Dept. of Commerce, Envir. Sci. Serv. Admin., Pub. 10-3, II, 49-70, 1969.

Shor, G., Seismic refraction studies off the coast of Alaska (1956-1957), *Bull. Seismol. Soc. Am., 42*, 37-57, 1962.

Singh, S. J., Static deformation of a multilayered half-space by internal sources, *J. Geophys. Res., 75*, 3257-3263, 1970.

Singh, S. J., Deformation of a multilayered half-space by stress dislocations and concentrated forces, *Bull. Seismol. Soc. Am., 61*, 1625-1638, 1971.

Singh, S. J., and A. Ben-Menahem, Displacements and strain fields due to faulting in a sphere, *Phys. Earth Planet. Interiors, 2*, 77-87, 1969.

Soeda, K., On the deformation produced in a semi-infinite elastic solid by an internal source of stress, *Kenshin Ziho, 13*, 263-291, 1944.

Starr, A. T., Slip in a crystal and rupture in a solid due to shear, *Cambridge Phil. Soc. Proc., 24*, 489-500, 1928.

Stauder, W., Tensional character of earthquake foci beneath the Aleutian Trench with relation to sea-floor spreading, *J. Geophys. Res., 73*, 7693-7701, 1968.

Stauder, W., and G. A. Bollinger, The focal mechanism of the Alaska earthquake of March 28, 1964, and of its aftershock sequence, *J. Geophys. Res.*, *71*, 5283-5296, 1966.

Steketee, J. A., On Volterra's dislocations in a semi-infinite elastic medium, *Can. J. Phys.*, *36*, 192-205, 1958a.

Steketee, J. A., Some geophysical applications of the elasticity theory of dislocations, *Can. J. Phys.*, *36*, 1168-1198, 1958b.

Stonley, R., The structural development of the Gulf of Alaska sedimentary province in southern Alaska, *Geol. Soc. London Quart. J.*, *123*, pt. 1, 25-57, 1966.

Sykes, L. R., Aftershock zones of great earthquakes, seismicity gaps, and earthquake prediction for Alaska and the Aleutians, *J. Geophys. Res.*, *76*, 8021-8041, 1971.

Sylvester, A. G., and D. D. Pollard, Afterslip on the Sylmar segment, *Calif. Div. Mines and Geol. Bull. 196*, in press, 1973.

Talwani, M., X. Le Pichon, and M. Ewing, Crustal structure of the mid-ocean ridges; 2. Computed model from gravity and seismic refraction data, *J. Geophys. Res.*, *70*, 341-352, 1965.

Thomson, W. T., Transmission of elastic waves through a stratified medium, *J. Appl. Phys.*, *21*, 89-93, 1950.

Tobin, D. G., and L. R. Sykes, Relationship of hypocenters of earthquakes to the geology of Alaska, *J. Geophys. Res.*, *71*, 1659-1667, 1966.

Toksöz, M. N., A. Ben-Menahem, and D. G. Harkrider, Source mechanism of the Alaska earthquake from long period seismic surface waves, *Trans. Am. Geophys. Union*, *46*, 154, 1965.

Tryggvason, E., Crustal structure of the Iceland region from dispersion of surface waves, *Bull. Seismol. Soc. Am.*, *52*, 359-388, 1962.

Tryggvason, E., Dissipation of Rayleigh wave energy, *J. Geophys. Res., 70*, 1449-1455, 1965.

Tryggvason, E., Surface deformation and crustal structure in the Myrdalsjokull area of south Iceland, *J. Geophys. Res., 78*, 2488-2497, 1973.

Tryggvason, E., and M. Bath, Upper crustal structure of Iceland, *J. Geophys. Res., 66*, 1913-1925, 1961.

Tsai, Y., Use of LP surface waves for source characterization, *Geophys. J. Roy. Astr. Soc., 31*, 111-130, 1972.

Tsai, Y., and K. Aki, Simultaneous determination of the seismic moment and attenuation of seismic surface waves, *Bull. Seismol. Soc. Am., 59*, 275-287, 1969.

Tsai, Y., and K. Aki, Precise focal depth determination from amplitude spectra of surface waves, *J. Geophys. Res., 75*, 5729-5743, 1970.

Tsai, Y., and K. Aki, Amplitude spectra of surface waves from small earthquakes and underground nuclear explosions, *J. Geophys. Res., 76*, 3940-3952, 1971.

Tsoboi, C., A. Jitsuakwa, H. Tazima, and A. Okada, Gravity survey along the line of precise levels throughout Japan by means of a Worden gravimeter, *Bull. Earthquake Res. Inst., Tokyo Univ., Suppl. Vol. IV, Part 1*, 1-45, 1953.

Tsubokawa, I., A. Okada, H. Tajima, I. Murata, K. Nagasawa, S. Izutuya, and Y. Ito, Leveling resurvey associated with the area of the Matsushiro earthquake swarms, *Bull. Earthquake Res. Inst., Tokyo Univ., 45*, 265-288, 1967.

Turnbull, L. S., D. F. Sun, and S. S. Alexander, Determination of seismic source parameters for several earthquakes using frequency dependent Rayleigh and Love wave radiation patterns, *Trans. Amer. Geophys. Union, 54*, 1133, 1973.

U.S. Geological Survey Staff, Surface faulting, *U.S. Geol. Surv. Prof. Pap. 733*, 55-76, 1971.

Volterra, V., Sur l'equilibre des corps elastiques multiplement connexes, *Ann. Sci. École Norm. Superieure, Paris, 24*, 401-517, 1907.

von Hake, C., and W. K. Cloud, *United States Earthquakes, 1964*, U.S. Dept. of Commerce, Envir. Sci. Serv. Admin., Coast and Geodetic Surv., Washington, D.C., 91 pp., 1966.

von Huene, R. E., R. J. Malloy, G. G. Shor, and P. St. Amand, Geologic structures in the aftershock region of the 1964 Alaskan earthquake, *J. Geophys. Res., 72*, 3649-3660, 1967.

Vvedenshaya, A. V., The determination of displacement fields by means of dislocation theory, *Bull. Acad. Sci. USSR, Geophys. Ser. 3, English Transl.*, 277-284, 1956.

Vvedenskaya, A. V., Displacements in the surface of a fracture, accompanied by slip, *Bull. Acad. Sci. USSR, Geophys. Ser. 2, English Transl.*, 102-105, 1958.

Wason, H. R., and S. J. Singh, Static deformation of a multilayered sphere by internal sources, *Geophys. J. Roy. Astr. Soc., 27*, 1-14, 1972.

Wentworth, C., and R. Yerkes, Geological setting and larger aftershocks of the San Fernando area, California, *U.S. Geol. Surv. Prof. Pap. 733*, 6-16, 1971.

Wesson, R. L., W. H. K. Lee, and J. F. Gibbs, Aftershocks of the earthquake, *U.S. Geol. Surv. Prof. Pap. 733*, 24-29, 1971.

Wesson, R. L., and D. H. Wilson, Faulting in the San Fernando earthquake of February 9, 1971, *Trans. Amer. Geophys. Union, 53*, 449, 1972.

Whipple, F. J. W., On the theory of the strain in an elastic solid bounded by a plane where there is a nucleus of strain at an internal point, and on the relation of the theory to seismology, *Mon. Not. Roy. Astr. Soc., Geophys. Suppl., 3*, 380-388, 1936.

Whitcomb, J., Fault plane solution of the February 9, 1971, San Fernando earthquake and some aftershocks, *U.S. Geol. Surv. Prof. Pap. 733*, 30-32, 1971.

Whitcomb, J. H., The 1971 San Fernando earthquake series focal mechanism and tectonics, Part II, Ph.D. thesis, California Institute of Technology, Pasadena, 1973.

Whitcomb, J. H., C. R. Allen, J. D. Garmany, and J. A. Hileman, San Fernando earthquake series, 1971: Focal mechanisms and tectonics, *Rev. Geophys., 11*, 693-730, 1973.

Whitten, C. A., Crustal movements associated with the Alaskan earthquake, *Trans. Amer. Geophys. Union, 45*, 633, 1964.

Whitten, C. A., Cartographic and geodetic effects of the Alaskan earthquake, *Geol. Soc. Amer. Spec. Pap., 82*, 822, 1965.

Wiggins, R. A., The general linear inverse problem: Implication of surface waves and free oscillations for earth structure, *Rev. Geophys., 10*, 251-285, 1972.

Wood, H. O., and C. Richter, A second study of blasting in southern California, *Bull. Seismol. Soc. Am., 23*, 95-110, 1933.

Wu, F. T., Parkfield earthquake of June 28, 1966: Magnitude and source mechanism, *Bull. Seismol. Soc. Am., 58*, 689-709, 1968.

Wyss, M., Preliminary source parameter determination of the San Fernando earthquake, *U.S. Geol. Surv. Prof. Pap. 733*, 38-40, 1971.

Wyss, M., and J. N. Brune, The Alaska earthquake of 28 March 1964: A complex multiple rupture, *Bull. Seismol. Soc. Am., 57*, 1017-1023, 1967.

Wyss, M., and T. C. Hanks, The source parameters of the San Fernando earthquake inferred from teleseismic body waves, *Bull. Seismol. Soc. Am., 62*, 591-602, 1972.

Yamakawa, N., On the strain produced in a semi-infinite elastic solid by an interior source of stress, *Zisin, 8,* 84-98, 1955.

Yamakawa, N., Stress fields in focal regions, *J. Phys. Earth, 19,* 347-355, 1971.

Zienkiewicz, O. C., *The Finite Element Method in Engineering Science,* McGraw-Hill, 1971.

APPENDICES

Appendix 1

Strain Fields From an Inclined Fault in a Homogenous Half-Space

The static displacement field u_m at some point $Q(x_1,x_2,x_3)$ due to an arbitrary dislocation at some point P on the fault surface Σ is given by Maruyama (1964) to be

$$u_m(Q) = \iint_{\Sigma} \Delta u_k(P)\ W^m_{k\ell}\ \nu_\ell(P)\ d\Sigma\ , \qquad \text{(A1.1)}$$

where

$\Delta u_k(P)$ = dislocation components on the fault surface

$\nu_\ell(P)$ = direction cosines

$W^m_{k\ell}$ = the Green's function solution for the superposition of strain nuclei on the fault surface which satisfies the surface boundary conditions.

Maruyama (1964) gives the expressions for the Green's function solution for a homogeneous half-space. The components of the strain field given by

$$E^{(Q)}_{nm} = \frac{\partial u_m(Q)}{\partial x_n} \qquad \text{(A1.2)}$$

can be found directly from equation (A1.1) by performing a differentiation of the integrand of (A2.1) and integrating the resulting expression over the fault surface. If we consider that the dislocation is constant across the fault surface, then the strain components can be found by calculating

$$E_{nm} = \iint_{\Sigma} \Delta u_k \; W_{k\ell}^{mn} \; \nu_\ell(P) \; d\Sigma \; , \qquad \text{(A1.3)}$$

where $W_{k\ell}^{mn} = \frac{\partial}{\partial x_n} W_{k\ell}^{m}$.

In practice the expressions for the Green's function solutions are easily differentiated, but the resulting expressions are very cumbersome to integrate analytically over arbitrarily oriented fault surfaces. Numerical integration techniques, however, can be employed to obtain satisfactory solutions of the strain field components given by (A1.3). Unfortunately, these numerical integration techniques are rather slow and expensive when the calculation is carried out to the desired accuracy for problems involving a mapping of the strain field.

The second way to calculate the strain field response to a dislocation in a half-space is to analytically evaluate equation A1.1 for an arbitrarily oriented fault, then apply equation A1.2 to the result. Mansinha and

Smylie (1971) give analytic expressions for the displacement fields from an inclined fault of arbitrary orientation and depth which are the result of evaluating directly equation A1.1. Their expressions assume that the shear dislocation is constant across the fault surface and that the Lamé constants for the homogenous half-space are equal. The integration is carried out over the coordinates $P(\xi_1,\xi)$ on the dislocation surface, Σ. ξ_1 is in the direction of the strike of the plane of discontinuity and ξ is normal to this direction in the direction of dip as seen in Figure A1.1. The fault coordinate ξ may be resolved into ξ_2 and ξ_3 by the following transformation

$$\xi_2 = \xi \cos(\delta)$$
$$\xi_3 = \xi \sin(\delta) \ .$$

The choice of the direction of ξ_1 is made such that the coordinate system (ξ_1,ξ_2,ξ_3) is right-handed.

The strain field components, as calculated by differentiating these expressions, are presented below in indefinite integral form. The notation of Chinnery (1961) is adopted for evaluation of these indefinite integrals.

$$E_{nm}(Q;\xi_1,\xi)\,|| = E_{nm}(Q;+L,D) - E_{nm}(Q;+L,d) - E_{nm}(Q;-L,D) + E_{nm}(Q;-L,d) \qquad (A1.4)$$

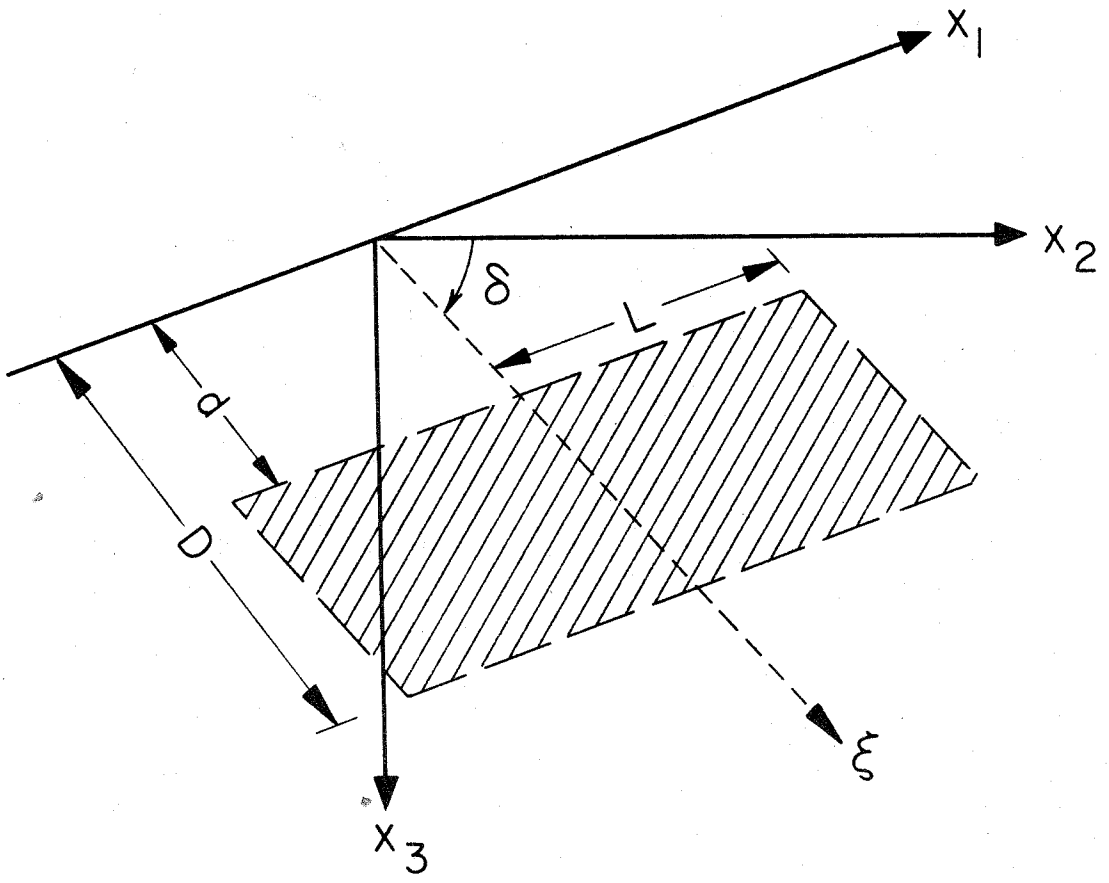

Figure A1.1. Fault model geometry and definition of symbols.

where L is the half-length of the dislocation surface, d is the distance to the top of the fault, D is the distance to the bottom of the fault as measured along the dip angle. The following definitions are used in the expressions for the components of the strain fields below:

$$\chi_1 = (x_1 - \xi_1)$$
$$\chi_2 = (x_2 - \xi_2)$$
$$\chi_3 = (x_3 - \xi_3)$$

$$R^2 = \chi_1^2 + \chi_2^2 + \chi_3^2$$
$$Q^2 = \chi_1^2 + \chi_2^2 + (x_3 + \xi_3)^2$$
$$r_2 = x_2 \sin\delta - x_3 \cos\delta$$
$$r_3 = x_2 \cos\delta + x_3 \sin\delta$$
$$q_2 = x_2 \sin\delta + x_3 \cos\delta$$
$$q_3 = -x_2 \cos\delta + x_3 \sin\delta$$
$$h^2 = q_2^2 + (q_3 + \xi)^2$$
$$K^2 = \chi_1^2 + q_2^2 .$$

STRIKE SLIP

$$E_{11} = \frac{\Delta u}{12\pi} \{ F_{111} - 6 \tan^2\delta F_{112} + 3F_{113} \}$$

$$F_{111} = \frac{2r_2[R^3+R^2(r_3-\xi) - 2R\chi_1^2 - \chi_1^2(r_3-\xi)]}{R^3[R + r_3 - \xi]^2}$$

$$- \frac{(4q_2-2x_3\cos\delta)[Q^3+Q^2(q_3+\xi)-\chi_1^2(2Q+q_3+\xi)]}{Q^3(Q+q_3+\xi)^2}$$

$$- 3\tan\delta \frac{[Q^2+Q(x_3+\xi_3)-\chi_1^2]}{Q(Q+x_3+\xi_3)} + 4q_2x_3\sin\delta \frac{[Q^2-2\chi_1^2]}{Q^5}$$

$$\frac{-4q_2q_3x_3\sin\delta}{Q^5(Q+q_3+\xi)^3} \Big\{ Q^2[2Q^2+3Q(q_3+\xi)+2(q_3+\xi)^2] - \chi_1^2[4Q^2+7Q(q_3+\xi)+3(q_3+\xi)^2] - 2Q\chi_1^3(2Q+q_3+\xi) \Big\}$$

$$F_{112} = \Big\{ \chi_1^2(q_3+\xi)\cos\delta \cdot \frac{1}{K}[(Q-K)+(K-q_2\cos\delta)(\frac{K}{Q}-1)+(q_3+\xi)\sin\delta] - (q_3+\xi)\cos\delta[(K-q_2\cos\delta)(Q-K)+(q_3+\xi)K\sin\delta] \Big\} /$$

$$\Big\{ \chi_1^2(q_3+\xi)^2\cos^2\delta+[(K-q_2\cos\delta)(Q-K)+(q_3+\xi)K\sin\delta]^2 \Big\}$$

$$F_{113} = \left\{ \frac{r_2 R(r_3-\xi) - \chi_1^2(r_3-\xi)\,\frac{r_2}{R}}{r_2^2R^2 + \chi_1^2(r_3-\xi)^2} \right\} - \left\{ \frac{q_2 Q(q_3+\xi) - \chi_1^2(q_3+\xi)\,\frac{q_2}{Q}}{q_2^2Q^2 + \chi_1^2(q_3+\xi)^2} \right\}$$

$$E_{21} = \frac{\Delta u}{12\pi}\left[F_{211} - 6\tan^2\delta F_{212} + 3F_{213}\right]$$

$$F_{211} = \frac{2R^2(R+r_3-\xi)\chi_1\sin\delta - 2r_2\chi_1[\chi_2(2R+r_3-\xi)+R^2\cos\delta]}{R^3(R+r_3-\xi)^2}$$

$$- \frac{4Q^2(Q+q_3+\xi)\chi_1\sin\delta - (4q_2-2x_3\cos\delta)\chi_1[\chi_2(2Q+q_3+\xi)-Q^2\cos\delta]}{Q^3(Q+q_3+\xi)^2}$$

$$+ \frac{3\tan\delta\ \chi_1\chi_2}{Q(Q+x_3+\xi_3)^2} + \frac{4\sin\delta x_3\chi_1[Q^2\sin\delta - 2q_2\chi_2]}{Q^5}$$

$$- \frac{4\sin\delta x_3\chi_1(2Q+q_3+\xi)(q_3\sin\delta - q_2\cos\delta) + 4\frac{q_2}{Q}q_3x_3\sin\delta\chi_1(2\chi_2 - Q\cos\delta)}{Q^3(Q+q_3+\xi)^2}$$

$$+ \frac{4q_2q_3x_3\sin\delta\chi_1(2Q+q_3+\xi)[3\chi_2(Q+q_3+\xi)+2Q(\chi_2-Q\cos\delta)]}{Q^5(Q+q_3+\xi)^3}$$

$$F_{212} = \chi_1(q_3+\xi)\cos\delta \left\{ \frac{(Q-K)}{K} (q_2\sin\delta - K\cos\delta\sin\delta) \right.$$

$$+ \frac{(K-q_2\cos\delta)}{QK} [K\chi_2 - Qq_2\sin\delta] - K\sin\delta\cos\delta$$

$$\left. + \frac{(q_3+\xi)}{K} q_2\sin^2\delta + \cos\delta\left[(K-q_2\cos\delta\frac{(Q-K)}{(q_3+\xi)} + K\sin\delta\right] \right\} /$$

$$\left\{ \chi_1^2(q_3+\xi)^2\cos^2\delta + [(K-q_2\cos\delta)(Q-K) + (q_3+\xi)K\sin\delta]^2 \right\}$$

$$F_{213} = \frac{r_2R\chi_1\cos\delta - \chi_1(r_3-\xi)\cdot[\frac{r_2}{R}\chi_2 + R\sin\delta]}{r_2^2R^2 + \chi_1^2(r_3-\xi)^2}$$

$$+ \frac{q_2Q\chi_1\cos\delta + \chi_1(q_3+\xi)[\frac{q_2}{Q}\chi_2 + Q\sin\delta]}{q_2^2Q^2 + \chi_1^2(q_3+\xi)^2}$$

$$E_{12} = \frac{\Delta u}{12\pi} [F_{121}\sin\delta + F_{122} + F_{123} + F_{124}]$$

$$F_{121} = \frac{3\tan\delta\sec\delta\chi_1}{Q(Q+x_3+\xi_3)} - \frac{\chi_1}{R(R+r_3-\xi)} - \frac{(1-3\tan^2\delta)\chi_1}{Q(Q+q_3+\xi)}$$

$$F_{122} = \frac{-2r_2^2\chi_1(2R+r_3-\xi)\sin\delta}{R^3(R+r_3-\xi)^2} - \frac{2r_2\chi_1\cos\delta}{R^3}$$

$$- \frac{2\sin\delta[2x_3(q_2\cos\delta - q_3\sin\delta) + q_2(q_2+x_2\sin\delta)]\chi_1(2Q+q_3+\xi)}{Q^3(Q+q_3+\xi)^2}$$

$$F_{123} = \frac{X_1 X_2 \tan\delta}{Q(Q+x_3+\xi_3)^2} - \frac{2\,X_1(q_2\cos\delta - q_3\sin\delta - x_3\sin^2\delta)}{Q^3}$$

$$F_{124} = -12q_2x_3X_1(X_2+q_3\cos\delta)\sin\delta$$

$$-4q_2^2q_3x_3X_1\sin^2\delta\left\{\frac{2Q(Q+q_3+\xi)-(2Q+q_3+\xi)[3(Q+q_3+\xi)+2Q]}{Q^5(Q+q_3+\xi)^3}\right\}$$

$$E_{22} = \frac{\Delta u}{12\pi}\,[F_{221}\sin\delta + F_{222} + F_{223} + F_{224}]$$

$$F_{221} = \frac{3\tan\delta\sec\delta X_2}{Q(Q+x_3+\xi_3)} - \frac{X_2+R\cos\delta}{R(R+r_3-\xi)} - \frac{(1+3\tan^2\delta)(X_2-Q\cos\delta)}{Q(Q+q_3+\xi)}$$

$$F_{222} = \frac{4r_2R(R+r_3-\xi)\sin^2\delta+2r_2(\frac{r_2}{R})\sin\delta[X_2(2R+r_3-\xi)+R^2\cos\delta]}{R^2(R+r_3-\xi)^2}$$

$$+ \frac{2R^2\sin\delta\cos\delta-2r_2X_2\cos\delta}{R^3}$$

$$- \frac{2Q(Q+q_3+\xi)\sin\delta[4x_3\sin\delta\cos\delta+3q_2\sin\delta+x_2\sin^2\delta]}{Q^2(Q+q_3+\xi)^2}$$

$$+ \frac{2\sin\delta[2x_3(q_2\cos\delta-q_3\sin\delta)+q_2(q_2+x_2\sin\delta)][X_2(2Q+q_3+\xi)+Q^2\cos\delta]}{Q^3(Q+q_3+\xi)^2}$$

$$F_{223} = \frac{[X_2^2 - Q(Q+x_3+\xi_3)]\tan\delta}{Q(Q+x_3+\xi_3)^2}$$

$$+ \frac{2\{2Q^2\sin\delta\cos\delta - X_2(q_2\cos\delta - q_3\sin\delta - x_3\sin^2\delta)\}}{Q^3}$$

$$F_{224} = \frac{4x_3\sin\delta}{Q^3}\left\{X_2\sin\delta + q_3\cos\delta\sin\delta + q_2\sin^2\delta\right.$$

$$+ \frac{3q_2X_2[X_2+q_3\cos\delta]}{Q^2} + \frac{q_2\sin\delta(2Q+q_3+\xi)[q_2\cos\delta - 2q_3\sin\delta]}{(Q+q_3+\xi)^2}$$

$$\left. - \frac{q_2^2q_3\sin\delta\{(Q+q_3+\xi)(2QX_2 - Q^2\cos\delta) + A_1\}}{Q^2(Q+q_3+\xi)^3}\right\}$$

where:

$$A_1 = (2Q+q_3+\xi)[3X_2(Q+q_3+\xi) + 2QX_2 - 2Q^2\cos\delta]$$

$$E_{13} = \frac{\Delta u}{12\pi}[F_{131}\cos\delta + F_{132} + F_{133} + F_{134}]$$

$$F_{131} = X_1\left\{\frac{1}{R(R+r_3-\xi)} + \frac{(1+3\tan^2\delta)}{Q(Q+q_3+\xi)} - \frac{3\tan\delta\sec\delta}{Q(Q+x_3+\xi_3)}\right\}$$

$$F_{132} = -2X_1\left\{\frac{r_2\sin\delta}{R^3} + \frac{(q_2+x_2\sin\delta)\sin\delta}{Q^3}\right\}$$

$$F_{133} = \frac{2r_2^2X_1(2R+r_3-\xi)\cos\delta}{R^3(R+r_3-\xi)^2}$$

$$- \frac{[4q_2x_3\sin^2\delta-2(q_2+x_2\sin\delta)(x_3+q_3\sin\delta)]\chi_1(2Q+q_3+\xi)}{Q^3(Q+q_3+\xi)^2}$$

$$F_{134} = \frac{-8q_2x_3\chi_1[(x_3+\xi_3)-q_3\sin\delta]}{Q^5}$$

$$+ \frac{4q_2^2q_3x_3\cos\delta\sin\delta\chi_1[8Q^2+9Q(q_3+\xi)+3(q_3+\xi)^2]}{Q^5(Q+q_3+\xi)^3}$$

$$E_{23} = \frac{\Delta u}{12\pi}[F_{231}\cos\delta + F_{232} + F_{233} + F_{234}]$$

$$F_{231} = \frac{(R\cos\delta+\chi_2)}{R(R+r_3-\xi)} + \frac{(1+3\tan^2\delta)(\chi_2-Q\cos\delta)}{Q(Q+q_3+\xi)} - \frac{3\tan\delta\sec\delta\chi_2}{Q(Q+x_3+\xi_3)}$$

$$F_{232} = \frac{2R^2\sin^2\delta-2r_2\chi_2\sin\delta}{R^3}$$

$$+ \frac{2\sin\delta[2Q^2\sin\delta-(q_2+x_2\sin\delta)\chi_2]}{Q^3}$$

$$F_{233} = \frac{-2R^2r_2(R+r_3-\xi)\sin\delta\cos\delta+2r_2^2\chi_2(2R+r_3-\xi)\cos\delta}{R^3(R+r_3-\xi)^2}$$

$$+ \frac{4x_3\sin^2\delta-4(x_3+q_3\sin\delta)\sin\delta+2(q_2+x_2\sin\delta)\cos\delta\sin\delta}{Q(Q+q_3+\xi)}$$

$$- \frac{\chi_2[4q_2x_3\sin^2\delta-2(q_2+x_2\sin\delta)(x_3+q_3\sin\delta)][2Q+q_3+\xi-\frac{Q^2\cos\delta}{\chi_2}]}{Q^3(Q+q_3+\xi)^2}$$

$$F_{234} = \frac{4x_3\sin^2\delta(x_3+\xi_3-q_3\sin\delta)+4q_2x_3\sin^2\delta\cos\delta}{Q^3}$$

$$- \frac{12q_2x_3\sin\delta(x_3+\xi_3-q_3\sin\delta)\chi_2}{Q^5}$$

$$-\left\{4q_2x_3\cos\delta\sin\delta(2Q+q_3+\xi)(2q_3\sin\delta-q_2\cos\delta) \right.$$
$$\left. +4q_2^2q_3x_3\cos\delta\sin\delta\left\{\frac{2\chi_2}{Q} - \cos\delta\right\}\right\} / Q^3(Q+q_3+\xi)^2$$

$$+ \frac{4q_2^2q_3x_3\cos\delta\sin\delta(2Q+q_3+\xi)[3\chi_2(Q+q_3+\xi)+2Q^2(\frac{\chi_2}{Q} - \cos\delta)]}{Q^5(Q+q_3+\xi)^3}$$

DIP SLIP

$$E_{11} = \frac{\Delta u}{12\pi}\left[G_{111}X_2\sin\delta - G_{112}\cos\delta + G_{113}\frac{3}{\cos\delta} + 6x_3G_{114}\right]$$

$$G_{111} = \frac{12\xi_3 x_3 X_1}{Q^5} + \frac{3X_1}{Q(Q+x_3+\xi_3)^2} - \frac{2X_1}{R^3} - \frac{4X_1}{Q^3}$$

$$G_{112} = \frac{3X_1}{Q(Q+x_3+\xi_3)} - \frac{2X_3X_1}{R^3} - \frac{4X_3X_1}{Q^3} - \frac{12\xi_3 x_3(x_3+\xi_3)X_1}{Q^5}$$

$$G_{113} = \frac{X_1}{Q(Q+x_3+\xi_3)} - \frac{X_1\sin\delta}{Q(Q+q_3+\xi)}$$

$$G_{114} = \frac{q_2X_1(2Q+q_3+\xi)\sin\delta}{Q^3(Q+q_3+\xi)^2} - \frac{X_1\cos\delta}{Q^3}$$

$$E_{21} = \frac{\Delta u}{12\pi}\left[X_2\sin\delta G_{211} + \sin\delta G_{212} - \cos\delta G_{213} + \frac{3}{\cos\delta}G_{214} + 6x_3G_{215}\right]$$

$$G_{211} = \frac{-2X_2}{R^3} - \frac{4X_2}{Q^3} + \frac{12\xi_3 x_3 X_2}{Q^5} + \frac{3X_2}{Q(Q+x_3+\xi_3)^2}$$

$$G_{212} = \frac{2}{R} + \frac{4}{Q} - \frac{4\xi_3 x_3}{Q^3} - \frac{3}{(Q+x_3+\xi_3)}$$

$$G_{213} = \frac{3X_2}{Q(Q+x_3+\xi_3)} - \frac{2X_3X_2}{R^3} - \frac{4X_3X_2}{Q^3} - \frac{12\xi_3 x_3(x_3+\xi_3)X_2}{Q^5}$$

$$G_{214} = \frac{\chi_2}{Q(Q+x_3+\xi_3)} - \frac{\chi_2 \sin\delta}{Q(Q+q_3+\xi)}$$

$$G_{215} = \frac{-\chi_2 \cos\delta}{Q^3} - \frac{\sin^2\delta}{Q(Q+q_3+\xi)} + \frac{q_2\chi_2(2Q+q_3+\xi)\sin\delta}{Q^3(Q+q_3+\xi)^2}$$

$$E_{12} = \frac{\Delta u}{12\pi}\left[G_{121}\sin\delta - G_{122}\cos\delta + 6G_{123}\right]$$

$$G_{121} = \frac{-1}{R} + \frac{1}{Q} + \frac{4}{Q^5}\left[\chi_2^2(3\xi_3 x_3 - Q^2) - Q^2\xi_3 x_3\right]$$

$$+ \frac{3Q(Q+x_3+\xi_3)-3\chi_1^2}{Q(Q+x_3+\xi_3)^2} - \frac{2\chi_2^2}{R^3}$$

$$G_{122} = \frac{-2\chi_2\chi_3}{R^3} + \frac{4\chi_2\chi_3}{Q^3} - \frac{12\xi_3 x_3 \chi_2 (x_3+\xi_3)}{Q^5}$$

$$+ \frac{6}{Q}\left\{\frac{(h+x_3+\xi_3)\chi_2[Q(Q+h)-\chi_1^2]}{(h+x_3+\xi_3)^2(Q+h)^2+\chi_1^2\chi_2^2}\right\}$$

$$- \frac{3}{Q}\left\{\frac{r(r_3-\xi)[RQ-\chi_1^2]}{r_2^2R^2+\chi_1^2(r_3-\xi)^2}\right\} + \frac{6}{Q}\left\{\frac{q_2(q_3+\xi)(Q^2+\chi_1^2)}{q_2^2Q^2+\chi_1^2(q_3+\xi)^2}\right\}$$

$$G_{123} = \frac{(q_3+\xi)\chi_1^2 B_1 [(K-q_2\cos\delta)(Q-K)+(q_3+\xi)K\sin\delta]}{QRK[\chi_1^2(q_3+\xi)^2\cos^2\delta + B_2^2]}$$

$$- \frac{x_3}{Q^3}(q_3+\xi+2q_2\cos\delta\sin\delta)$$

$$+ \frac{x_3 \sin^2\delta[Q^2(Q+q_3+\xi)-\chi_1^2(2Q+q_3+\xi)]}{Q^3(Q+q_3+\xi)^2}$$

where $B_1 = K(R-Q)(K-q_2\cos\delta)+QR[Q-K+(q_3+\xi)\sin\delta]$

$$B_2 = (K-q_2\cos\delta)(Q-K)+(q_3+\xi)K\sin\delta$$

$$E_{22} = \frac{\Delta u}{12\pi}(\sin\delta\ G_{221} - \cos\delta\ G_{222} + 6G_{223})$$

$$G_{221} = \frac{3\chi_2}{R(R+\chi_1)} + \frac{9\chi_2}{Q(Q+\chi_1)} - \frac{12\xi_3 x_3 \chi_2(2Q+\chi_1)}{Q^3(Q+\chi_1)^2}$$

$$- \frac{2\chi_2^3(2R+\chi_1)}{R^3(R+\chi_1)^2} - \frac{4\chi_2^3(2Q+\chi_1)}{Q^3(Q+\chi_1)^2}$$

$$+ \frac{4\xi_3 x_3 \chi_2^3(8Q^2+9Q\chi_1+3\chi_1^2)}{Q^5(Q+\chi_1)^3}$$

$$G_{222} = \frac{2\chi_3}{R(R+\chi_1)} + \frac{4\chi_3}{Q(Q+\chi_1)} + \frac{4\xi_3 x_3(x_3+\xi_3)(2Q+\chi_1)}{Q^3(Q+\chi_1)^2}$$

$$- \frac{2\chi_2^2\chi_3(2R+\chi_1)}{R^3(R+\chi_1)^2} - \frac{4\chi_3\chi_2^2(2Q+\chi_1)}{Q^3(Q+\chi_1)^2}$$

$$- \frac{4\xi_3 x_3(x_3+\xi_3)\chi_2^2(8Q^2+9Q\chi_1+3\chi_1^2)}{Q^5(Q+\chi_1)^3}$$

$$+ 6\chi_1 \left\{ \frac{(h+x_3+\xi_3)(Q+h)-B_3-B_4\chi_2(h+x_3+\xi_3)}{[(h+x_3+\xi_3)^2(Q+h)^2+\chi_1^2\chi_2^2]} \right\}$$

$$- 3\chi_1 \left\{ \frac{r_2R^2\cos\delta-(r_3-\xi)(R^2\sin\delta+r_2\chi_2)}{R[r_2^2R^2+\chi_1^2(r_3-\xi)^2]} \right\}$$

$$- 6\chi_1 \left\{ \frac{[q_2Q^2\cos\delta-(q_3+\xi)(Q^2\sin^2\delta+q_2\chi_2)]}{Q[q_2^2Q^2+\chi_1^2(q_3+\xi)^2]} \right\}$$

where: $B_3 = \chi_2 \frac{(Q+h)}{h} [q_2\sin\delta-(q_3+\xi)\cos\delta]$

$$B_4 = \frac{\chi_2}{Q} + \frac{[q_2\sin\delta-(q_3+\xi)\cos\delta]}{h}$$

$$G_{223} = \frac{\chi_1(q_3+\xi)\cos\delta[B_5-K\sin\delta\cos\delta+(q_3+\xi)\frac{q_2\sin^2\delta}{K}]}{\chi_1^2(q_3+\xi)^2\cos^2\delta+B_2^2}$$

$$+ \frac{\chi_1\cos^2\delta[(K-q_2\cos\delta)(Q-K)+(q_3+\xi)K\sin\delta]}{\chi_1^2(q_3+\xi)^2\cos^2\delta+[(K-q_2\cos\delta)(Q-K)+(q_3+\xi)K\sin\delta]^2}$$

$$-x_3\frac{\{Q(Q+\chi_1)\cos\delta(\sin^2\delta-\cos^2\delta)-2\cos^2\delta\sin^2\delta\cdot Q(Q+\chi_1)\}}{Q^2(Q+\chi_1)}$$

$$-x_3\frac{\chi_2(2Q+\chi_1)[(q_3+\xi)(\sin^2\delta\cos^2\delta)+2q_2\cos\delta\sin\delta]}{Q^3(Q+\chi_1)}$$

$$\frac{-x_3\chi_1\chi_2(2Q+q_3+\xi)}{Q^3(Q+q_3+\xi)^2}$$

where:

$$B_5 = (K-q_2\cos\delta)\left(\frac{\chi_2}{Q} - \frac{q_2\sin\delta}{K}\right)+(Q-K)\left(\frac{q_2\sin\delta}{K} - \sin\delta\cos\delta\right)$$

$$E_{13} = \frac{\Delta u}{12\pi}\left(\sin\delta\ G_{131} + \cos\delta\ G_{132} + 6x_3\ G_{133}\right)$$

$$G_{131} = \frac{-2\chi_2\chi_3}{R^3} - \frac{4\chi_2\chi_3}{Q^3} - \frac{4\chi_2\xi_3x_3(x_3+\xi_3)}{Q^5}$$

$$- \frac{6\chi_2(h+x_3+\xi_3)[Q(Q+h)-\chi_1^2]}{Q[(h+x_3+\xi_3)^2(Q+h)^2+\chi_1^2\chi_2^2]}$$

$$+ \frac{3r_2(r_3-\xi)(R^2-\chi_1^2)}{R[r_2^2R^2+\chi_1^2(r_3-\xi)^2]} - \frac{6q_2(q_3+\xi)(Q^2-\chi_1^2)}{Q[q_2^2Q^2+\chi_1^2(q_3+\xi)^2]}$$

$$G_{132} = \frac{1}{R} - \frac{1}{Q} + \frac{2\chi_3^2}{R^3} + \frac{4[(x_3+\xi_3)^2-\xi_3x_3]}{Q^3} - \frac{4\xi_3x_3(x_3+\xi_3)^2}{Q^5}$$

$$G_{133} = \frac{-2\cos\delta\sin\delta}{Q^3}(q_3+\xi)+\frac{\cos\delta\sin\delta[Q^2(Q+q_3+\xi)-\chi_1^2(q_3+\xi)]}{Q^3(Q+q_3+\xi)^2}$$

$$-q_2\frac{(\sin^2\delta-\cos^2\delta)}{Q^3}$$

$$E_{23} = \frac{\Delta u}{12\pi}\left(\sin\delta\, G_{231} + \cos\delta G_{232} + 6x_3\, G_{233}\right)$$

$$G_{231} = \frac{2\chi_3}{R(R+\chi_1)} \cdot \left\{ 1-\chi_2^2\left[\frac{1}{R^2} + \frac{1}{R(R+\chi_1)}\right] \right\}$$

$$+ \frac{4\chi_3}{Q(Q+\chi_1)} \cdot \left\{ 1-\chi_2^2\left[\frac{1}{Q^2} + \frac{1}{Q(Q+\chi_1)}\right] \right\}$$

$$- \frac{4\xi_3 x_3(x_3+\xi_3)(2Q+\chi_1)}{Q^3(Q+\chi_1)^2} + \frac{4\chi_2^2\xi_3 x_3(x_3+\xi_3)[8Q^2+9Q\chi_1+3\chi_1^2]}{Q^5(Q+\chi_1)^3}$$

$$+ \frac{3[r_2 R\chi_1\cos\delta-\chi_1(r_3-\xi)(\frac{r_2}{R}\chi_2+R\sin\delta)]}{[r_2^2R^2+\chi_1^2(r_3-\xi)^2]}$$

$$+ \frac{6[q_2 Q\chi_1\cos\delta+\chi_1(q_3+\xi)(\frac{q_2}{Q}\chi_2+Q\sin\delta)]}{[q_2^2Q^2+\chi_1^2(q_3+\xi)^2]}$$

$$G_{232} = \frac{\chi_2}{R(R+\chi_1)} - \frac{\chi_2}{Q(Q+\chi_1)} + \frac{2\chi_3^2\chi_2(2R+\chi_1)}{R^3(R+\chi_1)^2}$$

$$+ \frac{4\chi_2(2Q+\chi_1)[(x_3+\xi_3)^2-\xi_3 x_3]}{Q^3(Q+\chi_1)^2}$$

$$+ \frac{4\xi_3 x_3\chi_2(x_3+\xi_3)^2(8Q^2+9Q\chi_1+3\chi_1^2)}{Q^5(Q+\chi_1)^3}$$

$$G_{233} = \frac{-2\chi_2(q_3+\xi)(2Q+\chi_1)\cos\delta\sin\delta}{Q^3(Q+\chi_1)^2}$$

$$- \frac{\chi_1\chi_2\cos\delta\sin\delta[2Q+q_3+\xi - \frac{Q^2\cos\delta}{\chi_2}]}{Q^3(Q+q_3+\xi)^2}$$

$$- \frac{(\sin^2\delta-\cos^2\delta)[Q(Q+\chi_1)\sin\delta+q_2\frac{\chi_2}{Q}(2Q+\chi_1)]}{Q^2(Q+\chi_1)^2}$$

Appendix 2

Observed Gravity Changes Associated with Deformation Accompanying the 1971 San Fernando Earthquake

A2.1 Introduction

In the past there have been a limited number of studies of gravity changes which accompany earthquakes. The earliest of these studies were in Japan. Tsuboi et al. (1953) attempted to compare changes in gravity and precise line leveling changes following the Nankaido earthquake of 1946. However, a significant comparison could not be made due to the imprecise gravity values. Extensive gravity surveys in the area of the Matsushiro earthquake swarms of 1965-1968 were carried out by Harada (1968). A comparison of this data to the leveling resurvey associated with the earthquake swarms by Tsubokawa et al. (1967) has been reported by Kasahara (1970) and Hagiwara and Tajima (1973). In this study, the relation between the gravity change and the vertical upward displacement associated with the tectonic deformation of the earthquake swarms nearly coincided with a Bouguer gradient with a density taken to be 1.0 gram/cm^3. The maximum displacements that were observed where the gravity field was being monitored were just over 30 cm and the maximum gravity changes were about 0.06 mgal with an accuracy of $\pm$ 0.02 mgal. However, during the

period of ground subsidence the changes in the gravity field appeared to fall along the free-air gradient. As a whole the swarm process left no effective gravity change, even though the residual displacement was about 20 cm.

Barnes (1966) and Rice (1969) conducted remeasurements of gravity in an area affected by the deformation of the Alaska, 1964, earthquake. The changes in gravity were compared with changes in elevation determined by a post-earthquake releveling of a 1923 first-order geodetic line coincident with the gravity traverse. Because the area in which the traverse was located had a maximum elevation change of only 0.6 m, the relationship between gravity and elevation changes could not be determined accurately. However, the largest gravity differences indicated that the slope of the Δg-ΔE relationship was closer to the Bouguer gradient with a density of 2.67 gram/cm^3 than to the free air gradient.

Hunt (1970) has observed a relation between changes in the gravity field and elevation changes for the 1968 Anangahua earthquake. Although his data are meager, the gradient of Δg-ΔE relation between -0.15 and -0.20 mgal/m is much less than the free air gradient -0.309 mgal/m.

In each of these cited studies, the conclusions reached by the researchers were limited by either the inability to accurately measure the vertical component of

displacement or accurately determine changes in the gravity field at points where elevation changes are known. Thus in order to establish a meaningful correlation of deformation and accompanying gravity changes, the vertical displacements need to be large and accurately known, and reliable gravity stations need to have been established in the area prior to the earthquake. The calibration, stability and sensitivity of gravity meters are sufficient now to make gravity measurements for reliable studies. Once the correlation between ΔE and Δg has been established then the gravity meter could be used as a reconnaissance tool to map the extent of deformation rapidly following a large earthquake if previous gravity stations have been established.

Much of the tectonic deformation due to the 1971, San Fernando, California, earthquake fortunately occurred in an area in which there was a dense leveling net and enough reoccupiable gravity stations that a study could be carried out. The gravity stations in the San Fernando Valley were installed as part of a survey by Corbató (1963) using a Worden gravimeter (W88) and very tight control on the observed gravity values. Most of the stations described by Corbató were actually installed in 1958. These stations were reoccupied and the results are reported here. A compilation of all the observed gravity changes in the

area affected by this earthquake is given by Oliver et al. (1973). This study includes data in both the San Fernando Valey and the San Gabriel Mountains, both south and east of the epicenter and northwest of the earthquake area.

A2.2 Gravimeter Characteristics

All gravity measurements employed in this study were made with a Worden Master (W533) gravimeter. The small dial constant of this meter as determined from the tilt table method at the manufacturer (Texas Instruments) in 1968 was 0.33181 mgals per large scale division when the instrument is operating at 87°F. Most of the measurements taken in this study were taken when the internal temperature of the meter was between 70°F and 72°F. Since the response of the instrument is linear in this temperature range, a simple extrapolation gives the dial constant at 72°F to be 0.33145 mgals per large scale division. In addition, the meter was checked on a previously established seven station calibration loop between a station located at the University of California at Los Angeles (UCLA) and Mt. Wilson. The gravity station at the California Institute of Technology (Caltech) is the second station in this loop -- denoted MW2. This calibration loop was established by Harrison and Corbató (1965) using a LaCoste and Romberg geodetic gravimeter. Further discussions and descriptions of this loop can be found in Biehler (1964) and Robbins

et al. (1973). The total gravity change from MW2 to the station at Mt. Wilson is 323.80 mgals. Successive checks of the instrument over this loop yielded a calibration value of 0.3315 ± 0.0002 mgals per large scale division. With careful measurements and averaging values, instrument readings at individual stations are reproducible to within 0.1 large scale division, or 0.03 mgals. In the actual survey, readings at individual stations were tied to the base station by closed loops, with several readings being made at each of the individual stations.

The instrument drift due to tides, small temperature changes, internal fatigue, etc. varied somewhat but never seemed to exceed 0.15 mgals per hour. The instrument drift was linearly interpolated in time throughout the closure of each individual loop.

A2.3 Base Station Ties

All the reoccupation readings were based on ties to the base station at Caltech. The gravity station at Caltech, MW2, used here should not be confused with another close-by station described by Chapman (1966, p. 25, No. 309). A description of the location of this and all other stations referred to in this chapter is given by Robbins et al. (1973). Individual reoccupation stations were tied to the base station on at least four to five separate occasions, and it is thought that the maximum error of each

tied station is about ± 0.03 mgals based on the standard deviations of the scatter in the data about the mean values. Two of the reoccupation stations tied to the base station were checked with a LaCoste-Romberg gravimeter, with a calibration constant of about 0.1 mgals per large scale division, and the differences in the gravity readings between the two stations and the base station determined with this instrument agreed to within ± 0.01 mgal (Oliver, personal communication, 1971).

Since the original gravity stations installed by Corbató were based on direct ties to the gravity station at UCLA and the reoccupation of these stations were based on ties to Caltech, the question arises as to whether or not there was a relative change between Caltech and UCLA caused by the earthquake, or whether or not the absolute gravity changed at both of these stations. Oliver et al. (1973) reported that there was indeed no gravity change at Caltech within the reliability of 5 pre-earthquake and 6 post-earthquake measurements made relative to UCLA or to a station at Menlo Park, California. Supplementary evidence for this conclusion comes from the fact that a continuously recording tidal gravimeter operating at UCLA at this time of the earthquake indicated no perceptible change in the gravity field at that point relative to the accuracy of that instrument (±0.001 mgal). In addition, the Mt. Wilson

calibration loop was rechecked relative to a distant calibration loop, and no changes in the gravity values could be observed. Thus, we feel relatively comfortable in basing our reoccupation readings on ties to the gravity station at Caltech.

A2.4 Gravity Station Reoccupation.

Figure A2.1 shows the location and distribution of the reoccupied gravity stations in the San Fernando Valley. The stations are identified with a number corresponding to that given by Corbató (1963). The stations numbered 1-14 were the sub-base stations of Corbató's net and are well scattered throughout the San Fernando Valley. These sub-base stations were the first to be reoccupied, since immediately following the earthquake, before any precision leveling could be done, the areal extent of the tectonic deformation was sought. It was assumed that the deformation, if any, would be reflected into changes in gravity. The absolute gravity at these sub-base stations was more accurately determined than at the other stations, with the values generally known to within $\pm$ 0.03 mgals. Of the fourteen stations originally comprising the sub-base net, eleven could be recovered in 1971, although there was some slight uncertainty as to the exact location of three of the stations. These uncertain stations are marked with an asterisk in Table A2.1. At these uncertain stations, an

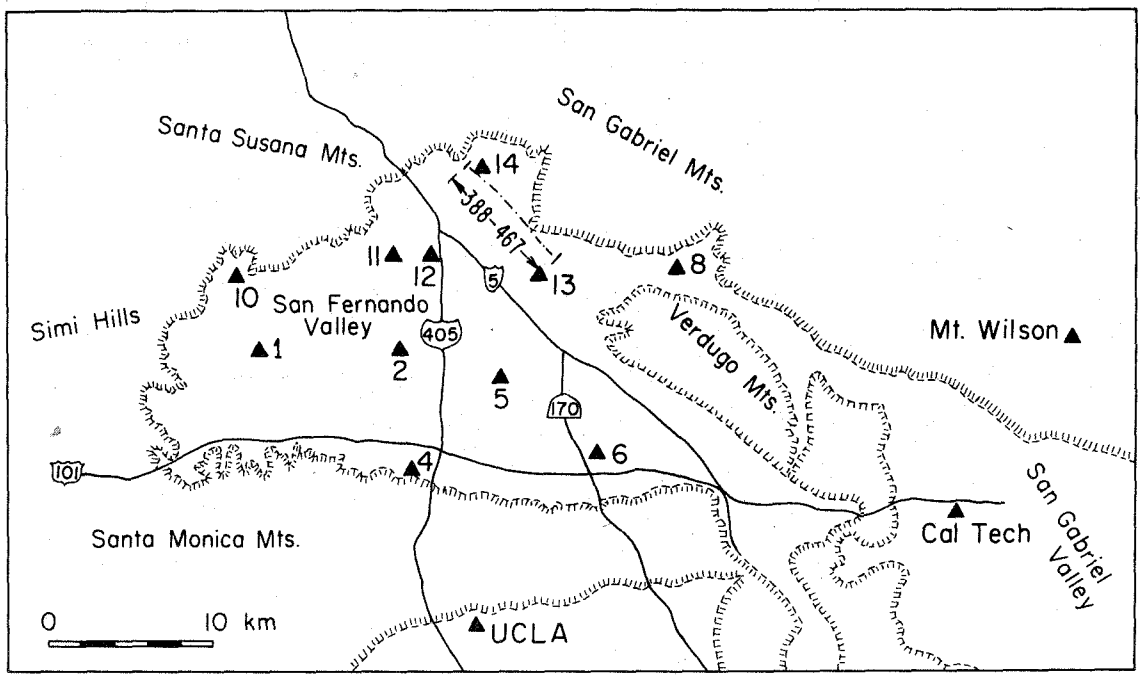

Figure A2.1. Index map of the San Fernando Valley showing the location of the reoccupied gravity stations.

TABLE A2.1

Stn. No.	Pre-1971 Gravity (mgals)	σ_{g_1} (mgals)	Post-Earthquake Gravity (mgals)	σ_{g_2} (mgals)	Δ_g (mgals)	σ_g (mgals)	ΔE (m)	σ_E (m)
1	567.35	.03	567.39	.03	0.04	.04	-	-
2	563.19	.03	563.20	.03	0.01	.04	-0.03	.03
4	589.34	.03	589.34	.08	0.00	.09	-	-
5	567.78	.03	567.75	.05	0.03	.06	-	-
6	579.19	.03	579.16	.03	-0.03	.04	-	-
8*	537.25	.03	537.09	.05	-0.16	.06	-	-
10	571.25	.03	571.25	.03	0.00	.04	-	-
11*	536.43	.03	536.23	.05	-0.20	.06	-	-
12	539.70	.03	539.55	.03	-0.15	.04	0.00	.03
13*	547.01	.03	546.98	.03	-0.03	.04	-	-
14	526.02	.03	525.72	.03	-0.30	.04	1.35	.05
388	543.97	.05	543.99	.03	0.02	.06	-0.05	.03
393	534.83	.05	534.78	.03	-0.05	.06	0.01	.03
444	530.38	.05	530.28	.03	-0.10	.06	0.25	.12
446	527.52	.05	527.40	.03	-0.12	.06	0.16	.03
448	525.03	.05	524.71	.03	-0.32	.06	1.47	.03
449	527.62	.05	527.57	.03	-0.05	.06	0.32	.03
458	523.38	.05	523.17	.03	-0.21	.06	1.17	.06
459	519.73	.05	519.54	.03	-0.19	.06	0.98	.05
460	515.30	.05	515.20	.03	-0.10	.06	0.58	.03
461	507.17	.05	507.08	.03	-0.09	.06	0.48	.03
464	521.28	.05	521.16	.03	-0.12	.06	0.82	.03
467	518.28	.05	518.20	.03	-0.08	.06	0.50	.03

Table A2.1. Observed gravity and elevation changes.

attempt was made to take the readings at about the same altitude as reported by Corbató (1963). The gravity values for all the stations for both the pre-earthquake and post-earthquake measurements are listed here. The absolute gravity values are the values listed plus 979.0 gals. The values given by Corbató (1963, Appendix B) are the pre-earthquake values rounded to the nearest 0.1 mgal. However, the values were actually calculated to the nearest 0.01 mgal (Corbató, personal communication, 1971). The uncertainties, σ_{g_1}, σ_{g_2}, are based on standard deviations about the mean values. The uncertainty of the resulting change in gravity, σ_g, is given by the square root of the sum of the squares of the standard deviations of the two measurements. The change in gravity, Δg, is defined to be the post-earthquake measurement minus the pre-earthquake measurement.

In the last two columns, the changes in elevation, ΔE, and their respective standard deviations for the stations, σ_E, are given when available. These values were obtained principally from the City of Los Angeles, Bureau of Engineering, Van Nuys Office. The measurements of elevation both before and after the earthquake are made relative to the mean tidal level in the City of San Pedro, California. Since most of the Corbató gravity stations were located on, or very near, city engineering monuments, these data were very useful. Supplementary leveling information from

Burford et al. (1971) was used. The estimated variance in the leveling data is from these sources. With the exception of two points, the changes in the leveling data are relative to the elevation determined in 1960. These two exceptions are Station 2 and Station 12 which are relative to measurements in 1970 and 1963 respectively. Station 12 is especially anomalous in that in the period 1963-1970 the elevation increased by 0.06 m, but between 1970 and post-earthquake 1971, the elevation decreased by 0.06 m.

From the upper part of this table, it is seen that the only significant changes in gravity occurred to the north of the observed surface ruptures, with the exception of Station 12, which is discussed below. Twelve more stations all concentrated above, or slightly below, the rupture zone were then reoccupied. The gravity values measured at these stations are listed in the lower half of Table A2.1.

A2.5 Relation of Gravity Differences to Observed Deformation.

The gravity stations listed in the lower half of Table A2.1 form a profile from the southeast to the northwest cutting across the main surface ruptures. The location of this profile in relation to the surface deformation can be seen in Figure A2.4. Figure A2.2 shows the results of the reoccupation of the stations along this profile. The top part of the figure gives the observed elevation change from 1960 to 1971 showing the sharp scarp where the profile

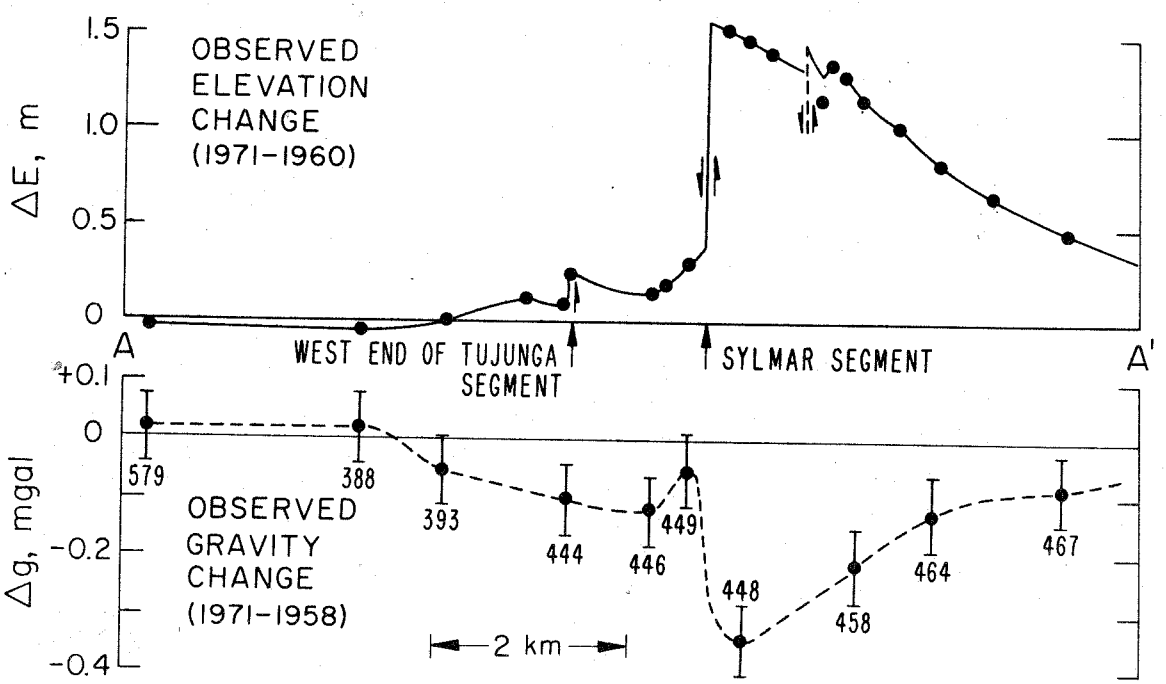

Figure A2.2. Gravity profile A-A' showing the relation of the changes in surface elevation to gravity changes.

crosses the Sylmar segment of the surface breaks. The profile crosses just at the western end of the Tujunga segment of the surface breaks. The lower part of the figure indicates the corresponding observed gravity change for this profile. It is clear that a good relationship exists between the observed elevation change and the observed gravity change. Now if we plot the significant changes in gravity versus their respective changes in elevation, we see that the relation is quite linear. Figure A2.3 shows this plot. The line fit to the data is a least squares relation given by

$$\Delta g = - 0.215\ \Delta E \pm 0.026 \qquad \text{(A2.1)}$$

where ΔE is the elevation change in meters and Δg is the gravity change in mgals. The gradient of this relation implies a Bouguer reduction density of 2.2 gram/cm^3, or about the density of the unsaturated surficial layers in the area, which are late Cenezoic sediments. If a Bouguer reduction density of 0.2 gram/cm^3 higher or lower than this value is chosen, the fit is only slightly degraded, with the standard error being increased. As an example, a gradient of - 0.224 mgals per meter is found when a Bouguer reduction density of 2.0 gram/cm^3 is used. The gradient for the relation for the interval of acceptable Bouguer

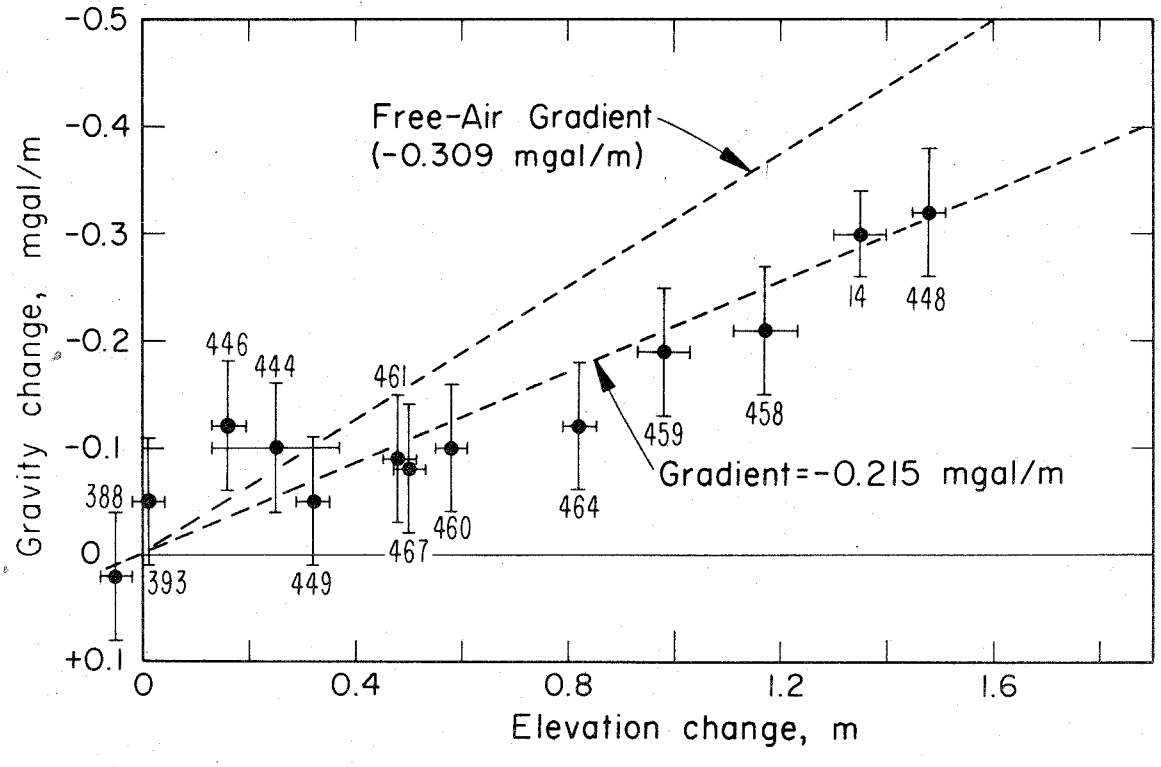

Figure A2.3. Least-squares fit of elevation changes to the gravity changes. The uncertainties in the measurements are indicated by the error bars for each numbered station. Points fall along a gradient significantly less than the free-air gradient.

reduction density values is still significantly less than the free air gradient of - 0.309 mgals per meter.

If the deformation as measured along this profile had occurred as the result of merely a vertical expansion over some depth, then the gravity changes would have fallen along the free air gradient. However, the fact that the values fall along a reasonable Bouguer reduction gradient indicate that by some means mass was added beneath the gravity stations. Within the resolving power of the gravity measurements, one can conclude that the overriding thrust block appeared to move as a unit. For the regions of uplift, it is clear that these areas of negative gravity change are now slightly heavier than before the earthquake due to the added mass from the stacking of the surficial layers on the pre-earthquake surface.

Equation A2.1 can be inverted to give the estimated elevation change for a known gravity change. This relation is

$$\Delta E = -4.65 \, (\Delta g + \sigma_g) \, . \qquad \text{(A2.2)}$$

Equation A2.2 implies that if the gravity changes at the stations reoccupied can be determined to $\pm$ 0.05 mgals, then the accompanying change in elevation is determined to $\pm$ 0.23 m.

The gravity change data accumulated in this study have been added to that obtained by the other authors in Oliver et al. (1973) to give a contour map of the gravity changes associated with this earthquake (Figures A2.4). Releveling data from both that obtained from the City of Los Angeles Engineering Bureau and that obtained by the U. S. Geological Survey, as reported in Burford et al. (1971) have been converted into changes in gravity and included into the gravity contours shown in this figure. The gravity changes that are obtained by conversion of leveling data are shown in parentheses along side the bench mark location and the year that the original elevation was obtained. Gravity data obtained directly are similarly shown without the parentheses. Examination of the two sets of data show that they are remarkably compatible within the uncertainties of each of the data sets. Of particular interest is a comparison of the gravity values from both data sets in the area just east of the Pacoima Reservoir. The gravity change from the converted elevation change (-0.15 mgals) is based on a 1929 elevation determination, where the direct gravity changes are based on measurements obtained in 1964 and 1970, yet the change based on the 1929 observation is about the same size as those based on much later observations. Savage et al. (1973) have postulated that this particular releveling datum might contain some pre-earthquake secular

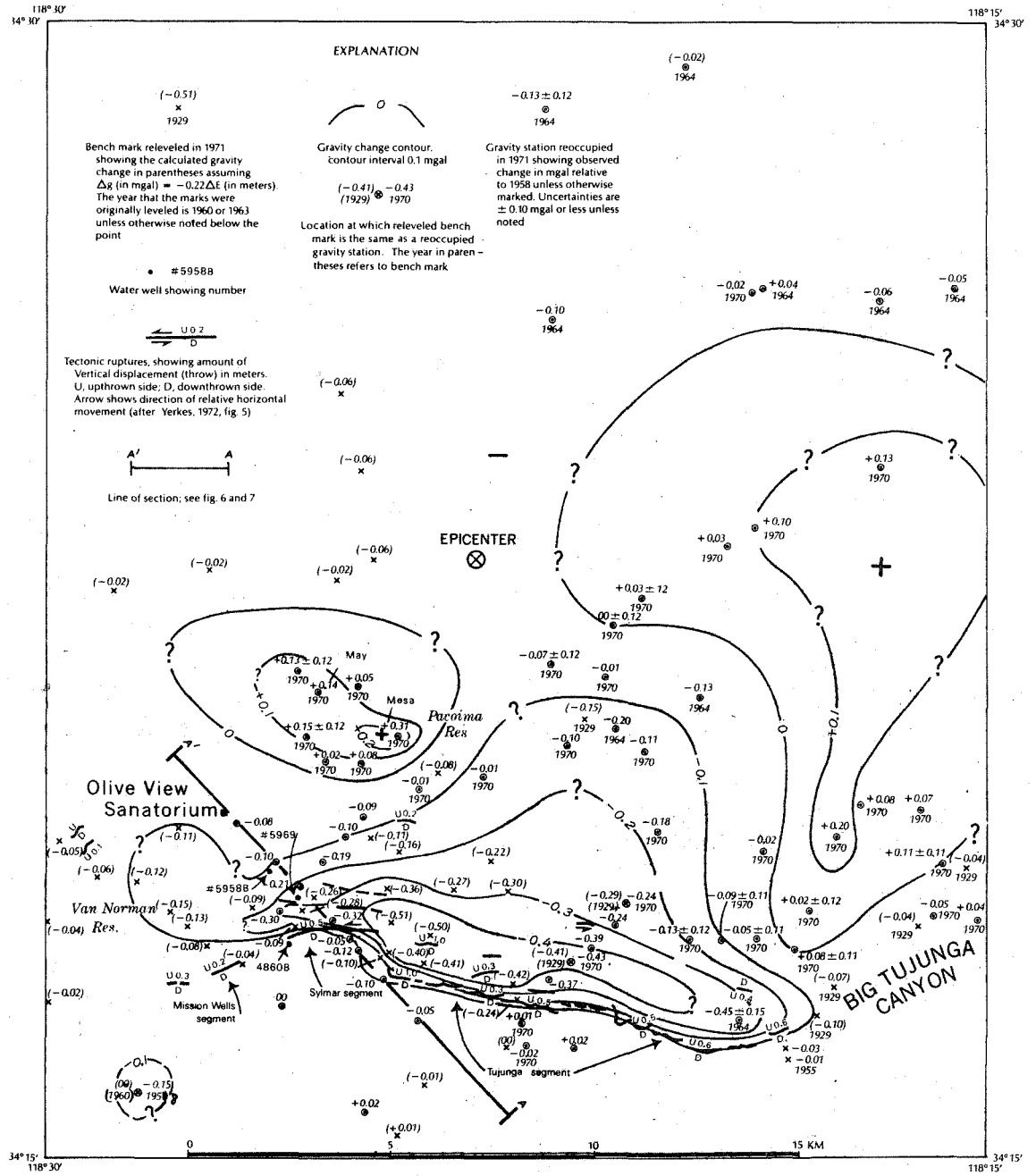

Figure A2.4. Contour map of the gravity changes associated with this earthquake. These data include elevation changes that have been converted to gravity changes by equation (A2.1).

uplift, however, the gravity measurements here suggest that most of the uplift in this area probably took place at the time of the earthquake and was not distributed in the 42 years preceding the earthquake.

Also indicated in Figure A2.4 are areas of positive gravity changes, indicating subsidence. These areas were not delineated by the leveling surveys because of lack of data. Although the data indicating these positive changes are less accurate than in this study, the majority of the points defining the positive change do have positive values when the maximum error is subtracted. If these gravity changes obey a similar Bouguer relationship with changes in elevation, then this is an indication that mass was removed from this area. No attempt has been made to balance the mass involved because of the poor nature of some of the data. However, the recognizance of this area of subsidence shows the usefulness and facility of making gravity measurements in tectonic areas whether or not they can be done in conjunction with leveling surveys. It is interesting to note that this area roughly forms an inverted "U" and corresponds to about the aftershock zone near the epicentral area (Allen et al., 1971).

A2.6 Bouguer Residuals.

Figure A2.5 shows the residual Bouguer anomaly for the profile A-A'. This residual was calculated from the formula,

$$\delta g_{BA} = \Delta g - 0.215\ \Delta E \ . \qquad \text{(A2.3)}$$

The residuals are plotted in the upper part of Figure A2.5. Although the residuals are fairly small when compared to the estimated errors for each observation, the calculated anomalies are systematic in the sense that the residuals are negative south of the surface ruptures and positive to the north of the surface ruptures. Although barely significant, these anomalies represent some rearrangement of the subsurface mass from 1958 to 1971. One obvious rearrangement of the subsurface mass is that which can be caused by the raising or lowering of the areal water table in the time interval between gravity measurements. Oliver et al. (1973) have considered this in some detail. They report that for the limited water table level data that are available for this area, the water table level changed in the short interval about the time of the earthquake only by the amount the surface was deformed. Thus the entire sedimentary unit sampled by the water wells moved as a unit during the earthquake. However, in the 13-year interval, 1958 to

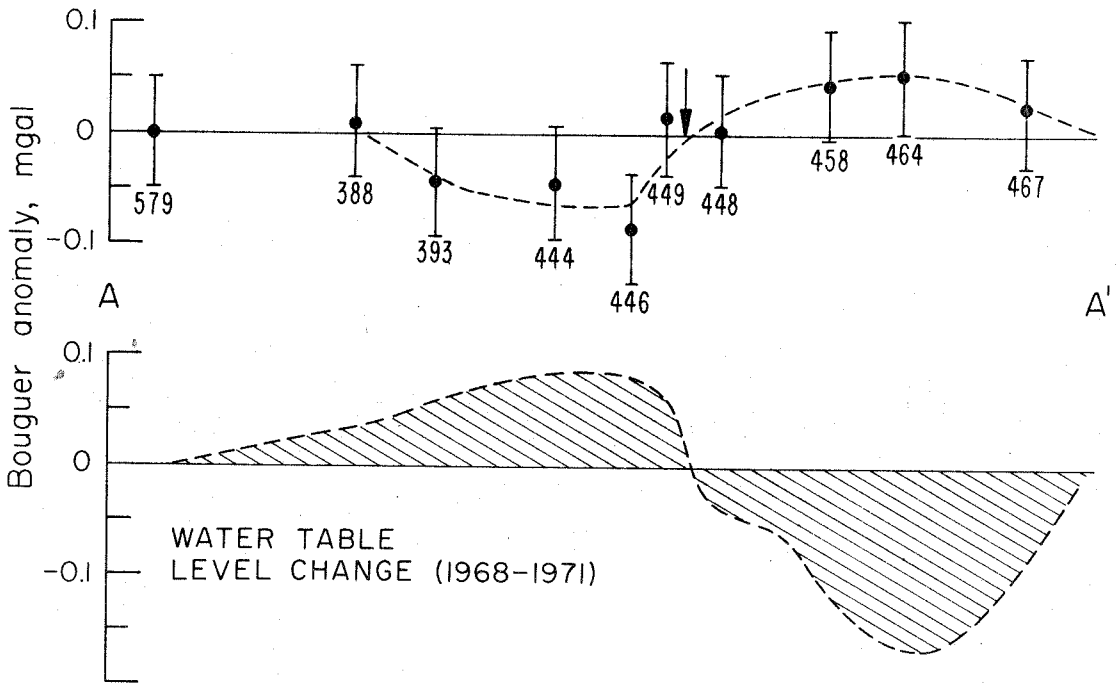

Figure A2.5. Upper--Observed Bouguer residuals for the gravity profile A-A'. Lower--Calculated gravity effects from the fluctuation in the water-table level, 1958-1971, for this profile.

1971, the total water table level, after seasonal effects are removed, was lowered in the area north of the surface ruptures and actually raised in the area to the south of the surface ruptures. Oliver (1972, personal communication) has calculated the gravitational effects of this net change in the water table level and his results for the profile A-A' are plotted in the lower half of Figure A2.5.

It is seen here that the water table effects give rise to about the size gravity anomaly as that observed, however, it is in the opposite direction. That is, the water table effect must be subtracted from the observed Bouguer anomaly to get the corrected total Bouguer anomaly. The errors in the gravity changes associated with the water table fluctuations are at least as large as the errors in the upper part of Figure A2.5 based on the uncertainty and paucity of the input data. It is not wished to emphasize this anomaly too much, other than perhaps the general form of the anomaly. No attempt was made in this study to model the anomaly, since not much is known about the original density distribution of the subsurface.

A2.7 Discussion.

The reoccupation of gravity stations after a major earthquake is shown to be a rapid and relatively inexpensive method of delineating the areas of deformation caused by the earthquake, provided a detailed gravity net is

established prior to the occurrence of such an event.

The occurrence of the San Fernando earthquake in an area where there was such good control on the elevation and gravity changes has presented the best opportunity to establish an accurate relation between these two variables for this particular type of faulting. A gravity station reoccupation traverse across the zone of the maximum thrust fault surface ruptures yielded a proportionality between the observed gravity changes and changes in elevation. The slope of the relationship shows rather convincingly that the elevation changes and the gravity changes are not related simply by the free air correction, but rather along a Bouguer gradient. The Bouguer reduction density found by a least-squares fit to the data indicates that the greatest portion of the gravity change could be explained by the stacking of the surficial layers on the pre-earthquake surface. In retrospect, this is exactly what would be expected from reverse thrust faulting. The Bouguer anomalies derived for this profile, although statistically barely significant, are systematic in that they are generally positive to the north of the rupture zone and negative to the south of the rupture zone.

Appendix 3

Derivation of Least-Squares Inversion Operators

In this appendix, we will derive the least-squares inverse and the associated operators for three cases. For convenience with respect to manuscript preparation, matrices will be given here in regular typed form, not boldface as in the rest of this thesis. This practice should cause no confusion in this case.

Case I: Least-Squares Inverse with no weighting of the model components and no inclusion of the data variances.

We define the forward problem to be

$$A\ \delta m = \delta d_o\ , \tag{A3.1}$$

where δd_o is the observed data vector, δm is the true model, and A is the operator which maps a function from the model space to the data space. We define the vector $b=\overline{\delta m}$ to be the best estimate of the model, δm, that we can obtain.

In this case, we wish to minimize the fit to the data such that

$$\varepsilon_1^2(b) = ||\delta d_o - \overline{\delta d}||^2 \tag{A3.2}$$

is minimized. Here we have $||Z||^2 = Z^*Z$, and $\overline{\delta d}$ is the calculated fit to the data given by

$$A\ b = \overline{\delta d}\ . \qquad \text{(A3.3)}$$

Substituting (A3.3) into (A3.2) and expanding, we get

$$\varepsilon_1^2(b) = \delta d_o{}^* \delta d_o - \delta d_o{}^* A\ b - b^* A^* \delta d_o + b^* A^* A\ b\ . \qquad \text{(A3.4)}$$

Now performing a first order perturbation in δb of (A3.4) and setting to zero implies

$$b = \overline{\delta m} = (A^*A)^{\dagger} A^* \delta d_o\ , \qquad \text{(A3.5)}$$

which is the result we are seeking.

Case II: Least-Squares Inverse with no weighting of model components and with the inclusion of the data variance.

Here we have the same forward problem as before, however, each datum, d_{o_i}, has associated with it some variance, σ_i^2. If we assume that the data are unbiased and are statistically independent, then we can write the variances in diagonal form

$$C_{nn} = \begin{bmatrix} \sigma_1^2 & . & . & . & . & 0 \\ . & \sigma_2^2 & & & & . \\ . & & . & & & . \\ . & & & . & & . \\ . & & & & . & . \\ 0 & . & . & . & . & \sigma_n^2 \end{bmatrix}$$

We want to minimize the fit to the data in a least-squares sense such that

$$\varepsilon_1^2(b) = ||\delta d_o - \overline{\delta d}||^2_{C_{nn}} \qquad \text{(A3.6)}$$

is minimized. This weighted norm, $||\cdot||_{C_{nn}}$, is defined by

$$||Z||^2_{C_{nn}} = Z^* C_{nn}^{-1} Z \ .$$

Substituting (A3.3) into (A3.6) and expanding, we get

$$\varepsilon_1^2(b) = \delta d_o^* C_{nn}^{-1} \delta d_o - \delta d_o^* C_{nn}^{-1} A\, b - (Ab)^* C_{nn}^{-1} \delta d_o + (Ab)^* C_{nn}^{-1} (Ab)$$

Performing the first order perturbation of δb on this last equation and setting the result to zero, we obtain

$$b = \overline{\delta m} = (A^* C_{nn}^{-1} A)^\dagger A^* C_{nn}^{-1} \delta d_o \ . \qquad \text{(A3.7)}$$

Case III: Least-Squares Inverse with weighting of the model components and with the inclusion of the data variance.

For some problems, it might be useful to consider a set of non-zero positive weights for the model components. These weighting, or model correlation coefficients, can be defined in the following manner,

$$C_{ss} = \begin{bmatrix} W_1 & . & . & . & . & 0 \\ . & W_2 & & & & . \\ . & & . & & & . \\ . & & & . & & . \\ . & & & & . & . \\ 0 & . & . & . & . & W_M \end{bmatrix} .$$

The error induced through the use of these correlation coefficients is given as the following,

$$\varepsilon_2^2(b) = b^* C_{ss}^{-1} b \ . \qquad \text{(A3.8)}$$

The error of the fit to the data is still given by equation (A3.6). For this case, we want to minimize some quadratic sum of these two errors.

$$\varepsilon^2(b) = \varepsilon_1^2(b)\cos\theta + \varepsilon_2^2(b)\sin\theta \ .$$

This minimization of $\varepsilon^2(b)$ proceeds as before giving

$$b = \overline{\delta m} = Q^{\dagger}(\theta)A^{*}C_{nn}^{-1}\delta d_o \qquad \text{(A3.9)}$$

where $Q^{\dagger}(\theta) = (A^{*}C_{nn}^{-1}A + \tan\theta C_{ss}^{-1})^{\dagger}$.

Substitution of (A3.9) into (A3.3) enables us to write

$$\overline{\delta d} = J\ \delta d_o \ .$$

J is called the data importance matrix and is given by

$$J = A\ Q^{\dagger}(\theta)A^{*}C_{nn}^{-1} \ .$$

The data importance matrix tells how the information in the data set is distributed (Wiggins, 1972). This operator serves the same role in the least-squares inverse as does the model response operator (equation 2.29) in the stochastic inverse. The data importance matrix gives us information as to how the model components as a whole "see" how large an effect individual data values have on the estimation of a model. Minster et al. (1974) show that the trace of this operator is invariant and given to be the number of independent linear combinations of the

data. For the inversion problem to be determinant, this sum must equal the number of independent model parameters.

In both the inversion procedures discussed in this thesis, we have neglected an obvious operator. We will call this operator the perturbation relaxation operator. These operators are defined below.

$$\overline{\delta d} = P_{S.}\,\delta d_o \qquad \text{(Stochastic inverse)}$$

$$\overline{\delta m} = P_{L.S.}\,\delta m \qquad \text{(Least-squares inverse)}$$

where

$$P_{S.} = AWA^{*}(AWA^{*}+C_{nn}\tan\theta)^{\dagger}$$

$$P_{L.S.} = (A^{*}C_{nn}^{-1}A+C_{ss}^{-1}\tan\theta)^{\dagger}(AC_{nn}^{-1}A)$$

These operators show simply that in the stochastic inverse case, when C_{nn} has large values for certain data, these data will be essentially neglected in the fit for the sake of fitting other better determined data. In the least-squares inverse case, when C_{ss} has a very small value for certain model components, the model will try to fit the data by ignoring the contributions from these particular model components. Also, we see that for C_{nn} and C_{ss} fixed,

the point along the trade-off curve influences the perturbation sizes in the iterative inversion scheme.

Appendix 4

Spectral Summation of Two Sources in the Frequency Domain

Consider the addition of two seismic sources by spectral summation. The first source is represented by an amplitude and a phase spectrum of the form $A_1(\omega)\, e^{i\phi_1(\omega)}$. The phase spectrum $\phi_1(\omega)$ contains information about both the source and the propagation path. To this spectrum we wish to add an additional source represented by $A_2(\omega)\, e^{i[\phi_2(\omega) + \Delta\phi_2(\omega)]}$, where $A_2(\omega)$ is the amplitude spectrum of the secondary source, $\phi_2(\omega)$ is the phase spectrum of the secondary source, and $\Delta\phi_2(\omega)$ is the additional phase of the secondary source caused by a spatial or temporal offset of the second source from the first source. Propagation effects for traveling a slightly different path from origin to receiver are taken into account with this term. If we let $\mathbf{z}$ be the total of the two sources, then we can write,

$$\mathbf{z} = Z(\omega)\, e^{i\psi(\omega)} = A_1(\omega)\, e^{i\phi_1(\omega)} + A_2(\omega)\, e^{i[\phi_2(\omega) + \Delta\phi_2(\omega)]}. \qquad \text{(A4.1)}$$

Thus,

$$Z(\omega) = \{A_1^2(\omega)+A_2^2(\omega)+2A_1(\omega)A_2(\omega)\cos[\phi_1(\omega)-\phi_2(\omega)-\Delta\phi_2(\omega)]\}^{1/2} \tag{A4.2}$$

and

$$\psi(\omega) = \tan^{-1} \frac{A_1(\omega)\sin[\phi_1(\omega)]+A_2(\omega)\sin[\phi_2(\omega)+\Delta\phi_2(\omega)]}{A_1(\omega)\cos[\phi_1(\omega)]+A_2(\omega)\cos[\phi_2(\omega)+\Delta\phi_2(\omega)]} . \tag{A4.3}$$

The phase delay of the single original source is given by

$$\tau_{p_1} = \frac{\phi_1(\omega)}{\omega} , \tag{A4.4}$$

and the new phase delay of the summed signal is

$$\tau_{p_Z} = \frac{\psi(\omega)}{\omega} . \tag{A4.5}$$

The group delay of the summed signal is given by

$$\tau_{g_Z} = \frac{\partial\psi(\omega)}{\partial\omega} . \tag{A4.6}$$

In practice in order to avoid as much as possible the difficulties encountered by the multivaluedness of the

trigonometric functions, we wish to compute only the additional group delay the additional source has over the group delay of the single original source. If we define this additional group delay by $\delta\tau_g$, then

$$\delta\tau_g = \tau_{g_z} - \tau_{g_1} , \tag{A4.7}$$

where τ_{g_1} is the group delay of the original signal. By defining $\frac{\partial\phi_2(\omega)}{\partial\omega} = \tau_{g_2}$ and $\frac{\partial\Delta\phi_2(\omega)}{\partial\omega} = \tau_{g_{2s}}$, we have by equation (A4.6)

$$\tau_{g_z} = \frac{A_1^2(\omega)\tau_{g_1} + A_2^2(\omega)\frac{\Gamma_+\Gamma_-}{2} + \Gamma_+ A_1(\omega)A_2(\omega)\cos(\alpha)}{A_1^2(\omega)+A_2^2(\omega)+2A_1(\omega)A_2(\omega)\cos(\alpha)} \tag{A4.8}$$

where

$$\alpha = \phi_2 + \Delta\phi_2 - \phi_1$$

$$\Gamma_+ = \tau_{g_1} + \tau_{g_2} + \tau_{g_{2s}}$$

$$\Gamma_- = \tau_{g_2} + \tau_{g_{2s}} - \tau_{g_1}$$

Substituting this expression into equation (A4.7) we get,

$$\delta\tau_g = \frac{A_2^2(\omega)\ \Gamma_- + A_1(\omega)A_2(\omega)\ \cos(\alpha)\ \Gamma_-}{A_1^2(\omega)+A_2^2(\omega)+2A_1(\omega)A_2(\omega)\cos(\alpha)} \tag{A4.9}$$

The additional phase delay caused by the spatial and temporal offset of the secondary source is given by

$$\tau_{p_{2s}} = \frac{\Delta\phi_2(\omega)}{\omega} = \frac{\hat{R}-R}{C(\omega)} + T_{d_2} . \qquad (A4.10)$$

Here R is the distance from the hypocenter of the first signal to the observer and $\hat{R}$ is the distance from the hypocenter of the second signal to the observer. $C(\omega)$ is the phase velocity of the medium. T_{d_2} is the delay in time after the initiation of the first source before the origin of the second source. This time delay can be expressed as an apparent rupture velocity given by $T_{d_2} = \frac{R_s}{V_R}$, where R_S is the separation distance for the two events.

Differentiation of $(\tau_{p_{2s}} \cdot \omega)$ with respect to ω yields the secondary group delay, $\tau_{g_{2s}}$ given by

$$\tau_{g_{2s}} = \frac{\hat{R}-R}{U(\omega)} + T_{d_2} , \qquad (A4.11)$$

where $U(\omega)$ is the group velocity of the medium.

It is seen that calculation of the group delay does not involve any inverse trigonometric functions so that the multivaluedness of the functions is not important. However, this is not the case for the calculation of $\psi(\omega)$. In practice, the values of $\psi(\omega)$ are numerically differenced

to obtain an approximate expression for the group delay. If this approximate group delay is more than one period different from the exact calculated group delay, then a period is added to the phase delay, τ_{p_z}, and the approximate group delay is recalculated. By starting with the phase and group delays of the long period end of the spectrum, the true phase can be unwound from that calculated numerically.

For the addition of many different sources, each offset in time and space with respect to one another, the above calculations are repeated for each source, with the original amplitude and phase spectra replaced by the partial sum spectra after each individual summation.

Appendix 5

Velocity-Density Models for Local Crustal Corrections

This appendix lists the multi-layered velocity-density models of the crust and upper mantle used in the computation of the local crustal corrections for the WWSSN stations used in the surface wave study in Chapter 5.

The following symbols are employed in the tables:

D = layer thickness in km

Alpha = compressional velocity in km/sec

Beta = shear velocity in km/sec

Rho = density in gram/cm^3.

References for the origin of the data used in the models are given below each table.

San Fernando Crust over Gutenberg Continent

D	Alpha	Beta	Rho
0.50	2.50	1.20	2.10
3.00	3.80	2.50	2.50
2.00	5.50	3.20	2.60
14.50	6.06	3.40	3.00
15.00	6.70	3.80	3.00
13.00	7.96	4.60	3.37
25.00	7.85	4.50	3.39
50.00	7.37	4.21	3.40
75.00	8.00	4.41	3.45
50.00	8.20	4.50	3.47
100.00	8.40	4.60	3.50
100.00	9.00	4.95	3.63
100.00	9.63	5.31	3.89

Source: Jungels (1973), Gutenberg (1944), Wood and Richter (1933), Harkrider *et al.* (1963).

Greenlandic Shield with Ice Cap

D	Alpha	Beta	Rho
2.50	3.93	1.94	0.91
16.50	6.25	3.74	2.80
23.70	6.60	3.85	2.85
37.30	8.05	4.67	3.30
25.00	8.10	4.72	3.30
100.00	8.20	4.54	3.44
100.00	8.30	4.51	3.53
80.00	8.70	4.76	3.60
100.00	9.30	5.12	3.76

Source: Gregersen (1970), Brune and Dorman (1963).

Iceland

D	Alpha	Beta	Rho
4.50	4.70	2.70	2.60
3.50	6.30	3.60	2.80
10.00	6.71	3.90	3.08
10.00	7.38	4.30	3.15
50.00	8.00	4.68	3.30
160.00	7.90	4.40	3.35
100.00	8.20	4.58	3.40
200.00	8.20	4.68	3.40

Source: Tryggvason (1962), Båth (1960), Tryggvason and Båth (1961), Tryggvason (1973).

Irish Continental Shelf

D	Alpha	Beta	Rho
0.50	1.52	0.00	1.03
1.50	2.20	1.57	2.55
2.00	5.40	3.18	2.70
20.00	6.10	3.55	2.82
6.00	7.30	4.21	3.10
50.00	8.10	4.61	3.30
100.00	8.10	4.40	3.40
100.00	8.10	4.60	3.55
200.00	8.10	4.89	3.60

Source: Blundell and Parks (1969), Bamford (1971).

Iberian Shield

D	Alpha	Beta	Rho
2.00	3.40	2.00	2.30
18.00	5.90	3.50	2.80
10.00	6.60	3.70	2.90
20.00	7.60	4.50	3.30
30.00	8.10	4.70	3.35
100.00	8.15	4.20	3.40
100.00	8.49	4.77	3.53
100.00	8.81	4.89	3.60
200.00	8.81	4.89	3.60

Source: Payo (1970), Payo (1964).

Mid-Atlantic Ocean

D	Alpha	Beta	Rho
4.50	1.51	0.00	1.03
0.05	1.52	0.15	1.65
0.10	1.60	0.19	1.70
0.10	1.71	0.37	1.79
0.10	1.80	0.53	1.86
2.00	5.00	2.85	2.66
4.50	6.69	3.90	3.06
50.00	8.00	4.68	3.30
160.00	7.90	4.60	3.35
200.00	8.20	4.68	3.40

Source: Ewing (1969), Talwani *et al.* (1965), Ewing *et al.* (1966), Katz and Ewing (1956), Officer *et al.* (1952).

Western America Tectonic

D	Alpha	Beta	Rho
2.50	3.00	1.73	2.40
24.50	6.20	3.58	2.83
13.00	6.80	3.87	2.99
45.00	7.80	4.25	3.30
50.00	8.20	4.38	3.43
100.00	8.20	4.38	3.52
100.00	8.20	4.50	3.57
100.00	8.20	4.70	3.62

Source: Kanamori (1970), Bucher and Smith (1971), Alexander (1963), Ewing and Press (1959), Heezen (1972).

Pacific Ocean East

D	Alpha	Beta	Rho
3.80	1.51	0.00	1.03
0.01	1.52	0.15	1.65
0.10	1.60	0.19	1.70
0.10	1.71	0.37	1.79
0.10	1.80	0.53	1.86
1.30	5.07	2.88	2.67
5.00	7.20	3.98	2.90
50.00	8.00	4.68	3.30
60.00	7.90	4.60	3.35
100.00	7.90	4.60	3.35
200.00	8.20	4.68	3.40

Source: Piermattei and Nowroozi (1969), Santo (1963), Saito and Takeuchi (1966), Dorman et al. (1960), Raitt (1956), Ewing et al. (1969), Latham and Nowroozi (1968), Kovach and Press (1961).

Pacific Ocean West

D	Alpha	Beta	Rho
5.50	1.51	0.00	1.03
0.10	1.60	0.30	1.65
0.70	5.07	2.88	2.67
4.50	7.20	3.98	2.90
50.00	8.20	4.72	3.30
60.00	7.90	4.40	3.35
100.00	7.90	4.40	3.35
200.00	8.50	4.74	3.40

Source: Piermattei and Nowroozi (1969), Santo (1963), Saito and Takeuchi (1966), Dorman et al. (1960), Raitt (1956), Ewing et al. (1969), Latham and Nowroozi (1968).

Andean

D	Alpha	Beta	Rho
5.00	5.00	2.88	2.67
15.00	6.00	3.46	2.87
25.00	6.60	3.58	2.99
100.00	7.90	4.45	3.30
100.00	8.00	4.40	3.32
100.00	8.00	4.40	3.32
100.00	8.20	4.67	3.38
100.00	8.20	4.68	3.38

Source: James (1971), Fisher and Raitt (1962), Cisternas (1961).

Central Japan

D	Alpha	Beta	Rho
1.00	2.50	1.47	2.50
5.00	5.50	3.18	2.70
16.00	6.00	3.40	2.80
10.00	6.50	3.70	3.00
30.00	7.70	4.37	3.20
100.00	8.00	4.50	3.30
200.00	8.00	4.50	3.30

Source: Kaminuma (1966), Mikumo (1966), Asada and Asano (1972), Kurita (1971).